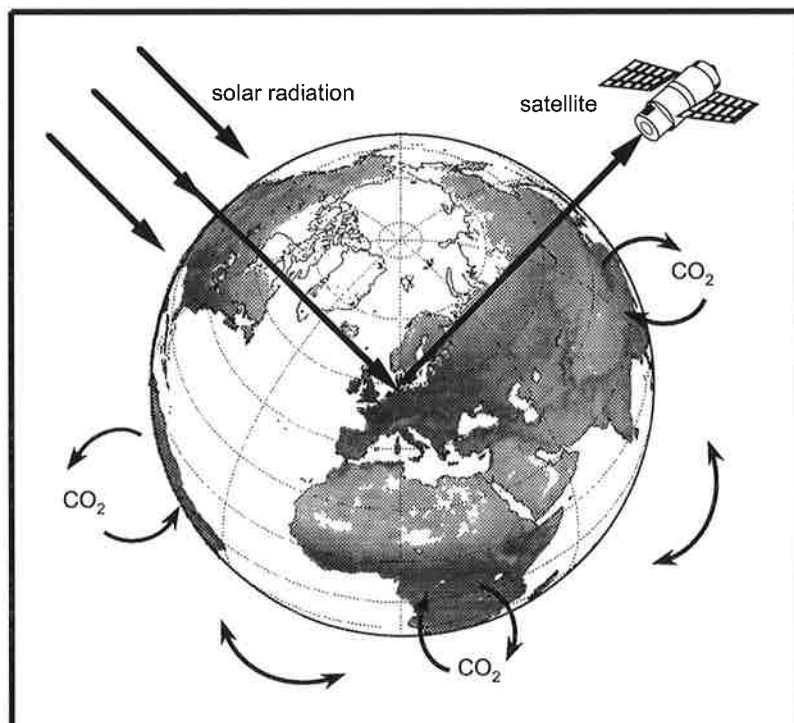




Max-Planck-Institut für Meteorologie

EXAMENSARBEIT Nr. 49



SATELLITE REMOTE SENSING AND MODELLING OF THE GLOBAL CO₂ EXCHANGE OF LAND VEGETATION: A SYNTHESIS STUDY

by
Wolfgang Knorr

English Edition
HAMBURG, January 1998

Doctoral thesis

Author:

Wolfgang Knorr

Geowissenschaften
der Universität Hamburg
Bundesstraße 55
D- 20146 Hamburg
Germany

MAX-PLANCK-INSTITUT
FÜR METEOROLOGIE
BUNDESSTRASSE 55
D - 20146 HAMBURG
GERMANY

Tel.: +49-(0)40-4 11 73-0
Telefax: +49-(0)40-4 11 73-298
E-Mail: <name> @ dkrz.de

Satellite Remote Sensing
and
Modelling of the Global CO₂ Exchange
of Land Vegetation:
A Synthesis Study

Doctoral thesis
submitted to the Faculty of Earth Sciences
of the University of Hamburg

by

Wolfgang Knorr

Hamburg
1997

This is the translation into English of the following PhD thesis: Knorr W. 1997. *Satellitengestützte Fernerkundung und Modellierung des globalen CO₂-Austauschs der Landvegetation: Eine Synthese*. Max-Planck-Institut für Meteorologie, Examensarbeit Nr. 49.

It was accepted by the Faculty of Earth Sciences of Hamburg University

after examination by Prof. Dr. K. Hasselmann
and Dr. M. Heimann

Hamburg, 18 June 1997

Prof. Dr. J.O. Backhaus
Representative of the Faculty of Earth Sciences

für Bettina

The best of man is like water,
Which benefits all things, and does not contend with them,
Which flows in places that others disdain,
Where it is in harmony with the Way.

LAO-TSE

Abstract

The terrestrial biosphere is believed to play a prominent role in the global carbon cycle at time scales from one year to several decades. Consequently, models are required that simulate vegetation activity on a global scale and are able to predict biogeochemical fluxes of plant and soil carbon, CO₂ and various isotopes.

However, recent biosphere model intercomparisons, some initiated by the International Biosphere Geosphere Programme (IGBP), have shown large discrepancies in model results, such as net primary production (NPP) or the net vegetation-atmosphere CO₂ flux. Those discrepancies probably arise from considerable conceptual uncertainties regarding how vegetation activity should be represented on large spatial scales. As a consequence, reliable validation strategies are needed in order to increase confidence in global vegetation models and eventually allow predictions into the future.

Long-term and global measurements of visible and near-infrared reflectances of the earth's surface carried out on board a series of NOAA polar orbiting satellites constitute a particularly well suited data set to check and improve global vegetation models. Such data have often been converted to vegetation indices (e.g. NDVI) and then translated into biophysical quantities, such as LAI or biomass. This approach, however, leads to serious problems of accuracy, because viewing conditions, soil background colour and atmospheric conditions have a large impact on the signal.

Such difficulties have so far seriously impeded quantitative exploitation of satellite data. Therefore, a different strategy is adopted in the present work that is able to avoid such problems to a large extent. Instead of using satellite measurements directly as input data, the study aims at a synthesis of vegetation modelling and remote sensing technology. It is decisive that the vegetation model developed in this context can be run on its own, without reference to satellite data.

The strategy consists of predicting the satellite signal by a combination of vegetation and radiative transfer models. It is thus possible to consider both errors in the process of measurement and uncertainties of vegetation modelling. As a next step, the model is constrained such that measurements and simulations agree within the estimated range of uncertainties. Only with this approach, quantifiable indications of the usefulness of satellite data for vegetation carbon-cycle modelling can be delivered.

The model developed within the context of this work simulates the photosynthetic rate of land plants embedded within a full energy and water budget of the earth's surface. The link between CO₂ uptake and water loss by transpiration through stomatal control is represented explicitly. Plant and soil respiration are also calculated. Various results with two photosynthesis schemes and different vegetation maps are compared, and the sensitivity of the model against uncertainties implied in several parametrisations is assessed. Mean global NPP is thus calculated to be 76 GtC (billion tons of carbon) with an error estimate of ± 50 GtC. It appears that the large scatter range between models mentioned above is a

true result of cumulated uncertainties involved in a mechanistic description of vegetation activity.

A comparison of simulated satellite data with measurements shows good agreement for most vegetation zones. Deviations exist for boreal coniferous forests (too "green" in the model), tundra (too barren) and for the contrast between wet and dry season in the tropics (too large). Human impact can also be detected in some instances. A constraint of model calculations to fit the satellite data reduces the global error estimate in NPP to ± 36 GtC. The impact is largest for needle-leaved forests and tropical savannas. This version of the vegetation model agrees with conclusions by other authors that large parts of the tropical rainforests depend on large soil water storage during the dry season.

Results are checked against the seasonal cycle of atmospheric CO₂ concentration through an atmospheric tracer transport model. Transport is prescribed from routine weather forecasts of high accuracy. It appears that within the modelling uncertainties, the simulations that have been constrained by satellite data all agree with CO₂ measurements – within the error implied by this test. By comparison, there is less agreement for the mean unconstrained simulation, and some simulations within the uncertainty range of the unconstrained model versions clearly contradict the measurements.

The conclusion is that on a global scale, satellite data have at least the same value for determining vegetation activity as have CO₂ measurements in the free atmosphere. In highly productive but water limited areas, most threatened by human impact or a possible climate change, their usefulness is particularly large. Because a multitude of micrometeorological and optical factors can influence the signal, a quantitative interpretation of those data is made possible only by a synthesis of observations and vegetation model simulations. At present, these two data sets probably constitute the main constraint we have on vegetation models.

Contents

| | | |
|----------|--|-----------|
| 1 | Introduction | 1 |
| 1.1 | Scientific background | 1 |
| 1.2 | The aim of this work | 2 |
| 1.3 | The global carbon cycle | 3 |
| 1.4 | Satellite remote sensing | 5 |
| 1.5 | Scientific question and method | 7 |
| 2 | The Vegetation Model BETHY | 10 |
| 2.1 | Model Requirements | 10 |
| 2.2 | Overview of the model structure | 10 |
| 2.3 | Input data: climate and soils | 13 |
| 2.4 | Vegetation maps and vegetation-specific parameters | 14 |
| 2.5 | Energy and water balance | 22 |
| 2.6 | Photosynthesis models: Monteith and Farquhar | 46 |
| 2.7 | Carbon balance | 53 |
| 2.8 | Phenology | 57 |
| 3 | Model Results and Comparison with Field Studies | 60 |
| 3.1 | Overview and definitions | 60 |
| 3.2 | Vapour pressure variability | 65 |
| 3.3 | Global results and sensitivity | 66 |
| 3.4 | Diurnal course of photosynthesis and canopy conductance compared to field measurements | 78 |
| 3.5 | Comparison with soil water measurements | 81 |
| 3.6 | Comparison with direct measurements of net primary productivity | 81 |
| 4 | Model Validation with Remote Sensing Data | 87 |
| 4.1 | Introduction | 87 |
| 4.2 | Data collection and processing | 93 |
| 4.3 | Versions of the vegetation model BETHY | 99 |
| 4.4 | First comparison: LAI-GEMI | 100 |
| 4.5 | The method of model validation | 104 |

| | | |
|----------|---|------------|
| 4.6 | Comparison of simulated and measured vegetation indices | 107 |
| 4.7 | Conclusions | 115 |
| 5 | Model Constraint with Remote Sensing Data | 117 |
| 5.1 | The method of model constraint | 117 |
| 5.2 | Computed FPAR-vegetation index relationships | 118 |
| 5.3 | The strategy of model constraint | 123 |
| 5.4 | Results | 127 |
| 5.5 | Error analysis | 134 |
| 5.6 | Summary and conclusions | 139 |
| 6 | A Consistency Check with CO₂ Measurements | 140 |
| 6.1 | Method and model versions | 140 |
| 6.2 | Results | 145 |
| 6.3 | CO ₂ data for model constraint | 154 |
| 6.4 | First concluding remarks | 158 |
| 7 | Summary and Further Applications | 161 |
| 7.1 | Summary of results | 161 |
| 7.2 | Outlook at further applications | 162 |
| 7.3 | Concluding remark | 164 |

List of Tables

| | | |
|-----|--|-----|
| 2.1 | List of vegetation types and parameters. | 16 |
| 2.2 | Land cover types and their associated vegetation types. | 18 |
| 2.3 | Land cover types and associated vegetation types for the remote sensing derived map. | 19 |
| 2.4 | Values for soil albedo. | 33 |
| 2.5 | Results of a curve fit to measurements of canopy conductance. | 42 |
| 2.6 | Parameters and constants for C3 and C4 photosynthesis calculations. | 49 |
| 3.1 | Description of the standard version '0' of the vegetation model BETHY. . . | 61 |
| 3.2 | Description of model variants of BETHY. | 63 |
| 3.3 | Daily average humidity for sufficient and limited evapotranspiration. | 66 |
| 3.4 | Gross (GPP) and net primary productivity (NPP) of the standard run '0' and NPP of version 'Pm'. | 68 |
| 3.5 | Comparison of the annual NPP for differences of initialisation and spatial as well as temporal resolution. | 77 |
| 3.6 | Mean results of canopy photosynthesis and conductance. | 80 |
| 4.1 | Channels of the AVHRR instrument on Board NOAA-11 with their spectral ranges and their significance for the remote sensing of land surfaces. | 95 |
| 4.2 | Description of some additional variants of the vegetation model BETHY. . . | 99 |
| 4.3 | Common parameters used for the calculation of synthetic satellite data. . . | 106 |
| 4.4 | Size parameters and leaf angle distribution of vegetation for the calculation of synthetic satellite data. | 107 |
| 5.1 | Parameters, correlation coefficient and standard error of the linear regression of FPAR against GEMI, NDVI and SR. | 119 |
| 5.2 | Test of the linear relationship between FPAR and GEMI for monthly maxima. . . | 122 |
| 5.3 | Prognostic and diagnostic net primary productivity sorted by vegetation type. . . | 130 |
| 5.4 | Mean and estimated error of the annual net primary productivity for different climate zones and globally. | 135 |
| 5.5 | Mean and estimated error of the annual NPP by vegetation type. | 137 |
| 6.1 | Test variants of the vegetation model BETHY concerning soil respiration. . . | 144 |

| | | |
|-----|--|-----|
| 6.2 | CO ₂ monitoring sites, from north to south. | 145 |
| 6.3 | Mean normalised deviation for the diagnostic standard version and the test variants of soil respiration. | 150 |
| 6.4 | Mean deviation from the observed CO ₂ seasonal cycle for the prognostic and the diagnostic model calculations with BETHY. | 153 |

List of Figures

| | | |
|------|--|----|
| 1.1 | Measured CO ₂ concentration at Mauna Loa station, Hawaii | 4 |
| 1.2 | Diagram illustrating the global carbon cycle. | 5 |
| 1.3 | An illustration of passive remote sensing with satellites | 6 |
| 2.1 | Structure of the BETHY model with input and output. | 11 |
| 2.2 | Energy and water balance of the BETHY model. | 26 |
| 2.3 | Respiration costs of vegetation and carbon content. | 54 |
| 2.4 | Respiration costs of vegetation and nitrogen content. | 55 |
| 3.1 | Position of measurement sites. | 64 |
| 3.2 | Simulated and measured daily average of absolute humidity. | 65 |
| 3.3 | Map of vegetation types. | 67 |
| 3.4 | Equal-area map of annual net primary productivity of the standard run '0' in gC per year and m ² | 69 |
| 3.5 | Sensitivity of the model for different photosynthesis schemes and respiration costs. | 70 |
| 3.6 | Sensitivity of the model for different vegetation maps. | 71 |
| 3.7 | Sensitivity of the model for different weather generator modes. | 71 |
| 3.8 | Sensitivity of the global annual NPP against various test versions. | 73 |
| 3.9 | Map of the defined climate zones. | 74 |
| 3.10 | Sensitivity for the mean annual NPP of the arctic zone. | 75 |
| 3.11 | Sensitivity for the mean annual NPP of the wet-temperate zone. | 75 |
| 3.12 | Sensitivity of the mean annual NPP of the arid zone. | 76 |
| 3.13 | Sensitivity for the mean annual NPP of the wet-tropical zone. | 76 |
| 3.14 | Measured and simulated canopy photosynthesis rate. | 79 |
| 3.15 | Measured and simulated canopy conductance. | 79 |
| 3.16 | Measured and simulated plant-available soil water content. | 82 |
| 3.17 | Measured annual NPP against simulated values. | 83 |
| 3.18 | Means and 90% confidence range of simulated and measured annual NPP. | 84 |
| 3.19 | Simulated and measured annual NPP for tropical grasses. | 84 |
| 3.20 | Difference and root mean-squared deviation between simulated and measured annual NPP differentiated by model version. | 85 |

| | | |
|------|--|-----|
| 4.1 | Spectral dependence of the reflectance for various surfaces. | 88 |
| 4.2 | Ratio of the reflectances between near-infrared and red, simulated with a bidirectional reflectance model for soil and vegetation. | 90 |
| 4.3 | Dependence of the vegetation indices GEMI, NDVI and SR on fractional cover for some characteristic values for the reflectances of soil and dense vegetation. | 94 |
| 4.4 | Example of GEMI from Hamburg and the rest of the world. | 98 |
| 4.5 | Monthly time series of GEMI at the equator. | 101 |
| 4.6 | Measured GEMI for non-vegetated and fully vegetated areas. | 102 |
| 4.7 | Latitudinal average of GEMI for non-vegetated and fully vegetated areas. | 103 |
| 4.8 | A diagram illustrating the proposed logic for using remote sensing data as a check on vegetation models. | 105 |
| 4.9 | Measured and simulated values of the vegetation index GEMI for March 1989. | 108 |
| 4.10 | Measured and simulated values of the vegetation index GEMI for July 1989. | 109 |
| 4.11 | Latitudinal average of measured and simulated monthly maxima of GEMI over non-vegetated and fully vegetated areas. | 110 |
| 4.12 | Latitudinal average of measured and simulated monthly maxima of GEMI with different versions of the water balance of tropical vegetation. | 112 |
| 4.13 | Latitudinal average of measured and simulated monthly maxima of GEMI with varying length of growing season. | 112 |
| 4.14 | Check of the simulated GEMI against the satellite derived value of 1989 for version 'x0' of the vegetation model. | 114 |
| 4.15 | Check of the simulated GEMI against the satellite derived value without deep roots for the evergreen tropical rainforest. | 115 |
| 5.1 | A diagram illustrating the proposed logic for using remote sensing data as a constraint for vegetation models. | 118 |
| 5.2 | Relationship between FPAR and various vegetation indices calculated with NADIWAS. | 120 |
| 5.3 | Number of valid monthly GEMI measurements on 1 degree latitude by longitude for the years 1989 and 1990. | 123 |
| 5.4 | Fractional cover assumed for the diagnostic simulation. | 124 |
| 5.5 | Computed relationship between FPAR and LAI. | 126 |
| 5.6 | Mean squared deviation between simulated and remote sensing derived FPAR without and with adaptation to the satellite data. | 128 |
| 5.7 | Mean and 90% confidence range of measured annual NPP compared to prognostic and diagnostic simulations. | 129 |
| 5.8 | Diagnostically computed annual NPP according to version 'd0' of the vegetation model BETHY and the difference to the corresponding prognostic version 'x0'. | 131 |

| | | |
|------|--|-----|
| 5.9 | Latitudinal average of the NPP of the prognostic and diagnostic model versions with photosynthesis according to Farquhar and Monteith. | 132 |
| 5.10 | Sensitivity of the prognostic and diagnostic model versions against various uncertainties in model parameters. | 133 |
| 5.11 | Estimated error of the NPP of the prognostic and diagnostic model versions. | 136 |
| 5.12 | Calculated maximum water content available for plants. | 138 |
| | | |
| 6.1 | Diagram illustrating model validation with measurements of the atmospheric CO ₂ concentration. | 141 |
| 6.2 | Position of the CO ₂ monitoring stations. | 143 |
| 6.3 | Observed seasonal cycle of CO ₂ concentrations and simulations for oceanic fluxes, fossil fuels and two variants of the vegetation model. | 146 |
| 6.4 | Observed and simulated seasonal cycle of CO ₂ concentrations for three test versions of soil respiration. | 148 |
| 6.5 | Observed and simulated CO ₂ cycle for two more test versions of soil respiration. | 149 |
| 6.6 | Comparison of the error range of the diagnostic versions in the simulated CO ₂ cycle with two extreme variants of the vegetation model. | 151 |
| 6.7 | Sensitivity of the seasonal cycle of CO ₂ against plant respiration. | 151 |
| 6.8 | Sensitivity of the seasonal cycle of CO ₂ against rooting depth. | 152 |
| 6.9 | Sensitivity of the seasonal cycle of CO ₂ for different parametrisations of phenology. | 152 |
| 6.10 | Mean and error range of the simulated seasonal cycle of CO ₂ for the prognostic versions of BETHY. | 155 |
| 6.11 | Mean and error range of the simulated seasonal cycle of CO ₂ for the diagnostic versions of BETHY. | 156 |
| 6.12 | The contribution of various vegetation types to the seasonal cycle at different stations. | 157 |
| 6.13 | Latitudinal average of the net CO ₂ flux and its annual course for five vegetation models and the diagnostic standard version of BETHY. | 159 |
| | | |
| A.1 | Check of the simulated GEMI against the satellite derived value of 1990. . . | 165 |
| A.2 | Measured and simulated values of the vegetation index GEMI for March and July 1990. | 166 |

Glossary

AVHRR: Advanced Very High Resolution Radiometer, instrument on board the NOAA series of satellites.

C3: Photosynthetic pathway of most land plants, with \rightarrow Rubisco as the primary CO_2 fixating enzyme.

C4: Photosynthetic pathway of many grasses growing in dry and warm environments, where CO_2 is first bound by the highly efficient enzyme \rightarrow PEPcase and stored in the form of malic acid, in order to be fixated again in the chloroplasts of the bundle sheath cells, in the same way as in \rightarrow C3 plants.

CL: Cramer-Leemans (climate data set).

MI: Moisture index, precipitation divided by potential evapotranspiration.

FC: Fractional cover, vegetated area divided by total ground area.

FPAR: The fraction of \rightarrow PAR absorbed by plants.

GEMI: Global Environment Monitoring Index, an advanced vegetation index for \rightarrow AVHRR data.

GPP: Gross primary productivity, equal to the gross photosynthesis rate (with photo respiration subtracted).

IGBP: International Geosphere-Biosphere Programme.

ISCCP: International Satellite Cloud Climatology Project.

LAD: Leaf angle distribution.

LAI: Leaf area index, one-sided leaf area per ground area.

NADIWAS: New Advanced Discrete model With Anisotropic Soil, model to simulate the reflectance at the earth surface.

NDVI: Normalised Difference Vegetation Index, traditional vegetation index.

NPP: Net primary productivity, \rightarrow GPP minus plant respiration.

PAR: Photosynthetically active radiation, portion of the visible light spectrum that is useful for photosynthesis.

PEPcase: Phosphoenol pyruvate carboxylase (\rightarrow C4 photosynthesis).

RES: Soil respiration. CO_2 release by soil organisms during decomposition of organic material.

Rubisco: Ribulose biphosphate carboxylase oxygenase (\rightarrow C3, C4)

SR: Simple Ratio, vegetation index.

GDD: Growing degree days.

a_s : Grade of absorption by the soil (for total solar spectrum).

$a_{s,0}$: Grade of absorption by the soil below dense vegetation.

a_v : Grade of absorption by vegetation.

b_e : Parameter of stomatal control.

c_i : Simulated CO₂ concentration in the free atmosphere.
 \bar{c}_i : Average of the $\rightarrow c_i$ simulations.
 $c_{i,obs}$: Measured CO₂ concentration in the free atmosphere.
 c_p : Specific heat of air at constant pressure ($\approx 1005 \text{ J kg}^{-1}\text{K}^{-1}$).
 c_w : Maximum supply rate of the root system (ca. 1 mm/h).
 d : Time in days, Julian day number.
 d_{fr} : Depth to which the soil is assumed frozen.
 d_{PAR} : The direct portion of \rightarrow PAR.
 d_{top} : Depth for the calculation of the soil albedo (10 cm).
 d_i : Depth of the i 'th soil layer.
 d_r : Rooting depth.
 d_s : Direct portion of $\rightarrow R_s$.
 e_a : Vapour pressure in air.
 e_{a0} : Daily minimum of vapour pressure in air.
 e_s : Saturation vapour pressure.
 e_v : Evergreen fraction of vegetation.
 f_1^{sand} : Sand fraction of the topmost soil layer.
 f_c : Fractional cover, \rightarrow FC.
 f_c^{eff} : Effective fractional cover, including shadows (light absorption).
 $f_{c,max}$: Maximum fractional cover.
 f_{C3} : Fraction of \rightarrow C3 grasses.
 f_{C4} : Fraction of \rightarrow C4 grasses.
 f_e : Ratio of actual to potential evapotranspiration.
 f_{PAR} : \rightarrow FPAR
 $f_{PAR,e}$: \rightarrow FPAR portion of evergreen vegetation.
 f_{PAR}^{max} : Maximum of the monthly means of \rightarrow FPAR.
 f_{Rd} : $\rightarrow R_{d,c} / \rightarrow A_{c,0}$.
 $f_{R,G}$: Growth respiration costs.
 $f_{R,leaf}$: Leaf fraction of total maintenance respiration.
 $f_{N,leaf}$: Leaf fraction of total plant nitrogen.
 $f_{R,0}$: Conversion factor from \rightarrow NPP to $\rightarrow A_{c,0}$.
 f_S : Shrub fraction of total vegetation.
 f_T : Tree fraction of total vegetation.
 f_v : Fraction of total vegetation assigned to vegetation type v .
 \bar{f}_w : Fraction of wet days on a monthly average.
 g : Surface gravity (9.81 m s^{-2}).
 g_s : Stomatal conductance.
 $g_{s,0}$: Stomatal conductance without water limitation.
 h : Height above mean sea level.

h_v : Vegetation height.
 \hat{h} : Relative amplitude of vapour pressure in air at potential evapotranspiration.
 h_0 : Relative humidity at sunrise and maximum soil drought.
 h_{sn} : Snow height.
 j^2 : Mean quadratic deviation of $\rightarrow c_i$ from $\rightarrow c_{i,obs}$ normalised by $\rightarrow \sigma_i^2$.
 k : CO₂ specificity of \rightarrow PEPcase (\rightarrow C4).
 k : von Karmann constant (0.41).
 l : Cumulative LAI counted from the surface (as z-axis in a canopy).
 n : Relative sunshine duration.
 n_c : Degree of cloudiness.
 n_s : Number of soil layers (for calculating the bucket size).
 p : Surface air pressure.
 p_0 : Standard air pressure at sea level (101.3 kPa).
 p_{wd} : Probability of a wet day following a dry day.
 p_{ww} : Probability of a wet day following a wet day.
 r^2 : Explained variance, square of the correlation coefficient.
 r_{C4} : Ratio of \rightarrow C4 grasses to the total amount of grasses.
 r_{PAR} : Ratio of potential to actual \rightarrow PAR.
 r_{PARd} : The ratio $\rightarrow r_{PAR}$ on dry days.
 r_{PARw} : The ratio $\rightarrow r_{PAR}$ on wet days.
 r_{\odot} : Sun-earth distance.
 s : Slope of the vapour pressure curve, $\rightarrow \partial e_s(T)/\partial T$.
 s_i^2 : Variance of the simulated value $\rightarrow c_i$.
 t : Time.
 $t_{l,v}$: Longwave transmissivity of vegetation.
 t_{PAR} : Atmospheric transmissivity for \rightarrow PAR.
 $t_{PAR,D}$: Transmissivity for the direct portion of \rightarrow PAR.
 t_s : Evaporation time (status variable of the Ritchie model).
 u : Wind speed above canopy.
 $w_{i,max}$: Capacity of skin reservoir per leaf area.
 A : Net photosynthesis rate, assimilation rate.
 A_0 : Assimilation rate without water limitation.
 $A_{c,0}$: Canopy assimilation rate without water limitation.
 C_a : CO₂ concentration in air.
 C_i : CO₂ concentration inside the leaf.
 $C_{i,0}$: CO₂ concentration inside the leaf without water limitation.
 $C_{i,min}$: Minimum CO₂ concentration inside the leaf (for Monteith photosynthesis scheme).
 C_{drm} : Carbon content of dry matter (0.45 gC/g).
 D : Demand for evapotranspiration.

E: Rate of evapotranspiration.
E: Activation energy for several variables (photosynthesis).
E_{eq}: Equilibrium evapotranspiration.
E_i: Evaporation from the skin reservoir on leaves.
E_s: Soil evaporation.
E_{s,max}: Potential soil evaporation.
E_{sn}: Snow evaporation.
E_{sn,max}: Potential snow evaporation.
E_t: Transpiration rate, evaporation through leaf stomata.
E_v: Evapotranspiration from vegetation ($\rightarrow E_t + \rightarrow E_i$).
E_{v,max}: Potential evapotranspiration from vegetation.
E_{PAR}: Energy content of \rightarrow PAR quanta (220 kJ/mol).
F: Conversion factor from solar radiation to \rightarrow PAR.
F_i: Mean daily degree of leaf wetting.
F_{dir}: Conversion factor for the direct portion of \rightarrow PAR.
G: Soil heat flux.
G_a: Aerodynamic conductance between the canopy and the reference height (10 m).
G_c: Canopy conductance (in m/s).
G_{c,0}: Canopy conductance without water limitation.
H: Sensible heat flux.
H_{eq}: Sensible heat flux at equilibrium evapotranspiration.
H_s: Sensible heat flux from the soil.
H_v: Sensible heat flux from the vegetation.
I_{PAR}: Rate of \rightarrow PAR absorption.
J: Electron transport rate.
J_C: Carboxylase limited assimilation rate (Farquhar model).
J_E: Electron transport limited assimilation rate (Farquhar model).
J²: Mean of $\rightarrow j^2$ over the error range of simulations.
J_c: Carboxylase limited assimilation rate (\rightarrow C4).
J_e: Combined electron transport and \rightarrow Rubisco limited rate (\rightarrow C4).
J_i: Electron transport limited assimilation rate (\rightarrow C4).
J_C: Carboxylase limited assimilation rate (Farquhar model).
J_E: Electron transport limited assimilation rate (Farquhar model).
K: Extinction coefficient (light absorption).
K₁₂: Extinction coefficient at noon (light absorption).
K_C: Michaelis-Menten constant of carboxylation.
K_O: Michaelis-Menten constant of oxygenation.
L: Lapse rate of the standard atmosphere (6 K/km).
M_a: molar mass of dry air (28.964 g/mol).

M_c : molar mass of carbon (12 gC/mol).
 N_v : Number of vegetation types at a model pixel.
 N_l : Number of layers for light absorption within a canopy.
 O_x : O_2 concentration inside the leaf.
 P : Precipitation rate.
 \bar{P} : Monthly mean of precipitation.
 P_i : Intercepted precipitation by vegetation.
 P_s : Precipitation rate arriving at the surface.
 P_{sn} : Snowfall.
 \bar{P}_w : Mean precipitation on wet days.
 Q : Heat stored in vegetation and canopy air.
 Q_B : Biochemical heat.
 Q_{10} : Soil respiration change factor at a temperature rise of 10°C .
 R : General gas constant ($8.314 \text{ J K}^{-1} \text{ mol}^{-1}$).
 R_\uparrow : Upward light flux within 2-flux scheme.
 R_\downarrow : Downward light flux within 2-flux scheme.
 R_d : Leaf or dark respiration.
 $R_{d,c}$: Canopy integral of dark respiration.
 R_s : Solar radiation.
 $R_{L\uparrow}$: Longwave radiation from the surface.
 $R_{L\downarrow}$: Longwave radiation from the atmosphere down to the surface.
 R_n : Net radiation balance.
 R_{ns} : Radiation balance of the surface.
 R_{nv} : Radiation balance of vegetation.
 R_{OA} : Solar radiation above the atmosphere.
 R_{PAR} : \rightarrow PAR at the surface.
 R_G : Growth respiration.
 R_M : Maintenance respiration.
 S : Water supply from the roots.
 S_0 : Solar constant (1360 Wm^{-2}).
 S_m : Rate of snow melt.
 T : Near-surface air temperature.
 \bar{T} : Daily average temperature.
 \hat{T} : Daily temperature amplitude.
 $T_{0.5}$: Soil temperature at 0.5 m depth.
 $T_{0.5max}$: Annual maximum of the monthly averages of $\rightarrow T_{0.5}$.
 $T_{1.5}$: Soil temperature at 1.5 m depth.
 T_K : Air temperature in Kelvin.
 \bar{T}^a : Annual mean temperature.

T_c : Average temperature of the coldest month.
 \hat{T}_d : Daily temperature amplitude on dry days.
 T_{min} : Daily temperature minimum.
 T_v : Canopy or vegetation temperature.
 T_w : Average temperature of the warmest month.
 \hat{T}_w : Daily temperature amplitude on wet days.
 T_ϕ : Phenological temperature for calculating $\rightarrow \Lambda_w$.
 \hat{T}_ϕ : Temperature saturation for calculating $\rightarrow \Lambda_w$.
 V_m : Maximum \rightarrow Rubisco capacity.
 W : Total water amount at the surface (snow, soil and skin reservoir).
 W_i : Amount of water on vegetation, skin reservoir.
 $W_{i,max}$: Maximum storage of the skin reservoir on leaves.
 W_s : Plant available amount of soil water.
 W_s^{eff} : Effective amount of soil water for calculating the supply rate, $\rightarrow S$.
 $W_{s,max}$: Maximum plant available soil water.
 W_{sn} : Snow amount.
 α : Efficiency of photon capture (0.28).
 α_i : Integrated C4 quantum efficiency (0.04, \rightarrow C4 photosynthesis).
 β : Forward scatter factor (light absorption).
 β_0 : Forward scatter factor for the direct beam (light absorption).
 γ : Psychrometric constant ($\approx 65 \text{ Pa K}^{-1}$).
 ϵ : light-use efficiency (Monteith photosynthesis scheme, Section 2.6).
 ϵ_O : Thermal surface emissivity (0.97).
 ϵ_{AO} : Thermal emissivity of the cloud-free atmosphere.
 η : Aspect ratio of vegetation (light absorption).
 θ : Curve parameter for $\rightarrow J_e$.
 θ_s : Solar zenith angle.
 θ_o : Zenith angle of observation (remote sensing).
 κ_s : Desorptivity of the soil (Ritchie model).
 λ : Latent heat of vaporisation (2.45 MJ kg^{-1} at 20°C).
 μ : Cosine of $\rightarrow \theta_s$.
 $\bar{\mu}$: Mean of $\rightarrow \mu$ over hemisphere (2-flux scheme).
 μ_{12} : Cosine of the solar zenith angle at noon up to 60° (snow albedo).
 ξ_{sn} : Density of old snow.
 ξ_{sn}^n : Density of new snow.
 ρ : Density of air ($\approx 1.29 \text{ kg m}^{-3}$).
 ρ_S : Surface reflectance (for total solar spectrum).
 ρ_s : Soil reflectance.
 ρ_s^{PAR} : Surface reflectance in the \rightarrow PAR region.

$\rho_{s,d}$: reflectance of dry soil.
 $\rho_{s,w}$: reflectance of wet soil.
 ρ_v : Albedo of densely vegetated surfaces.
 σ : Stefan-Boltzmann constant ($5.6703 \times 10^{-8} \text{ W m}^{-2} \text{ K}^{-4}$).
 σ_L : Specific leaf area, in m^2 per kg dry mass.
 σ_i^2 : Variance of $\rightarrow c_{i,obs}$.
 τ : Daylength in hours.
 ϕ : Geographical latitude.
 ω : Single scattering albedo of leaves (in \rightarrow PAR region).
 Γ_* : CO_2 compensation point without leaf respiration.
 Δe : Vapour pressure deficit in air.
 Δt : Time step (1 day).
 Λ : Leaf area index, \rightarrow LAI.
 $\hat{\Lambda}$: Maximum leaf area index.
 Λ_0 : \rightarrow LAI threshold for calculating $\rightarrow f_c$.
 Λ_C : Growth limited leaf area index.
 Λ_{NPPopt} : Leaf area index at maximum \rightarrow NPP.
 Λ_T : Temperature limited leaf area index.
 Λ_W : Moisture limited leaf area index.
 Λ_c : $\rightarrow \Lambda / \rightarrow f_c$.
 Λ_c^{eff} : $\rightarrow \Lambda / \rightarrow f_c^{eff}$.
 Λ_{max} : Annual maximum of the monthly values of $\rightarrow \Lambda$.
 ΣE_1 : Phase-1-evaporation (Ritchie model).
 ΣE_s : Soil evaporation sum (Status variable of Ritchie model).
 Φ : Rain and melt water runoff.

Chapter 1

Introduction

1.1 Scientific background

The continuous rise of the atmospheric carbon dioxide content, known since the late 1950's (Keeling 1960), and the threat of a sustained warming of the global climate (Houghton et al. 1996) have much boosted research into the various components of the global carbon cycle. A major part of this important biogeochemical system is the terrestrial biosphere, composed of photosynthetically active plants and the organic fraction of soils. This importance is underlined, for example, by the indication of a substantial sink for carbon dioxide within the northern biosphere that might absorb no less than a third of the amount that is being emitted from energy production (Schimel et al. 1996). Also, fluctuations of the atmospheric CO₂ content both within one year (Heimann and Keeling 1989) and over time spans of about a decade (Francey et al. 1995, Kaduk and Heimann 1994, Friedlingstein et al. 1995) seem to be caused primarily by terrestrial vegetation. Changes within the global carbon budget over longer periods can be even more drastic: It has been estimated that the carbon pool of the terrestrial biosphere has increased by a factor of 1.5 to 2 since the height of the last ice age, at approximately 21,000 years before present (Crowley 1995, Adams et al. 1990). During this time, the atmospheric content has risen from around 180 parts per million (ppm) to around 280 ppm (Barnola et al. 1987), until industrialisation has lead to a rapid increase to 360 ppm today (Etheridge et. al. 1996, Fig. 1.1). While the CO₂ produced by mankind is now probably being absorbed to even proportions by the atmosphere, the oceans, and the land biosphere (see below), the latest transition from ice age to a warmer climate has seen a massive transfer from the oceans into the atmosphere and the land biosphere.

There are two principle techniques being applied in the research of the global carbon cycle (Heimann 1997): On the one hand, measurements of trace gases in combination with various geological and biogeochemical methods are used to diagnose the present and past state of the system. This technique only uses very simple models. On the other hand, complex models are being constructed that represent laws of supposedly universal significance. Such models are then used to extrapolate from a few spatially distributed measurements to the

globe, and from the present state to past and future states of the system. However, this latter technique requires a well developed understanding of the underlying processes as well as a high degree of generalisation and simplification. While generalisation is just the nature of physical laws, for biological rules such a development is still much in its infancy (Walker and Steffen 1995, Körner 1991, Martin 1993). As a consequence, modelling the global carbon cycle, and in particular its biospheric component, is bound to have a high degree of uncertainty. Therefore, as far as the land biosphere is concerned, the two most urgent tasks are:

1. to define the present state more accurately;
2. to clarify which processes are most significant for accurate modelling.

At present, a whole range of mechanistic, i.e. process orientated, models exist, and there appears to be much consensus about which processes should be represented. However, the results of model calculations often diverge dramatically, as it has been demonstrated by a comparison initiated by the International Geosphere Biosphere Programme (IGBP, Kicklighter et al. 1997, Ruimy et al. 1997). A further comparison by Heimann et al. (1997) comes to the same conclusion. Such uncertainties, as suggested above, primarily reflect conceptual problems when extrapolating from findings in laboratory and small field studies to continental scales. Nevertheless, no estimate of the approximate error involved in those model calculations has yet been presented, since it has become customary to publish only one value for the productivity of vegetation per model grid point.

A particularly suitable data set for checking and possibly for improving such global vegetation models are long-term measurements of the optical reflectance at the earth's surface from satellites. For that reason, the IGBP has, among others, decided to archive such data globally and with a high spatial resolution (Townshend et al. 1994). Reflectance values are usually converted into so-called "vegetation indices" that are then translated into various biophysical quantities. However, this method leads to some serious problems concerning accuracy, since conditions of observation, soil background colour and the state of the atmosphere can significantly modify the signal (Verstraete 1994). Whether such data are suitable for improving vegetation models will therefore depend on the accuracy of vegetation modelling as well as on the accuracy of the satellite-based measurements.

1.2 The aim of this work

The aim of the present work follows the scientific questions raised above. First of all, it consists of the calculation of the CO₂ exchange fluxes between the land vegetation and the atmosphere on a global scale with a mean climate and for a time resolution of around one month. In other words, the contribution of the land biosphere to the global carbon cycle should be clarified.

Apart from the calculation of a mean value for these fluxes, estimating the possible error in those calculations is also an important goal of this study. Once this is done consistently within one model (instead of through comparison of different models, see above), those processes can be identified that contribute most to the uncertainties. Such information can then be of vital interest for the further development of such models, and for an increased understanding of the causes that lead to changes and fluctuations in the global carbon cycle.

It is a further aim of this work to develop a method for checking and improving such model calculations with the help of global observations. The data set used here consists of satellite measurements of reflected sunlight at the earth's surface. The use of another global data set – CO₂ measurements in the free atmosphere – is also discussed. Eventually, this work also intends to promote various techniques for the application of satellite data.

The work presented here should be seen as part of a comprehensive undertaking with the aim of developing a model of the complete global carbon cycle that can eventually be used for reliable predictions of the future. However, as for models of the general circulation of the atmosphere and the oceans, one of the prerequisites for acceptable predictions is a satisfactory representation of the present state. For this reason, the present work restricts itself to the present and uses global data sets for model validation as a major component. Hence it can be called a “diagnostic” study of the vegetation part of the earth's carbon cycle.

1.3 The global carbon cycle

The global carbon cycle essentially comprises the exchange of carbon between four pools: the atmosphere, the oceans, fossil carbon, and the land biosphere. The rapid and still accelerating rise of the atmospheric CO₂ content – with presently ca. 750 GtC (Gigatons of carbon, 1 Gt = 10¹² kg) – is probably the best documented change in the global carbon cycle caused by human activity. This is most clearly seen in long-term measurements on Hawaii by the National Oceanic and Atmospheric Administration (NOAA) of the USA (Keeling et al. 1996). This rise is shown in Fig. 1.1 together with the concentration that would exist, if all CO₂ from fossil fuel combustion had remained in the atmosphere since 1958, the beginning of the measurements. The yearly average of those emissions during the 1980's was 5.5 GtC, while the atmospheric value only increased by 3.2 GtC per year. The difference can largely be attributed to the oceans: Their uptake rate is estimated at around 2.0 GtC a⁻¹, with an uncertainty of 1 GtC a⁻¹ (Heimann 1997). According to this budget, the land biosphere appears to be close to equilibrium. However, statistics of deforestation indicate an additional human-created source of 1.6±1.0 GtC a⁻¹, primarily in the tropics (Houghton 1995). This source is compensated by regrowth of forests on former agricultural land in the temperate zone, and by a largely unknown sink, also in the north (Schimel 1997). This so-called “missing sink” is still an important stimulus for research.

In contrast to the longer-term fluxes explained above, the fluctuations seen in Fig. 1.1

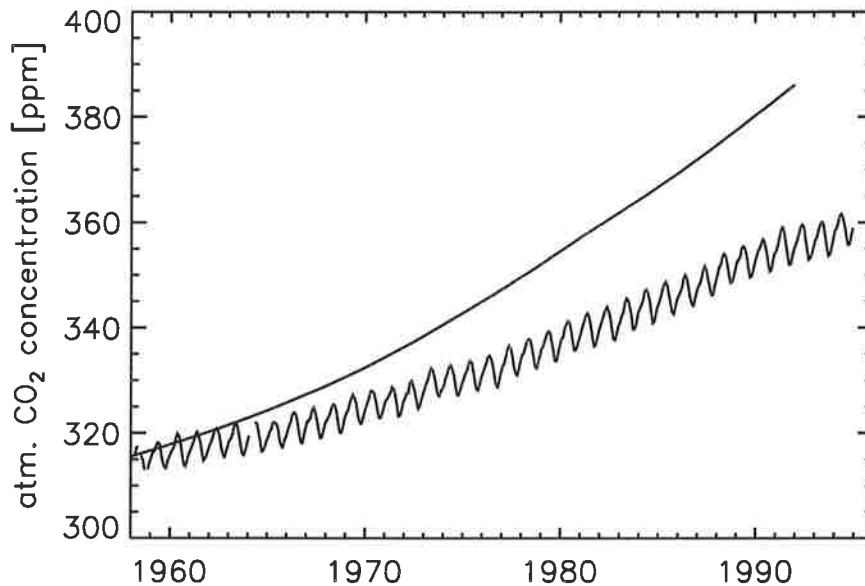


Figure 1.1: Measured CO₂ concentration at Mauna Loa station, Hawaii. For comparison, the upper curve indicates the cumulative emissions since 1958 from the combustion of fossil fuels.

a largely an expression of the photosynthesis of land vegetation (cf. Chapter 6). In this process, plants take up an annual amount of approximately 100 GtC, with around half of that being returned by plant respiration. This rate is much larger than the ones mentioned before, even though its size is still not very well known.

An overview of the global carbon cycle is offered by Fig. 1.2. Again it should be borne in mind that many of the numbers given carry large uncertainties with them, such as those 100 GtC for global photosynthesis. One of the well know facts is that the largest amount of carbon (ca. 38,000 GtC) resides within the deep ocean. The exchange with the surface ocean (ca. 1000 GtC pool size) is determined by the large-scale ocean circulation that runs on time scales of centuries. The surface ocean, i.e. the 50 m thick well mixed surface layer, is in diffusive contact with the atmosphere (ca. 750 GtC), so that several millennia after all fossil fuel has been used up (a few thousand GtC) there will be a new equilibrium between the atmosphere and the deep ocean with most of the carbon remaining in the ocean. For even longer time spans, the formation of sediments also plays a role, while the oceanic biosphere, which is only a very small pool (ca. 3 GtC), is of major significance for the seasonal exchange of CO₂ between the ocean surface layer and the atmosphere (Six and Maier-Reimer 1996). It also accelerates the transfer of carbon from the surface to the deep ocean.

The land biosphere represents the second largest active carbon pool within the system,

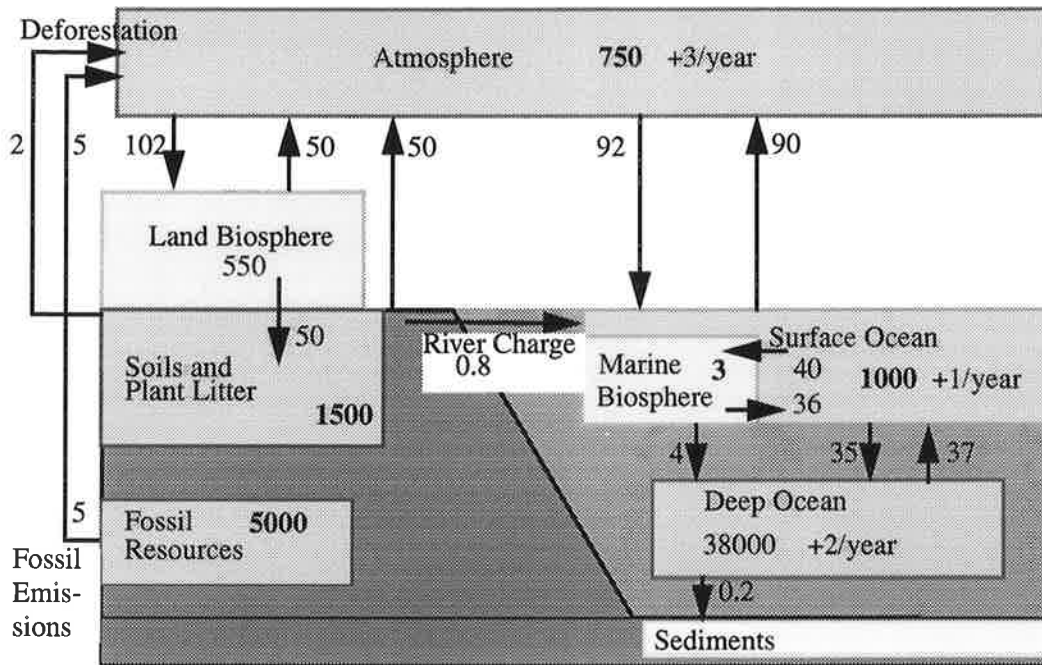


Figure 1.2: Diagram illustrating the global carbon cycle.

with a third of it made up of living plants, and two thirds of soil carbon and plant litter. As mentioned above, the size of this pool has changed significantly since the last ice age. On short time scales, fluxes are determined by the CO_2 uptake during plant growth and by fast decomposition of plant litter, whereas longer-term changes concern, among others, the build-up and decline of peat bogs, growth cycles of forests with fires and pest outbreaks, and succession, such as the intrusion of forests into steppes. Here, human influence can play an important role, e.g. through deforestation (see above) or the creation of arable land.

Such changes, however, only create fluxes that are small compared to uptake rates from photosynthesis (gross primary production, GPP) or the net uptake during plant growth (net primary production, $\text{NPP} = \text{GPP} - \text{plant respiration}$). In fact, NPP and decomposition of litter and soil carbon are in close balance over one year. Since only short-term exchanges will be investigated, this will be a basic assumption of this modelling study.

1.4 Satellite remote sensing

Fig. 1.3 illustrates the type of passive remote sensing used in this study, that is carried out by measuring the reflected sunlight coming from the earth's surface. A comprehensive introduction will be given in Section 4.1; therefore, it is enough to state here that the three angles given (θ_s , θ_v and $\Delta\phi$) as well as the atmosphere between sensor and surface can change the signal significantly, and that the contrast in reflectance between photosynthetically active light (red) and photosynthetically useless longer wave radiation (near infrared, NIR) can be related to the amount of living vegetation at the surface.

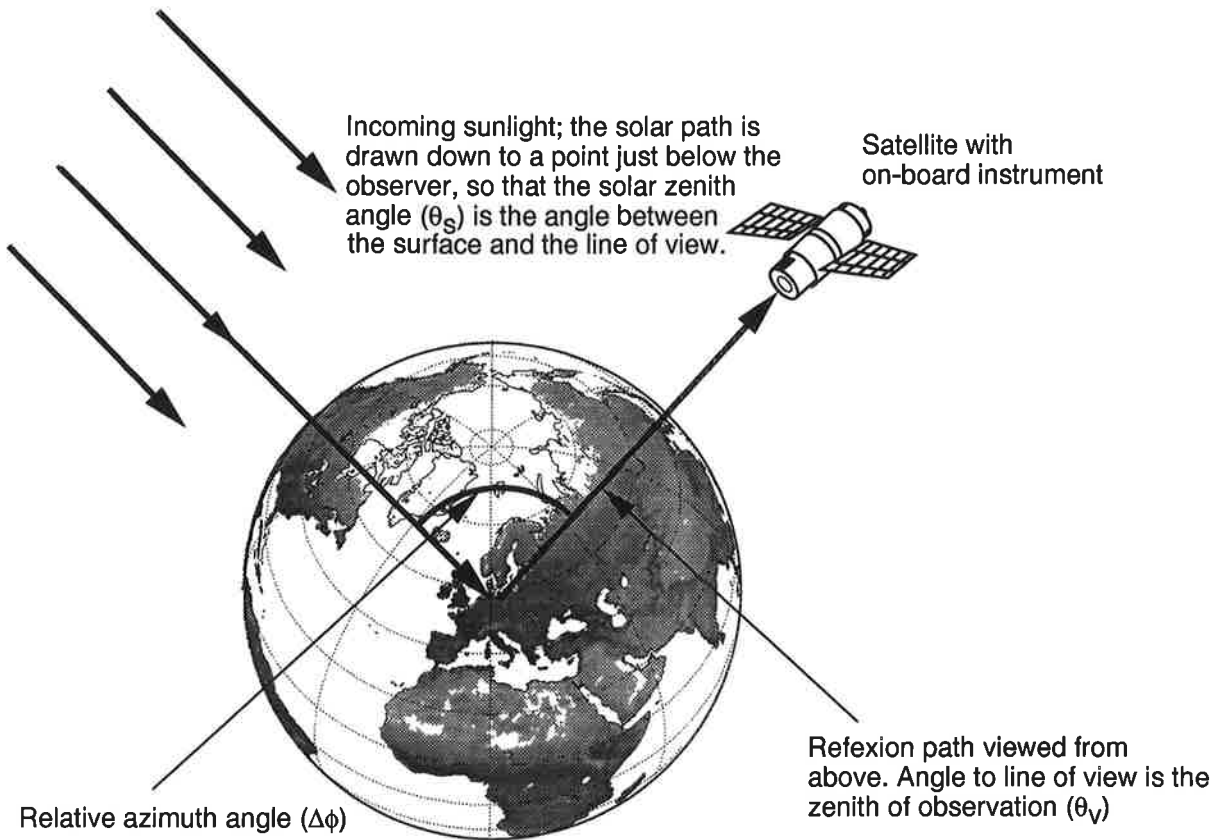


Figure 1.3: An illustration of passive remote sensing with satellites. Orbital height is strongly overstated (usually 800-900 km for polar orbits).

Three principle techniques for the validation of vegetation models with satellite data can be characterised: classification of land cover through time series analysis, calculation of the terrestrial energy budget or one of its components, and determination of the fraction of green vegetation on the land surface through optical contrast, as above. Since a global land type classification already exists (DeFries and Townshend 1994), Section 3.3 shows a comparison of calculations with this map and with another vegetation map derived from standard sources. The second technique is based on the fact that the energy budget and the closely connected water budget strongly determine the micrometeorological environment in which plants grow. In particular, evapotranspiration rates constitute a major limiting factor of photosynthesis (cf. Section 2.5). Relevant measurements have already been carried out within the Earth Radiation Budget Experiment (ERBE, Barkström 1984). A sensitivity analysis in Section 3.3 shows that net radiation is indeed one of the more significant factors for vegetation modelling.

The third technique, the one used in this work, is usually carried out through the formation of various vegetation indices, e.g. NDVI (normalised difference vegetation index), defined as reflectances $(NIR-Red)/(NIR+Red)$. However, no general concept exists that defines which quantity should be derived from the vegetation index. Various authors have

used biomass, leaf area, absorbed photosynthetically active radiation, potential photosynthetic rate, ratio of actual to potential evapotranspiration, and more. Clearly, a single value cannot deliver all of those quantities, unless they strongly correlate. In fact, the relationships used are only approximate, without an appropriate assessment of their accuracy. This question will be raised again in Chapter 4, where it will be shown that the fraction of absorbed red, i.e. photosynthetically active radiation is the best suited quantity, and that better results can be achieved with the Global Environment Monitoring Index (GEMI, Pinty and Verstraete 1992a), a more modern index than NDVI.

1.5 Scientific question and method

The aim set out in Section 1.2 will be investigated through the remaining part of this work by the following representative scientific question:

To what degree will the uncertainty that is associated with the mathematical modelisation of global vegetation activity change, if the model is constrained to satisfy the satellite observations used – within their own degree of accuracy?

The method employed for answering this question constitutes a first synthesis of global vegetation modelling with remote sensing data. Several steps have to be followed:

- (1) Relevant data sets are collected and a vegetation model is constructed that can calculate net primary production (NPP) and soil respiration (RES), as well as the quantities relevant for remote sensing observation of vegetation. This model should reflect the current state of mechanistic modelling, with the possibility of exchanging alternative model parts within it (Chapter 2).
- (2) The sensitivity of the results against variations of input data, model parameters and various model concepts is assessed and a possible error is calculated. Such simulations will be termed “prognostic” (Chapter 3).
- (4) Results of the vegetation model are translated into satellite observations through a remote sensing model. The possible error involved is also assessed (Sections 4.5 and 5.2).
- (5) The vegetation model is first checked against satellite data (Chapter 4) and then modified in such a way that predicted and measured values match within the accuracy of the measurements (Chapter 5). The error assessment is then repeated with the constrained model, a calculation that will be termed “diagnostic”.
- (6) The error ranges calculated before and after adapting the model to satellite data are compared (Section 5.5). In this way, the gain in accuracy from remote sensing is evaluated. For a consistency check of results with another set of globally comprehensive data, simulated CO₂ fluxes are fed into an atmospheric tracer transport model

and predicted and measured CO₂ concentrations at various monitoring stations are compared (Chapter 6).

Evidently, when constructing the vegetation model, already existing models should be checked for their suitability. Examples of relatively mechanistic models are SiB2 (Sellers et al. 1996), CARAIB (Warnant et al. 1994), Hybrid 3.0 (Friend et al. 1996), DOLY (Woodward et al. 1995) and SILVAN (Kaduk 1996). However, of those models only SiB2, Hybrid 3.0 and DOLY consider the full energy and water balance (cf. Section 2.5), which is essential for an error assessment of photosynthesis calculations. Of those three, Hybrid 3.0 is rather focused on processes of plant type succession, so that it tends to be too difficult to handle for the questions treated here. Further, SiB2 can only be run globally within a climate model, another serious obstacle for adapting this model directly, in particular as far as computing time is concerned. A decision against DOLY is eventually based on the observation that a link between leaf area and unstressed evapotranspiration as assumed in the model cannot be supported by empirical data (Kelliher et al. 1995, cf. Section 2.5). However, a fact that should be mentioned here is that all those models calculate CO₂ uptake with a biochemical model based on that of Farquhar et al. (1980, cf. Section 2.6); this model will also be used in the present work.

A more simplified photosynthesis model without the parametrisation of enzyme kinetics is used in the models TEM (Raich et al. 1991), BIOME-BGC (Running and Hunt 1993) and FBM (Lüdeke et al. 1994). There is another important group of models that can also be called semi-mechanistic (CASA: Potter et al. 1993, TURC: Ruimy et al. 1996, GLO-PEM: Prince and Goward 1996), in which photosynthesis is calculated following a concept of Monsi and Saeki (1953) and Monteith (1965a). Here, NPP is calculated as the product of absorbed solar radiation and a, usually vegetation dependent, light-use efficiency (cf. also Section 2.6), with the degree of absorption by vegetation being estimated from satellite data. Since this absorption has to be calculated prognostically in the present work, such models cannot be applied directly; however, the Monteith photosynthesis scheme will be used as an alternative possibility alongside the Farquhar model.

It seems appropriate to name also a number of correlative models that calculate NPP directly from climate variables: the MIAMI model (Lieth 1975, p. 238 ff.; based on this OBM, Esser 1991, HRBM, Esser et al. 1994, and models by Dai and Fung 1993, and Friedlingstein et al. 1995) and the grassland model of Sala et al. (1988). Those models do neither represent quantities that can be monitored from space, as for example leaf area, nor any of the processes considered in mechanistic models; this does not, however, imply that they are less accurate.

Finally it is also hoped that the method developed within this study will deliver some additional results that go beyond the topic of global carbon cycle research:

- The sensitivity studies should indicate useful hints for ecophysiologicals concerning the importance of various physiological and micrometeorological processes from a global

perspective.

- The error analysis should serve the general question of whether vegetation processes can be modelled with reasonable accuracy for investigations of the global carbon cycle.
- Quantitative methods for the remote sensing of vegetation should be promoted.

Chapter 2

The Vegetation Model BETHY

2.1 Model Requirements

From the goals set out in the preceding chapter, and the course of action derived from them, it becomes evident that the model should meet the following requirements:

- (1) The model computes net primary productivity (NPP) and soil respiration (RES) monthly and with a time step similar to the time resolution of global remote sensing data.
- (2) State variables of vegetation that can be observed through remote sensing are modelled explicitly, in particular fractional cover (FC) and leaf area index (LAI). This leads to the exclusion of correlative models.
- (3) Description of processes should be as mechanistic as possible and should reflect the current state of ecosystem modelling. This is meant to facilitate portability to changed conditions and easy extension of the model.
- (4) It should be possible to quantify uncertainties of the simulated microclimate through parameter variation. Uncertainties of the way how processes should be described may be considered by choosing between alternative model components.

In the following sections, a model will be presented that meets the above requirements as far as this can be done with acceptable effort. Following a general overview, a detailed account of the various model components is given.

2.2 Overview of the model structure

The model chosen here is called the “Biosphere-Energy-Transfer-Hydrology” model, abbreviated BETHY. It simulates CO₂ uptake by vegetation as a process that is simultaneously limited by light, heat, soil water and nitrogen. Light limitation is considered by the computation of incoming and absorbed photosynthetically active radiation (PAR) and heat

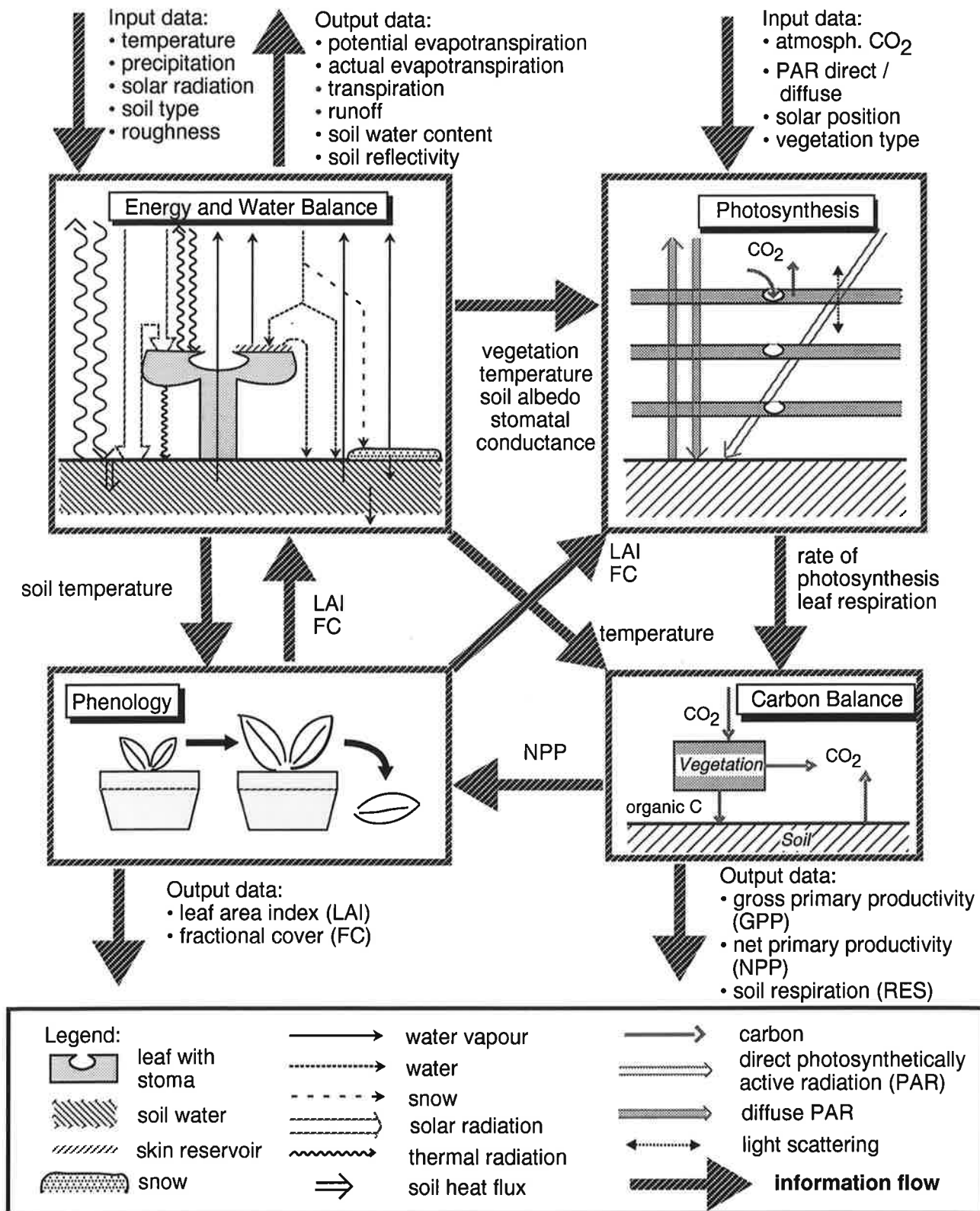


Figure 2.1: Structure of the BETHY model with input and output as well as information flow between the four model components. Various fluxes of water, light and carbon are also displayed.

limitation through the energy and water balance at the vegetated surface. Further, water limitation is calculated with a soil water model at daily time steps, whereas nitrogen limitation is treated as a long-term process with fixed values of photosynthetic capacity, which is closely related to leaf nitrogen content.

Fig. 2.1 gives an overview of the vegetation model's structure, consisting of energy and water balance, photosynthesis, carbon balance, and phenology.

The *energy balance* requires input data of temperature, precipitation, solar radiation, soil texture, soil albedo and roughness length. Additional data required from the phenology part are LAI and FC. From this, surface albedo, net radiation, latent and sensible heat fluxes and air humidity are computed, together with the soil water and snow balance. The energy balance is computed hourly, the water and snow balance daily. Additionally, the energy balance can be computed for every single day, or for a fixed amount of days each month.

The *photosynthesis* part takes PAR, solar angle, soil albedo, atmospheric CO₂ content and vegetation-type dependent parameters (capacity and pathway of photosynthesis) as input, plus LAI and FC from the phenology part, and air humidity and transpiration rate from the energy balance. Calculated variables are PAR absorption and gross CO₂ uptake (equal to GPP, i.e. gross primary productivity). The time step is also one hour and execution is carried out either for every day or for several days a month.

The *carbon balance* part receives GPP from the photosynthesis part, soil water content and leaf temperature from the energy balance and air temperature and vegetation specific leaf nitrogen content as input. These are used to compute plant, or "autotroph", and soil respiration (RES). NPP is then calculated as the difference of GPP minus plant respiration. Its annual sum equals the annual transfer of carbon from the vegetation to the soil. RES, i.e. release of carbon from the soil, is calculated daily and NPP each time the photosynthesis part is executed.

The *phenology* part computes the time course of LAI, simultaneously controlled by temperature and water, from air temperature and vegetation-specific phenological parameters (evergreen / deciduous) as input. In the water limited case, LAI is set as an optimal value for leaf growth, with the optimum calculated through a feedback loop from the phenology part to the photosynthesis and carbon balance parts and back. Carbon limitation of leaf growth is also considered. The phenology is usually recalculated a few times per month.

The model computes the water, energy and carbon balance separately for each grid point, so that it can be run with any desired spatial resolution. Standard full resolution, however, is 0.5° latitude by longitude with 62,438 points excluding Antarctica, because this is the resolution of the standard climate input data. For speeding-up purposes, the resolution most often used is an equal-area mapping with an equatorial resolution of 1°×1° with only 11,069 grid points. GPP, NPP, RES, LAI, FC, surface reflectance, plant available soil water, actual and potential evapotranspiration, soil evaporation and rain water runoff are computed after two years of spin-up and transferred to output as monthly means. Input

data are the mean monthly climate at each grid point and gridded maps of vegetation and soil type.

If daily precipitation is simulated stochastically, output is the mean annual course of a prescribed number of model years, whereas for periodic rainfall, the model is run to a steady state of the soil water balance and only the last year is written to output.

2.3 Input data: climate and soils

Activity and distribution of land vegetation are primarily determined by the mean climate and the quality of the substrate on which the plants grow. Accordingly, the model requires monthly means of temperature, precipitation, number of rainy days and solar insolation of the mean climate, and a map of soil types, as described in the preceding section.

Precipitation and near-ground air temperature as daily mean and amplitude are taken from the climatology of Cramer and Leemans (CL; Cramer 1995, pers. comm., Leemans and Cramer 1991) on a grid of 0.5 degrees latitude by longitude for all land areas but Antarctica (62,483 points, see above). For spatial interpolation, a special scheme by the authors has been used that derives temperature change with altitude explicitly from the data. The climatology by Cramer and Leemans is probably the most reliable available today.

For stochastic simulation of daily precipitation, the model also requires the monthly mean *fraction of rainy days*. The gridded data used here have been computed by Andrew Friend (Friend 1997) from a spatially explicit regression of the number of rainy days against the monthly precipitation amount at 896 stations from the data set by Müller (1982). The regression parameters have been spatially interpolated and then applied to the CL climatology.

As a further input, the ratio of potential to actual *solar radiation* in the photosynthetically active domain is used for the computation of photosynthesis and energy balance. For lack of direct ground measurements of solar radiation, a satellite-based data set of global PAR of 1987 is used, with a spatial resolution of 2.5 degrees (International Satellite Cloud Climatology Project ISCCP, Pinker and Laszlo 1992). Potential PAR is calculated by a method of Weiss and Norman (1985, see Section 2.5), then the ratio $r_{PAR} = \text{potential PAR} / \text{ISCCP-PAR}$ is formed with a resolution of 2.5 degrees.

In order to increase the resolution to the standard of 0.5 degrees, the data set of relative sunshine duration from the CL climatology, n , is used. A comparison with r_{PAR} yields the following approximate relationship:

$$r_{PAR} \approx 0.5 + 0.4n \quad (1)$$

Thus, the 0.5 degree version of r_{PAR} , r'_{PAR} , is calculated from:

$$r'_{PAR} = r_{PAR} \frac{0.5 + 0.4n'}{0.5 + 0.4n} \quad (2)$$

Here, r_{PAR} and n represent the bilinear interpolation to 0.5 degrees of the 2.5 degree data sets, while n' denotes the original data set with 0.5 degree resolution. (That is, to compute n , n' is first averaged to 2.5 degrees resolution and then interpolated back to 0.5 degrees.)

The model also use *elevation* from the CL climatology to calculate surface pressure and the optical path for the computation of potential solar radiation.

As *soil map*, the data set by Dunne and Willmott (1996) is used, an update of an earlier work by Webb et al. (1991) with an increase in resolution from 1 to 0.5 degrees. Both are based on the map of the Food and Agricultural Organisation (FAO), the only comprehensive global soil map currently available. The map by Dunne and Willmott assigns one of 128 possible soil types to each grid point, with a fixed soil depth and a vertical structure for each type. A maximum of five soil horizons is given with relative amounts of clay, silt and sand (grain sizes up to 2 μm , 2 to 50 μm and 50 to 2000 μm , respectively, according to US Department of Agriculture definitions). From this distribution of soil texture, the model calculates the water holding capacity of the soil (see Section 2.5).

Apart from hydrological soil features, the model also requires the soil albedo. This value is derived from a global map by Wilson and Henderson-Sellers (1985) of light, medium and dark soils. The definition of soil albedo follows the suggestions given by the authors (see also Section 2.5).

Additional soil properties, such as nutrient content, are not considered in the model. As mentioned in the preceding section, nutrient cycling is a slow process compared to the time scale studied here. As far as the impact of soil quality on vegetation type is concerned, this should be included through the use of vegetation maps, as explained in detail in the following section. Further, a link between NPP and soil nutrient content is often difficult to establish as most nutrients are often contained within the plants. In Chapter 5 it will also be shown that satellite data can sometimes be used to identify areas of impeded growth, caused for example by nutrient limitation.

2.4 Vegetation maps and vegetation-specific parameters

In addition to climate and soil factors, the prevailing vegetation type is a second-order factor that determines productivity. This is the result of different adaptation strategies to the local environment requiring different amounts of production. As an example, evergreen species with a lower productivity might, at certain places, supersede deciduous species because they have to produce less leaf material, with the consequence that evergreen plants have on average a lower light-use efficiency than deciduous plants (cf. Table 2.1). Human activity can also change productivity of entire regions, since agricultural crops are usually supplied much better with nutrients and hence reach much higher growth rates than natural vegetation at the same place. To take this into account, the vegetation model developed here uses a number of vegetation specific parameters that determine the phenological type under cold and dry conditions, as well as productivity at a given LAI. What is not determined by

those parameters, however, is the distribution of LAI itself, i.e. the amount of vegetation at a given place (with the exception of the category "ice").

Three methods of determining the predominant vegetation type are used in this study: (1) from atlases; (2) from time series analysis of the vegetation index NDVI derived from satellite measurements; (3) from mean climate. While the first two are intended to describe the actual vegetation distribution, a potential vegetation cover is described the third method. Using more than one land cover map makes it possible to account for the uncertainty inherent in global vegetation classification. The three methods each have their advantages and their limitations: For example, the NDVI-based method under (2) allows a globally consistent classification, while maps according to (1) contain more information. The advantage of a climate derived map (3) is consistency with the climatic input data. In this way, it can be excluded that, through inaccuracies in either vegetation or climate maps, vegetation is assumed to grow at a place where it couldn't according to our understanding of its ecology.

The model uses 14 natural and 9 agricultural vegetation types that have been chosen to account for the information available in the vegetation maps. A set of vegetation-specific parameters is assigned to each type according to Table 2.1. These are light-use efficiency (Ruimy et al. 1994 and Section 2.6), parameters of photosynthetic efficiency (V_m and J_m , Beerling and Quick 1995, see Section 2.6), specific leaf area (Schulze et al. 1994), typical vegetation height to derive aerodynamic conductance (after Kelliher et al. 1993) and rooting depth (Kelliher et al. 1993).

The photosynthesis parameters V_m and k for C4 plants (cf. Section 2.6) are chosen according to Collatz et al. (1992), from where the cited values for maize and sugar cane are adopted without modification. By comparison, data are extremely sparse for natural C4 grasses, with for example only one value for nitrogen content given in Schulze et al. (1994). Nevertheless, it can be argued that the ratio of V_m to k should be conservative, as the ratio of V_m to J_m for C3 plants (Wullschleger 1993, Berling and Quick 1995). The values given in Table 2.1 are therefore determined by equal downscaling of the values for maize, adapting productivity to that of co-existing C3 grasses. V_m and k , besides R_d/V_m (Section 2.6), are thereby set in such a way that at certain grid points, both GPP and NPP of C3 and C4 grasses are equal. Those grid points are defined by: (1) C3 and C4 grasses are the two dominant vegetation types; and (2) the C3/C4 ratio of grasses according to Equ. 3 (see below) lies between 0.45 and 0.55.

Further entries of Table 2.1 concern the photosynthetic pathway and the phenological type, i.e. cold-evergreen (all evergreen conifers) or warm-evergreen (tropical evergreen and sclerophyllous), unless deciduous.

Rooting depth is 1 m for all vegetation types, except in savannas, where it is 1 m for grasses and 3 m for trees. Those values correspond approximately to those of the biosphere models TEM (Raich et al. 1991), CASA (Potter et al. 1993) and SILVAN (Kaduk 1996).

In some cases, the assignment of a vegetation type to the categories of Berling and Quick or Ruimy

Table 2.1: List of vegetation types and there parameters: ϵ : light-use efficiency in g dry mass per MJ PAR, V_m : maximum carboxylation rate at 25°C in $\mu\text{mol}(\text{CO}_2)\text{m}^{-2}\text{s}^{-1}$, J_m : maximum electron transport rate at 25°C in $\mu\text{mol}(\text{CO}_2)\text{m}^{-2}\text{s}^{-1}$ (C3) or k : CO_2 specificity at 25°C in $\text{mmol}(\text{CO}_2)\text{m}^{-2}\text{s}^{-1}$ (C4), σ_L : specific leaf area in m^2kg^{-1} (dry mass), h_v : height in m, C4: C4 photosynthetic pathway, unless C3, Ph.: phenology, unless deciduous. Further abbreviations are BL: broad-leaved, temp.: temperate, trop.: tropical, C-E: cold-evergreen, W-E: warm-evergreen and I-W: irrigated or wetland; -: not used.

| Number | vegetation type | ϵ | V_m | J_m/k | σ_L | h_v | C4 | Ph. |
|--------|----------------------------|------------|-------|---------|------------|-------|----|-----|
| 1 | Trop. BL evergreen trees | 0.62 | 62 | 118 | - | 30.0 | | W-E |
| 2 | Trop. BL deciduous trees | 1.01 | 90 | 179 | 13.2 | 15.0 | | |
| 3 | Temp. BL evergreen trees | 0.62 | 41 | 82 | - | 15.0 | | W-E |
| 4 | Temp. BL deciduous trees | 1.01 | 35 | 70 | 11.4 | 15.0 | | |
| 5 | Evergreen coniferous trees | 1.57 | 29 | 52 | - | 15.0 | | C-E |
| 6 | Deciduous coniferous trees | 1.57 | 53 | 95 | 11.3 | 15.0 | | |
| 7 | Evergreen shrubs | 0.62 | 52 | 102 | - | 1.0 | | W-E |
| 8 | Deciduous shrubs | 1.01 | 160 | 266 | 11.4 | 1.0 | | |
| 9 | C3 short grass | 1.26 | 42 | 80 | 16.9 | 0.3 | | |
| 10 | C3 long grass | 1.26 | 42 | 80 | 16.9 | 2.0 | | |
| 11 | C4 short grass | 1.63 | 8 | 140 | 16.9 | 0.3 | x | |
| 12 | C4 long grass | 1.63 | 8 | 140 | 16.9 | 2.0 | x | |
| 13 | Tundra vegetation | 0.62 | 20 | 37 | - | 0.3 | | C-E |
| 14 | Swamp vegetation | 1.26 | 20 | 37 | 16.9 | 0.3 | | I-W |
| 15 | Arable crops | 2.71 | 117 | 220 | 24.5 | 0.6 | | |
| 16 | Irrigated crops | 2.71 | 123 | 227 | 23.6 | 0.6 | | I-W |
| 17 | Trop. tree crops | 1.74 | 60 | 106 | - | 2.0 | | W-E |
| 18 | Citrus crops | 1.71 | 60 | 106 | - | 2.0 | | W-E |
| 19 | Temp. deciduous tree crops | 2.72 | 123 | 227 | 10.1 | 2.0 | | |
| 20 | Sugar cane | 3.51 | 39 | 700 | 9.0 | 2.0 | x | |
| 21 | Maize | 3.51 | 39 | 700 | 26.3 | 2.0 | x | |
| 22 | Rice | 2.71 | 98 | 190 | 16.6 | 0.3 | | |
| 23 | Cotton | 2.71 | 123 | 227 | 20.0 | 2.0 | | |

et al. is ambiguous. Therefore, a detailed description with the underlying assumptions is added here. It should be noted that, in contrast to Ruimy et al. (1994), the values for light-use efficiency are here defined under conditions of sufficient water supply, since water stress is modelled explicitly. (Abbreviations are: BQ Berling and Quick 1995; R&a Ruimy et al. 1994; S&a Schulze et al. 1994)

2 ϵ as 4

3 V_m, J_m after BQ, Table 1, footnote e, multiplied by 12.7/10.8 (A_{max} after S&a for temperate-evergreen trees / A_{max} after BQ in the same line)

6 V_m, J_m after BQ, Table 1, footnote h, multiplied by 12.0/12.4 (A_{max} after S&a for deciduous coniferous trees / A_{max} after BQ)

7 ϵ as 4; V_m, J_m after BQ, Table 1, footnote i, multiplied by 9.9/25.7 (A_{max} after S&a for evergreen shrubs / A_{max} after BQ)

8 V_m, J_m after BQ, Table 1, footnote i

9, 10 V_m, J_m after BQ, Table 1, footnote k

11, 12 ϵ as 9 multiplied by the C4/C3 efficiency ratio for crops from R&a (3,51/2,71); V_m, k for C4 plants, see above

- 13 ϵ , V_m , J_m as 9, following R&a
 14 ϵ , V_m , J_m as 9, following R&a
 15, 16 mean ϵ of C3 crops from R&a; V_m , J_m after BQ, Table 1, footnote l (15) or m (16), respectively
 17 ϵ for tropical/subtropical/moist tree crops from R&a; V_m , J_m after BQ, Table 1, footnote n
 18 ϵ for Mediterranean tree crops assumed, as in R&a (no measurements); V_m , J_m as 17
 19 V_m , J_m as 16 (one category in BQ)
 20,21 ϵ for C4 crops from R&a; J_m and V_m , see above
 22 ϵ for C3 crops from R&a; V_m , J_m after BQ, Table 1, footnote q
 23 ϵ for C3 crops from R&a; V_m , J_m as 16 (one category in BQ)

The following subsections describe in detail, how each land-cover or climatic type is assigned a well defined set of vegetation types and their relative amounts. The maximum number of vegetation types is $N_v \leq 3$ with one set of parameters each according to Table 2.1. If $N_v > 1$, the model is either run N_v times at the same grid point with an identical climate and the result is taken as the mean over the fractions f_v of the N_v vegetation types, or one vegetation type out of N_v is chosen by means of a random number generator, with the probability of choosing type v equal to f_v .

Traditional vegetation map (1)

The traditional, i.e. atlas derived map by Wilson and Henderson-Sellers (1985) comprises a total of 52 different land cover types. To those, the authors have assigned relative fractions of 19 vegetation types and 5 non-vegetation land types. In order to account for the vegetation-specific data available, the list has been extended to 23 vegetation types, which are also used for the other two vegetation maps (see above and Table 2.1). The distribution of the vegetation types by Wilson and Henderson-Sellers has been modified accordingly (see Table 2.2).

Since the data set by Wilson and Henderson-Sellers does not allow the distinction between C3 and C4 grasses, the fraction of short and long grasses (types 9/11 and 10/12) is split up again. The fraction of C4 grasses of the total grass fraction, r_{C4} , is thereby computed according to the following regression against the mean temperature of the warmest month, T_w (in °C):

$$r_{C4} = -1.185 + 0.0731T_w \quad (3)$$

The regression equation has been derived by assigning the value of T_w from the CL climatology to the value of r_{C4} from a total of 61 ecosystem studies from North America with at least 20% grasses. With $r^2 = 0.47$, a satisfactory correlation is achieved. Including annual precipitation, explaining 15% of the variation on its own, has not been considered, because the multiple regression coefficient only increases to $r^2 = 0.49$. Applying this to areas of much differing annual potential evapotranspiration seems also questionable.

The definition of savanna for the assignment of rooting depth is given by the codes 23, 26, 32, 37 and 73.

Table 2.2: The land cover types from the data set of Wilson and Henderson-Sellers (1985) and their associated vegetation types. D: dense, O: open.

| Code | Description | Type 1 | Frac. | Type 2 | Frac. | Type 3 | Frac. |
|------|---------------------------------------|--------|-------|--------|-------|--------|-------|
| 2 | Bog or marsh | 14 | 1.00 | | | | |
| 4 | Paddy rice | 22 | 1.00 | | | | |
| 5 | Mangrove (tree swamps) | 1 | 0.60 | 7 | 0.40 | | |
| 10 | D needleleaf evergreen forest | 5 | 1.00 | | | | |
| 11 | O needleleaf evergreen woodland | 5 | 0.65 | 9/11 | 0.35 | | |
| 12 | D mixed forest | 5 | 0.50 | 4 | 0.50 | | |
| 13 | O mixed woodland | 5 | 0.35 | 4 | 0.35 | 9/11 | 0.30 |
| 14 | Evergreen broadleaf woodland | 3 | 0.65 | 9/11 | 0.35 | | |
| 15 | Evergreen broadleaf cropland | 19 | 0.75 | 9/11 | 0.25 | | |
| 16 | Evergreen broadleaf shrub | 7 | 0.70 | 9/11 | 0.30 | | |
| 17 | O deciduous needleleaf woodland | 6 | 0.70 | 9/11 | 0.30 | | |
| 18 | D deciduous needleleaf forest | 6 | 1.00 | | | | |
| 19 | D evergreen broadleaf forest | 3 | 1.00 | | | | |
| 20 | D deciduous broadleaf forest | 4 | 0.90 | 9/11 | 0.10 | | |
| 21 | O deciduous broadleaf woodland | 4 | 0.65 | 9/11 | 0.35 | | |
| 22 | Deciduous tree crops (temperate) | 19 | 0.65 | 9/11 | 0.35 | | |
| 23 | O tropical woodland | 10/12 | 0.40 | 2 | 0.30 | 1 | 0.30 |
| 24 | Woodland + shrub | 4 | 0.65 | 8 | 0.35 | | |
| 25 | D drought deciduous forest | 2 | 1.00 | | | | |
| 26 | O drought deciduous woodland | 2 | 0.75 | 10/12 | 0.25 | | |
| 27 | Deciduous shrub | 8 | 0.65 | 9/11 | 0.35 | | |
| 28 | Thorn shrub | 7 | 0.75 | 10/12 | 0.25 | | |
| 30 | Temp. meadow and perm. pasture | 9/11 | 1.00 | | | | |
| 31 | Temp. rough grazing | 9/11 | 0.85 | 8 | 0.15 | | |
| 32 | Trop. grassland + shrub | 10/12 | 0.75 | 8 | 0.25 | | |
| 33 | Trop. pasture | 10/12 | 0.75 | 9/11 | 0.25 | | |
| 34 | Rough grazing + shrub | 9/11 | 0.75 | 8 | 0.25 | | |
| 35 | Pasture + tree | 9/11 | 0.80 | 4 | 0.20 | | |
| 36 | Semi-arid rough grazing | 10/12 | 0.60 | 7 | 0.40 | | |
| 37 | Trop. savanna | 10/12 | 0.80 | 2 | 0.10 | 1 | 0.10 |
| 39 | Pasture + shrub | 9/11 | 0.85 | 8 | 0.15 | 7 | |
| 40 | Arable cropland | 15 | 0.75 | 9/11 | 0.25 | | |
| 41 | Dry farm arable | 15 | 0.75 | 9/11 | 0.25 | | |
| 42 | Nursery and market gardening | 15 | 1.00 | | | | |
| 43 | Cane sugar | 20 | 0.90 | 10/12 | 0.10 | | |
| 44 | Maize | 21 | 0.60 | 15 | 0.40 | | |
| 45 | Cotton | 23 | 0.90 | 15 | 0.10 | | |
| 46 | Coffee | 17 | 0.75 | 15 | 0.25 | | |
| 47 | Vineyard | 8 | 0.75 | 15 | 0.25 | | |
| 48 | Irrigated cropland | 16 | 0.85 | 9/11 | 0.15 | | |
| 49 | Tea | 8 | 0.75 | 10/12 | 0.25 | | |
| 50 | Equatorial rainforest | 1 | 0.90 | 2 | 0.10 | | |
| 51 | Equatorial tree crop | 17 | 0.80 | 10/12 | 0.10 | 14 | 0.10 |
| 52 | Trop. broadl. forest (slight season.) | 1 | 0.50 | 2 | 0.35 | 10/12 | 0.15 |
| 61 | Tundra | 13 | 1.00 | | | | |
| 62 | Dwarf shrub (tundra transition) | 13 | 0.45 | 7 | 0.35 | 8 | 0.20 |
| 70 | Sand desert and barren land | 7 | 1.00 | | | | |
| 71 | Scrub desert and semi desert | 7 | 0.75 | 10/12 | 0.25 | | |
| 73 | Semi desert + scattered trees | 2 | 0.65 | 10/12 | 0.35 | | |
| 80 | Urban | 4 | 1.00 | | | | |

Table 2.3: Land cover types from the data set of DeFries and Townshend and associated vegetation types as defined in Table 2.1. Only one type of crop is considered (15), the types 16 to 23 do not appear, nor do 14 (swamp) or 10 (C3 long grass).

| Code | Description | Type 1 | Fraction | Type 2 | Fraction |
|------|---|--------|----------|--------|----------|
| 1 | Broadleaf evergreen forest | 1 | 0.90 | 2 | 0.10 |
| 2 | Broadleaf deciduous forest | 4 | 0.80 | 9 | 0.20 |
| 3 | Mixed conif. / broadleaf dec. forest / woodland | 4 | 0.50 | 5 | 0.50 |
| 4 | Coniferous forest and woodland | 5 | 0.80 | 9 | 0.20 |
| 5 | High latitude forest and woodland | 6 | 0.60 | 9 | 0.40 |
| 6 | Wooded C4 grassland | 12 | 0.70 | 2 | 0.30 |
| 7 | C4 grassland | 11 | 1.00 | | |
| 9 | Shrubs | 8 | 1.00 | | |
| 10 | Tundra | 13 | 1.00 | | |
| 11 | Desert | 7 | 1.00 | | |
| 12 | Cultivation | 15 | 0.70 | 9 | 0.30 |
| 14 | Wooded C3 grassland | 9 | 0.70 | 4 | 0.30 |
| 15 | C3 grassland | 9 | 1.00 | | |

In order to match the vegetation map by Wilson and Henderson-Sellers onto the CL climatology, the data set has been converted to a 0.5 degree grid, where missing land points have been set to the value of the most frequent neighbour type. A few points required manual setting based on other sources. (For its minor effect globally, details have been omitted here.)

When eventually assigning up to 3 vegetation types to each 0.5 degree grid point, the primary cover type of Wilson and Henderson-Sellers is assumed to account for 70% of the land area, and the secondary type for 30%, yielding a maximum of 8 types (after C3/C4 redistribution). After excluding those covering less than 5% of the vegetated area, the fractions of the remaining 0 to $N_v \geq 3$ most common types are renormalised to 100%.

NDVI derived vegetation map (2)

The second land cover map used is the one by DeFries and Townshend (1994), that has been generated by a combination of atlas and satellite data. In the process, areas are first defined for which several sources agree in the cover type. Then, a typical annual course of the vegetation index NDVI is defined for those types. The remaining land points are eventually assigned the cover type whose NDVI profile most closely matches the observed one, with closeness defined by a metric that takes the statistical variation of each monthly NDVI value into account. The method can be described as a NDVI based interpolation scheme of traditional map data.

The map data by DeFries and Townshend are also transferred to the 0.5 degree grid of the CL climatology, with undefined land points set to the most common value among neighbouring points. For 234 land points left undefined, the assignment is based on the vegetation map by Matthews (1983), or is done arbitrarily (21 cases).

To a total of 13 vegetation cover types, 10 different vegetation types are assigned as listed in Table 2.3. Some cover types have only one vegetation type, others two. In this case, savannas (deep roots) are defined by cover type 6. Since the map by DeFries and Townshend has only a few, rather general land cover types, cultivated land is uniformly set to 70% C3 crops and 30% C3 grasses. Neither C4 crops, nor the coexistence of C3 and C4 grasses are accounted for.

Climate derived vegetation map (3)

As a third possibility, a map of potential vegetation based on mean climate can be chosen. "Potential" in this case means a vegetation distribution in equilibrium with the prevailing climate at a given place, without human interference. Consequently, there is no cultivated vegetation on such a map. Succulents and less significant types are also left out. Global vegetation is thus separated into 4 functional types, trees, shrubs, C3 and C4 grasses.

According to Box (1981), the fraction of trees is calculated from the annual moisture index (MI), defined as the ratio of annual precipitation to annual potential evapotranspiration (see Section 2.5 for computation). It is assumed that at a MI of 1.0, the tree fraction, f_T , is 100%, linearly decreasing to 0% at a MI of 0.6. To define the tree line in cold areas, it is assumed according to Woodward (1987), that trees require a growing degree-day sum, GDD_5 , of 900 for full growth and that their cover fraction becomes zero at $GDD_5 = 350$ (GDD_5 is defined as the sum of the temperature of all days with at least 5 °C minus 5°C, in units of °C×days):

$$f_T = f(MI)f(GDD_5) \quad (4a)$$

$$f(MI) = \begin{cases} 0 & \text{for } MI < 0.6 \\ (MI - 0.6)/0.4 & \text{for } 0.6 < MI < 1.0 \\ 1 & \text{for } MI > 1 \end{cases} \quad (4b)$$

$$f(GDD_5) = \begin{cases} 0 & \text{for } GDD_5 < 350 \\ (GDD_5 - 350)/550 & \text{for } 350 < GDD_5 < 900 \\ 1 & \text{for } GDD_5 > 900 \end{cases} \quad (4c)$$

In this model, the northern tree line runs slightly north of James Bay in Canada, close to the Finish-Norwegian border and along the polar circle in Siberia. The arid tree line runs north-south approximately along the Mississippi river in the USA, while in the Mediterranean, northern Spain, southern France, the Apennine mountains and the Balkans, except eastern Greece, are forested. In Africa, the Congolese and the Guinean rainforests are predicted correctly, as are the Ethiopian highlands and eastern Madagascar. In Asia, Indonesia and the complete monsoon effected region from Burma to Korea and Japan appear forested, as does most of South America, with the exception of the Guayanas, northern Venezuela, the Cerrados of Brazil, the Andean highlands, Patagonia and the steppe and grassland zone stretching from northern Argentina to Paraguay and the Mato Grosso in Brazil. The

Argentine pampas are incorrectly predicted to be 50% forest covered, as it is known from other models, too (Box 1981).

The fraction of the remaining functional types is calculated from an empirical correlative model of Paruelo and Lauenroth (1996), which has originally been developed for the non-forested areas of North America and has later been tested successfully for South America (Paruelo et al. 1997). Although not developed explicitly for those areas, it correctly predicts a high shrub fraction for the winter-rain regions stretching from the Mediterranean to Iran, of southern Africa and of Australia, and a dominance of C4 grasses in tropical-arid regions with summer rains. For the treeless tundra, the predicted ratio is approximately three quarters C3 grasses and one quarter shrubs.

The regressions by Paruelo and Lauenroth are based on annual mean temperature, \bar{T}^a , average annual precipitation, P_a , and the fraction of precipitation falling either during the three summer or winter months, P_{sum} and P_{win} (summer for the northern hemisphere: June to August, winter: December to February):

$$f_S = 1.7105 - 0.2918 \ln P_a + 1.5451 P_{win} \quad (5a)$$

$$f_{C4} = -0.9837 + 0.000954 P_a + 1.3528 P_{sum} + 0.2710 \ln \bar{T}^a \quad (5b)$$

$$f_{C3} = 1.1905 - 0.02909 \bar{T}^a + 0.1781 \ln P_{win} - 0.2383 n_{BIOM} \quad (5c)$$

f_S , f_{C3} and f_{C4} denote shrub, C3 grass and C4 grass fraction, respectively. Precipitation (P_a , P_{sum} and P_{win}) is given in mm, temperature (\bar{T}^a) in °C. The value for n_{BIOM} is 2, if $f_S > 0.2$, else it is 1.

In order to account for the fact that in the oceanic climate of Western Europe, summers are considerably cooler at equal annual mean temperature than in North America or Argentina, \bar{T}^a is not used directly, but it is derived from a linear regression against T_w (mean temperature of warmest month) for the 73 locations given in Paruelo and Lauenroth (1996):

$$\bar{T}^a = -19.1337 + 1.26893 T_w \quad (6)$$

The correlation computed with the CL climatology is high with $r^2 = 0.88$. Prediction of the C3 and C4 grass distribution is hardly affected for continental and tropical areas by the use of T_w .

After applying Equ. 5a to 5c, the relative fractions f_S , f_{C3} and f_{C4} are normalised to $1 - f_T$. The fractions f_{C3} and f_{C4} are either assigned to types 9 and 11, respectively (short grass), or to types 10 and 12 (long grass). The border between long and short grass is assumed at a moisture index (MI, see above) of 0.5, with long grass at $MI > 0.5$. In the North American prairies, the line defined by $MI = 0.5$ lies well within the observed transition zone along the 100th parallel (Walter and Breckle 1991). Further, the fraction f_S is counted as Type 7 (evergreen shrubs), if $GDD_5 > 900$, else as Type 12 (tundra vegetation). Vegetation types 8 (deciduous shrubs), 14 (swamp vegetation) and 15 to 23 (crops) are not used.

Assignment of the tree fraction, f_T , to vegetation types 1 to 6 is largely based on the work by Woodward (1987), according to which absolute minimum temperatures limit the

establishment of certain tree species. Instead of the absolute minima, the mean temperature of the coldest month, T_c , is used following Prentice et al. (1992), based on a regression from the temperature data of Müller (1982). In addition, according to Box (1981, p. 42, Table 8), the MI is used to distinguish between tropical evergreen and tropical deciduous trees. Box assumes a threshold of around 1.1 for the occurrence of forests in general. Since evergreen rainforests can also contain deciduous species (Box 1981, Walter and Breckle 1990), it is assumed here that the fraction of evergreen trees linearly rises from 0% at MI=1.0 to 100% at MI=1.2. The definitions in detail:

Type 1: tropical broadleaf evergreen trees at $T_c > 15.5^\circ\text{C}$ and MI 1.0 or higher;

Type 2: tropical broadleaf deciduous trees at $T_c > 15.5^\circ\text{C}$ at MI from larger than 1.0 up to a value of 1.2; for MI between 1.0 and 1.2, their fraction linearly decreases as that of type 1 increases accordingly;

Type 3: temperate broadleaf evergreen trees at T_c between 5°C and 15.5°C ;

Type 4: temperate broadleaf deciduous trees at T_c between -15°C and $+5^\circ\text{C}$ and $\text{GDD}_5 > 1300$;

Type 5: needleleaf evergreen trees at T_c between -15°C and -35°C , or at higher temperatures, if $\text{GDD}_5 < 1300$;

Type 6: needleleaf deciduous trees (larches) at $T_c < -35^\circ\text{C}$.

As with the vegetation map by Wilson and Henderson-Sellers, types with a fraction of less than 5% are excluded and up to three of the most common types are chosen. The vegetation-specific parameters eventually assigned are given in Table 2.1. In this case, savannas (deep roots) are defined as those areas, where the MI lies between 0.6 and 1.0 with T_c at least 15.5°C .

2.5 Energy and water balance

The energy balance at the earth's surface can be written in the following way:

$$R_n - G - H - \lambda E = \dot{Q} + \dot{Q}_B \quad (7)$$

On the left of the equal sign are net radiation, R_n (incoming solar radiation plus longwave radiation of the atmosphere minus longwave radiative loss of the surface), soil heat flux, G , caused by heat conductance, sensible heat flux, H , between the surface and the air above, caused primarily by turbulent mixture of warm and cold air, and evapotranspiration, E , multiplied by the latent heat of vaporisation (2.45 MJ kg^{-1} at 20°C). The balance is closed by the time derivatives (denoted by a dot) of the thermal energies Q and Q_B . Q stands for the heat that is stored both in the vegetation itself and in the air within the vegetated

layer, and Q_B for the heat stored in biochemical products, so that \dot{Q}_B is equal to the energy gain of photosynthesis minus the heat amount produced by respiration of both plants and soil organism. The two quantities on the right hand side almost always amount to less than 10% of R_n and are therefore neglected in most applications (Jones 1983, p. 85).

The water balance, by comparison, can be described by this equation:

$$P - E - \Phi = \dot{W} \quad (8)$$

P is the precipitation rate, W the amount of water stored in the soil, on the vegetation and on the soil as snow, and Φ is the (above and below ground) runoff.

Energy and water balance at the surface are intimately linked. This is a consequence of a high vaporisation heat, λ , causing a considerable fraction of the incoming radiation to be consumed for the evaporation of water – more than half on average for all land surfaces (Budyko 1974). Therefore, the significance of the energy balance for the carbon cycle does not lie as much in the relatively small energy requirement of photosynthesis ($\approx \dot{Q}_B$ during daytime), but in the degree to which the energy balance controls vegetation temperature. On the one hand, vegetation temperature determines transpiration rates and thus forces the plants to reduce carbon uptake when closing their stomata (see below); on the other hand, temperature influences biochemical activity to a large degree, with consequences both for photosynthesis and for plant respiration.

Significance of stomata and stomatal modelling

Because plants rely on gas exchange with the surrounding air to carry out photosynthesis, thereby letting carbon dioxide diffuse with the air through stomata into the inner parts of the leaves, they constantly lose water through diffusion of vapour in the opposite direction. This process, called transpiration, usually accounts for most of the total evapotranspiration, E , in particular when the soil is dry and when LAI is larger than two (Ritchie 1972, Kelliher et al. 1995). In order to prevent desiccation, most plants have the ability to regulate the diffusive conductance of their stomata, with the result of a close link between photosynthesis and transpiration that is determined by a number of environmental factors (Farquhar and Sharkey 1982).

Because of the great significance of transpiration for the surface energy balance at the land surface, models have been developed that include a description of stomatal function. Those so-called SVAT models (Soil Vegetation Atmosphere Transfer) have been designed to improve the energy balance in models of the atmospheric circulation (i.e. climate and weather prediction models, see Dickinson et al. 1991 for an overview). The stomatal conductance, g_s , is most often prescribed in an empirical form as first proposed by Jarvis (1976; e.g. SiB, Sellers et al. 1986 and BATS, Dickinson et al. 1993):

$$g_s = g_s^{max} f(D) f(R_s) f(T) f(W) \quad (9)$$

The functions $f(\dots)$ take on values between 0 and 1, depending on vapour pressure deficit (D), solar radiation (R_s), temperature (T) and soil water content (W). Models of this type have been successfully fitted to local measurements (e.g. Stewart 1988, Dolman et al. 1991, Kim and Verma 1991a). It has further been shown that the inclusion of this kind of stomata description into mesoscale (i.e. regional) climate models has considerable influence on simulated evapotranspiration rates (e.g. Avissar and Pielke 1991, Mascart et al. 1991). So far, however, for lack of a theoretical basis for the determination the appropriate constants on a global scale, a formulation within "reasonable" bounds is required (Dickinson et al. 1991). It is another shortcoming of the formulation, that environmental factors influence g_s independently of each other, which is improbable to occur in nature (Friend 1995).

A different formulation by Collatz et al. (1991) is used in an advanced version of the SiB model with embedded carbon cycling (SiB2, Sellers et al. 1992). There, a dependence of the stomatal conductance, g_s , on relative humidity above the leaf surface and photosynthetic rate is assumed, both depending themselves on g_s , which has therefore to be solved in an iterative procedure. The scheme does not always deliver stable solutions and in some cases leads to unrealistic behaviour (Collatz et al. 1991, p. 127 top). This model still lacks a consistent functional basis, in particular the dependence of stomatal conductance on relative humidity (cf. Schulze et al. 1987). A simulated feedback between photosynthesis and the laminar boundary resistance of leaves has also not been found in plant ecological studies (Zeiger et al. 1987). Therefore, it must be concluded that this model is also based primarily on the measurements cited and falls into the same category as the one by Jarvis.

Another model that starts entirely from ecophysiological arguments is that of Cowan and Farquhar (1977). According to it, the daily course of stomatal conductance can be determined by the condition that the marginal gain of carbon uptake per transpired water stays constant over a day (i.e. $\partial A/\partial E = \text{const.}$, where A stands for photosynthetic rate), leading to a maximum carbon uptake at a given amount of water loss. The amount of transpired water per day, however, is not specified in the model. As Cowan (1982) observes in a later study, optimal behaviour of the plant strongly depends on competition from other plants.

In a similarly designed model (PGEN), Friend (1995) assumes that it is not carbon uptake that is maximised, but the expansion rate of new plant tissue. If the leaf water potential falls, this rate decreases more strongly than does photosynthetic uptake (cf. also Luxmoore 1991). A strongly negative leaf water potential occurs, whenever transpiration rates increase too strongly at low soil water potential. While in the Cowan model, optimal behaviour at limited water supply means increased transpiration rates particularly in the morning, shifting too much of the transpiration from midday to morning hours can be unfavourable with PGEN, since high transpiration rates at dry soils lead to a highly negative leaf water potential.

This type of behaviour in PGEN approaches the much simpler model of Federer (1979,

1982), that can be formulated as:

$$E = \min\{S; D\} \quad (10)$$

Here, S stands for supply rate, i.e. for the amount of water available from the root system per unit time, and D for atmospheric demand, i.e. transpiration rate at unlimited water supply. In this model, the stress is less on stomatal behaviour than on the meteorological parameters that determine the atmospheric demand.

This corresponds to the theory of equilibrium evapotranspiration (Jarvis and McNaughton 1986, McNaughton and Jarvis 1991), according to which the control of stomata on transpiration rates decreases with increasing length scale of vegetation-atmosphere interaction. On the stand level with sufficient soil moisture, net radiation already determines the transpiration rate to a good degree. On a regional scale, corresponding approximately to one grid cell in a global circulation model, negative feedback loops within the planetary boundary layer have an additional effect, so that the significance of the stomata decreases even further. The transpiration rate thus approaches the equilibrium rate, which only depends on net radiation and temperature. Indeed, Shuttleworth (1988) found a deviation of only 5-10% from the value for the annual evapotranspiration of an Amazonian forest, with larger deviations on individual days.

The parametrisation of stomatal conductance chosen in this study combines a reduced form of the Jarvis model (with only one function of variable form) with a dependence on the photosynthetic rate as in Collatz et al. (1991) and the concept of a root-dependent supply rate according to Federer. Several results from the physiology of stomatal function are considered in this scheme: First, light is the primary regulating factor, probably caused by the demand for CO_2 by photosynthesis (Sharkey and Ogawa 1987). Second, and as a consequence of the first point, leaf internal CO_2 content stays near constant over a wide range of conditions (Morison 1987). Third, a root signal is probably responsible for the closing of stomata so that a vapour pressure deficit of the surrounding air will not result in a reduction of stomatal conductance, as long as root supply is sufficient (Gollan et al. 1985, Schulze et al. 1987). This also corresponds to the finding of Cowan (1982), mentioned earlier, that plants, for reasons of competition, largely exhaust their water resources to increase production.

An immediate adoption of the model by Friend is prevented by the fact that global modelling of root and leaf water potential does not appear to be feasible, and is also impossible with the bucket model chosen (see below). Therefore, a simple empirical dependence on water vapour deficit is chosen, with a variable form depending on daily soil water content. Its exact formulation is explained in the subsection "evapotranspiration from vegetation" of the current section.

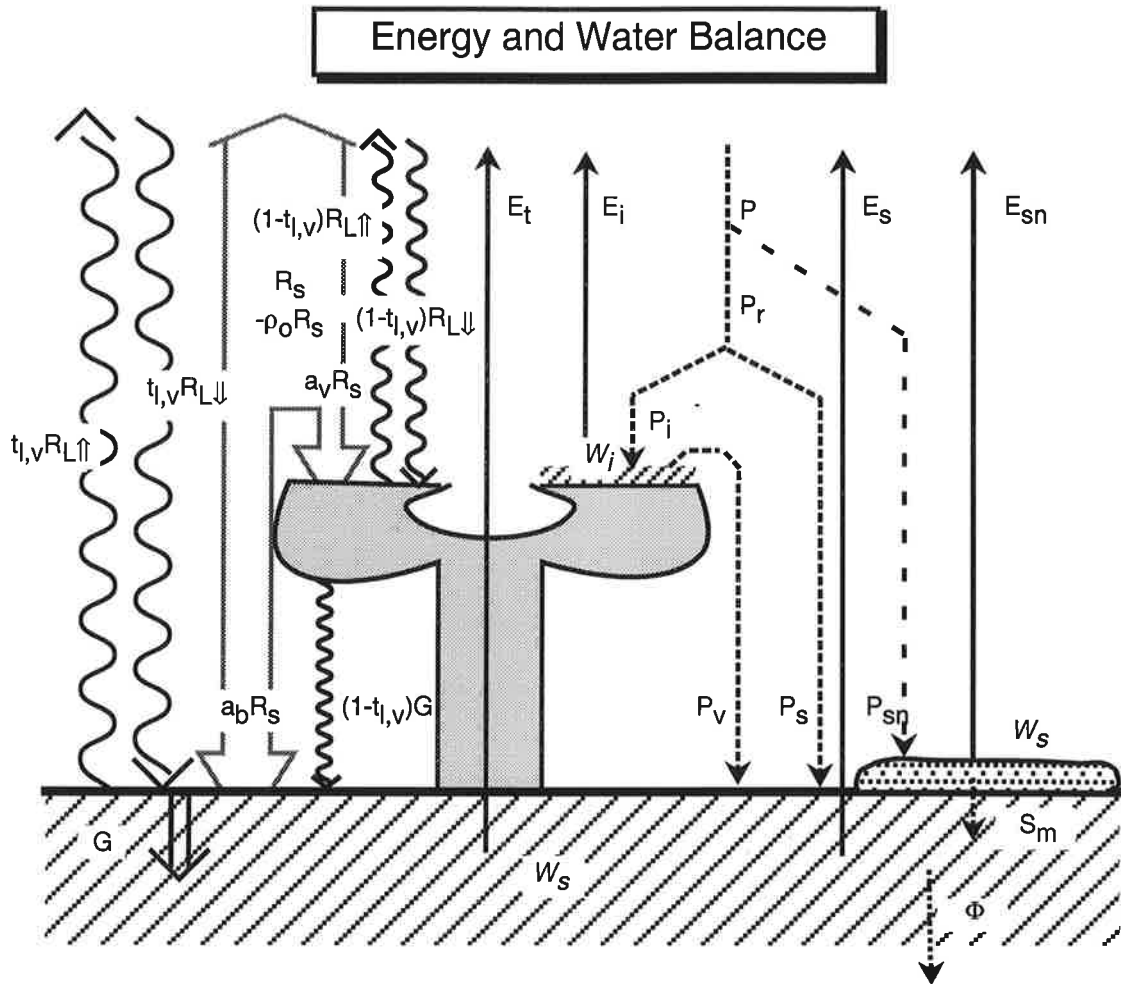


Figure 2.2: Energy and water balance of the BETHY model with symbols for fluxes (normal) and reservoirs (italics).

Overview of fluxes and reservoirs

An overview of modelled energy fluxes, water fluxes and water reservoirs is shown in Fig. 2.2. The model considers a total of three water pools: soil water (W_s), a skin or intercepted reservoir on leaves and other plant parts (W_i) and snow (W_{sn}). The total amount of water at the surface, W , from Equ. 8, is thus partitioned into three components (cf. Equ. 51, 55 and 59):

$$W = W_s + W_i + W_{sn} \quad (11)$$

The largest part by far is W_s . The precipitation rate, P , and the rate of evapotranspiration, E , are also divided into further quantities:

$$P = P_s + P_i + P_{sn} \quad (12)$$

and

$$E = E_s + E_{sn} + E_i + E_t \quad (13)$$

Here, P_s is the amount of rain falling directly on the soil, P_i the part intercepted by vegetation and P_{sn} the snowfall. The partitioning of total precipitation, P , into snow (P_{sn}) and rain ($P_r = P_s + P_i$) is calculated from Equ. 60 (see subsection "snow balance") and the interception rate, P_i , according to Equ. 56 (see the following subsection). Further variables are E_{sn} (snow evaporation, Equ. 88), E_i (evaporation from the skin reservoir, Equ. 70), E_t (transpiration, Equ. 72) and E_s (soil evaporation, Equ. 91).

Through the energy balance (Equ. 7), surface temperature and thereby evaporation and transpiration rates are highly dependent upon net radiation, R_n . Consequently, it is in the interest of the plant to absorb sunlight as effectively as possible, while at the same time keeping the absorbed radiative energy, R_n , as small as possible. In fact, plants absorb photosynthetically active light to almost 90% and reflect or scatter around 90% of the light in the near infrared, which is of now value for photosynthesis (see Section 2.9). Besides this, through "clumping" and keeping leaves in an erect position, vegetation can reduce light absorption during midday, while increasing it in the morning and the evening when atmospheric demand for transpiration is lowest. To simulate such effects, net radiation and with it the entire energy balance is split into a vegetation, R_{nv} , and a soil part, R_{ns} . The energy balance for both parts can thus be written as:

$$R_{nv} = H_v + \lambda(E_t + E_i) \quad (14)$$

and

$$R_{ns} - G = H_s + \lambda(E_s + E_{sn}) \quad (15)$$

Thus, there are two evaporation fluxes controlled by R_{nv} (transpiration and skin reservoir evaporation) and two controlled by R_{ns} (soil and snow evaporation), while both subsystems are linked by a common reservoir, W_s , for the two dominant fluxes, E_t and E_s .

Precipitation

Two different models are available for the simulation of daily precipitation, P , where \bar{P} is the monthly mean precipitation rate in mm/day, \bar{P}_w the monthly mean of the precipitation rate on rainy (i.e. "wet" days, which includes snowy days) and \bar{f}_w the mean fraction of wet days of a month, with $\bar{P} = \bar{f}_w \times \bar{P}_w$:

Periodic mode: The monthly precipitation rates are interpolated linearly and it rains (or snows) every $1/f_w$ days. For f_w the average of each month, \bar{f}_w , is taken.

Stochastic mode: Daily precipitation is generated with a stochastic weather generator according to Geng et al. (1986) using Gamma distribution and a first-order Markov chain. The probability of a wet day following a dry day is given as $p_{wd} = 0.75f_w$, and that of a wet day following a wet day as $p_{ww} = 0.25 + p_{wd}$.

In this mode, f_w is interpolated linearly from \bar{f}_w (like the precipitation rate in the periodic mode). The precipitation amount on wet days has the probability distribution $f(P_w) = e^{-P_w/\beta} \beta^{-\alpha} P_w^{\alpha-1} / \Gamma(\alpha)$ with $\alpha = P_w/\beta$ and $\beta = -2.16 + 1.83P_w$ for $P_w \geq 3$ and $\beta = 1.11P_w$ for $P_w < 3$.

Temperature

The monthly means of temperature and the daily temperature amplitude are interpolated linearly to daily mean values, denoted \bar{T} and \hat{T} (as the precipitation rate in periodic mode). In an optional weather generator mode, the daily temperature amplitude is reduced on wet days (\hat{T}_w) and increased on dry days (\hat{T}_d):

$$\hat{T}_w = \hat{T} / (x + (1-x)f_w) \quad (16)$$

$$\hat{T}_d = \hat{T} / (1 + (1/x - 1)f_w) \quad (17)$$

The value for $x = \hat{T}_d/\hat{T}_w$ is set to $x = 2$ for sensitivity studies described in Chapter 3 (Version 'V+'), i.e. dry days have twice the temperature range of wet days. (Solar radiation is varied in a similar fashion when this mode is chosen, see subsection "radiation").

For the daily course of temperature, it is assumed that the daily mean temperature, \bar{T} , lies half way between the daily maximum and minimum, and that the minimum temperature is reached at sunrise and the maximum at 14:00 h solar time. From sunrise to sundown, a sinusoidal temperature course is assumed, after sundown a linear decline (Rosenberg 1974, p. 91):

$$T(t) = \begin{cases} \bar{T} + \hat{T} \cos\left(\pi \frac{t-14}{\tau/2+2}\right) & \text{for } 12 - \tau/2 < t < 12 + \tau/2 \\ T(12 + \tau - 2) + x \left(T(12 - \tau/2) - (\bar{T} - \hat{T})\right) & \text{else.} \end{cases} \quad (18)$$

with

$$x = \begin{cases} \frac{t - (\tau/2 + 2)}{24 - \tau} & \text{for } t > 12 + \tau/2 \\ \frac{t + 24 - (\tau/2 + 2)}{24 - \tau} & \text{for } t < 12 - \tau/2 \end{cases} \quad (19)$$

Here, t stands for solar time in hours and τ for daylength. If daylength is less than 4 hours or more than 20 hours, a constant air temperature is assumed (i.e. $T = \bar{T}$).

Air humidity

Since no reliable data of near-surface air humidity exist for purposes of global modelling, this quantity has to be estimated. In such cases (e.g. Running et al. 1987) it is often assumed that the daily mean of the vapour pressure is equal to the saturation vapour pressure at the daily minimum temperature. Friend (1997) has checked this assumption with climate data by Müller (1982) and has found a good agreement for Europe and North America. For weather stations in arid regions, however, agreement is much less satisfactory, resulting in an overall correlation coefficient of $r^2 = 0.87$ for 805 stations. An overestimate of the

vapour pressure occurs, when the air is not saturated at the minimum temperature, T_{min} , as under severe drought (Running et al. 1987), and an underestimate, when the vapour pressure rises during the day because of evapotranspiration (Rosenberg 1974, p. 132ff.).

In order to account for such findings, the daily course of the vapour pressure, $e_a(t)$, is calculated from instantaneous saturation vapour pressure, $e_s(T)$, saturation vapour pressure at sunrise, $e_s(T_{min})$, and the ratio f_e of daily mean evapotranspiration and daily mean evaporative demand (cf. subsection "soil water balance"). Variation of the dependence is achieved through the parameters h_0 (relative humidity at sunrise, when $T = T_{min}$, and total drought, i.e. $f_e = 0$) and \hat{h} (daily amplitude of the vapour pressure under moist conditions, i.e. $f_e = 1$, as a fraction of the amplitude at constant saturation):

$$e_a = e_{a0} + f_e \hat{h} (e_s(T) - e_{a0}) \quad (20)$$

where

$$e_{a0} = (h_0 + (1 - h_0)f_e) e_s(T_{min}) \quad (21)$$

and

$$f_e(t) = \frac{E(t - \Delta t)}{E_{t,max}(t - \Delta t) + E_{s,max}(t - \Delta t)} \quad (22)$$

f_e is defined as the ratio of actual evapotranspiration (Equ. 13) to potential evapotranspiration from vegetation (Equ. 81) and soil (Equ. 87). For the computation of e_a , the value of the preceding time step Δt of one day is taken. The saturation vapour pressure over water or ice, $e_s(T)$, is calculated from Murray (1967):

$$e_s(T) = \begin{cases} 610.78 \exp(17.269T/(237.3 + T)) & \text{for } T > 0 \\ 610.78 \exp(22.33T/(271.15 + T)) & \text{for } T < 0 \end{cases} \quad (23)$$

e_s is given in units of Pa and T in °C.

Instead of a dependence on actual evapotranspiration, Friend (1997) has chosen a formulation for the daily mean vapour pressure depending on precipitation rate and daily minimum temperature developed empirically on the basis of the data by Müller. The formulation uses separate regression constants for 704 weather stations. The parameters h_0 and \hat{h} are therefore set such that the results with the parametrisation of this model agree with the formulations found by Friend, i.e. $\bar{e}_a = (a + bP)e_s(T_{min})$ (see Section 3.2).

Radiation

The radiative balance at the surface is computed in three steps:

1. Solar elevation, earth-sun distance and solar flux are computed from geographical latitude, Julian day and solar hour.
2. The ratio r_{PAR} of potential to actual photosynthetically active radiation (PAR) is used to calculate total and PAR fraction of incoming solar radiation at the surface, and their direct and diffuse components. PAR is also used for the calculation of the photosynthetic rate.

3. The radiative balance at the surface is computed from total incoming solar radiation, surface albedo, vapour pressure, temperature, and cloudiness estimated from r_{PAR} .

When the previously introduced weather generator mode is chosen, the value for r_{PAR} is also differentiated between dry and wet days. This is done by first assuming a value of $r_{PAR,w} = 0.3$ for wet days, which is similar to the ratio of solar radiation at 100% against 0% cloudiness by Linacre (1968). The value $r_{PAR,d}$ for dry days is then computed such that the mean of all days within a month is again r_{PAR} , i.e. $r_{PAR} = r_{PAR,w}f_w + r_{PAR,d}(1 - f_w)$. If this value is greater than 1, $r_{PAR,d} = 1$ is assumed and, instead of $r_{PAR,d}$, $r_{PAR,w}$ is determined from the preceding equation.

The first step begins with the computation of the inverse squared earth-sun distance in astronomical units, r_{\odot}^{-2} (ie. in units of the average distance) according to Paltridge and Platt (1976):

$$r_{\odot}^{-2} = 1.00011 + 0.034221 \cos(\alpha_0) + 0.0128 \sin(\alpha_0)0.000719 \cos(2\alpha_0) + 0.000077 \sin(2\alpha_0) \quad (24)$$

with $\alpha_0 = 2\pi(d - 1)/365$ and the Julian day d (1: January 1st; 365: December 31st). Solar elevation, μ , defined as the cosine of the angle between zenith and the position of the sun (i.e. $\mu = 1$ if the sun stands at zenith and $\mu = 0$ if the sun is at the horizon), is computed in the following way:

$$\mu = \sin(\phi) \sin(\delta) - \cos(\phi) \cos(\delta) \cos(\pi t/12) \quad (25)$$

ϕ is the latitude and $\delta = -23.4(\pi/180) \cos(2\pi(d + 10)/365)$ is the position of the sun within the ecliptic. The solar flux above the atmosphere through a plane parallel to the earth's surface, R_{OA} , is given by

$$R_{OA} = S_0 r_{\odot}^{-2} \mu \quad (26)$$

with the solar constant $S_0 = 1360 \text{ Wm}^2$.

In the second step, PAR at the surface is first calculated according to Weiss and Norman (1985):

$$R_{PAR} = 0.44 t_{PAR} r_{PAR} R_{OA} \quad (27)$$

with

$$t_{PAR} = 0.4 + 0.6 t_{PAR,D} \quad (28)$$

and

$$t_{PAR,D} = \exp\left(\frac{0.185 p}{\mu p_0}\right) \quad (29)$$

The fraction of direct radiation in PAR, d_{PAR} , is also calculated according to Weiss and Norman (the rest being diffuse radiation from clouds and atmosphere):

$$d_{PAR} = \begin{cases} 0 & \text{for } r_{PAR} < 0.2 \\ \left(1 - \left(\frac{0.9 - r_{PAR}}{0.7}\right)^{2/3}\right) \frac{t_{PAR,D}}{t_{PAR}} & \text{for } 0.2 < r_{PAR} < 0.9 \\ 1 & \text{for } r_{PAR} > 0.9 \end{cases} \quad (30)$$

Here, p is the surface air pressure and $p_0 = 1.01325 \times 10^5$ Pa. p is computed from elevation, h , in m and daily mean temperature, \bar{T} , in K with the lapse rate of the standard atmosphere, \mathcal{L} (6×10^{-3} K/m, Houghton 1986):

$$p = p_0 \left(\frac{1}{1 + h\mathcal{L}/\bar{T}} \right)^{gM_a/(R\mathcal{L})} \quad (31)$$

with the gas constant R ($8.314 \text{ J K}^{-1} \text{ mol}^{-1}$), the standard surface gravity, g (9.81 m s^{-1}), and M_a , the molar mass of dry air ($28.964 \times 10^{-3} \text{ kg/mol}$). The use of the ratio r_{PAR} in Equ. 27 insures that the monthly mean of R_{PAR} is equal to the satellite-derived value by Pinker and Laszlo (1992). Total solar irradiance, R_s , which also contains the photosynthetically passive part from 0.7 to 4.0 μm , is calculated from R_{PAR} and the conversion factor, \mathcal{F} , according to Pinker and Laszlo:

$$R_s = R_{PAR}/\mathcal{F} \quad (32)$$

This conversion factor depends primarily on solar elevation, μ , and the optical depth of clouds, χ . In order to formulate an appropriate dependence of \mathcal{F} on r_{PAR} , it is assumed that r_{PAR} follows χ by $r_{PAR} = (1 + 0.1\chi)^{-1}$ (this is the solution of the 2-flux equation with a single-scattering albedo of 1, i.e. clouds to not absorb PAR, and a forward-scatter fraction of 0.9, cf. Houghton 1986, p. 84f.) and thus the following equation is fitted to simulation results by Pinker and Laszlo for the dependence of \mathcal{F} on χ and μ :

$$\mathcal{F} = \frac{1}{1 + (1.185 - 0.437r - 0.494r^2) \exp \{ (0.0305 - 0.208r + 0.495r^2) / \mu \}} \quad (33)$$

with $r = 1 - r_{PAR}$. The deviation of this fit is much less than 5% for $\mu \geq 0.2$ ($\approx 78^\circ$ from zenith). The form of the dependence of \mathcal{F} on μ in Equ. 33 results from the assumption that differential Rayleigh scattering is the main cause for the decrease in the PAR fraction at increasing zenith angle:

$$\mathcal{F} \approx \frac{ae^{b/\mu}}{ae^{b/\mu} + (1-a)e^{c/\mu}}$$

with constants a , b and c to be determined.

The direct fraction of total solar radiation, d_s , is computed from the direct fraction of PAR, d_{PAR} , the conversion factor for total radiation, \mathcal{F} , and the conversion factor for direct radiation only, \mathcal{F}_{dir} :

$$d_s = d_{PAR}\mathcal{F}/\mathcal{F}_{dir} \quad (34)$$

\mathcal{F}_{dir} has been fitted to data by Ross (1975):

$$\mathcal{F}_{dir} = \frac{1}{1 + 1.184e^{0.1061/\mu}} \quad (35)$$

Finally, the third step consists of calculating the radiative balance at the surface:

$$R_n = R_{L\downarrow} - R_{L\uparrow} + (1 - \rho_s)R_s \quad (36)$$

where ρ_S stands for surface albedo, $R_{L\downarrow}$ for longwave thermal radiation from the atmosphere to the surface and $R_{L\uparrow}$ for longwave radiation back from the surface. As explained above, net radiation is divided into a vegetation and a soil part ($R_n = R_{nv} + R_{ns}$):

$$R_{nv} = (1 - t_{l,v})(R_{L\downarrow} - R_{L\uparrow} - G) + a_v R_s \quad (37a)$$

and

$$R_{ns} = t_{l,v}(R_{L\downarrow} - R_{L\uparrow}) + a_s R_s + (1 - t_{l,v})G \quad (37b)$$

$t_{l,v}$ is the longwave (thermal) transmissivity of vegetation, a_v and a_s the shortwave (solar) effective absorptivity of vegetation and soil, respectively (with $1 - \rho_S = a_v + a_s$, see below) and G is the soil heat flux. According to Verma et al. (1986), G is assumed to be a constant fraction of net radiation (cf. also Rosenberg 1974, p. 179ff.):

$$G = 0.036R_n \quad (38)$$

It is assumed that the fraction $(1 - t_{l,v})$ of the soil heat flux is equal to the thermal radiation from the vegetation to the soil, so that this amount enters the radiative balances of both vegetation and soil (negative and positive).

Thermal upward radiation from the surface, $R_{L\uparrow}$, is computed from air temperature with a single value for surface emissivity, ε_O , of 0.97 (average for land surfaces, Brutsaert 1982, p. 137):

$$R_{L\uparrow} = \varepsilon_O \sigma T_K^4 \quad (39)$$

with the Stefan-Boltzmann constant σ ($5.6703 \times 10^{-8} \text{ Wm}^{-2}\text{K}^{-4}$) and the air temperature in Kelvin ($T_K = T + 273.16$).

Downward thermal radiation, $R_{L\downarrow}$, is computed with a temperature and humidity dependent emissivity of the cloudless atmosphere, ε_A , and a correction term depending on cloudiness, $r_{\varepsilon A}$:

$$R_{L\downarrow} = \varepsilon_A r_{\varepsilon A} \sigma T_K^4 \quad (40)$$

with

$$\varepsilon_A = \varepsilon_{A0} \left(\frac{e_a}{T_K} \right)^{\frac{1}{7}} \quad (41)$$

according to Brutsaert (1982, p. 139), where e_a is given in Pa and T_K in K, and an average correction from Bolz (1949),

$$r_{\varepsilon A} = 1 + 0.22n_c^2 \quad (42)$$

Here, cloud fraction, n_c , is estimated from r_{PAR} following Equ. 1 in Section 2.3 (with $n_c = 1 - n$):

$$n_c = \begin{cases} 1 & \text{for } r_{PAR} < 0.5 \\ (0.9 - r_{PAR})/0.4 & \text{for } 0.5 < r_{PAR} < 0.9 \\ 0 & \text{for } r_{PAR} > 0.9 \end{cases} \quad (43)$$

According to Brutsaert, the standard value for ε_{A0} is 0.64.

Table 2.4: Values for the soil albedo of three different brightness classes according to Wilson and Henderson-Sellers (1985), for both wet ($\rho_{s,w}$) and dry ($\rho_{s,d}$) soils.

| | wet | dry |
|--------|--------------|--------------|
| | $\rho_{s,w}$ | $\rho_{s,d}$ |
| light | 0.18 | 0.35 |
| medium | 0.10 | 0.20 |
| dark | 0.07 | 0.15 |

Since thermal radiation is computed from air temperature, T , the effect of warming or cooling of both vegetation and soil surfaces is neglected. This effect can be accounted for by the concept of isothermal conductivity, which will be discussed in the following subsection "evapotranspiration". Transmission of radiation through the vegetation canopy is computed from the two-flux equation with $\omega = 0$ (cf. Section 2.9), which is equivalent to Beer's Law of radiation absorption:

$$t_{l,v} = f_c \exp(-\bar{\mu}\Lambda/f_c) + (1 - f_c) \quad (44)$$

with $\bar{\mu} = 1$ and f_c according to Equ. 137 in Section 2.9. In order to insure radiative balance between vegetation and soil, it is further assumed that the fraction $(1 - t_{l,v})$ of the soil heat flux comes from the net radiation of the vegetation canopy (see above).

Absorptivity of vegetation and soil, a_v and a_s , depends in a complex fashion on structure and distribution of the leaves, and on the optical properties of leaves and the soil. Here, both values are estimated on the basis of f_{PAR} , the fraction of absorbed PAR computed in the photosynthesis part of the model (see Section 2.6, Equ. 125):

$$a_s = (1 - \rho_s) - (1 - \rho_s - a_{s,0})f_{PAR} \quad (45)$$

where $a_{s,0} = 0.05$ is the fraction absorbed by the soil under a closed canopy, and

$$a_v = (1 - \rho_v - a_{s,0})f_{PAR} \quad (46)$$

ρ_v is the albedo of dense vegetation (standard value: 0.15, Brutsaert 1982, p. 136). With these two equations, surface albedo, ρ_S , can be expressed as

$$\rho_S = 1 - a_v - a_s = \rho_s + (\rho_v b - \rho_s)f_{PAR} \quad (47)$$

The given value for $a_{s,0}$ has been found with the two-flux equations for PAR and NIR at medium soil brightness (0.15 and 0.25) and a LAI of 3 (cf. Section 2.6). Since the required accuracy for net radiation is lower than for absorption of PAR for photosynthesis calculations, this mode of estimate should be sufficient for the complete range of f_{PAR} . The necessity to solve the two-flux equations for both PAR and NIR is thus avoided.

The value for the soil albedo, ρ_s , depends either on soil water content, W_s , and the brightness class of the soil, or, in the presence of snow ($h_{sn} > 0$, see subsection “snow balance”, Equ. 64), on snow albedo, ρ_{sn} . The influence of solar elevation, μ , and cloudiness, n_c , on snow albedo is also taken into account (Loth and Graf 1996):

$$\rho_s = \begin{cases} x\rho_{s,w} + (1-x)\rho_{s,d} & \text{if } h_{sn} = 0 \\ \rho_{sn} & \text{if } \mu_{12} \leq 0 \\ \rho_{sn} + (1-\rho_{sn})\rho_{sn}^3 \left(n_c^2 + (1-1.3n_c^2)e^{1-(1-\mu_{12})^{-2}} \right) & \text{if } \mu_{12} > 0 \end{cases} \quad (48)$$

The albedo for wet and dry soils, $\rho_{s,w}$ and $\rho_{s,d}$, listed in Table 2.4, is determined by the brightness classification by Wilson and Henderson-Sellers (1985), which is part of the input data (see Section 2.3). If plant available soil water content is at field capacity (i.e. $W_s = W_{s,max}$), the wet-soil value is assumed ($x = 1$). If the soil has dried out down to a depth of $d_{top} = 10$ cm, the value for dry soils is taken ($x = 0$), while for intermediate values of the soil water content, the albedo is linearly interpolated between the two values ($0 \leq x \leq 1$). Since vertical soil water distribution is unknown, it is assumed that the soil dries evenly from top to bottom. (It should be noted that soil water below rooting depth is ignored, cf. subsection “soil water balance”). x is therefore computed from the following equation:

$$x = \max \left\{ 1 - \frac{d_r}{d_{top}} \left(1 - \frac{W_s}{W_{s,max}} \right); 0 \right\} \quad (49)$$

If snow is present ($h_{sn} > 0$), ρ_s follows the snow albedo, ρ_{sn} , calculated as in the snow model by Loth and Graf (1996). ρ_{sn} is a status variable set to the value of wet soil, $\rho_{s,w}$, at the start of a model run. Each time there is snowfall (see the following subsection “snow balance”), ρ_{sn} is increased by $P_{sn}/\xi_{sn}^n \times 10 \text{ m}^{-1}$ after a time step of one day, where P_{sn} is daily snowfall in kg m^{-2} and ξ_{sn}^n the density of fresh snow from Equ. 65. ρ_{sn} is allowed to reach a maximum of 0.8, the albedo of fresh snow. In order to simulate the decrease in snow albedo during aging, its value is decreased after each one-day time step, at a rate depending on daily average temperature, \bar{T} . If $\bar{T} < 0$, a constant rate of 0.006 per day is assumed, while for temperatures above freezing the decrease in albedo is also affected by melting and thus depends on snow height, h_{sn} . If h_{sn} lies above a critical value of 25 cm, daily decrease is $0.107 - 0.214\rho_{sn}$, while below that value the decrease is 0.071. In addition, it is assured that ρ_{sn} does not fall below the value of the snow-free soil.

A correction for the effect of solar elevation and cloudiness is also included in Equ. 48. The cloud fraction, n_c , is calculated from r_{PAR} following Equ. 43 and μ_{12} according to Equ. 25 with $t = 12$ and the condition

$$\mu_{12} = \min \{ \mu(t = 12); \cos(60^\circ) \} \quad (50)$$

Following is a summary of the calculations described so far: Of the values that appear in the energy balance equation (7), R_n (Equ. 36) and G (Equ. 38) have been explained

completely; variables used are air temperature, T , vapour pressure in air, e_a , and surface albedo, ρ_S . Variables not yet described are LAI, Λ , (see Section 2.8), plant available soil water content, W_s , the same quantity at field capacity, $W_{s,max}$ (see next subsection), snow height, h_{sn} (see subsection "snow balance") and the demand/supply ratio of evapotranspiration, f_e (see following subsections). Since the heat storage terms \dot{Q} and \dot{Q}_B in Equ. 7 are neglected, the remaining variables are H (sensible heat flux) and E (evapotranspiration rate). Additional unexplained variables from the water balance equation (8) are Φ (runoff) and \dot{W} (change in total water storage). Calculation of these variables is described in the next subsections, followed by the various evapotranspiration fluxes, and, to close the energy balance, by the sensible heat flux.

Soil water balance

The soil water balance can now be expressed as

$$W_s(t) - W_s(t - \Delta t) = (P_s(t) + P_v(t) + S_m(t) - E_t(t) - E_s(t) - \Phi(t))\Delta t \quad (51)$$

with a time step Δt of one day. The flux terms on the right hand side of the equation are therefore daily averages in $\text{kg m}^{-2}\text{s}^{-1}$. P_s and P_v are, respectively, the precipitation rates arriving at the soil directly, or being intercepted by vegetation first and then dripping through to the ground. P_s is calculated from $P_s = P - P_{sn} - P_i$ with P_{sn} from Equ. 60 and P_i from Equ. 56; P_v is given by Equ. 57 (next subsection), S_m , the rate of snow melt, by Equ. 61 (subsection "snow balance"), E_t by Equ. 72 (transpiration, subsection "evaporation from vegetation") and E_s by Equ. 91 (soil evaporation, subsection "evaporation from the soil").

The remaining quantity to be explained is Φ , which represents the sum of above-ground runoff of rain and melt water and below-ground drainage of soil water. Of these, above-ground runoff can be expressed as the difference between rain and melt water input ($P_s + P_v + S_m$) and the rate of infiltration. Infiltration is generally considered a highly complex process that is difficult to model. It not only depends on the water content of the soil, but also on vertical and horizontal heterogeneity, caused e.g. by cracks and faults, and on the short-term intensity and spatial distribution of rain events (Hillel 1980). It is therefore understandable that, despite its great significance for agriculture, no generally applicable model exists to-date that is able to describe such processes in a satisfactory manner.

For this reason, a simplified model for the water storage of soils is used here, that is, a so-called "bucket" model. It is based on the observation that below a certain water content, termed "field capacity", the water is bound to the soil so tightly that any vertical movement within the soil is virtually stopped. Above this value, hydraulic conductivity increases so fast that subsequent below-ground drainage can be considered immediate. The assumption made here is that any water input above field capacity leads to immediate runoff, Φ , while it remains undetermined whether it is surface runoff by non-infiltrating rain or melt water, or subsurface drainage assumed instantaneous compared to a time step

of one day. When determining the size of the “bucket”, only the part of the soil is considered that can be reached by plant roots, while higher soil depths are ignored. Soil water that cannot be extracted by plants is also ignored, the corresponding water content is called the “permanent wilting point”.

To summarise, the soil water balance only considers the plant available amount of soil water, W_s , and is not allowed to increase above the plant available water content at field capacity, $W_{s,max}$. Runoff, Φ , can thus be formulated according to

$$\Phi(t)\Delta t = \max \{W_s(t - \Delta t) + (P_s + P_v + S_m - E)\Delta t - W_{s,max}; 0\} \quad (52)$$

The soil water holding capacity of the soil, $W_{s,max}$, is calculated at each grid point by the following procedure: From the data set by Dunne and Willmott (1996, cf. Section 2.3), each grid point is assigned a soil profile with up to five soil horizons, each with fractions of clay, silt and sand. For a possible extension of the model to several soil layers, each soil profile is mapped onto several layers of uniform depth, where both number and depth can be set freely. The standard setting is five layers down to depths of 10, 30, 70, 150 cm and, the fifth layer, to the total depth of the soil profile, except when the soil is shallower than 150 cm. In this case, the number of layers is reduced accordingly, with the lowest layer always reaching to total soil depth. Eventually, each layer is assigned the clay, silt and sand fraction of the horizon that has the largest overlap with that layer. (E.g. if the first horizon goes down to 25 cm, its properties are assigned to layers 1 and 2.)

Since roots often penetrate the bedrock in very shallow mountain soils (Walter and Breckle 1994, p. 115), a minimum rooting depth of 30 cm is assumed throughout. If soil depth is less than this value, the depth of the lowest horizon (usually the only one) is set to that value.

Calculation of $W_{s,max}$ is done according to the soil hydraulic equations by Saxton et al. (1986), by determining the volumetric soil water content both at the permanent wilting point, Θ_w , and at field capacity, Θ_f . The permanent wilting point is defined by a soil suction of 1.8 MPa and the field capacity by a hydraulic conductivity of 2 mm/day (Federer 1979). $W_{s,max}$ is then calculated from:

$$W_{s,max} = \sum_{i=1}^{n_s} d_i (\Theta_f - \Theta_w) \quad (53)$$

n_s is the number of layers and d_i the thickness of each layer, as far as it is within the root zone:

$$d_i = \min\{l_{i-1}; d_r\} - \min\{l_i; d_r\} \quad (54)$$

where l_i is the depth of the lower boundary of layer i (with $l_0 = 0$) and d_r the rooting depth according to the vegetation map used (Section 2.4).

A special case of the water balance is given by irrigated agriculture and wetlands (I-W in Table 2.1). For these, $W_s = W_{s,max}$ is assumed throughout.

Skin reservoir balance

The balance equation of the skin or intercepted reservoir, W_i , is

$$W_i(t) - W_i(t - \Delta t) = (P_i(t) - E_i(t) - P_v(t))\Delta t \quad (55)$$

If rain falls on dense vegetation (approx. LAI > 3), most of it falls on leaves and branches. A considerable fraction initially remains as a thin film on the vegetation, while another fraction, depending on the size of raindrops and the interception capacity of the canopy, reaches the ground. While rainfall continues, the skin reservoir, W_i , reaches a maximum and the water begins to drip through to the ground. A good approximation for the LAI dependence of interception is the vertical projection of the leaf area divided by the ground area. When this value approaches 1, it is assumed that 100% of rainfall is intercepted by the vegetation canopy:

$$P_i = f_c \left(1 - e^{-0.5\Lambda/f_c}\right) P_r \quad (56)$$

f_c is the fractional cover of vegetation and Λ the LAI of the total area (vegetated and non-vegetated). Finally, the daily throughfall of rain through the canopy, $P_v\Delta t$, is calculated according to:

$$P_v\Delta t = \max\{W_i(t - \Delta t) + P_i\Delta t - W_{i,max}; 0\} \quad (57)$$

Thereby it is assumed that the skin reservoir fills up to a capacity of $W_{i,max}$ and that no evaporation happens during rain. The wetting capacity of the vegetation, $W_{i,max}$, is assumed proportional to LAI as in the BATS model (Dickinson et al. 1993)

$$W_{i,max} = w_{i,max}\Lambda \quad (58)$$

with an area-specific capacity, $w_{i,max}$, of 0.1 kg m^{-2} . Because of $W_i(t) \geq 0$, the daily evaporation from the skin reservoir is limited by the sum of the rain input and the size of the reservoir:

$$E_i\Delta t \leq (P_i - P_v)\Delta t + W(t - \Delta t)$$

This is taken into account in Equ. 70 when computing E_i .

Snow balance

The effect of snowfall on the energy and water balance is twofold: On the one hand, snow increases the maximum amount of water that can be stored at the land surfaces; on the other hand, snow, and fresh snow in particular, has a very low albedo, decreasing net radiation at the surface (Equ. 36) and thereby evaporation (Equ. 88). Since snow height enters the calculation of the snow albedo, a simple formulation is included for this variable.

The snow balance is described by the following equation:

$$W_{sn}(t) - W_{sn}(t - \Delta t) = (P_{sn}(t) - S_m(t) - E_{sn}(t))\Delta t \quad (59)$$

The snowfall rate, P_{sn} , depends on the daily average temperature, \bar{T} , and the precipitation rate, P (Wigmosta et al. 1994):

$$P_{sn} = \begin{cases} P & \text{for } \bar{T} \leq -1.1^\circ\text{C} \\ \frac{3.3-\bar{T}}{4.4}P & \text{for } -1.1^\circ\text{C} < \bar{T} < 3.3^\circ\text{C} \\ 0 & \text{for } \bar{T} \geq 3.3^\circ\text{C} \end{cases} \quad (60)$$

For snow melt, a simple function of temperature is chosen (in $\text{kg m}^{-2}\text{day}^{-1}$, Hagemann and Dümenil 1996):

$$S_m = 3.22 \max\{T/^\circ\text{C}; 0\} \text{ kg m}^{-2}\text{day}^{-1} \quad (61)$$

with T in $^\circ\text{C}$. Since $W_{sn}(t)$ in Equ. 59 is not allowed to assume negative values, the maximum for S_m is given by

$$S_m(t)\Delta t \leq W_{sn}(t - \Delta t) + (P_{sn}(t) - E_{sn}(t))\Delta t \quad (62)$$

The value for snow evaporation, E_{sn} , is calculated from the formula for equilibrium evapotranspiration with the latent heat of sublimation and the slope of the vapour pressure curve above ice (Equ. 88, subsection "snow evaporation"). From balancing arguments, however, it is not allowed to lie above the following value:

$$E_{sn}(t)\Delta t \leq W_{sn}(t - \Delta t) + P_{sn}(t)\Delta t \quad (63)$$

When calculating the snow balance, the snowfall rate is first determined (P_{sn} , Equ. 60), then the evaporation rate E_{sn} from Equ. 87, taking account of the relationship 63. Once these two variables are known, the limitation of the rate of snow melt, S_m (Equ. 61), can be determined from the relationship 62. Finally, the updated value for the snow pool size, W_{sn} , is calculated from Equ. 59.

Snow height, h_{sn} , is calculated from old-snow, ξ_{sn} , and fresh-snow density, ξ_{sn}^n :

$$h_{sn} = \frac{W_{sn} - P_{sn}}{\xi_{sn}} + \frac{P_{sn}}{\xi_{sn}^n} \quad (64)$$

with (in kg m^{-3} , Loth and Graf 1996):

$$\xi_{sn}^n = \begin{cases} 30 & \text{for } \bar{T} \leq -22.5^\circ\text{C} \\ 10 + \frac{8}{3}(\bar{T} + 30) & \text{for } -22.5^\circ\text{C} < \bar{T} \leq -15^\circ\text{C} \\ 50 + 1.7(\bar{T} + 15)^{1.5} & \text{for } \bar{T} \geq -15^\circ\text{C} \end{cases} \quad (65)$$

and daily average temperature, \bar{T} , in $^\circ\text{C}$.

Assuming vertically uniform density, i.e.

$$\xi_{sn}(t - \Delta t) = \frac{W_{sn}(t - \Delta t)}{h_{sn}(t - \Delta t)} \quad (66)$$

density of old snow is computed with a compaction rate by Anderson (1976) as follows:

$$\xi_{sn}(t) = \xi_{sn}(t - \Delta t) \left(1 + \frac{g}{\eta_c^0} \exp[-a_c \xi_{sn}(t - \Delta t) + b_c T] \frac{\Delta t}{2W_{sn}(t - \Delta t)} \right) \quad (67)$$

The constants are set according to the recommendations of Anderson: $\eta_c^0 = 3.7 \times 10^7 \text{ kg m}^{-1}\text{s}^{-1}$, $a_c = 2.1 \times 10^{-2} \text{ m}^3 \text{ kg}^{-1}$ and $b_c = 8 \times 10^{-2} \text{ K}^{-1}$.

Evaporation from vegetation

Total evapotranspiration from vegetation ($E_v = E_t + E_i$) is primarily driven by the net radiative balance of the vegetation (R_{nv} , Equ. 37a) and is limited by the available amount of soil (W_s , Equ. 51) and skin water (W_i , Equ. 55). If the vegetation surfaces are wet ($W_i > 0$), the canopy conductance is infinite ($G_c \rightarrow \infty$) so that evaporation follows its maximum rate, $E_{v,max}$, with the evaporated water coming from the skin reservoir:

$$E_v = E_i = E_{v,max} = \frac{sR_{nv} + \rho c_p(e_s(T) - e_a)G_a}{s + \gamma} \quad (W_i > 0) \quad (68)$$

Here, E_i is allowed to assume negative values during dew formation. When the vegetation is dry ($W_i = 0$), evapotranspiration is determined by G_c , which is the combined conductance of all stomata within the plant canopy. The transpiration rate is then calculated from the Penman-Monteith formula (Monteith 1965b):

$$E_v = E_t = \frac{sR_{nv} + \rho c_p(e_s(T) - e_a)G_a}{s + \gamma(1 + G_a/G_c)} \quad (W_i = 0) \quad (69)$$

An additional condition is given by $E_t \geq 0$, i.e. transpiration is only allowed from the vegetation to the atmosphere.

The daily integral of the evaporation rate E_i also depends on the size of the skin reservoir, W_i , and the rain input:

$$E_i(t)\Delta t = \min \left\{ \int_{1 \text{ day}} E_{v,max}(t') dt'; \quad W_i(t - \Delta t) + (P_i(t) - P_v(t))\Delta t \right\} \quad (70)$$

with a one-day time step Δt . In the model, this and all other daily integrals are approximated by summing up hourly values of the instantaneous rates.

According to Equ. 69, transpiration can only happen when the vegetation is dry. To account for this fact when calculating the daily rate $E_v\Delta t$, a time average wetness fraction is defined:

$$\mathcal{F}_i = \frac{E_i(t)\Delta t}{\int_{1 \text{ day}} E_{v,max}(t') dt'} \quad (71)$$

and daily transpiration is reduced accordingly:

$$E_t(t)\Delta t = (1 - \mathcal{F}_i) \int_{1 \text{ day}} \frac{sR_{nv} + \rho c_p \Delta e G_a}{s + \gamma(1 + G_a/G_c)} dt \quad (72)$$

The aerodynamic conductance, G_a , between the canopy and a reference height of 10 m is estimated from vegetation height, h_v (from Table 2.1):

$$G_a = \frac{ku}{\left[\ln\left(\frac{10}{0.1h_v} + 1\right) \right]^2} \quad (73)$$

with h_v in metres, a roughness length of $0.1h_v$ and a wind speed, u , 10 m above the canopy. u is set to a uniform value of 2 m/s, and k is the von Karmann constant (0.41). For temperate broadleaf and coniferous forests ($h_v = 15$ m), this amounts to a value of 0.198 m/s, while for short grass ($h_v = 0.3$ m) it is 0.024 m/s, in good agreement with the average observed values in Kelliher et al. (1993).

Further, ρ is the density of air (≈ 1.29 kg m⁻³), c_p the specific heat of air at constant pressure (≈ 1005 J kg⁻¹K⁻¹), γ the psychrometric constant (≈ 65 Pa K⁻¹), s the strongly temperature dependent slope of the vapour pressure curve, $\partial e_s(T)/\partial T$ (Equ. 23, in Pa K⁻¹), and λ the latent heat of evaporation (2.45 MJ kg⁻¹ at 20°C). Since snow sublimation is also modelled, e_s , s and λ are calculated differently for temperatures above or below 0°C, e_s and s according to Equ. 23, and λ (in J kg⁻¹, with T in °C) from

$$\lambda = \begin{cases} 2.501 \times 10^6 - 2.38 \times 10^3 T & \text{for } T > 0^\circ\text{C} \\ 2.834 \times 10^6 & \text{for } T < 0^\circ\text{C} \end{cases} \quad (74)$$

with a slightly temperature dependent evaporation heat (Jones 1983) and a fixed sublimation heat (Anderson 1976). The density of air follows

$$\rho = \frac{M_a p}{RT_K} \quad (75)$$

with the gas constant ($R = 8.314$ J K⁻¹mol⁻¹), the molar mass of air ($M_a = 28.964 \times 10^{-3}$ kg mol⁻¹), the air pressure, p (from Equ. 31, subsection "radiation") and the air temperature in Kelvin ($T_K = T + 273$). Finally, the psychrometric constant, γ , is defined as

$$\gamma = \frac{p c_p}{0.622 \lambda} \quad (76)$$

The remaining variable to be determined for the calculation of the transpiration rate is the canopy conductance, G_c . As mentioned before, it can be expressed as the sum of the stomatal conductances, g_s , of all leaves within the canopy (Raupach and Finnigan 1988, Raupach 1994):

$$G_c = \int_0^\Lambda g_s(l) dl \quad (77)$$

Λ denotes the leaf area index (LAI) of the canopy, and dl its differential element. A dependence of g_s on the following external factors is known (Farquhar and Sharkey 1982): Light (Sharkey and Ogawa 1987), intercellular CO₂ concentration (Morison 1987), potential evapotranspiration, i.e. leaf-to-air gradient of vapour pressure (Fischer and Turner 1978, Schulze 1986, Schulze et al. 1987) and soil water content (Schulze 1986, Turner 1986, Schulze et al. 1987). According to Schulze et al. (1994), its maximum value, $g_{s,max}$, i.e. the value at sufficient light and water supply, increases with leaf nitrogen content. Since maximum photosynthetic rate, A_{max} , also increases with leaf nitrogen (Field and Mooney 1986), there is a close relationship between $g_{s,max}$ and A_{max} . In fact, the photosynthetic rate, A , can be expressed by the following diffusion equation (in mol(CO₂)m⁻²s⁻¹, e.g. Jones 1983):

$$A = 0.625 g_s (C_a - C_i) \frac{p}{RT_K} \quad (78)$$

The factor 0.625 takes the lower diffusivity of CO₂ against water vapour into account. C_a and C_i are the CO₂ concentrations of free air and of air within the intercellular air spaces in mol(CO₂)/mol(air) = 10⁶ ppm. The factor behind the brackets is given for the conversion into units of mol(CO₂)/m³(air) (= 40.9 mol(air)/m³(air) at 25°C and standard pressure). Assuming a typical value for the intercellular CO₂ concentration under conditions of sufficient water supply, $C_{i,0}$, the non-water-limited stomatal conductance can be calculated from

$$g_{s,0} = \frac{1.6A_0}{C_a - C_{i,0}} \frac{RT_K}{p} \quad (79)$$

Integration across the canopy yields:

$$\begin{aligned} G_{c,0} &= \frac{1.6}{C_a - C_{i,0}} \int_0^\Lambda A_0(l) dl \frac{RT_K}{p} \\ &= \frac{1.6A_{c,0}}{C_a - C_{i,0}} \frac{RT_K}{p} \end{aligned} \quad (80)$$

Here, $A_{c,0}$ is the non-limited canopy photosynthesis rate. There are two important assumptions contained in this last equation:

First, the integrated conductance of a canopy does not, as assumed by Woodward (1987) in a modelling study on water limited LAI, increase linearly with the leaf area index, Λ . In fact, like $A_{c,0}$, $G_{c,0}$ saturates at high values of LAI, reaching approximately three times the maximum stomatal conductance, $g_{s,0}$. This is the result of a literature review on field measurements by Kelliher et al. (1995). If soil evaporation is also included, the total surface conductance appears to be largely independent of the LAI. The consequence is, that evapotranspiration from vegetated areas is not controlled by LAI, but by the net radiation, R_n . Therefore, a comprehensive description of the energy balance is a prerequisite for mechanistic modelling of the coupled system of evapotranspiration and photosynthesis. This is also underlined by the results of the sensitivity runs of the following chapter.

Second, the equation shown above suggests a linear relationship between maximum photosynthetic rate and maximum canopy conductance. Such a relationship is the result of an overview by Schulze et al. (1994). Equating the terms "maximum surface conductance" and "maximum canopy CO₂ assimilation" with $G_{c,0}$ and $A_{c,0}$, respectively, the values for C3 plants cited in Schulze et al. (1994) yield

$$G_{c,0} = 0.883A_{c,0}$$

with $G_{c,0}$ in mm/s and $A_{c,0}$ in $\mu\text{mol}(\text{CO}_2)\text{m}^{-2}\text{s}^{-1}$. Inserting this into Equ. 80 yields $C_a - C_{i,0} = 45$ ppm or $C_{i,0}/C_a = 0.87$ (at $C_a = 355$ ppm, 25°C and standard pressure). Indeed, it has often been observed that the ratio of leaf internal to external CO₂ concentration stays nearly constant when incident light intensity or external CO₂ concentration changes (Morison 1987). Therefore, to compute $G_{c,0}$ from Equ. 80, $C_{i,0}$ is set to a uniform value of $C_{i,0} = 0.87C_a$ for all C3 plants. For C4 plants, this ratio is set to 0.67, which has been computed from the relationship $G_{c,0} = 333A_{c,0}$ found for tropical grasses by Schulze et al.

Table 2.5: Results of a curve fit of $g_s = g_0/(1 + b_e\Delta e)$ to measurements by Turner et al. (1984), after minimising the root mean squared (r.m.s.) difference between curve and measurements. g_0 is in $\text{mmol m}^{-2} \text{s}^{-1}$, b_e in kPa^{-1} .

| Species | g_0 | b_e | r.m.s. | n |
|--------------------------|-------|-------|--------|---|
| <i>Helianthus annuus</i> | 707 | 0.35 | 9.5 | 5 |
| <i>Vigna unguiculata</i> | 2161 | 3.23 | 13.7 | 4 |
| <i>Pistacia vera</i> | 606 | 0.85 | 11.7 | 5 |
| <i>Nerium oleander</i> | 344 | 0.39 | 12.1 | 5 |
| <i>Prunus dulcis</i> | 209 | 0.39 | 6.4 | 5 |

(1994). (A lower value for C4 against C3 plants follows from the different enzyme kinetics of CO_2 uptake, and has been measured regularly, cf. Morison 1987). Calculation of the non-limited canopy photosynthesis, $A_{c,0}$, is described in Section 2.6.

With Equ. 80, the potential transpiration rate is now defined:

$$\lambda E_{t,max} = \frac{sR_{nv} + \rho c_p \Delta e G_a}{s + \gamma(1 + G_a/G_{c,0})} \quad (81)$$

This value is called “demand” by Federer (1979) and is equal to the transpiration rate without water limitation (see above, first subsection).

As explained at the beginning of this section, calculation of the actual canopy conductance, G_c , and the actual transpiration rate, E_t , follows a combination of the approaches by Jarvis and Federer. There is only one empirical multiplicative factor (cf. Equ. 9) depending on vapour pressure deficit, $\Delta e = e_s(T) - e_a$, and with a functional form proposed by Lindroth and Halldin (1986):

$$G_c = G_{c,0} \frac{1}{1 + b_e \Delta e} \quad (82)$$

A test of this form with measurements by Turner et al. (1984) is shown in Table 2.5. A curve described by $g_s = g_0/(1 + b_e\Delta e)$ with two free parameters is fitted by minimising the root mean squared (r.m.s.) deviation from the measurement. The success of the test is documented by the fact that the deviation is always much smaller than g_0 .

Studies by Turner et al. (1984) and Schulze et al. (1987) suggest that a signal transmitted by hormones from the roots is responsible for the closing of stomata under water limitation. To account for this effect, another multiplicative factor could be added to Equ. 82, as in the Jarvis approach. This would mean that stomata close even under sufficient water supply as a reaction to rising vapour pressure deficit. However, stomata do not react directly to vapour pressure deficit of the surrounding air, but to a rise in the evaporative demand (Schulze et al. 1987); as long as the supply of soil water is sufficient, stomata tend to remain open even under high atmospheric drought.

A different approach is therefore chosen here, following Federer's model: The empirical constant b_e is redefined at each daily integration such that at the time of the highest transpirational demand, $E_{t,max}$, assumed at 13:00 hours in the model, the transpiration rate from Equ. 69 is less or equal to a supply rate, S . This rate is constant over a day and depends on soil water content and root density. Without detailed knowledge of soil hydrology and root distribution, a reasonable approximation according to Federer (1982) is

$$S = c_w \frac{W_s^{eff}}{W_{s,max}} \quad (83)$$

with values for c_w in the range of 0.5 to 2.0 mm/hour and an effective soil water content, W_s^{eff} (Equ. 84). In particular, $b_e = 0$ if demand, $E_{t,max}$, is less than S throughout the day.

Thus, the only remaining free parameter of the stomatal model is the rate c_w . This is justified by the fact that this parameter represents the root system that is not described explicitly. All other elements of the model are based on general principles of stomatal control (cf. subsection "significance of stomata...") or on empirical findings. An empirical approach is chosen in Equ. 82 instead of a mechanistic description of stomatal response to atmospheric demand (Schulze et al. 1987, Friend 1995), because designing a global model of detailed soil hydraulic processes appears to be unfeasible. Further, results presented in Chapter 3 show that the exact choice of c_w is of minor significance for the global modelling of the carbon and water balance; a numerically much more detailed model, as the one by Friend (1995), even if it can simulate the diurnal course of G_c a little more realistically, would therefore not be justified.

The last point described in this subsection is the dependence of stomatal conductance on soil and air temperature as assumed in the model: On the one hand, the temperature dependence of G_c is given by the temperature dependence of $A_{c,0}$ through Equ. 80 (Section 2.6). Also, $A_{c,0} = 0$ if the daily average of air temperature, \bar{T} , is zero degrees or less, and thus $G_c = 0$ and $E_t = 0$. On the other hand, if the soil is partly frozen while the air is already warmer than 0°C , there is a dependence on soil temperature through the effective soil water content, W_s^{eff} :

$$W_s^{eff} = \begin{cases} \max\left\{W_s \left(1 - \frac{d_{fr}}{d_r}\right); 0\right\} & \text{if } \bar{T} > 0 \text{ and } \bar{T} > T_{1.5} \\ 0 & \text{if } \bar{T} < 0 \\ W_s & \text{else.} \end{cases} \quad (84)$$

d_r is the rooting depth, $T_{1.5}$ the soil temperature at 1.50 m depth and d_{fr} the frost penetration depth. $T_{1.5}$ is estimated in the following way: Assuming a thermal conductivity of the soil of $7.5 \times 10^{-7} \text{ m}^{-2}\text{s}^{-1}$ (DKRZ 1992, this is the global value assumed in the climate model ECHAM3), the annual temperature cycle at approximately 1.5 m depth has a delay of 1 month and an amplitude of around 60% compared to air temperature (Rosenberg 1974, p. 66ff.). This leads to:

$$T_{1.5}(d) = \bar{T}^a + 0.6 [\bar{T}(d - 30) - \bar{T}^a] \quad (85)$$

where d is the Julian day number and \bar{T}^a the annual mean temperature. To determine the frost depth, d_{fr} , a linear temperature course is assumed up to the surface. With this assumption, d_{fr} can be computed for the first case in Equ. 84:

$$d_{fr} = \frac{1.50m\bar{T}}{\bar{T} - T_{1.5}} \quad (86)$$

This assumption is certainly unrealistic for a rooting depth much bigger than 1.50 m. However, in areas of very low winter temperatures, permafrost often occurs so that rooting depth tends to be small (Walter and Breckle 1994).

The following effect is neglected in the model described here: When calculating net radiation of vegetation, R_{nv} , or soil, R_{ns} , longwave upward radiation after Equ. 39 is calculated from air instead of skin temperature. For example, the skin temperature of vegetation, T_v , depends itself on the sensible heat flux $H_v = R_{nv} - \lambda E_v$. To a linear approximation, this can be accounted for by the concept of isothermal conductivity, G_i (e.g. Jones 1983), that has to be added to the surface conductivity. Its value can be calculated from $G_i = 4\sigma T^4 t_{i,v} / (pc_p M_a)$, which is 3.5 mm/s at 0°C and 6.0 mm/s at 40°C, $p = p_0$ and $t_{i,v} = 1$. This is an order of magnitude smaller than G_a for a typical grassland and even two orders of magnitude for coniferous forests (Kelliher et al. 1993), so that G_i can generally be neglect in large-scale studies.

Evaporation from the ground

Equilibrium evaporation is taken for the potential snow evaporation rate, $E_{sn,max}$, derived from the energy input to the ground, $R_{ns} - G$ (cf. Equ. 37b and 38):

$$\lambda E_{sn,max} = \frac{s(R_{ns} - G)}{s + \gamma} \quad (87)$$

$E_{sn,max}$ is thus determined primarily by net radiation, R_{ns} , and depends to a large extent on snow albedo. For the calculation of the daily snow evaporation, the amount of snow on the ground and the snowfall rate have to be taken into account:

$$E_{sn}(t)\Delta t = \min\{E_{sn,max}(t)\Delta t; W_{sn}(t - \Delta t) + P_{sn}(t)\Delta t\} \quad (88)$$

with a time step Δt of one day. The use of the equilibrium rate follows from the fact that the roughness of snow surfaces is small so that $G_a \rightarrow 0$ can be assumed.

Equilibrium evaporation is also assumed for the potential rate of soil evaporation (Philip 1957), reduced by the rate of snow evaporation, E_{sn} ;

$$\lambda E_{s,max} = \frac{s(R_{ns} - G)}{s + \gamma} - E_{sn} \quad (89)$$

For the simulation of soil evaporation, the model by Ritchie (1972) is applied, which describes soil evaporation in two phases: it starts with phase 1 at the potential rate up to a total evaporated amount of ΣE_1 , while in the ensuing phase 2, the cumulative evaporation

is proportional to the square root of time, with a proportionality factor κ_s , called "desorptivity". This model, originally developed for crops, has been successfully tested for the arid conditions of the Patagonian steppe by Paruelo et al. (1991). Following is a description of how the Ritchie model has been adopted to fit into the structure of the vegetation model developed in this study.

The two status variables of the Ritchie model are evaporation time, t_s , and the total evaporation, ΣE_s . Evaporation time is the time that has passed without additional rainfall since the beginning of phase 2, with a total phase 2 evaporation of $\Sigma E_s - \Sigma E_1$ (cf. Equ. 93). Daily evaporation is at first calculated in the following way:

$$E_{s,0}(t)\Delta t = \begin{cases} E_{s,max}(t)\Delta t & \text{if } \Sigma E_s(t - \Delta t) - P'_s(t)\Delta t < \Sigma E_1 \\ 0.8P'_s(t)\Delta t & \text{if } \Sigma E_s(t - \Delta t) - P'_s(t)\Delta t \geq \Sigma E_1 \\ \kappa_s (\sqrt{t_s + \Delta t} - \sqrt{t_s}) & \text{and } P'_s(t)\Delta t > 1.25\kappa_s(\sqrt{t_s + \Delta t} - \sqrt{t_s}) \\ & \text{else,} \end{cases} \quad (90)$$

where t_s is taken at the time step $t - \Delta t$, i.e. $t_s \equiv t_s(t - \Delta t)$. The precipitation rate arriving at the ground is $P'_s = P_s + P_v$. The first case represents phase 1 evaporation at the potential rate, $E_{s,max}$, and the last case phase 2 evaporation, controlled by desorptivity, κ_s . In between there is another case with additional rain input.

In a second step, the evaporation rate in phase 2 is limited by the atmospheric demand, i.e. the potential rate, and a case is included where evaporation is at the transition from phase 1 to phase 2. Actual soil evaporation is thus calculated from:

$$E_s(t)\Delta t = \begin{cases} E_{s,max}(t)\Delta t - 0.4 [\Sigma \tilde{E}_s(t - \Delta t) - \Sigma E_1] \Delta t & \text{if } \Sigma E_s(t - \Delta t) - P'_s(t)\Delta t < \Sigma E_1 \\ & \text{and } \Sigma \tilde{E}_s(t - \Delta t) > \Sigma E_1 \\ \min\{E_{s,0}(t); E_{s,max}(t)\}\Delta t & \text{else,} \end{cases} \quad (91)$$

with

$$\Sigma \tilde{E}_s(t - \Delta t) = \max\{\Sigma E_s(t - \Delta t) - P'_s(t)\Delta t; 0\} + \min\{E_{s,0}(t); E_{s,max}(t)\}\Delta t$$

At the end of the time step Δt , the two status variables are advanced:

$$\Sigma E_s(t) = \max\{\Sigma E_s(t - \Delta t) - P'_s(t)\Delta t; 0\} + E_s(t)\Delta t \quad (92)$$

and

$$t_s(t) = \begin{cases} 0 & \text{if } \Sigma E_s(t) < \Sigma E_1 \\ (\Sigma E_s(t) - \Sigma E_1)^2 / \kappa_s^2 & \text{else.} \end{cases} \quad (93)$$

The parameters desorptivity, κ_s , and phase 1 evaporation, ΣE_1 , are set depending on the sand fraction of the uppermost soil layer, f_1^{sand} , following the values given in Ritchie (1972):

$$\kappa_s = 5.62 - 2.56f_1^{sand} \quad (94)$$

in $\text{kg m}^{-2} \text{ day}^{-0.5}$ and

$$\Sigma E_1 = 14.29 - 9.23 f_1^{sand} \quad (95)$$

in kg m^{-2} .

To close the energy balance given by Equ. 7 or by Equ. 14 and 15, the calculation of the sensible heat flux, H , is also explained:

$$\begin{aligned} H &= H_v + H_s \\ &= R_n - G - \lambda E \\ &= R_{nv} + R_{ns} - G - \lambda(E_t + E_i + E_s + E_{sn}) \end{aligned} \quad (96)$$

In particular, at equilibrium evapotranspiration, E_{eq} , (Equ. 87 and Equ. 89, when $E_s = 0$), it is

$$\lambda E_{eq} = \frac{s(R_n - G)}{s + \gamma} \quad (97)$$

and

$$H_{eq} = \frac{\gamma(R_n - G)}{s + \gamma} \quad (98)$$

2.6 Photosynthesis models: Monteith and Farquhar

In this section, two models of photosynthesis, i.e. of the primary uptake of CO_2 by plants, are described. The first model goes back to the observation by Monteith (1977) that net primary productivity (NPP) is almost linearly related to the amount of photosynthetically active radiation (PAR) absorbed by the plants (the principle of light-use efficiency, cf. Section 1.5). As an extension of this model, it is possible to consider water in addition to light as a growth limiting factor. This is done by reducing canopy conductance at reduced soil water supply, as described in the preceding section.

As a second model, an enzyme kinetic parametrisation by Farquhar et al. (1980) for the photosynthesis of C3 plants is used; for C4 plants, it is an adaptation of the model by Collatz et al. (1992), without the stomata parametrisation by the authors.

The Monteith approach

Here, a linear relationship between canopy photosynthesis without water limitation, $A_{c,0}$ (in $\text{mol}(\text{CO}_2) \text{ m}^{-2}\text{s}^{-1}$) and absorbed PAR (in $\text{W m}^{-2}\text{s}^{-1}$) is assumed. The connection is expressed through the NPP-related light-use efficiency according to Table 2.1 in Section 2.4 (ϵ in $\text{g dry matter per MJ PAR}$). Translation of the NPP related rates is done by the factor $f_{R,0}$ (see Section 2.7, Equ. 131):

$$A_{c,0} = \epsilon \frac{C_{drm}}{f_{R,0} M_c} f_{PAR} R_{PAR} \quad (99)$$

C_{drm} is the carbon content of dry matter (0.45 gC/g , Ajtay et al. 1979) and $M_c = 12 \text{ gC mol}(\text{CO}_2)^{-1}$. Further variables are f_{PAR} , the grade of PAR absorption by plants,

computed on the basis of LAI, radiative and canopy geometry (FPAR, Equ. 125, see below) and R_{PAR} , the PAR fraction of direct and diffuse radiation taken together (Section 2.5, Equ. 27).

Initially, $A_{c,0}$ determines the non-limited canopy conductance, $G_{c,0}$ (Equ. 80) and thus the potential transpiration rate, $E_{t,max}$ (Equ. 81). Then, if water availability is limited, $G_{c,0}$ is reduced according to Equ. 82. The result, G_c , determines the actual transpiration rate, E_t (Equ. 72). In the case of $G_c < G_{c,0}$ the stomata are closed too far for the requirement of the potential photosynthesis, $A_{c,0}$. To account for the ensuing reduction of photosynthesis, the actual rate, A_c , is calculated analogous to Equ. 80 (in $\text{mol}(\text{CO}_2)\text{m}^{-2}\text{s}^{-1}$):

$$A_c = 0.625G_c(C_a - C_i) \frac{P}{RT_K} \quad (100)$$

The net leaf assimilation, A_c , is calculated in a similar fashion in the model Forest-BGC by Running and Caughlan (1988), where a fixed value for the intercellular CO_2 concentration, C_i , is used (Running 1984). In this study, however, it is assumed that C_i decreases at increasing drought stress down to a minimum value of $C_{i,min}$. This value is set to $0.3C_a$ (ca. 100 ppm) for C3 and to $0.15C_a$ (ca. 50 ppm) for C4 photosynthesis:

$$C_i = C_{i,min} + (C_{i,0} - C_{i,min})G_c/G_{c,0} \quad (101)$$

By comparison, the non-water-limited CO_2 concentration, $C_{i,0}$, is $0.87C_a$ for C3 and $0.67C_a$ for C4 plants (see Section 2.5). The exact value of $C_{i,min}$ is relatively uncritical, since even at the compensation point of C3 photosynthesis, Γ_* (45 ppm at 30°C , see below), A_c is only 20% higher than at $C_i = C_{i,min}$ (cf. Equ. 100). Other than in the Farquhar model, below, where C_i is computed independently for several layers, the intercellular CO_2 concentration is assumed uniform throughout the canopy. Successful use of a constant value for C_i in Forest-BGC has, however, demonstrated that this is a useful approximation for forests; in arid environments, LAI is usually small so that light absorption and leaf-internal CO_2 concentration do not vary much within the vegetation layer. The controlling factor for C_i , $G_c/G_{c,0}$, is taken from Equ. 82.

The advantage of this model is that the rate of photosynthesis does not have to be integrated from the leaf to the canopy level. Because the canopy conductance, G_c , is calculated from $A_{c,0}$, both photosynthesis and transpiration can be calculated from FPAR alone, without reference to LAI. This is important, since FPAR can be derived from satellite data more accurately than the LAI (see Chapter 5, Section 5.2).

The Farquhar approach

The non-limited photosynthetic rate, A_0 , is again calculated at a fixed intercellular CO_2 concentration, $C_{i,0}$. Calculation of the actual assimilation rate, A , at the leaf level as a function of the actual intercellular CO_2 concentration, C_i , is first explained for the C3 pathway, following Farquhar et al. (1980). A is formulated as the minimum of an electron

transport limited rate, J_E , and a rate, J_C , limited by the carboxylating enzyme Rubisco (in molar units, i.e. $\text{mol}(\text{CO}_2)\text{m}^{-2}\text{s}^{-1}$):

$$A = \min\{J_C; J_E\} - R_d \quad (102a)$$

with

$$J_C = V_m \frac{C_i - \Gamma_\star}{C_i + K_C(1 + O_x/K_O)} \quad (102b)$$

$$J_E = J \frac{C_i - \Gamma_\star}{4(C_i - 2\Gamma_\star)} \quad (102c)$$

R_d is the leaf or "dark" respiration, and J the electron transport rate. J depends on the rate of PAR absorption, I , in $\text{mol photons m}^{-2} \text{ s}^{-1}$ in the following way:

$$J = \frac{\alpha I J_m}{\sqrt{J_m^2 + \alpha^2 I^2}} \quad (103)$$

where $I = I_{PAR}/E_{PAR}$, with the PAR absorption rate I_{PAR} in W m^{-2} and the energy content of PAR quanta, (220 kJ/mol, Jones 1983, p. 160). The temperature dependence of the maximum electron transport rate, J_m , is calculated according to Farquhar (1988) from the canopy temperature, T_v , in $^\circ\text{C}$ and the respective rate at 25°C from Table 2.1:

$$J_m(T_v) = J_m(25^\circ\text{C}) \times T_v/25 \quad (104)$$

For the CO_2 compensation point without leaf respiration, Γ_\star (in $\mu\text{mol}(\text{CO}_2)\text{mol}(\text{air})^{-1}$), a linear dependence on vegetation temperature (in $^\circ\text{C}$) is assumed, again following Farquhar (1988):

$$\Gamma_\star = 1.7T_v \quad (105)$$

At sufficient light, the rate of photosynthesis is limited by V_m , the maximum turnover rate of the primary CO_2 fixating enzyme, Rubisco, while at low light levels, it is J_m limiting the assimilation rate. Following Farquhar et al. (1980) and in accordance with Berling and Quick (1995), a sharp transition from Rubisco to light limited photosynthesis is assumed. In nature, this so-called 'Blackman' curve is observed with a certain transition zone, where both rates are simultaneously limiting. The argument used by Farquhar et al. is that this co-limitation is a suboptimal behaviour that tends to be minimised (Collatz et al. 1990). Nonetheless, a certain co-limitation is often introduced by a curve parameter (e.g. Farquhar et al. 1980, Collatz et al. 1991). Because its actual size is difficult to determine for a global simulation, and because the result does not deviate much from that according to Equ. 102a, this parameter is not used here.

The values for V_m and J_m are vegetation specific and are listed in Table 2.1 for the standard temperature of 25°C . α is assigned a value related to incoming light taken from Berling and Quick (1995) divided by a leaf absorption of 0.86 according to Collatz et al.

Table 2.6: Values of the kinetic parameters and constants for the calculation of the C3 photosynthetic rate with the Farquhar model; lower part: additional constants for C4 photosynthesis. E is the activation energy in J/mol; s.t.: see text, const.: no temperature dependence, F&a: Farquhar et al. (1980), C: Collatz et al. (1992), F: Farquhar (1988), BQ: Berling and Quick (1995)

| symbol | description | value at 25°C | unit | E | reference |
|------------|---|---------------|--------------------------------------|----------|-----------|
| α | efficiency of photon capture | 0.28 | - | (const.) | BQ |
| Γ_* | CO ₂ compensation point | 42.5 | $\mu\text{mol m}^{-2} \text{s}^{-1}$ | s.t. | F |
| O_x | O ₂ partial pressure | 0.21 | mol/mol | 35948 | F&a |
| K_C | Michaelis-Menten constant for CO ₂ | 460 | $\mu\text{mol/mol}$ | 59356 | F&a |
| K_O | Michaelis-Menten constant for O ₂ | 0.33 | mol/mol | 35948 | F&a |
| V_m | carboxylation capacity | s.t. | $\mu\text{mol m}^{-2} \text{s}^{-1}$ | 58520 | BQ F&a |
| J_m | electron transport capacity | s.t. | $\mu\text{mol m}^{-2} \text{s}^{-1}$ | s.t. | BQ F |
| R_d | leaf or dark respiration | s.t. | $\mu\text{mol m}^{-2} \text{s}^{-1}$ | 50967 | C |
| α_i | integrated C4 quantum efficiency | 0.04 | mol/mol | (const.) | C |
| k | PEPcase CO ₂ specificity | s.t. | $\text{mmol m}^{-2} \text{s}^{-1}$ | 50967 | C |
| θ | curve parameter for J_e | 0.83 | - | - | C |

(1991). The temperature dependence of V_m , J_m and all other rates with an activation energy given in Table 2.6 is computed from the following equation (with T_v in °C):

$$k(T_v) = k(25^\circ\text{C}) \exp \left\{ \frac{(T_v - 25)E}{298R(T_v + 273)} \right\} \quad (106)$$

where k stands for the rate in question. Rates and constants that do not depend on vegetation type are also listed in Table 2.6.

In closed canopies, the light-saturated assimilation rate is normally differentiated according to light availability. Therefore, in accordance with Sellers et al. (1996), an exponential reduction in V_m and J_m from top to bottom is assumed for $\Lambda > \Lambda_0 = 3$ (cf. Equ. 137):

$$V_m(l) = V_m \times K_{12} e^{-K_{12}l} \quad (107)$$

$$J_m(l) = J_m \times K_{12} e^{-K_{12}l} \quad (108)$$

where V_m and J_m are the temperature dependent values according to Equ. 106 and 104, and K_{12} the extinction coefficient at noon (Equ. 119c with $\mu(t = 12)$). This scaling of photosynthetic capacity is applied to trees, shrubs and crops, not to grasses or tundra vegetation.

The non-limited photosynthesis, A_0 , is first calculated from Equ. 102a to 102c with $C_i = C_{i,0}$ ($C_{i,0}$ as in the preceding section); then the canopy rate is formed as an integral over the leaf area (cf. Equ. 80):

$$A_{c,0} = \int_0^\Lambda A_0(I_{PAR}(l)) dl \quad (109)$$

This integral is solved approximately by summing over several layers, each with PAR absorption, I_{PAR} , calculated separately (see below, subsection "light absorption").

The canopy temperature, T_v , can lie above or below the air temperature, T , depending on the energy balance of the vegetation canopy in the following way:

$$T_v = T + \frac{R_{nv} - E_t}{\rho_a c_p G_a} \quad (110)$$

E_t is calculated according to Equ. 69, with G_c from $G_{c,0}$ after Equ. 82. The influence of skin reservoir evaporation (E_i) is neglected (i.e. $E_v = E_t$, cf. Equ. 69). Since $G_{c,0}$ depends through Equ. 80 on $A_{c,0}$, itself dependent on T_v , $A_{c,0}$ and, through Equ. 80, $G_{c,0}$ are computed at a temperature of $T_v = T$. Then, the actual canopy conductance, G_c , is calculated from Equ. 82, with the dependence on vapour pressure deficit assumed throughout the canopy (cf. Equ. 79):

$$\begin{aligned} g_s(l) &= g_{s,0}(l)G_c/G_{c,0} \\ &= \frac{1.6A_0(l)}{C_a - C_{i,0}} \frac{RT_K}{p} \frac{1}{1 + b_e \Delta e} \end{aligned} \quad (111)$$

Both transpiration, E_t , and canopy temperature, T_v , are now determined from G_c . A self-consistent calculation, where T_v has to be reinserted iteratively into the equation for $A_{c,0}$, is not carried out here. Since the calculation of $A_{c,0}$ and $G_{c,0}$ at a uniform $C_{i,0}$ has mainly the purpose of formulating a generally applicable dependence of the stomatal conductance on incident light, the error involved is comparatively small.

The actual assimilation rate, A , is eventually computed at a fixed stomatal resistance, g_s , and at a canopy temperature, T_v , computed as described above. The relevant equations are on the one hand Equ. 102a to 102c of the Farquhar model, on the other hand the diffusion equation for CO_2 :

$$A(l) = 0.625g_s(l)(C_a - C_i) \frac{p}{RT_K} \quad (112)$$

Besides A , the undetermined variable is C_i . Equ. 112 is therefore solved for C_i and inserted into Equ. 102b and 102c. The results are quadratic equations for J_C and J_E ; the minimum of the respective lesser solutions of those quadratic equations yields $A(l)$. Finally, the canopy photosynthesis, A_c in $\text{mol}(\text{CO}_2)\text{m}^{-2}\text{s}^{-1}$, is taken as the integral over the leaf area:

$$A_c = \int_0^\Lambda A(l)dl = \frac{0.625p}{RT_K} \int_0^\Lambda g_s(l) (C_a - C_i(l)) dl \quad (113)$$

For C4 photosynthesis, Equ. 102a to 102c are replaced according to Collatz et al. (1992) by the following:

$$A = \min\{J_c; J_e\} - R_d \quad (114a)$$

$$J_c = kC_i \quad (114b)$$

$$J_e = \frac{1}{2\theta_s} \left[V_m + J_i - \sqrt{(V_m + J_i)^2 - 4\theta_s V_m J_i} \right] \quad (114c)$$

$$J_i = \alpha_i \frac{I_{PAR}}{E_{PAR}} \quad (114d)$$

As with C3 photosynthesis, a gradual onset of light limitation is assumed, with a sudden transition from J_c to J_e limitation at rising C_i . Another reason for not using a curve parameter for this transition is mathematical: thus, after calculation of $g_s(l)$ as above, $A(l)$ can be derived from:

$$A(l) = \min \left\{ J_e; \frac{C_a + R_d/g'_s(l)}{1/k + 1/g'_s(l)} \right\} - R_d \quad (115)$$

with $g'_s = 0.625g_s p/(RT_K)$.

Following Farquhar et al. (1980), leaf or dark respiration, R_d , at 25°C is assumed proportional to V_m , also at 25°C. The constant of proportionality depends on photosynthetic pathway and is 0.011 for C3 plants (Farquhar et al. 1980, Collatz et al. 1991). As a result of the complex, two-step process, the value for C4 plants should be significantly higher. In fact, with 0.021, the value assumed for maize in Collatz et al. (1992) is almost twice as high. However, during the calculations described in Chapter 3 it has turned out that at such a value, respiration costs for C4 grasses are considerably lower than for C4 grasses on a global average. For this reason, and also because only few data are available for this vegetation type, the respiration constant for C4 grasses is determined together with V_m and k from the principle of coexistence. The condition is that at places with an equal proportion of C3 to C4 grasses, both GPP and NPP are equal for the two vegetation types (see Sections 2.4 and 2.7). Taking this into account, the actual formulation for leaf respiration used here is:

$$R_d(25^\circ\text{C}) = \begin{cases} 0.011V_m(25^\circ\text{C}) & \text{(C3)} \\ 0.042V_m(25^\circ\text{C}) & \text{(C4)} \end{cases} \quad (116)$$

The temperature dependence of R_d is again given by Equ. 106 with an activation energy according to Table 2.6.

Light absorption

Light absorption in the photosynthetically active spectrum is calculated within the two-flux approximation, following Sellers (1985), expressed by the following equations (with the cumulative leaf area index, l , as the vertical coordinate, where $l = 0$ at the top, and $l = \Lambda$ at the bottom of the canopy):

$$\begin{aligned} \bar{\mu} \frac{dR_\downarrow}{dl} + [1 - (1 - \beta)\omega]R_\downarrow - \omega\beta R_\uparrow &= \omega\bar{\mu}K(1 - \beta_0)R(l) \\ -\bar{\mu} \frac{dR_\uparrow}{dl} + [1 - (1 - \beta)\omega]R_\uparrow - \omega\beta R_\downarrow &= \omega\bar{\mu}K\beta_0 R(l) \end{aligned} \quad (117)$$

R_\downarrow and R_\uparrow are the diffuse fluxes downward and upward, and $R(l)$ is the direct flux with $R(0) = d_{PAR}R_{PAR}$ (Equ. 27 and 30):

$$R(l) = R(0)e^{-Kl} \quad (118)$$

Further, ω is the leaf single scattering albedo, β the forward scatter fraction for the diffuse flux, β_0 the same for the direct flux, K the extinction coefficient for the direct flux and $\bar{\mu}$ the mean of K^{-1} over the downward hemisphere ($\int_0^1 K^{-1}(\mu)d\mu$).

The following simplifications are used: (1) There is no preferred leaf orientation, i.e. distribution of leaf angles is isotropic; (2) leaf reflectivity and transmissivity are equal (the sum of the two is ω). These assumptions yield:

$$\beta = \frac{1}{2} \quad (119a)$$

$$\beta_0 = \frac{1}{2} \quad (119b)$$

$$K = \frac{1}{2\mu} \quad (119c)$$

$$\bar{\mu} = 1 \quad (119d)$$

where μ is the cosine of the solar zenith angle (cf. Equ. 25).

The following boundary conditions are also needed for the solution of Equ. 117: (1) $R_{\downarrow}(0)$ equals diffuse incoming radiation; (2) the reflection at the lower boundary is given by the soil reflectivity in the PAR region, ρ_s^{PAR} :

$$R_{\downarrow}(0) = (1 - d_{PAR})R_{PAR} \quad (120)$$

$$R_{\uparrow}(\Lambda) = \rho_s^{PAR}(R(\Lambda) + R_{\downarrow}(\Lambda)) \quad (121)$$

The standard value for the single scattering albedo for PAR is set to $\omega = 0.12$, while ρ_s^{PAR} is computed from the soil albedo in the total solar spectrum, ρ_s :

$$\rho_s^{PAR} = 0.92\rho_s - 0.015 \quad (122)$$

This dependence has been derived from the “soil line” by Price and Bausch (1995), a linear relationship between PAR and NIR (near infrared) reflectivity for moist soils, with the assumption $\rho_s = (\rho_s^{PAR} + \rho_s^{NIR})/2$ (cf. Section 4.5).

Under arid conditions, the ground is usually covered only partially with vegetation, to a degree described by the fractional cover, f_c . The calculation of f_c in the model is given in Section 2.9 (Equ. 137). This type of spatial concentration, or “clumping” of vegetation has a strong influence on the dependence of FPAR on LAI (Asrar et al. 1992), and thus on photosynthesis and the energy balance. If one neglects the effect of vegetation height, then the two-flux equations (117) are taken for the fraction f_c of a grid cell alone, with the LAI, Λ , replaced by the “clump” LAI, $\Lambda_c = \Lambda/f_c$. This is the approximation used in the standard model.

If f_c is much smaller than 1 and the ratio of height to width of the vegetation clumps significantly larger than 0, the vegetation can absorb considerably more light than calculated by the approximation described above. (Except for direct radiation from directly above, i.e. $\mu = 1$). Such a three-dimensional radiative transfer problem for describing the height effect cannot easily be applied to the two-flux approximation. In order to give at least an estimate of this effect within a larger sensitivity study (test ‘G’ in Table 3.2, Chapter 3), an effective fractional cover, f_c^{eff} , is defined that is larger than f_c for $\mu < 1$. A detailed description is given in the appendix; in the standard case, it is $f_c^{eff} = f_c$.

The rate of light absorption per leaf area is calculated for the light limited photosynthetic rate (Equ. 102c or 114d, respectively) as the sum over N_l layers of equal distance in l -coordinates, going from $l = l_{k-1}$ to $l = l_k$ with $l_0 = 0$ and $l_{N_l} = \Lambda_c^{eff}$:

$$\begin{aligned} I_k^{PAR} &= \frac{1}{l_k - l_{k-1}} \int_{l_{k-1}}^{l_k} \left\{ -\frac{d}{dl} (R + R_{\downarrow} + R_{\uparrow}) \right\} dl \\ &= \{ [R(l_{k-1}) + R_{\downarrow}(l_{k-1}) - R_{\uparrow}(l_{k-1})] \dots \\ &\quad \dots - [R(l_k) + R_{\downarrow}(l_k) - R_{\uparrow}(l_k)] \} / (l_k - l_{k-1}) \end{aligned} \quad (123)$$

where R , R_{\downarrow} and R_{\uparrow} are the solutions to the Equ. 117, 120 and 121 with $\Lambda = \Lambda_c^{eff}$ ($= \Lambda_c$ in the standard case). The canopy photosynthesis is then

$$A_c = f_c^{eff} \sum_{k=0}^{N_l} A(I_k^{PAR}) \quad (l_k - l_{k-1}) \quad (124)$$

and FPAR can be calculated from

$$\begin{aligned} f_{PAR} &= \{ [R(0) + R_{\downarrow}(0) - R_{\uparrow}(0)] - [R(\Lambda) + R_{\downarrow}(\Lambda) - R_{\uparrow}(\Lambda)] \} / (R(0) + R_{\downarrow}(0)) \\ &= 1 - \frac{R_{\uparrow}(0) + (1 - \rho_s^{PAR})(R(\Lambda) + R_{\downarrow}(\Lambda))}{R(0) + R_{\downarrow}(0)} \end{aligned} \quad (125)$$

Equ. 124 is the approximation used for the integrals of Equ. 109 and 113. Following the arguments by Sellers (1985), no separate layer for sunlit leaves is introduced.

2.7 Carbon balance

Gross primary productivity (GPP)

The carbon balance is computed in one-day times steps and in units of gC per m² and day. A part of it, that is the net leaf assimilation, A_c , has already been discussed in the preceding section (2.7). The gross primary productivity (GPP) is calculated from this quantity in the following way:

$$\text{GPP} = M_c \int_{1 \text{ day}} (A_c(t') + R_{d,c}(t')) dt' \quad (126)$$

The factor $M_c = 12 \text{ gC/mol}(\text{CO}_2)$ is used because photosynthesis is expressed in molar units of carbon. In the case of the Farquhar photosynthesis scheme, $R_{d,c}$ is the integral of R_d over the differential leaf area index, l :

$$R_{d,c} = \int_0^{\Lambda} R_d(l) dl \quad (127a)$$

For the Monteith model it is assumed, following Ryan (1991a), that maintenance respiration (see below) amounts to 40% of GPP under non-water-limited conditions, of which 40% is assigned to maintenance respiration of leaves ($f_{R,leaf}$, see below). Hence, $R_{d,c} = 0.16(A_{c,0} + R_{d,c})$, or:

$$R_{d,c} = f_{Rd} A_{c,0} \quad (127b)$$

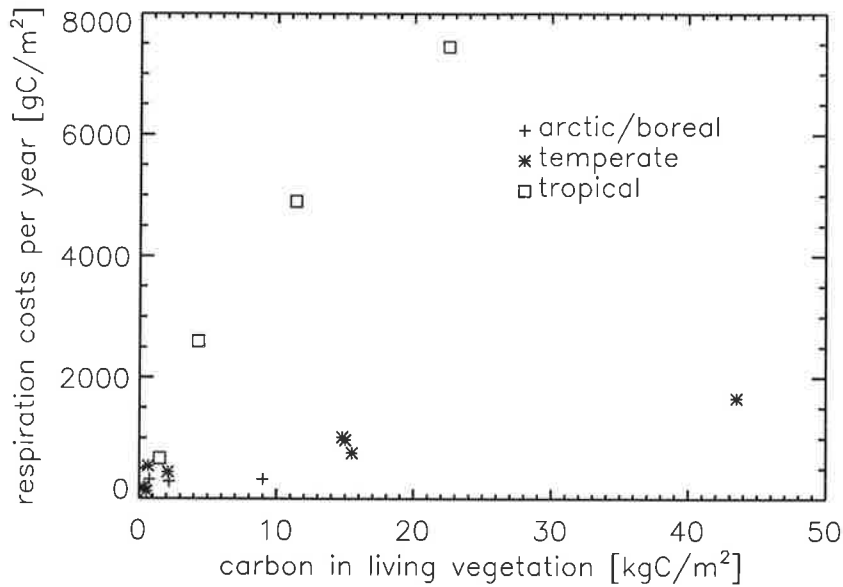


Figure 2.3: Respiration costs of vegetation for the field studies used to calibrate the biosphere model TEM, as far as cited, against total carbon content. With $r^2 = 0.19$, correlation is only moderate.

with $f_{Rd} = 0.14$. The use of $A_{c,0}$ has the effect that under drought stress, only CO_2 uptake is reduced, but not maintenance respiration.

Net primary productivity (NPP)

$R_{d,c}$ is one part of the total plant respiration, R_A . Following Ryan (1991a), R_A is divided into two parts, maintenance (R_M) and growth respiration (R_G). The difference between the two is that the so-called growth respiration occurs only when $\text{NPP} > 0$. In a number of vegetation models, e.g. TEM (Raich et al. 1991) and SILVAN (Kaduk 1996), this concept is used in such a way that R_M is proportional to biomass, i.e. to the carbon content, C_{tot} . However, Ryan (1991a) stresses that R_M and the nitrogen content of vegetation, N_{tot} , are usually much better correlated. As can be seen in Fig. 2.3 and 2.4, this is also true for the ecosystem studies used to calibrate TEM.

According to Ryan (1991a), R_M is approximately $0.30 \mu\text{mol}(\text{CO}_2)\text{m}^{-2}\text{s}^{-1}$ per gN at 25°C (same temperature dependence as for R_d assumed). Since V_m is nearly proportional to the nitrogen content of leaves (Farquhar et al. 1980) with around $45 \mu\text{mol}(\text{CO}_2)\text{m}^{-2}\text{s}^{-1}$ per gN (at 25°C , with 20% of N in Rubisco), it follows from Equ. 116 for C3 plants that R_d is approximately $0.5 \mu\text{mol}(\text{CO}_2)\text{m}^{-2}\text{s}^{-1}$ per gN, somewhat more than R_M . It seems that leaves, in terms of their nitrogen content, take up a higher proportion of total plant respiration than the remaining plant parts. Further, from the data by Ryan (1991b) it

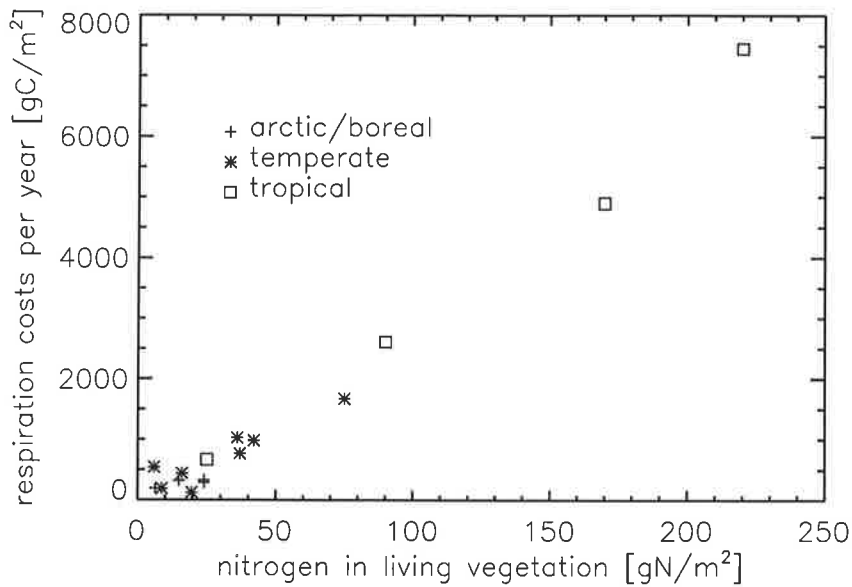


Figure 2.4: Respiration costs of vegetation for the TEM field studies, in this case against total nitrogen content. There is a high correlation with $r^2 = 0.98$.

follows that typically 40% of maintenance respiration takes place in the leaves. Out of this reason, the following equation will be used:

$$R_M = M_c R_{d,c} / f_{R,leaf} = 1.67 M_c R_{d,c} / f_{N,leaf} \quad (128)$$

$f_{R,leaf}$ is the leaf fraction of the plant-total maintenance respiration, and $f_{N,leaf}$ the leaf fraction of total nitrogen. The factor 1.67 accounts for the higher respiration rates per N in leaves (0.5 against 0.3, see above).

In a subtropical dry forest in Puerto Rico (Lugo and Murphy 1986), leaf nitrogen was 189 kg/ha of a total of 916 kg/ha, i.e. 21%, whereas in an equatorial moist forest in Zaïre (a 28-year-old secondary forest) 143 kg/ha were found in leaves for a 593 kg/ha total (Greenland and Kowal 1960), this is a portion of 24%. (With Equ. 128, this would mean $f_{R,leaf} \approx 0.4$). The similarity contrasts with the fact that with 25%, the root fraction of total nitrogen was significantly lower in the moist than in the dry forest, where it amounted to as much as 60%. It appears that the value of $f_{N,leaf}$ is a conservative quantity compared to the distribution of biomass between leaves, stem and roots. A possible explanation is that trees, because of competition with other trees, accumulate woody biomass until a certain critical value of $f_{N,leaf}$ around 20 to 25% is reached, from where on a reduction in NPP prevents further reduction of the relative leaf fraction. This might also be true for grasses, which increase root biomass under arid conditions until a similar value of $f_{N,leaf}$ is reached. This would explain why respiration costs relative to GPP are remarkably similar for grasses and trees (Ryan 1991a). Therefore, in this study a uniform value of $f_{N,leaf} = 0.14$ will be

used, or $f_{R,leaf} = 0.40$.

A mean value for growth respiration according to Ryan (1991a), which will be used here, is 0.25 gC per gC biomass produced:

$$R_G = f_{R,G}NPP = f_{R,G}(GPP - R_M - R_G) \quad (129)$$

with $f_{R,G} = 0.25$. Hence, the equation for net primary productivity is:

$$NPP = \frac{1}{1 + f_{R,G}}(GPP - R_M) \quad (130)$$

To calculate net leaf assimilation, $A_{c,0}$, for the Monteith model from Equ. 99, the factor $f_{R,0}$ is needed for the ratio of NPP to $A_{c,0}$. From Equ. 128 and 127b it follows for $A_c = A_{c,0}$:

$$R_M = \frac{M_c f_{Rd} A_{c,0}}{f_{R,leaf}}$$

and with Equ. 130 and 126

$$NPP = \frac{M_c}{1 + f_{R,G}} \left(A_c + f_{Rd} A_c - \frac{f_{Rd} A_{c,0}}{f_{R,leaf}} \right)$$

Hence, with $f_{R,0} = NPP/A_{c,0}$, NPP at $A_c = A_{c,0}$ (non-water-limited):

$$f_{R,0} = \frac{1 + f_{Rd}(1 - 1/f_{R,leaf})}{1 + f_{R,G}} \quad (131)$$

Inserting the standard values given above yields $f_{R,0} = 0.61$.

Soil respiration (RES)

According to Raich and Potter (1995), the most important factor determining the rate of soil respiration (RES) is temperature. In a summary of a large number of studies, the authors have found a clear temperature dependence with a Q_{10} of 1.58 related to air temperature for natural vegetation and of 1.49 for all types of vegetation. (Q_{10} is a multiplicative factor describing the rise in respiration for a temperature increase of 10°C.)

The second most important factor is precipitation, whereas no significant relationship of RES with soil carbon content is found. According to Meentemeyer (1978), RES is also, to a good approximation, proportional to the actual evapotranspiration, E . Since in this study, the focus is on the seasonality of CO₂ fluxes, it is further assumed that the annual respiration at each grid point of the model equals the annual NPP:

$$RES(t) = \frac{\int_{1 \text{ year}} NPP(t') dt'}{\int_{1 \text{ year}} f_e(t') Q_{10}^{\bar{T}(t')/10} dt'} f_e(t) Q_{10}^{\bar{T}(t)/10} \quad (132)$$

with the daily average air temperature, \bar{T} . Following Meentemeyer, the moisture factor is chosen as $f_e = E/(E_{s,max} + E_{t,max})$, that is the ratio of actual to potential evapotranspiration according to Equ. 22. (In Chapter 6, additional variants will be defined.) RES is

calculated with a time step of one day, which is also the time step for solving the integrals above.

It is possible that the above assumption is not valid for some ecosystems, as it has in fact been found for many temperate broadleaf and coniferous forests (Wofsy et al. 1993, Dixon et al. 1994, Kurz and Apps 1994). The difference between global NPP and RES, with an NPP in the range of 40 to 80 GtC (Houghton 1995 and Chapter 3), could be around 1 to 2 Gt or 0.6 to 2.5%. The effect of such an imbalance on the seasonal cycle of CO₂ fluxes should therefore be small and is consequently neglected here (see Chapter 6).

2.8 Phenology

The phenology of vegetation describes the timing of both leaf onset and shedding for deciduous plants and grasses. The main purpose of such a periodical buildup and loss of leaves is the avoidance of frost and drought damage. In this study, phenology is defined in a wider sense by the determination of the time dependence of the LAI as a function of air temperature, drought and the carbon balance. This also includes evergreen species. In the following subsections, the calculation of a temperature (Λ_T) and a water (Λ_W) controlled LAI, and a growth limited LAI (Λ_C) will be discussed, while the actual LAI at time step t is given as the minimum of those three values:

$$\Lambda(t) = \min\{\Lambda_T(t); \Lambda_W(t); \Lambda_C(t)\} \quad (133)$$

The LAI is here defined as the one-sided leaf area per grid cell divided by the complete grid cell area (not by the vegetation covered part, f_c , see below).

Temperature controlled phenology

The ecological reason for leaf shedding in cold climates is the avoidance of frost. Hence, the phenology should depend on the probability of low-temperature extremes at a given place. The actual mechanism controlling leaf onset and shedding, however, can be different in different plant types; for example, leaf shedding in most broadleaf trees is controlled by daylength (Walter and Breckle 1994, p. 7), while this behaviour is itself the result of an adaptation to the prevailing climate.

Here, such relatively complex and varying processes are not modelled in detail. Instead, following Dickinson et al. (1993), a mean temperature-dependent LAI of the various occurring species is defined:

$$\Lambda_T(t) = \begin{cases} 0 & \text{if } T_{0.5}(t) < T_\phi \\ \hat{\Lambda} \left[1 - \left(\frac{\hat{T}_\phi - T_{0.5}(t)}{\hat{T}_\phi - T_\phi} \right)^2 \right] & \text{if } T_\phi < T_{0.5}(t) < \hat{T}_\phi \\ \hat{\Lambda} & \text{if } T_{0.5}(t) > \hat{T}_\phi \end{cases} \quad (134)$$

where $T_{0.5} = (2\bar{T} + T_{1.5})/3$ is the assumed daily mean temperature at 0.5 m soil depth, which is calculated daily (with $T_{1.5}$ from Equ. 85). The standard values chosen are $\hat{\Lambda} = 5$ (Dickinson et al. 1993, where $\hat{\Lambda} = 6$ related to 80% vegetation cover, i.e. 4.8 related to total area), $T_\phi = 5^\circ\text{C}$ and $\hat{T}_\phi = 15^\circ\text{C}$. The temperature values are derived from the observed spring onset in mid April and leaf shedding at the end of October in Central Europe (Walter and Breckle 1994, p. 6ff.).

This equation is valid for all vegetation types except cold-evergreen (C-E, see Table 2.1) and arable crops (Codes 15, 16 and 20 to 22); the latter have a value of $T_\phi = 12^\circ\text{C}$. For cold-evergreen vegetation (i.e. conifers except larches), Λ_T is kept constant over one year and for $T_{0.5}$ in Equ. 134, the mean value of the warmest month is taken, i.e. $T_{0.5} = (2T_w + T_{1.5max})/3$, where $T_{1.5max}$ is the value of $T_{1.5}$ of the warmest month.

Soil water controlled phenology

When formulating drought motivated phenology, it is assumed that the reason for leaf shedding and wilting lies in a negative NPP, not in direct desiccation. It is, therefore, the carbon balance of the previous section that is responsible for the “dry” phenology. The model thus follows the hypothesis of functional convergence (Field 1991), according to which the uptake capacity for CO_2 of a plant, here determined by LAI, will not be larger than the rate allowed by the largest limiting factor, in this case the soil water content. By avoiding surplus investment, a maximum growth rate is achieved (Mooney and Winner 1991). A dependence of this kind can easily be reproduced in this model, because the link between the carbon and water budget through the stomata is explicitly described. A similar approach, differentiated by leaf layers, is used in the dynamic ecosystem model Hybrid 3.0 (Friend et al. 1996).

To calculate the maximum LAI allowed at a given soil water content, Λ_W , it is assumed that plants follow a strategy of optimising annual growth. During the growth season, LAI is therefore increased to an optimal value, while it is kept constant during drought until a negative NPP forces the plant to shed leaves:

$$\Lambda_W(t) = \begin{cases} \Lambda(\text{NPP} = 0) & \text{if } \text{NPP}(\Lambda(t - \Delta t), t) < 0 \\ \max\{\Lambda_{\text{NPPopt}}; \Lambda_W(t - \Delta t)\} & \text{if } \text{NPP}(\Lambda(t - \Delta t), t) \geq 0 \\ \Lambda(t - \Delta t) & \text{if } T_c < 5.5^\circ\text{C} \text{ and } T_m < T_{m-1} \end{cases} \quad (135)$$

Δt is the one-day time step, Λ_{NPPopt} the value of LAI where the daily integral of NPP is at a maximum, and $\text{NPP}(\Lambda(t - \Delta t), t)$ stands for daily NPP at time step t , calculated with the LAI of the previous time step, $t - \Delta t$. The third line of the equation constitutes a test of the condition of senescence in winter-cold climates ($T_c > 5.5^\circ\text{C}$, cf. Section 2.4). T_m stands for the average temperature of the current, and T_{m-1} for that of the preceding month. The reason is that, if the end of the summer drought period lies already in autumn, no second growth period is observed (Walter and Breckle 1994, p. 4ff.)

The difference between warm-evergreen (W-E) and other vegetation according to Table 2.1 is that for W-E plants, $\Lambda_W(t) > \Lambda_W(t - \Delta t)$ is allowed only during the spin-up phase of the model run. After this initialisation (cf. Section 2.2), only a reduction in LAI is allowed, in order to determine the maximum LAI that can be sustained by W-E vegetation.

Growth limited leaf area

For all non-evergreen plant types, growth of LAI is also limited by net primary productivity, itself a function of LAI. The difficulty lies in the fact that a certain amount of carbon investment is always necessary to initialise leaf growth. However, this starting investment in the form of seeds (annuals) or starch reserves (perennials) is difficult to quantify. It is therefore assumed that the LAI is growth limited only from a value of 0.5 onwards, by

$$\Lambda_C(t) = \Lambda(t - \Delta t) + \frac{1}{2} \frac{\text{NPP}(t - \Delta t)}{C_{drm}} \sigma_L \quad (136)$$

with the one-day time step Δt , the specific leaf area, σ_L according to Table 2.1, and $C_{drm} = 0.45 \text{gC/g}$ (cf. Equ. 99). The factor one half corresponds to the assumed maximum allocation to leaves.

Fractional cover

In this model it is assumed that there is a maximum fraction of each grid cell, $f_{c,max}$, that can be covered by vegetation. In the standard case, this maximum fractional cover is 0.9 throughout (cf. 0.8 in BATS, Dickinson et al. 1993). This is meant to account for the fact that at large length scales, there is only rarely a uniform vegetation cover, with various forms of gaps in between, such as water bodies, settlements, roads, rocks, etc. It is further assumed that sparse vegetation is not uniformly spread out, but that it occurs in separated clumps (cf. Section 2.6, "light absorption"). Therefore, if the maximum annual LAI, Λ_{max} , is less than $\Lambda_0 = 3$, the maximum LAI of the clumps is set to Λ_0 . This results in a fractional cover, f_c , of:

$$f_c = \begin{cases} f_{c,max} \Lambda_{max} / \Lambda_0 & \text{for } \Lambda_{max} < \Lambda_0 \\ f_{c,max} & \text{for } \Lambda_{max} \geq \Lambda_0 \end{cases} \quad (137)$$

f_c is recalculated after each one-year simulation. After the spin-up phase, the highest monthly mean LAI of the preceding valid simulation years is taken for Λ_{max} (cf. Section 2.2). During the spin-up phase, only the LAI of one year earlier is taken.

Chapter 3

Model Results and Comparison with Field Studies

3.1 Overview and definitions

In this chapter, after first defining a standard model version of BETHY with several variants, results computed in prognostic mode will be presented. The purpose of this exercise is to give a general error estimate and to gain insight into the sensitivity of the model against various parameters. The simulations are characterised as “prognostic”, because only those input data are used that are also available for scenario calculations of future or past climates. These are temperature, precipitation, radiation, mean CO₂ concentration of the atmosphere, soil type and vegetation distribution. The first three can in principle be predicted by climate models (Kattenberg et al. 1996), future CO₂ concentration with global models of the carbon cycle on long time scales, in combination with assumptions of future fossil fuel emissions (Schimel et al. 1996), and the last two with models of vegetation dynamics, which, over very long periods, also determines the formation of soils (Melillo et al. 1996). Other observations, such as vegetation distribution captured by satellites, direct measurements of productivity, or distribution and seasonal change of atmospheric CO₂ concentration, are not used. Consequently, only vegetation *type* is taken from input data, not vegetation *amount* (usually expressed by the leaf area index, LAI). The latter is derived solely from the principles of temperature, light and water limitation.

Only when the Monteith photosynthesis scheme is used, field measurements of plant productivity enter the calculation indirectly in the form of light-use efficiency, that is the ratio of net primary productivity (NPP) to absorbed radiation. For the Farquhar model, only a plant-type specific maximum rate of photosynthesis is used, a value that is more characteristic of the plant’s nitrogen balance than of its actual productivity. All other parameters of the Farquhar model are usually considered universal, because they are the result of enzyme kinetics of photosynthesis.

To make the standard model version independent of the various non-prognostic types

Table 3.1: Description of the standard version ‘0’ of the vegetation model BETHY.

| | |
|-----------------------|--|
| Resolution | 1° equal area (11069 land points) 2 years spin-up, 3 years simulation 10-daily phenology update |
| Land cover | vegetation map by Wilson and Henderson-Sellers up to 3 vegetation types per grid cell, thereof 1 selected at random |
| Daily climate | stochastic daily precipitation with γ distribution temperature and radiation linearly interpolated from monthly means |
| Photosynthesis | Farquhar model with 3 layers |
| Stomata | $c_w = 1.0$ mm/h, $C_{i,0} = 0.87C_a$ (C3) and $C_{i,0} = 0.67C_a$ (C4) |
| Phenology | max. LAI, $\hat{\Lambda} = 5$ threshold, $\Lambda_0 = 3$ max. fractional cover $f_{c,max} = 0.9$ leaf onset temperature, $T_\phi = 5^\circ\text{C}$ arable crops: $T_\phi = 12^\circ\text{C}$ saturation, $\hat{T}_\phi = 15^\circ\text{C}$ |
| Autotroph respiration | leaf fraction, $f_{R,leaf} = 0.40$ construction costs, $f_{R,G} = 0.25$ |
| Soil respiration | temperature factor with $Q_{10} = 1.5$ humidity factor is f_e |
| Humidity | minimum, $h_0 = 0.92$ amplitude, $\hat{h} = 0.49$ |
| Radiation | vegetation albedo, $\rho_v = 0.15$ atmospheric longwave emissivity, $\varepsilon_{A0} = 0.64$ leaf single scattering albedo, $\omega = 0.12$ |
| Wind | above-canopy wind speed, $u = 2$ m/s |
| CO ₂ | atmospheric CO ₂ content, $C_a = 355$ ppm. |

of input, it uses the Farquhar photosynthesis model (Section 2.6) and the vegetation map by Wilson and Henderson-Sellers (Section 2.3). More details can be found in Table 3.1. In addition to the standard version, a number of variants for sensitivity and error studies are defined and listed in Table 3.2. Those sensitivity tests are either defined by exchanging model parts (‘Pm’), input data sets (‘C’ and ‘M’), or a coherent set of model parameters of the standard version, and they reflect a possible global and systematic error, not a local one. The only exception is given by the test H-/H+ of the humidity parameters. Here, the values for h_0 and \hat{h} are set in such a way that for H-(H+) simulated mean values according to Table 3.3 lie one standard error below (above) the mean of the standard run at the grid points of 588 calibration stations (see next section). If those stations were representative

of the microclimate of all simulated pixels, the estimated uncertainty for the global means of \hat{h} and h_0 would be smaller by a factor of $1/\sqrt{588} \approx 0.04$. However, in order to consider possible systematic deviations between the plant-own microclimate and that captured at those measurement sites, a global error of 20% of the calculated standard error is assumed (see Section 3.3).

The sensitivity against climate input data ('C') is tested with data from ECMWF routine weather forecasts, with daily temperature amplitude and number of wet days remaining unchanged because such data were not available in a suitable form. The year 1987 is chosen for compatibility with the ISCPP radiation data, and 1990 because at that time the forecast scheme had been updated significantly (Arpe 1991). In both cases, however, the radiation is used from the standard version so that the test is only for differences in temperature and precipitation fields.

Further criteria for defining sensitivity tests are described below: For the net-radiation test (N-/N+), the higher value of the vegetation albedo is that for grasses, the lower one that for coniferous forests from Brutsaert (1982); an error of +/- 10% for the atmospheric emissivity is also taken from Brutsaert (1982, Fig. 6.6, p. 141). Further, an error of 15% for the soil albedo in the data set of Wilson and Henderson-Sellers (1985) is considered reasonable. The variation of the temperature phenology (T-/+) corresponds to a delayed/accelerated start of spring by 10 days in Central Europe; an error of +/- 1 is finally assumed for the LAI of dense, close vegetation. The lower and upper values for the parameter of root-water controlled stomata regulation (c_w) are taken from the article of Federer (1979, Table 4, halved/doubled root density). The same variational range is assumed for two quantities about which little is known globally, that is rooting depth (D-/+) and wind speed above canopy (X-/+). The estimated variation of the parameter for growth respiration ($f_{R,G}$) is determined from Ryan (1991a) by taking a value for pine trees (as a mean of stem and needles) as the lower value, and results from the Californian Chaparral vegetation (in the range of 0.23 to 0.40) as an indication of an upper bound. The higher value for the leaf fraction of maintenance respiration ($f_{R,leaf}$) is estimated from Ryan (1991b, simulated values from 0.41 to 0.6), whereas the lower one takes into consideration that the belowground fraction of productivity is often underestimated (Long et al. 1989).

In addition, there are three tests of the sensitivity against temporal and spatial resolution of the model ('0-/0+/0++') for which, as described in Chapter 2, the daily course of photosynthesis and the energy balance is recomputed only three times each month; if soil moisture content drops below 1 mm, gross photosynthesis and transpiration are set to zero until the next daily course is calculated, and a new water limited LAI with it. Eventually, there is a sensitivity test that concerning only the initialisation of the model ('0v').

In Section 3.3, the results (mainly NPP) are presented as global means, as means over vegetation types (according to Table 2.1), as latitudinal averages, and as averages over five climate zones defined there. As mentioned above, the purpose of the comparison is to give a general impression of the model's sensitivity against the most important parameters and

Table 3.2: Description of model variants of BETHY.

| Code | Sensitivity test | Description |
|-----------------|-------------------------|---|
| 0 0v | standard | standard modified random numbers |
| 0- 0+ 0++ | resolution | recalculation of daily course only every 10 days 0.5° grid (62483 points), daily course every 10 days up to 3 veg. types at a grid point, daily course every 10 days |
| Ms Mp | vegetation map | from satellite data (DeFries/Townshend) potential vegetation |
| Pm | photosynthesis | Monteith model |
| C87 C90 | climate data | ECMWF forecasts of 1987 ECMWF forecasts of 1990 |
| V- V+ | daily variability | reduced, precipitation every $1/f_w$ days increased, temperature amplitude and radiation coupled to precipitation |
| N- N+ | net radiation | low absorption: soil albedo (ρ_s) + 15% atmospheric emissivity (ε_{A0}) - 10% (0.58) vegetation albedo, $\rho_v = 0.20$ high absorption: soil albedo (ρ_s) - 15% atmospheric emissivity (ε_{A0}) + 10% (0.70) vegetation albedo, $\rho_v = 0.10$ |
| X- X+ | exchange | aerodynamic conductance (G_a) halved, $u = 1\text{m/s}$ aerodynamic conductance (G_a) doubled, $u = 4\text{m/s}$ |
| G | geometry | vegetation height considered for light absorption |
| H- H+ | humidity | reduced by standard error: $h_0 = 0.69$ and $\hat{h} = 0.12$ increased by standard error: $h_0 = 1.17$ and $\hat{h} = 0.89$ |
| S- S+ | stomata | early closure: $c_w = 0.5\text{mm/h}$ late closure: $c_w = 2.0\text{mm/h}$ |
| D- D+ | rooting depth | halved doubled |
| T- T+ | temperature phenology | short: $T_\phi = 7^\circ\text{C}$ (arable 14°C) and $\hat{T}_\phi = 17^\circ\text{C}$ long: $T_\phi = 3^\circ\text{C}$ (arable 10°C) and $\hat{T}_\phi = 13^\circ\text{C}$ |
| L- L+ | leaf area | low, $\hat{\Lambda} = 4$ high, $\hat{\Lambda} = 6$ |
| A- A+ | “autotroph” respiration | low, $f_{R,G} = 0.2$ and $f_{R,leaf} = 0.5$ high, $f_{R,G} = 0.3$ and $f_{R,leaf} = 0.3$ |

modelling variants, it does not, however, allow a definitive test of the model's predictive performance. For this reason, the ensuing Section 3.4 presents a simulation where the model is driven with measurements from the First ISLSCP Field Experiments (FIFE, Sellers et al. 1988) and results are compared to half-hourly values of photosynthesis rate and canopy conductance. This allows to demonstrate whether the daily course of CO_2 and water fluxes and its dependence on soil moisture is described realistically in the model.

A further comparison that concerns only the simulated water cycle uses multi-year measurements of the plant available soil water content from the former Soviet Union. The simulations are driven with the standard climatology. The purpose is to check whether the order of magnitude and the seasonal cycle of soil water content can be reproduced satisfactorily, with special attention given to the peak caused by spring snow melt.

Model results are also compared to data of annual NPP from a larger number of field studies covering most of the earth's vegetation zones. This is the only globally comprehensive comparison with field data and is again not considered a method of final model validation, because scatter and possible error of such field measurements are naturally large (cf. Kaduk 1996, p. 71ff.). The question asked here is rather, whether with this type of data differences in the quality of different model variants can be detected.

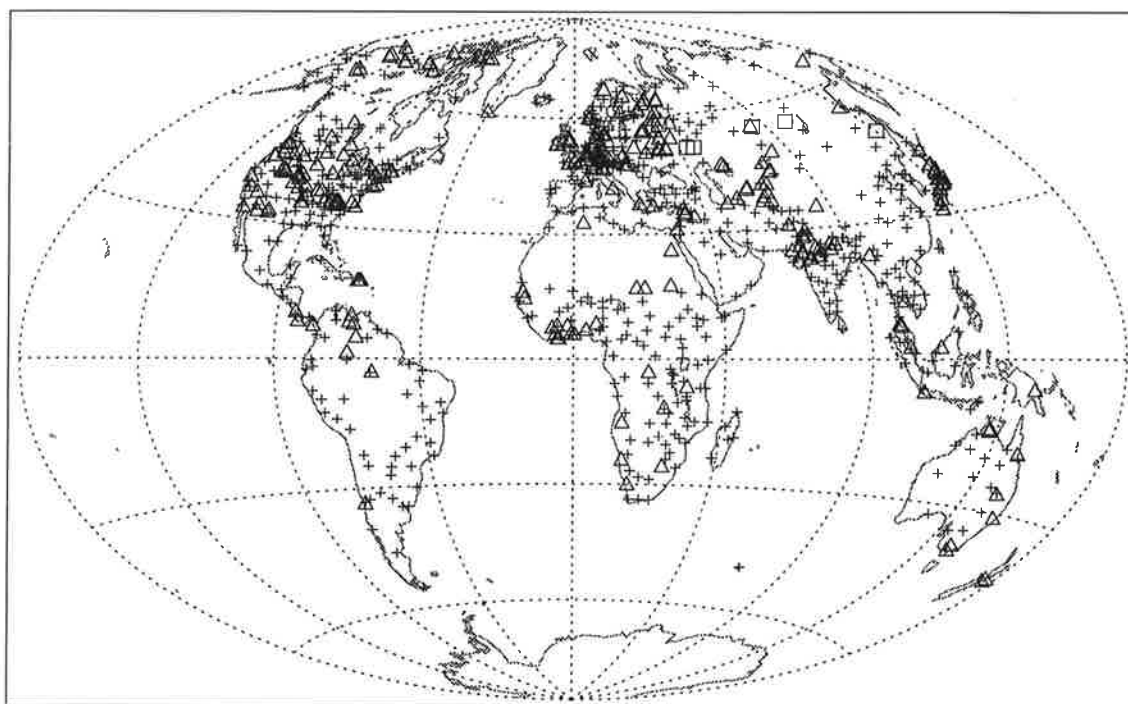


Figure 3.1: Position of the 588 stations of the data set by Müller (+). The position of 6 measurement sites for soil moisture in the former USSR (□) and of the sites of various ecosystem studies (△) are also shown.

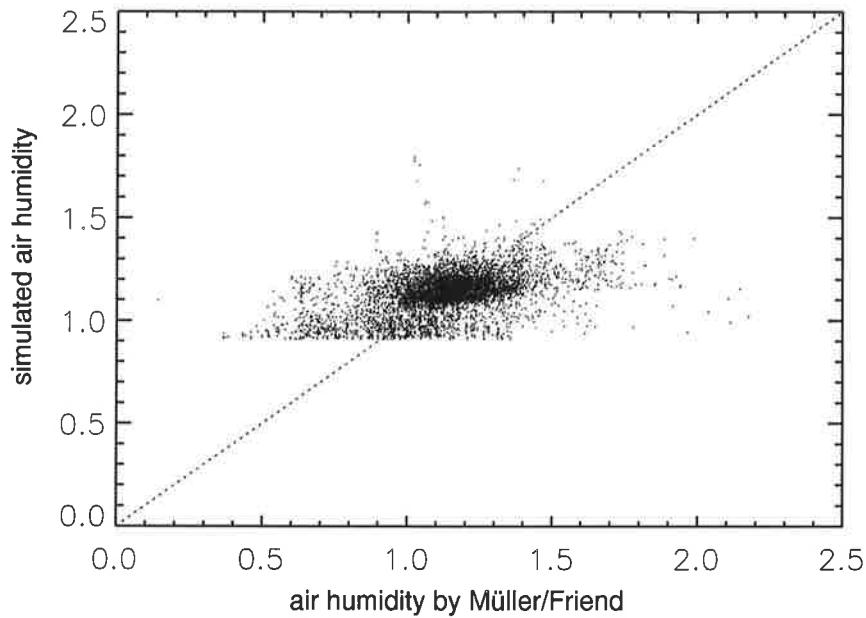


Figure 3.2: Measured daily average of absolute humidity against data by Müller and Friend, each expressed as multiples of the absolute humidity at sunrise, $e_s(T_{min})$. There are 12 monthly values for each station.

3.2 Vapour pressure variability

In this section, the model-simulated vapour pressure near the ground is compared to those values derived from the data set of Müller (1982) according to a method by Friend (1997) for the grid points corresponding to 588 stations of the Müller data set (cf. Fig. 3.1). With this method, daily mean vapour pressure is calculated as

$$e_a = (a + bP)e_s(T_{min})$$

where P is monthly average precipitation, T_{min} the daily temperature minimum and e_s the saturation vapour pressure. a and b are the constants determined separately for each station from the data set by Müller, whereas P and T_{min} are taken from the model's standard input data. This insures consistency of the assumed vapour pressure with the climate data used by the model.

In Fig. 3.2 the value of $e_a/e_s(T_{min})$ is plotted for all 12 months and 588 stations according to Friend against the value simulated by the model (Equ. 20, Chapter 2). The model is run in version V-, i.e. with periodic rainfall every $1/f_w$ days. (Stochastic weather generation has been switched off to insure simulated rainfall equals input data.) There is generally a large degree of scatter, and the correlation is only $r^2 = 0.18$. Table 3.3 also shows average and standard error (root mean squared deviation between simulated and measured) of all grid points where the ratio f_e of potential to actual evapotranspiration (Equ. 22 of Chapter 2) is less or greater than $1/2$. The parameters h_0 and \hat{h} have been determined in such a way

Table 3.3: Daily average humidity in the model and according to the data by Müller and Friend as multiples of $e_s(T_{min})$, for 588 stations with 12 monthly values each and averaged over cases with actual evapotranspiration (AET) more or less than half the potential rate (PET), respectively. The correlation of simulations with the observed data (r^2), and the standard error are also listed (defined as the root mean squared deviation between both). The AET/PET criterion follows the calculation with the standard values of h_0 and \hat{h} (0.96 and 0.49, second line).

| h_0 | \hat{h} | r^2 | error | AET < PET/2 | r^2 | error | AET \geq PET/2 | r^2 | error |
|----------|-----------|-------|-------|-------------|------------|-------|------------------|------------|-------|
| observed | | | | 1.015 | $n = 2166$ | | 1.175 | $n = 5178$ | |
| 0.96 | 0.49 | 0.20 | 0.179 | 1.011 | 0.11 | 0.232 | 1.164 | 0.08 | 0.151 |
| 0.71 | 0.17 | 0.18 | 0.259 | 0.776 | 0.11 | 0.332 | 1.018 | 0.03 | 0.221 |
| 1.22 | 0.86 | 0.09 | 0.256 | 1.242 | 0.05 | 0.328 | 1.310 | 0.07 | 0.219 |

that the means of the simulations are equal to the values determined from the regression equation by Friend (see above). As suggested by Fig. 3.2, a considerable root mean squared deviation (or standard error) remains. Therefore, h_0 and \hat{h} are determined again such that simulated means (for $f_e >$ and $< 1/2$) are equal to the observed value plus/minus one standard error (Table 3.3).

The reason for the demonstrated high spatial variability is probably a high local dependence of the controlling factors, such that humidity is a variable that can hardly be captured by climate maps. Lateral processes, not represented in this model, are of particular importance, such as the transport of moisture from areas of high to low evapotranspiration caused by roughness differences, slope, water bodies etc. (cf. Brutsaert 1982, p. 154ff.). As a result, the consequences of this variability for model simulations can only be estimated. This is done by the variants H- and H+ (see next section).

3.3 Global results and sensitivity

Results of the standard run '0' in the form of NPP and GPP are listed in Table 3.4 by vegetation type (definition in Table 2.1, or below), with the global sum in the last line. The NPP of version 'Pm' is shown for comparison, calculated with the light-use efficiency of Ruimy et al. (1994).

The global NPP of the standard version turns out to be somewhat greater than a number of earlier estimates, such as 45 GtC by Fung et al. (1983), 47 GtC by Lieth (1975), 48 GtC by Potter et al. (1993), and around 60 GtC by Olson et al. (1983), Ruimy et al. (1994) and Knorr and Heimann (1995). Remarkable is a high proportion of C4 grasses with 30% of global NPP (types 10 and 12); when adding C3 grasses (9/11), the total amounts to even more than half of that figure. By contrast, temperate forests (types 3 to 6) contribute only 9%, less than agriculture (10%). The great significance of the tropics, where most of C4

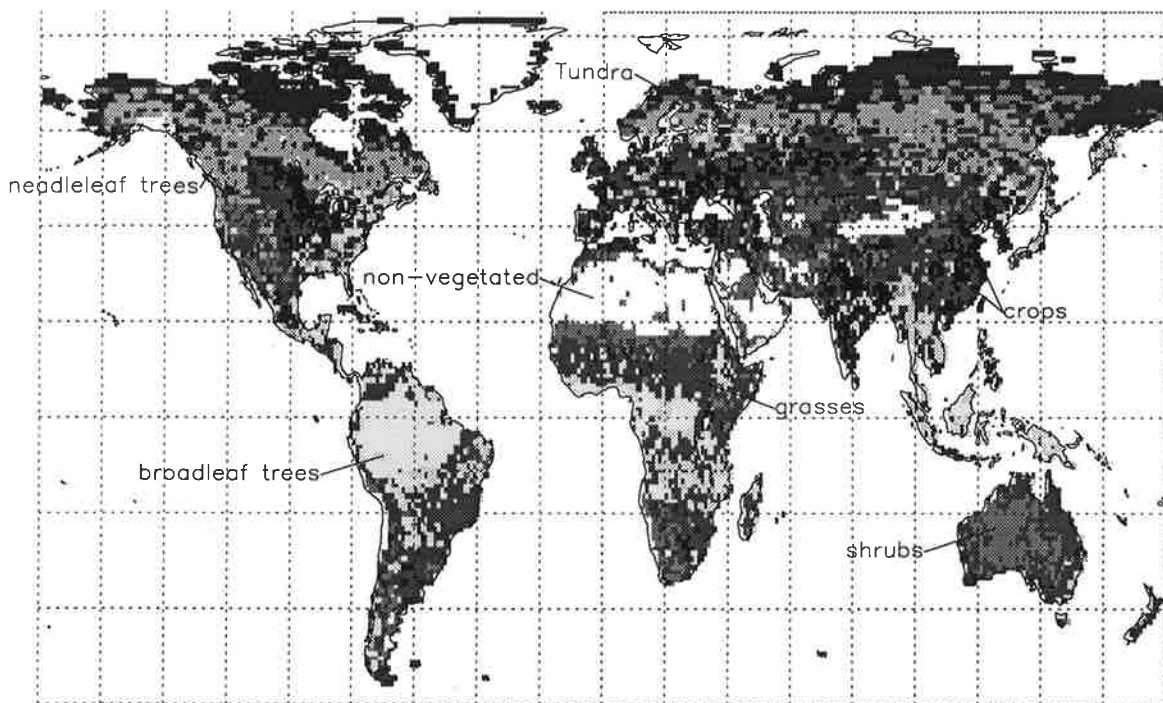


Figure 3.3: Vegetation types assumed in the standard and sensitivity runs for the 11069 land pixels. One is chosen among the three dominant types according to the land cover map of Wilson and Henderson-Sellers by a random number generator, with a probability equal to the relative abundance of that type. A total of 23 vegetation types is grouped into 5 categories (1-4, 5-6, 7-8, 9-12, 13-14 and 15-23).

long grass grows (type 12, 24%) is also documented by a 24% contribution of tropical trees (1/2). These, and the C4 grasses, achieve the highest productivity values, followed by C3 grasses (10). An average productivity is achieved by broadleaf deciduous trees (4), C3 long grass (9), wetlands (14) and agriculture (15-23), a relatively low one by conifers (5/6) and evergreen broadleaf trees of the temperate zone (3), and the lowest by shrubs (7/8) and tundra (13).

The high productivity of grasses is repeated by the calculations with the Monteith/Ruimy version 'Pm' ($\approx 37 \text{ GtC a}^{-1}$), where tropical grasses (12) dominate a little more over temperate grasses (9). The reason for this can partly be attributed to the missing temperature dependence of plant respiration in this version, which evidently tends to favour plants in warm climates. A global NPP of 84 GtC that is considerably higher than for version '0' is the most obvious difference, a result that comes primarily from agriculture (ca. 10 GtC difference, types 15-23) and from evergreen conifers (ca. 3.5 GtC, type 5). Other productivity values agree quite well with version '0'.

The ratio of NPP to GPP on a global average is approximately 0.45 in the standard

Table 3.4: Gross (GPP) and net primary productivity (NPP) of the standard run '0' as spatial total and mean according to vegetation type and for all areas with at least partial vegetation cover (last line); NPP of version 'Pm', calculated using the values of light-use efficiency by Ruimy et al. (1994), is also shown.

| type | Version '0' | | | Version 'Pm' | | area 10 ⁶ km ² |
|-------|----------------------------------|----------------------------------|---|----------------------------------|---|---|
| | total GPP GtC a ⁻¹ | total NPP GtC a ⁻¹ | mean NPP gCm ⁻² a ⁻¹ | total NPP GtC a ⁻¹ | mean NPP gCm ⁻² a ⁻¹ | |
| 1 | 25.55 | 9.39 | 771 | 8.15 | 669 | 12.17 |
| 2 | 21.71 | 7.66 | 986 | 8.77 | 1129 | 7.77 |
| 3 | 0.21 | 0.11 | 342 | 0.10 | 331 | 0.32 |
| 4 | 3.97 | 2.18 | 551 | 2.32 | 587 | 3.94 |
| 5 | 5.72 | 3.29 | 346 | 6.87 | 724 | 9.48 |
| 6 | 1.26 | 0.80 | 381 | 0.78 | 372 | 2.09 |
| 7 | 0.50 | 0.22 | 17 | 0.20 | 16 | 12.19 |
| 8 | 2.24 | 0.71 | 258 | 0.95 | 343 | 2.76 |
| 9 | 16.55 | 9.18 | 558 | 7.29 | 443 | 16.44 |
| 10 | 10.49 | 5.14 | 871 | 5.21 | 883 | 5.90 |
| 11 | 9.98 | 5.01 | 702 | 5.65 | 792 | 7.13 |
| 12 | 33.80 | 16.66 | 850 | 18.57 | 948 | 19.58 |
| 13 | 2.51 | 1.69 | 167 | 0.83 | 82 | 10.08 |
| 14 | 1.38 | 0.74 | 558 | 0.84 | 632 | 1.33 |
| 15-23 | 24.35 | 6.95 | 573 | 17.64 | 1455 | 12.13 |
| 1-23 | 160.23 | 69.71 | 565 | 84.17 | 682 | 123.29 |

version, which is similar to most comparable modelling studies (e.g. Ruimy et al. 1997, with 0.44 ± 0.03 as an average of 7 models). There are, however, considerable differences between plants of different climate zones on the one hand, and between C3 and C4 photosynthesis on the other hand. For example, respiration costs for tropical trees (types 1 and 2) are 63 and 65%, respectively, while for conifers and tundra vegetation (types 5, 6 and 13), the figure reaches only 42, 36 and 33%. For the tropical grasses (type 12), often coexisting with tropical trees, respiration costs are comparatively small with 42%, close to the value for conifers (type 5) and C3 grasses (type 9, 45%). Eventually, there is a remarkably high value for crops (71%, types 15-23). The reason for these differences lies on the one hand in the temperature dependence of plant respiration (tropical vs. temperate trees), and on the other hand in the higher water-use efficiency of C4 grasses that reach higher rates of photosynthesis than C3 plants at equal stomatal closure. The extreme values for agriculture are the result of a coupling between plant respiration and V_m , which is assumed proportional to the leaf nitrogen content (cf. Section 2.7). It is possible that this relationship is not directly applicable to highly fertilised crops.

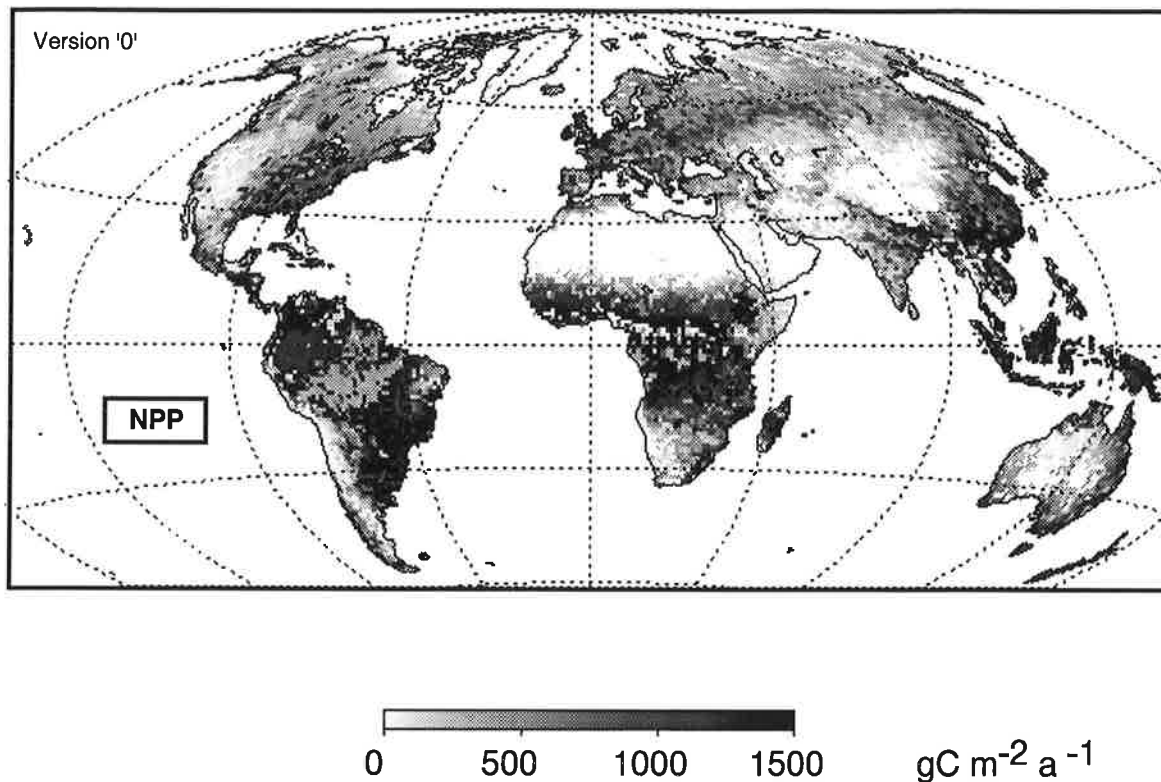


Figure 3.4: Equal-area map of annual net primary productivity of the standard run '0' in gC per year and m².

Another outstanding feature of the simulations is the extremely low productivity of evergreen shrubs (type 7) occurring in highly arid environments. The reason is that the model does not allow negative NPP values, thus keeping evergreen LAI low. This is probably a realistic assumption, except that the model might underestimate this plant type's ability to adapt to aridity by assuming either respiration costs that are too high, or too little water storage capacity. The topic will reappear in Chapters 4 and 5 with additional satellite observations.

If one assumes, from the comparison with other studies above, that the global NPP values simulated here are too high, then there are two possible explanation for the overestimate: either maximum photosynthesis is too high in both photosynthesis schemes; or the reason does not lie in the productivity but in the estimated vegetation amount, that is in the simulated LAI. The first possibility will be looked at in Section 3.6, the second in the next two chapters, where validation and improvement of model results with the help of satellite data is investigated. In general, however, it should be noted that it is a potential amount of vegetation that is simulated by the model, determined by light, temperature and water limitation at a given, plant-type specific nitrogen status. In reality, there might be additional limiting factors, such as nutrient supply or various types of land use.

Fig. 3.4 shows the geographical distribution of NPP according to version '0'. As it has

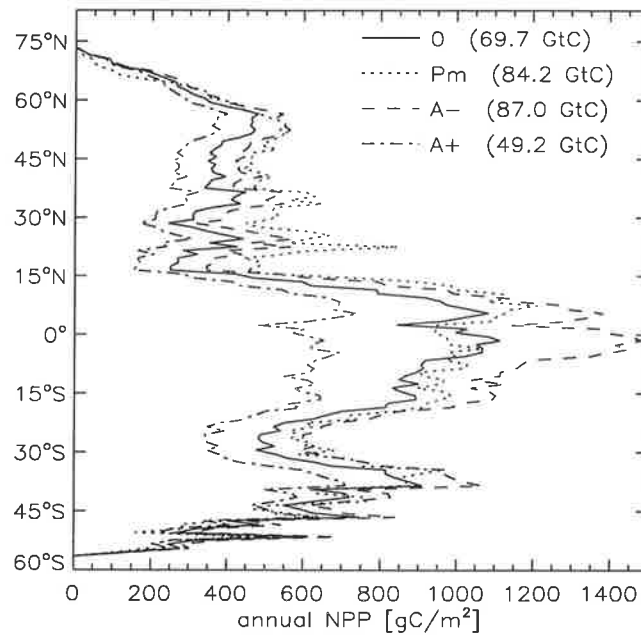


Figure 3.5: Latitudinal average of the annual NPP of land areas with the standard version (0), the Monteith version (Pm) and two versions with reduced and increased plant (“autotroph”) respiration (A-/A+), in gC/m^2 . Values in parentheses are global totals.

already become evident from Table 3.4, tropical vegetation is clearly dominating. However, within this high-productivity zone, there is a remarkable drop in NPP in some transitional areas from rainforest to grassland or savanna (cf. Fig. 3.3). The explanation for this deviation from a general trend of high NPP is, that an already well developed dry season at those sites leads to a relatively low LAI for the evergreen trees assumed there, because the phenology scheme (Section 2.9) keeps the LAI constant from model year 3 on. (Similar to the evergreen shrubs, type 7, see above.) The reason probably lies in the fact that the rooting depth of 1 m assumed in the standard case is probably not realistic for those areas (Nepstad et al. 1994, Kleidon and Heimann 1997, cf. Section 4.3).

A latitudinal comparison in Fig. 3.5 shows that both photosynthesis models, i.e. versions ‘0’ and ‘Pm’, have a similar productivity in the tropics as well as in the southern hemisphere, but that ‘Pm’ is clearly higher in northern temperate latitudes; the considerable deviation around 25°N is a result of extremely high tropical crop productivity with ‘Pm’. However, as stated by Ruimy et al. themselves, according to Esser (1991), productivity of natural vegetation is always higher than that of agriculture. Applying the productivity figures by Ruimy et al. (1994) to tropical agriculture might not be appropriate; also, potential vegetation cover as simulated in the model might not normally be reached on agricultural land. In addition, Fig. 3.5 shows the variation of NPP depending on the parametrisation of plant respiration. Because of high temperatures, the largest effect is found in the tropics

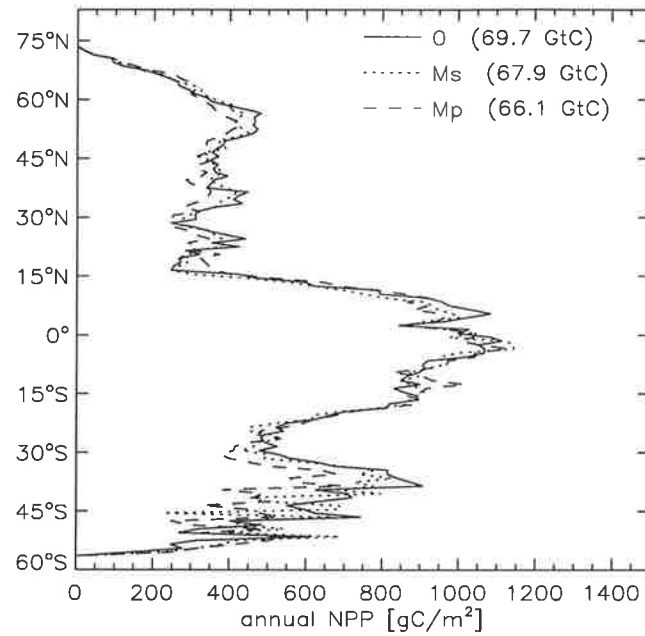


Figure 3.6: The standard version (0) compared to two versions where the vegetation distribution is either derived from satellites (Ms), or from the mean climate (potential vegetation, Mp).

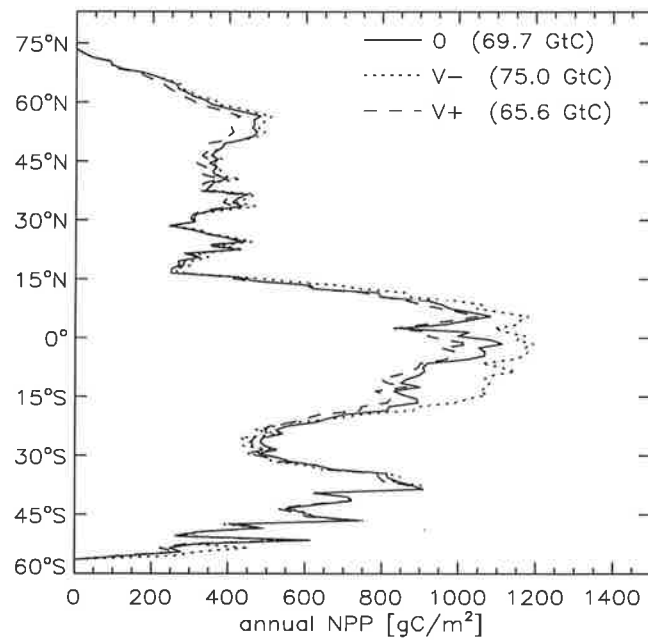


Figure 3.7: Sensitivity of the standard version against different models of the weather generator.

where it is more important than the choice of the photosynthesis scheme. By contrast, for northern temperate latitudes 'Pm' lies even above 'A-'. Possibly, the light-use efficiency by Ruimy et al. is inappropriate for the needleleaf forests that dominate area and NPP in the north (see Table 3.4). The values for this type come from three measurements in Japan and two in Sweden, with a relatively warm climate and little or no nitrogen limitation. The parameters for the Farquhar model, by comparison, have been explicitly chosen by Beerling and Quick (1995) such that they are more appropriate for natural, non-fertilised conditions.

Fig. 3.6 shows the effect of exchanging the vegetation map on which the calculations are based, from an atlas derived one ('0': Wilson and Henderson-Sellers 1985), to a satellite-supported map ('Ms': DeFries and Townshend 1994), and a potential vegetation distribution ('Mp': Section 2.4). As a first impression, the differences are much smaller than for the comparison of photosynthesis and plant respiration formulations. Only in the middle latitudes, potential vegetation has a clearly lower NPP than actual vegetation. The main reason for this is higher productivity of grasses against trees, considering that many grass covered areas of today are potentially covered by forests. The difference between the simulations with the two actual vegetation maps is generally small, which clearly demonstrates that the strategy to improve NPP models with qualitative satellite data, i.e. with satellite derived classifications, will not be successful because uncertainties in representation and parametrisation of processes are much larger than the likely benefits from improved classification. In general, vegetation type is of much smaller significance for NPP than the prevailing climate.

Fig. 3.7 shows the effect of changing the day-to-day climate variability on NPP, again as a latitudinal average. A positive impact of a more constant weather, and a negative one, when variability is increased, is clearly visible. Particularly in the northern mid latitudes, plants are under increased stress when radiation and daily temperature amplitude vary more strongly. In the tropics, it is stochastic versus periodic rainfall in '0' against 'V-' that has the largest effect. Around 5°N and S, the earlier described drop in NPP can be seen on the graph, while version 'V-' shows a significantly increased NPP against version '0'. It can therefore be concluded that a rooting depth of only 1 to 2 m leads to realistic results only with an even distribution of precipitation (as it is still used in many terrestrial ecosystem models).

In the following part of this section, which is also the most important one, the sensitivity of the model against all test variants according to Table 3.2 is presented, both as a global mean (Fig. 3.8) and (Fig. 3.10 to 3.13) as a mean over the three following climate zones (cf. Fig. 3.9):

- 1 Arctic north of 60°N

- 2 Wet-temperate south of 60°N
 coldest month colder than 15.5°C
 moisture index ≥ 1

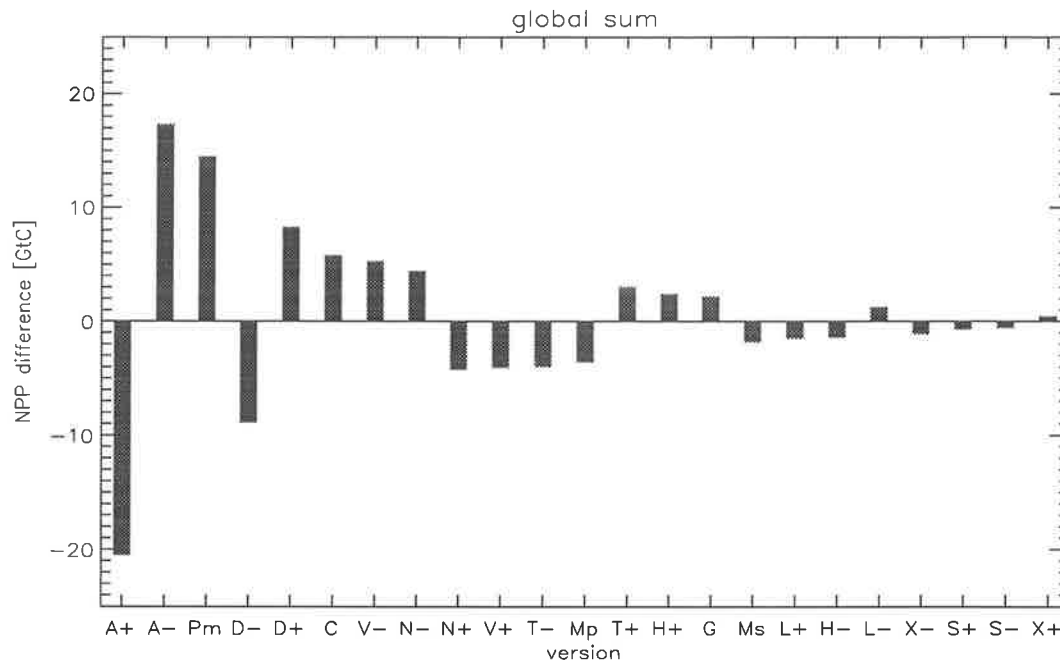


Figure 3.8: Sensitivity of the global annual NPP against various test versions. The difference against the standard version '0' (69.7 GtC) is displayed in descending order of the absolute value.

- | | | |
|---|--------------|--|
| 3 | Arid | south of 60°N moisture index < 1 |
| 4 | Wet-tropical | coldest month warmer than 15.5°C moisture index ≥ 1 |

The different versions are displayed in descending order of the absolute difference to the standard version, which is assumed to be the estimated error. There are two important differences to the definitions in Table 3.2: As explained above, the estimated error associated with sensitivity test 'H+/H-' is set to 20% of the difference to version '0'; and the sensitivity test 'C' is defined as the difference 'C90' minus 'C87', to reflect the difference in precipitation and temperature between two years of weather forecast data. Apart from real weather differences, model changes also play a role here.

It should be remembered that for those sensitivity tests that do not, as for example 'A-/+', lead to a change in NPP in a uniform direction, large regional differences can be hidden behind small differences in the total value. An example is given by the test 'Mp', which only lies in the middle range for the global totals, but is among the most important in the temperate zone.

As it could already be gathered from Fig. 3.5, the formulation of plant respiration (Test

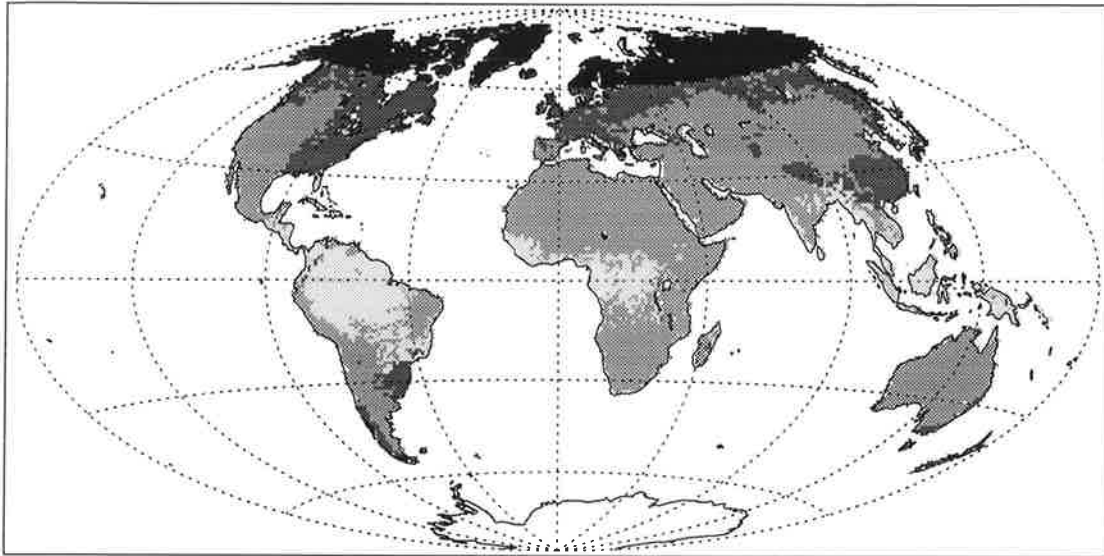


Figure 3.9: Map of the climate zones defined in the text, from arctic (1: black), over wet-temperate (2: dark grey), arid (3: medium grey), to wet-tropical (4: light-grey). The model excludes Antarctica. The equal-area projection by Aitoff is used.

‘A’) and the choice of the photosynthesis scheme (‘P’) are globally the largest uncertainty factors. Next comes rooting depth (‘D’), which is partly the result of the large contribution of the tropics (cf. Fig. 3.13; note again that the rooting depth chosen here and in other vegetation models might often be too small, see also Sections 3.6 and 4.3).

In the middle section there are sensitivities against yearly weather (‘C’), phenology (‘T’) and those that have to do with the daily microclimate, i.e. net radiation (‘N’) and day-to-day variability (‘V’). Contrary to using potential vegetation cover (‘Mp’), there is little change when using a satellite derived vegetation map (‘Ms’), something that has already been discussed earlier. Parametrisation of the local humidity (‘H’) is also relatively uncritical; the significance is constantly well below that of the water storage capacity (determined by rooting depth, i.e. ‘D’). It is most remarkable that the effect of vegetation height on NPP through light absorption (‘G’) is of similar size, considering that this type of effect has never before been accounted for in global vegetation models. The effect is largest in arid areas (Fig. 3.12) and in the arctic (Fig. 3.13), where the sign is reversed. Although it is not certain whether the description of the height dependence is accurate, this result, together with the significance of net radiation (‘N’), shows that a truly mechanistic computation of

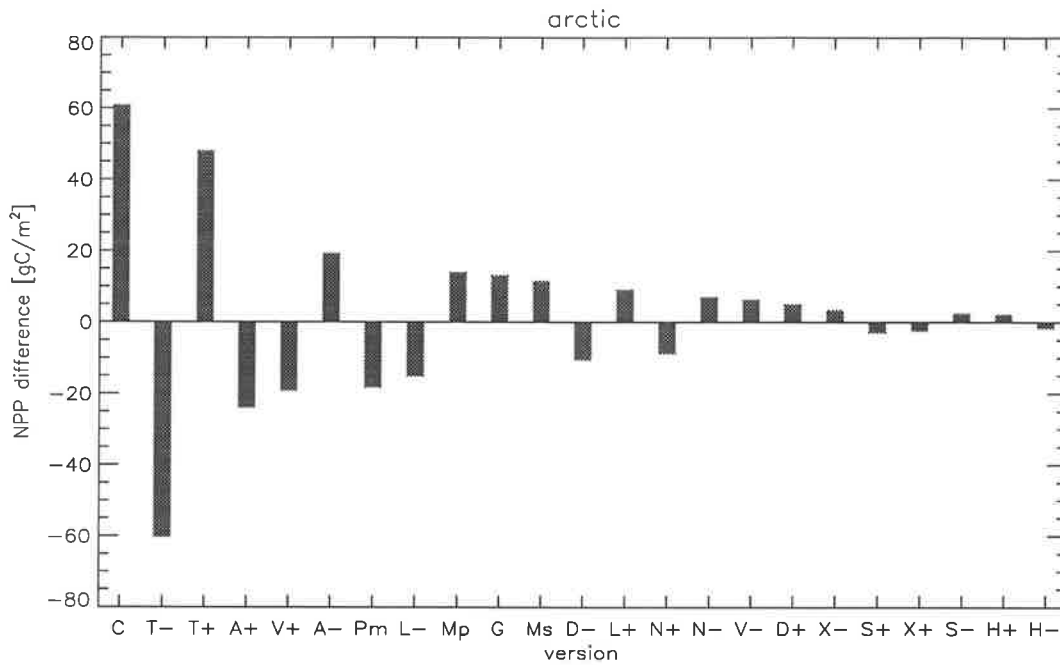


Figure 3.10: Sensitivity for the mean annual NPP of the arctic zone. The mean value of version '0' is 189 gC/m².

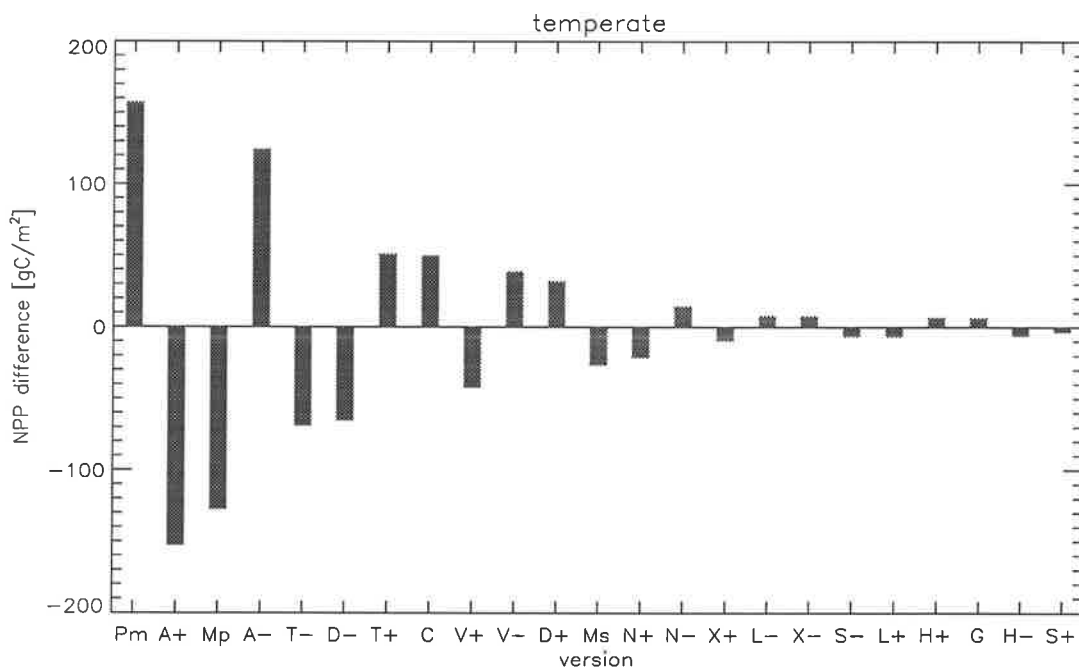


Figure 3.11: Sensitivity of the mean annual NPP of the wet-temperate zone. The mean value of version '0' is 667 gC/m².

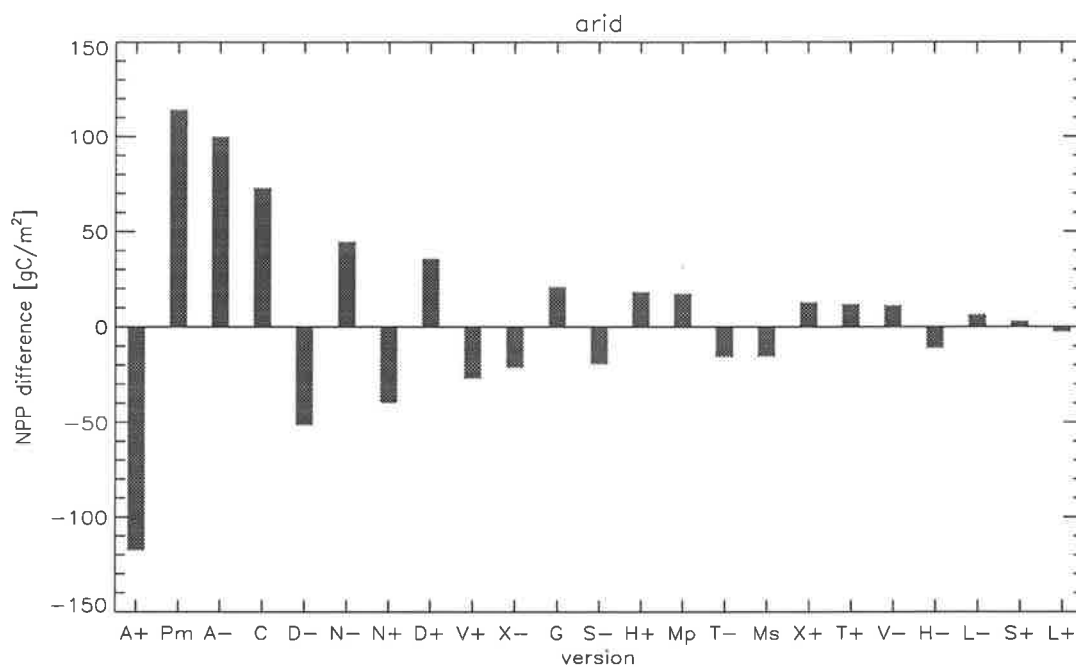


Figure 3.12: Sensitivity of the mean annual NPP of the arid zone. The mean value of version '0' is 381 gC/m².

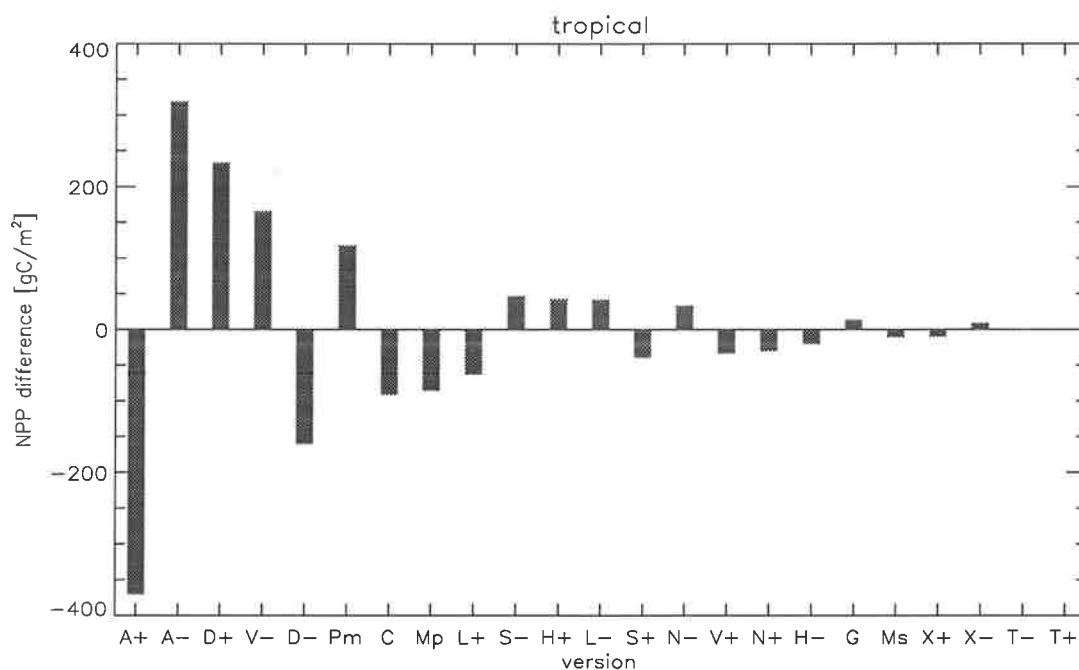


Figure 3.13: Sensitivity of the mean annual NPP of the wet-tropical zone. The mean value of version '0' is 1044 gC/m².

Table 3.5: Comparison of the annual NPP for differences of initialisation and spatial as well as temporal resolution.

| test | mean in $\text{gC m}^{-2}\text{a}^{-1}$ | | | | global in GtC a^{-1} |
|------|---|---------------|-------|--------------|----------------------------------|
| | arctic | wet-temperate | arid | wet-tropical | |
| 0 | 189.1 | 666.5 | 380.6 | 1044.2 | 69.71 |
| 0v | 189.9 | 666.3 | 380.2 | 1053.6 | 69.89 |
| 0- | 191.7 | 660.7 | 376.9 | 1005.8 | 68.55 |
| 0+ | 191.3 | 660.5 | 380.9 | 993.5 | 68.47 |
| 0++ | 190.0 | 663.7 | 378.2 | 1007.0 | 68.72 |

photosynthesis has to be done embedded in a realistic description of energy balance and radiation absorption.

Contrary to comparisons affecting the microclimate or the water budget, those concerning the regulation of transpiration by plants, i.e. stomata parametrisation ('S') and turbulent transfer ('X'), are relatively unimportant for global NPP calculations. Only in arid and tropical regions, 'S-' turns out to be a little more significant, while above-canopy wind speed is an uncritical variable in all cases. This justifies the choice of 2 m/s as a globally uniform value, and it agrees with the hypothesis by Jarvis and McNaughton (1986), that the significance of stomatal control decreases strongly with length scale.

The significance of choosing a uniform maximum LAI, $\hat{\Lambda}$, is tested by 'L'. Changing this value by one is of larger importance only in the arctic and in the wet tropics. The fact that increasing $\hat{\Lambda}$ leads to some reduction in NPP globally documents that at maximum LAI, canopy photosynthesis is already largely light saturated (so that an increase in LAI mainly leads to an increase in respiration). This does not apply to the arctic (Fig. 3.10), because $\hat{\Lambda}$ is only reached at some places. Here, low temperatures and low irradiation also have the effect that net radiation ('N') is of little, but phenology ('T','L') of large significance for NPP calculations. The large difference between the two ECMWF climates ('C') might also be the result of changes in the forecast model.

The results for the wet-temperate zone (Fig. 3.11) largely repeat the global picture, with the exception of potential vegetation ('Mp'), reflecting large-scale transformations from forests to grasslands and agriculture (see above).

For the arid zone (Fig. 3.12) it is remarkable that, despite water limitation, plant respiration ('A') is even more significant than rooting depth ('D'). This comes from high temperatures, with the consequence that the version 'Pm', with no temperature dependence of respiration, reaches the highest NPP.

The results for the wet tropics (Fig. 3.13) eventually show a great significance of deeper roots ('D+'), an effect that can largely be compensated by periodic rainfall ('V-') as seen on Fig. 3.7, and a high degree of uncertainty concerning plant respiration ('A') because of high temperatures.

For completeness, the results of some variants are listed in Table 3.5, for which no data sets or parameters have been changed, but only the initialisation of the random number generator ('0v'), the spatial and temporal resolution ('0+/-'), or the mode of selecting vegetation types ('0++', cf. Table 3.2). Compared to the preceding sensitivity tests, the changes are only small. It is therefore not necessary to compute the daily course of energy balance and photosynthesis for each day of the month ('0' vs. '0-'), so that the version '0++' serves as a standard in the next chapter.

3.4 Diurnal course of photosynthesis and canopy conductance compared to field measurements

The purpose of this section is to test whether the model is able to simulate the daily course of CO₂ and H₂O fluxes correctly. The model is driven with half-hourly data of air temperature, photosynthetically active radiation (PAR) and vapour pressure deficit, and with daily constant values of LAI and relative plant available soil water content ($W_s/W_{s,max}$). Those data (Kim and Verma 1991b) were recorded in 1987 at four different days during the FIFE project in north-eastern Kansas (39°03'N, 96°32'W, 445 m altitude). It is a typical tall-grass prairie with 85.9% C4 grasses. Apart from the input data described above, the model largely uses the standard settings of version '0' for vegetation type 12. The model also computes the solar zenith angle from geographical position and altitude (with legal time converted to solar time) and thus potential PAR and the fractions of direct and diffuse PAR of total solar radiation. For computing net radiation and the energy balance, a medium light soil is chosen. The simulations are for a maximum supply rate, c_w , of both 0.5 mm/h and 1.0 mm/h. Other than the standard model, the time of maximum atmospheric demand is determined explicitly, and not generally assumed at 13.00 hours.

During the simulation it has turned out that the constants V_m and k determined from the principle of convergence with C3 grasses (Section 2.6) yield photosynthesis rates that are too low. However, taking the values by Collatz et al. (1992) directly, derived from measurements on maize ($V_m = 14 \mu\text{mol m}^{-2}\text{s}^{-1}$, $k = 255 \text{ mmol m}^{-2}\text{s}^{-1}$, cf. Table 2.1, Chapter 2), the agreement improves considerably.

The simulated canopy photosynthesis rate, A_c , is shown in Fig. 3.14, together with the measurements by Kim and Verma (1991b). The CO₂ fluxes were measured with the eddy-flux correlation technique, so that, in order to determine A_c , the authors have subtracted the contribution of soil and root respiration (estimated from the night-time fluxes). On days when water supply was sufficient, 5 June ($W_s/W_{s,max}=0.78$) and 2 July (0.73), the difference between the two simulations is only small and the deviation from the measurements is $10 \mu\text{mol m}^{-2} \text{ s}^{-1}$ at maximum. By comparison, the model behaves quite differently depending on the choice of c_w on days with water shortage (30 July: 0.30; 20 August: 0.53). At 0.5 mm/h, the reduction of photosynthesis rates to values around zero is well reproduced; the midday depression (Tenhunen et al. 1987), well developed in the measurements, is also

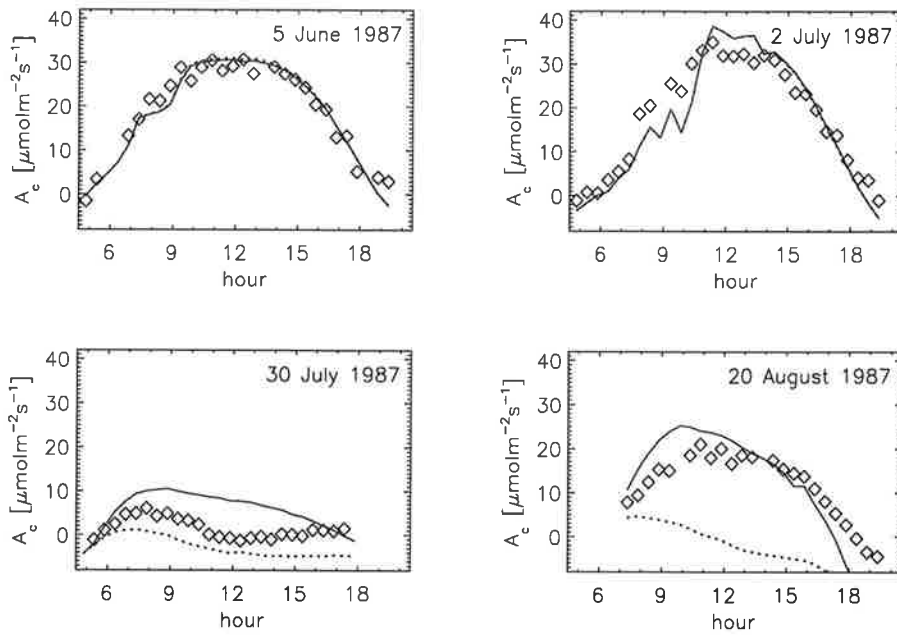


Figure 3.14: Measured (\diamond) and simulated canopy photosynthesis rate, A_c , for a C4 dominated grassland. Simulations with $c_w = 0.5$ mm/h (- -) and 1.0 mm/h (—); relative plant available soil water content is 78, 73, 30 and 53%, leaf area index (green leaves only) 1.9, 2.3, 2.5 and 2.3, ordered by date.

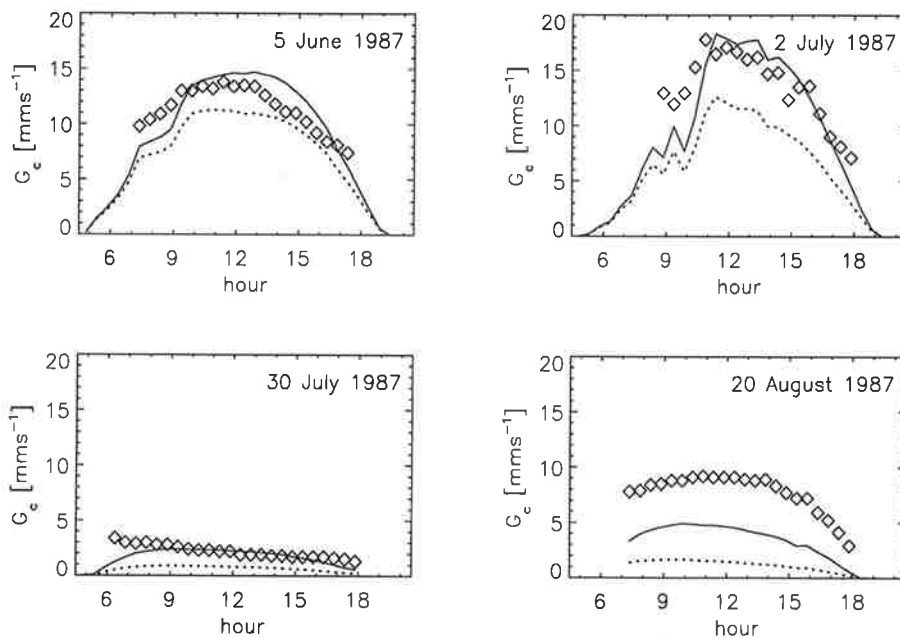


Figure 3.15: Measured (\diamond) and simulated canopy conductance, G_c , from the same campaign.

Table 3.6: Mean results of canopy photosynthesis, A_c ($\mu\text{mol m}^{-2}\text{s}^{-1}$), and conductance, G_c (mm s^{-1}), excluding times with missing data.

| Date | A_c | | | G_c | | |
|-----------|-------------|-------------|----------|-------------|-------------|----------|
| | $c_w = 0.5$ | $c_w = 1.0$ | measured | $c_w = 0.5$ | $c_w = 1.0$ | measured |
| 5 June | 19.77 | 19.57 | 19.77 | 9.22 | 11.81 | 11.40 |
| 2 July | 17.29 | 17.37 | 18.30 | 8.53 | 12.89 | 13.57 |
| 30 July | -2.65 | 6.22 | 1.48 | 0.69 | 1.85 | 2.18 |
| 20 August | -3.23 | 11.72 | 11.73 | 1.22 | 3.67 | 7.77 |

visible in the simulation, although it is less pronounced. On 20 August, however, a value of 1.0 mm/h captures the prevailing conditions of soil water limitation better. The calculated time of highest atmospheric demand is 12.50, 13.20, 11.50 and again 12.50 hours, i.e. close to 13.00 as assumed in the standard runs.

As a check of the simulated H_2O fluxes, the simulated canopy conductance, G_c , is compared to the values found by Kim and Verma (1991a, 1991b). It has to be taken into account that measured vapour fluxes have been converted to G_c by inverting the Penman-Monteith equation, without subtracting a possible contribution from soil evaporation. After strong rain and at a low LAI, this contribution can become significant, as it is the case for 20 August, when the LAI is only 2.3 after a number of storms in mid August. Correspondingly, the measured values lie significantly above the simulated ones. For the other days, however, the agreement is good, in particular when $c_w = 1.0$ mm/h.

Simulated and measured daily averages of A_c and G_c , excluding hours without measurements and night-time fluxes, are shown in Table 3.6. The agreement is good for days of sufficient water supply. On dry days, $c_w = 1.0$ mm/h appears to be more appropriate. As already explained, for the canopy conductance, G_c , some additional contribution from direct soil evaporation has to be accounted for.

As a general conclusion from this comparison it can be said that the photosynthesis scheme and the stomata parametrisation agree well with measurements, as far as the diurnal cycle and the dependence on soil water content is concerned. In particular, a standard value of 1.0 mm/h for c_w appears to be appropriate, not only for trees as stated by Federer (1982), but also for the strongly differing conditions of C4 grasses, physiologically as well as micrometeorologically. In fact, the exact value of c_w is not critical because of negative feedbacks through the water balance, a favourable situation for global modelling considering the uncertainties of mapping soil hydraulic properties. If c_w is increased, the soil water is used up more quickly and the LAI is reduced earlier because of negative NPP values, which in turn reduces transpiration and water loss. The effect is demonstrated by a low sensitivity of the global NPP against halving/doubling this parameter ('S+/-', see previous section).

3.5 Comparison with soil water measurements

Fig. 3.16 shows simulated and measured soil water content at six stations in the former USSR (Robock et al. 1995). Simulations are for five years after spin-up with version '0', i.e. with the climate and soils data of the model and without reference to locally measured meteorological data, with a rooting depth set to 1 m. There are two more simulations where the weather generator mode has been changed ('V-/+'). In the strongly continental climate, there is a pronounced maximum following snow melt at all stations, and a well developed dry-out during the summer months. In winter, the soil water content stays constant because of freezing, with a certain jump from December to January as the result of interannual variations in the simulations. This might also be the reason for such variations in the measurements, while the magnitude of those variations suggests a considerable error in the measurements.

Nevertheless, the comparison shows that even without local weather data, all simulations are in the correct range and the annual cycle is well reproduced. As expected, simulated soil moisture tends to be lowest when using a – more realistic – stochastic weather generator because of increased runoff ('0' vs. 'V-'); this effect is even more pronounced when the energy balance is varied in the same fashion (through temperature and radiation, 'V+').

3.6 Comparison with direct measurements of net primary productivity

The field data of annual NPP used in this section have been compiled by E. Box (Box and Bai 1993), G. Esser, D. Kicklighter and J. Kaduk, and they are described in Kaduk (1996). As far as possible, measurements are assigned a vegetation type according to Table 2.1, or a vegetation formation as in Table 2.2. For more than one vegetation type at a site, the model does not, as before, select one at random, but the simulation is carried out subsequently for each type with the weighted mean written to output. The geographical position of the field sites are marked in Fig. 3.1 by triangles.

In Fig. 3.17, simulated and measured values are plotted against each other. A linear regression (dashed line) yields $y = 334 + 0.56 \times x$ with a correlation of only $r^2 = 0.20$. A value as low as this has often been found for direct comparisons of NPP measurements with simulations on the basis of non-local climate data (Kaduk 1996, Warnant et al. 1994, Potter et al. 1994). A further comparison is given by Fig. 3.18 showing the means of simulated and measured NPP with the corresponding 90% confidence ranges, first for the grid points with unknown vegetation ('U', $n = 78$) and for all points where the vegetation is known ('A', $n = 175$), then grouped by vegetation type with a minimum of 10 sample points. (Bare figures signify single vegetation types according to Table 2.1, figures in brackets mixed formations as in Table 2.2). There is a significant difference between simulated and measured NPP for both groups of known and unknown vegetation type. By contrast,

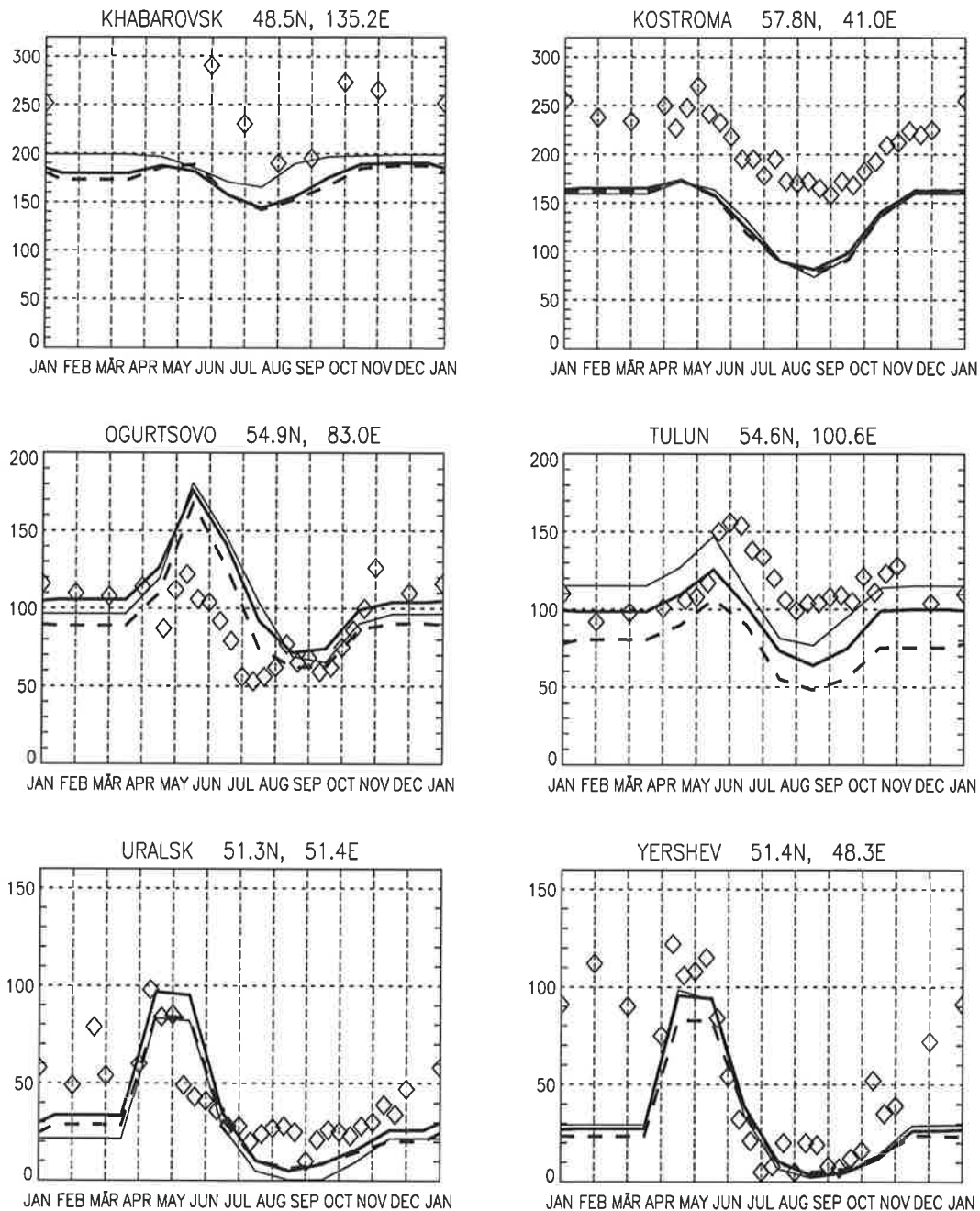


Figure 3.16: Measured (\diamond) and simulated plant-available soil water content of the upper 1 m in mm for several stations in the former USSR. 5-year average of simulations by version '0' (thick line), 'V-' (thin line) and 'V+' (dashed). Simulations are with standard climate and soils data.

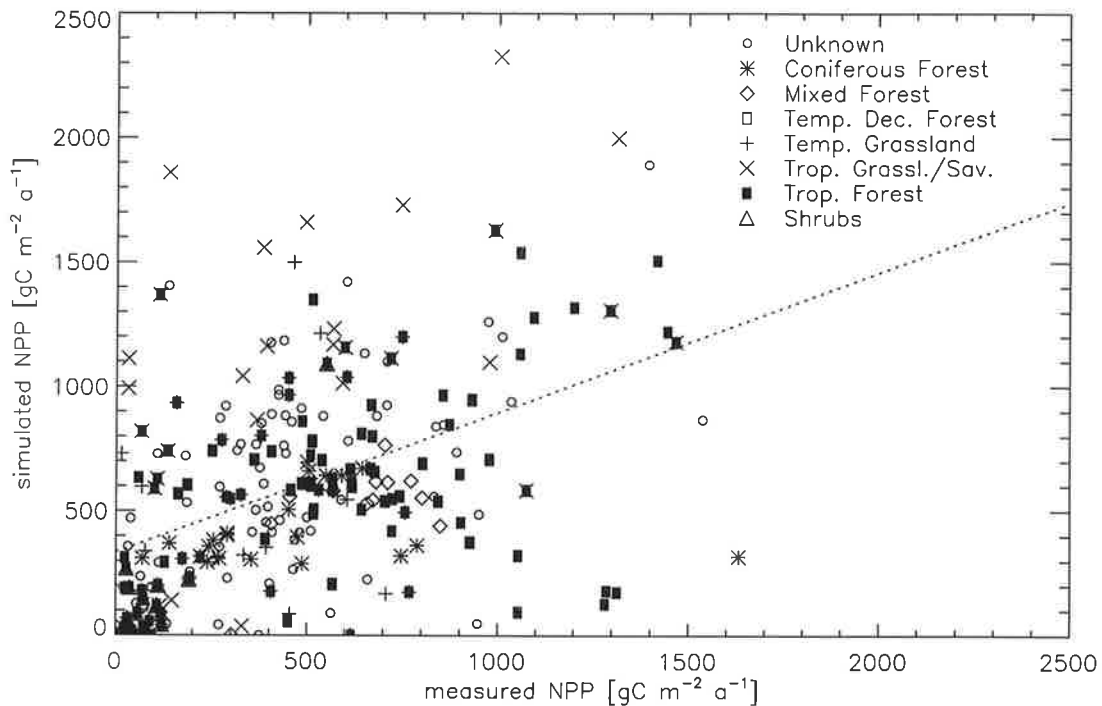


Figure 3.17: Measured annual net primary productivity (NPP) against simulated values.

for specific formations the difference is significant only for savannas [37]. In general, the difference between simulations and measurements is not independent of the vegetation type: there is a 99.4% probability that the differences in the quality of the agreement between groups are not random.

The general overestimate of NPP by simulations appears to be largely the result of the high productivity of grasses. Another interesting feature is the much higher range of simulated values for tropical rainforest sites [50], which probably comes from the known problems of insufficient rooting depth (see above). The apparent overestimate of C4 grass productivity is opposed to the fact that the measurements of the FIFE experiment (Section 3.4) show an even higher CO₂ uptake rate than the model in the standard setup, i.e. around 10 gC/m² per day during the growing season. Similarly high NPP values have actually been measured, with 1714 gC/m² for a 150-day growth period (Murphy et al. 1975). A comparison of the dependence of tropical grass productivity on annual precipitation between simulations and data by Murphy et al. is shown in Fig. 3.19. It is evident that the simulated values (+) show a similar dependence as the measurements (*), but also that simulations are mostly higher, especially in the upper precipitation range. The same is also true for savannas, where measurements (△) are even higher above simulations (◇). If, however, the choice is restricted to the few NPP measurements that include below-ground growth, the agreement turns out to be rather good. This suggests that direct measurements of

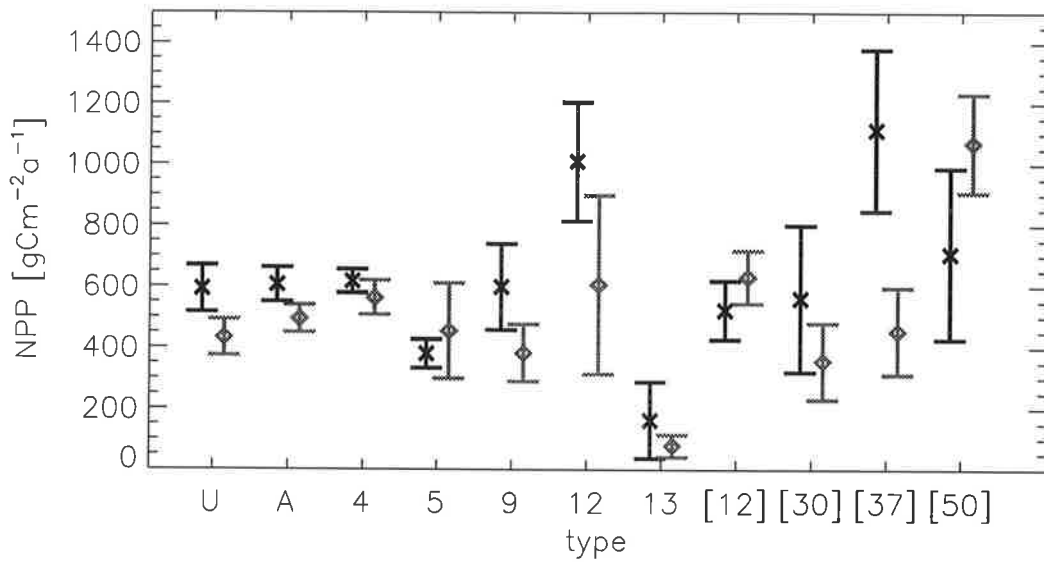


Figure 3.18: Means and 90% confidence range of simulated (black) and measured (grey) annual NPP, sorted by groups of observations with at least 10 samples: ‘U’ unknown type, $n = 78$; ‘A’ all cases with known type, $n = 178$; Pure vegetation types are ‘4’: broadleaf deciduous trees, $n = 30$; ‘5’: conifers, $n = 17$; ‘9’: C3 grass, $n = 18$; and ‘13’: tundra, $n = 10$; Mixed formations are [12] mixed forest, $n = 12$; [30] C3/C4 grasses, $n = 11$; [37] savanna, $n = 19$; and [50] tropical rainforest, $n = 12$.

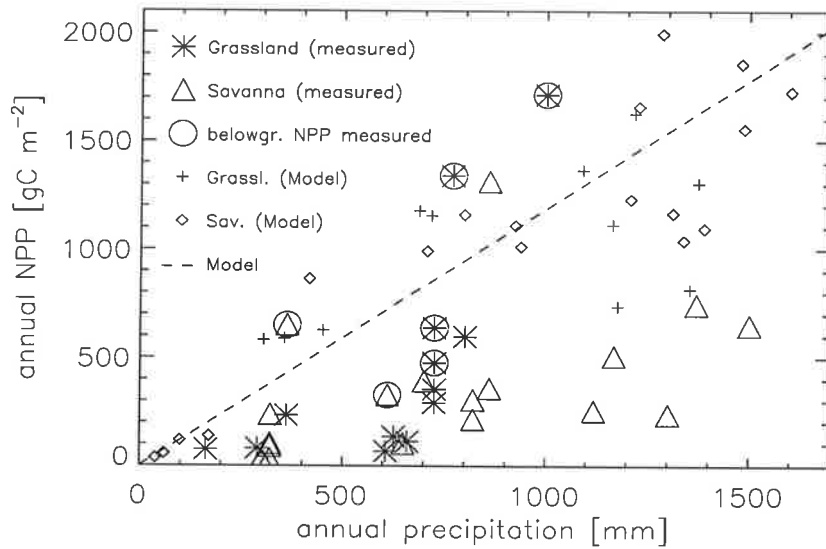


Figure 3.19: Simulated and measured annual NPP for tropical grasses and savannas against annual precipitation.

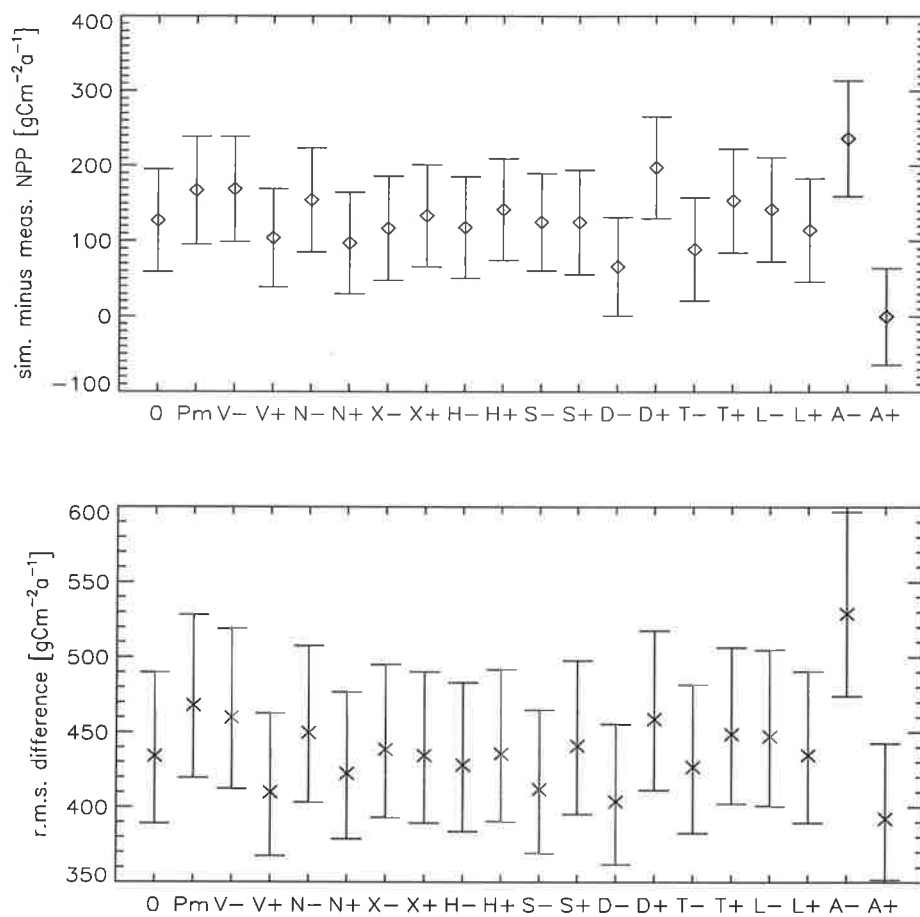


Figure 3.20: Mean (above) and root mean squared (below) difference between simulated and measured annual NPP differentiated by model version. Bars indicate a 95% confidence range. The number of measurements is 253.

NPP, because of a lack of standardised techniques and the great difficulties associated with capturing below-ground production (Long et al. 1989), are not suitable for a definitive check of vegetation models.

To conclude this chapter, the question is asked whether measured NPP can be used to compare the performance between versions of the vegetation model. Two ways of measuring the performance are used, first by looking at the mean deviation from the measured values, then by taking the root mean squared deviation instead. Whereas the first criterion allows a compensation of positive and negative deviations, in particular caused by random fluctuations of the local climate as opposed to the climate maps used, such variation is added to the mean error when the second criterion is used. To get a picture of the statistical significance of the test, the 95% confidence intervals of both values are also computed.

As it can be seen from Fig. 3.20, in most cases it is impossible to conclude a difference

in performance between two versions of the vegetation model from measured NPP data. The mean deviation (above) is usually a good indicator also of the mean error (below), which means that systematic deviations dominate. Usually, the lower the NPP, the better is the agreement, which puts version 'A-' into the best performing position. Whether this is real, or it is caused by a general trend of direct NPP measurements to underestimate NPP, is difficult to say. A possible check with atmospheric CO₂ data is the subject of Chapter 5.

Concluding Remarks

Some concluding remarks concerning the sensitivity tests and comparisons of this chapter appear to be appropriate: Since the actual errors of the global data sets and those associated with global parameter settings are unknown, those sensitivity studies only constitute a first estimate of the relative significance of various processes and representations of processes during the exercise of global mechanistic biosphere modelling. Also, when comparing simulations with field measurements, it becomes evident that driving the model with local weather station data would be highly desirable. Nevertheless, it is unlikely that this would change the general picture and the most important conclusions, which are:

- An improved understanding of plant respiration appears to be one of the most important tasks of global biosphere modelling; here, the largest uncertainties are found.
- Improved data sets about productivity of different vegetation types are urgently needed.
- Rooting depth, especially in the tropics, has so far been underestimated in terrestrial biosphere models. This error is partially compensated by neglecting high-frequency variations in precipitation.
- Energy balance and day-to-day weather fluctuations are more important for mechanistic modelling than the choice of the stomatal model or the magnitude of the turbulent transfer.
- The improvement of vegetation maps with satellite data would have only a relatively small effect for modelling global vegetation activity.
- Currently, direct measurements of net primary productivity are probably not suitable for checking global mechanistic biosphere models, because of the large uncertainties associated with them, and because they are difficult to interpolate spatially. Some of the reason lies in problems of capturing below-ground production, and in the insufficient coverage of globally significant regions, in particular the tropical rainforests.

Whether some of those uncertainties can be reduced with the help of global observational data will be the topic of the following chapters. Those data are satellite measurements (Chapters 4 and 5) and measurements of the atmospheric CO₂ content (Chapter 6).

Chapter 4

Model Validation with Remote Sensing Data

4.1 Introduction

In the following chapter, the question is asked whether optical measurements of terrestrial reflectance from satellites can be used to validate different versions of the biosphere model introduced before. This study deals with so-called passive instruments that measure the sunlight reflected by the earth's surface, from which the reflectance can be computed for certain wavelengths by taking account of the incoming solar flux.

It is clear that global modelling as done in this study calls for globally comprehensive data sets with sufficient time resolution to capture the seasonal development of vegetation. In fact, such archives do exist for an uninterrupted period from 1982 until today (Townshend 1994). They come from a series of weather satellites run by the National Oceanic and Atmospheric Administration (NOAA) of the United States, with a quasi-polar, nearly sun-synchronous orbit, and are measured by an instrument called the "Advanced Very High Resolution Radiometer" (AVHRR). The spatial resolution of the data product of the type "Global Vegetation Index" (GVI), is approximately 15 km, time resolution one or two weeks (Kidwell 1990). It is a subset of the original daily data with a spatial resolution of 1.1×1.1 km in nadir direction (straight down). Although further earth observation systems are being planned, only the NOAA series of satellites currently delivers continuous, globally comprehensive optical data from the earth's surface with sufficient time resolution (Townshend 1994).

It is commonly assumed that important biophysical quantities can be derived from such data, and that those quantities are useful for research on the global carbon cycle. For example, an archiving project to store those data at the full resolution of the sensor has recently been put into operation as part of the International Geosphere Biosphere Programme (IGBP, Townshend et al. 1994). Requiring the coordination of a network of globally distributed receiving stations, it was originally planned to last for 18 months beginning on 1.

April 1992, but has later been extended until 30 September 1996.

Before going into the technical details of global monitoring, it will be explained in the following section why it is at all possible to capture vegetation amount and distribution from an altitude of almost 1000 km; then, the main advantages of this method are mentioned that have lead several scientific organisations to implement large-scale monitoring and archiving operations. In a following discussion it is argued that such data have so far only been used in a rather qualitative way and that truly quantitative studies have either been carried out on a small scale, or they have had to rely to a significant degree on other sources of information.

After this introduction, attention is referred back to the initial question, whether those satellite data contain useful information for global biosphere modelling that are not already known from traditional sources. An answer will be tried with the help of the vegetation model developed here. The theory of optical remote sensing will be largely left out, for a comprehensive introduction see Asrar (1989) and Sabins (1987).

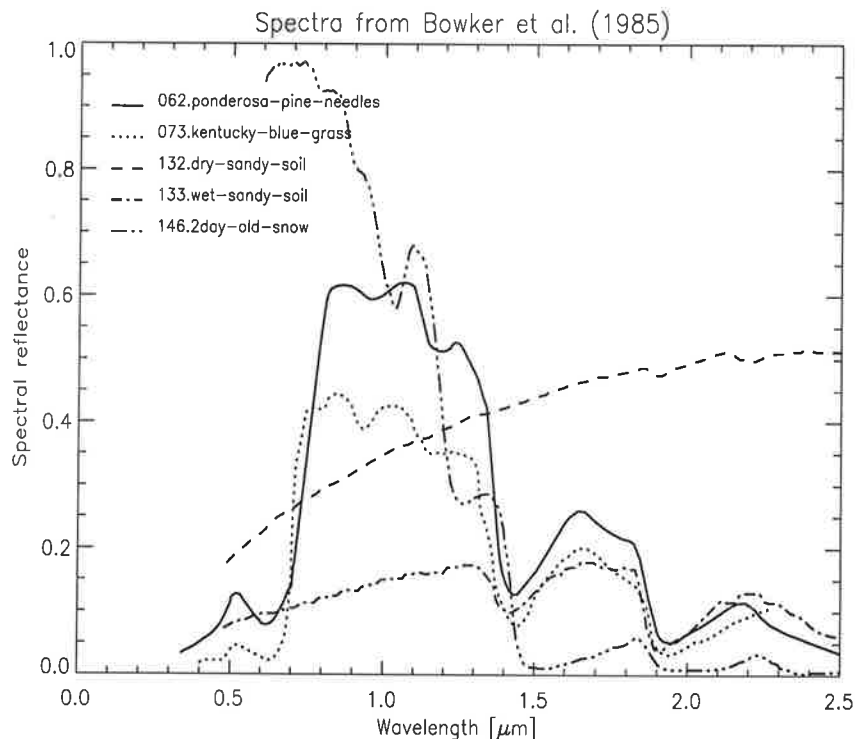


Figure 4.1: Spectral dependence of the reflectance of various surfaces: pine needles, grass, dry and wet sandy soil, and snow; taken from Bowker (1985).

The principle of optical remote sensing of vegetation

Some of the principles of optical remote sensing can be explained from Fig. 4.1: it shows that green leaves and needles have a characteristic spectral signature in the wavelength

range from the visible (0.38 to 0.72 μm) to the near-infrared (0.72 to 1.3 μm : NIR). This signature is characterised by strong absorption in the visible and photosynthetically active portion of the spectrum – with a weak maximum in the green part that is also visible to the human eye – and high reflection in the longer-wave and photosynthetically useless NIR. Here, absorption is as low as 10%, and the rest is transmitted (Jones 1983, Brakke et al. 1989). This property of green leaves is of great importance for the water balance of plants, since almost half of the solar energy is contained in the NIR (cf. Section 2.5). The sudden rise in reflectance between 0.7 and 0.75 μm is contrasted by a much more continuous rise for other surfaces, in particular for soils. By comparison, vegetation and wet soils show a very similar behaviour in the middle infrared, i.e. the part ranging from 1.3 to 2.5 μm , which is characteristic of their water content. This spectral region, in which the solar flux is also much smaller, is therefore not suited to deliver a marked contrast between vegetation and soil.

The contrast in the spectral range from red to NIR has led to the development of a technique for the “spectral mapping” of vegetation (Pearson and Miller 1972). It is illustrated by Fig. 4.2 and is still used without significant modifications (Justice 1986, Sellers et al. 1994, Running et al. 1994). Instead of the simple ratio Red/NIR (denoted SR), the “normalised difference” is usually taken, defined as $\text{NDVI} = (\text{NIR} - \text{Red}) / (\text{NIR} + \text{Red})$ (Deering et al. 1975, “Normalised Difference Vegetation Index”, cf. Section 1.4). It must be noted, however, that this is not an exact measurement, for example of biomass, leaf area index (LAI) or FPAR (the fraction of absorbed photosynthetically active radiation, cf. Equ. 125, Chapter 2). Rather, the quantitative interpretation rests on empirical relationships found in the field. Such a principle is followed by several biosphere models (Heimann and Keeling 1989, Potter et al. 1993, Knorr and Heimann 1995, Ruimy et al. 1996), in which FPAR is derived from data of the NDVI (Prince 1991, Ruimy et al. 1994). The uncertainties involved in this procedure are discussed in the following Chapter 5.

It may be important to note that the kind of quantitative interpretation of satellite data explained above accounts for only a small part of their use. Examples of a qualitative interpretation of such data on continental to global scales are: classification of land use and land cover (cf. Section 1.4, e.g. Norwine and Gregor 1983, Tucker et al. 1985, Thomas and Henderson-Sellers 1987, Lloyd 1990, Ehrlich and Lambin 1996, Mayaux and Lambin 1997) and change analysis and detection (Tucker et al. 1984, Malingreau 1986, Malingreau et al. 1989, Hellden 1991, Tucker et al. 1991, Lambin and Strahler 1994 and others).

Possibilities and limitations of quantitative remote sensing

Which are now the advantages of global satellite-based monitoring of vegetation and vegetation-specific quantities compared to traditional mapping? Probably the most important one is the globally uniform coverage with high repetition rates, including otherwise inaccessible terrain. It is the global consistency of observations that guarantees independence of local traditions, such as the way how vegetation formations are classified. The

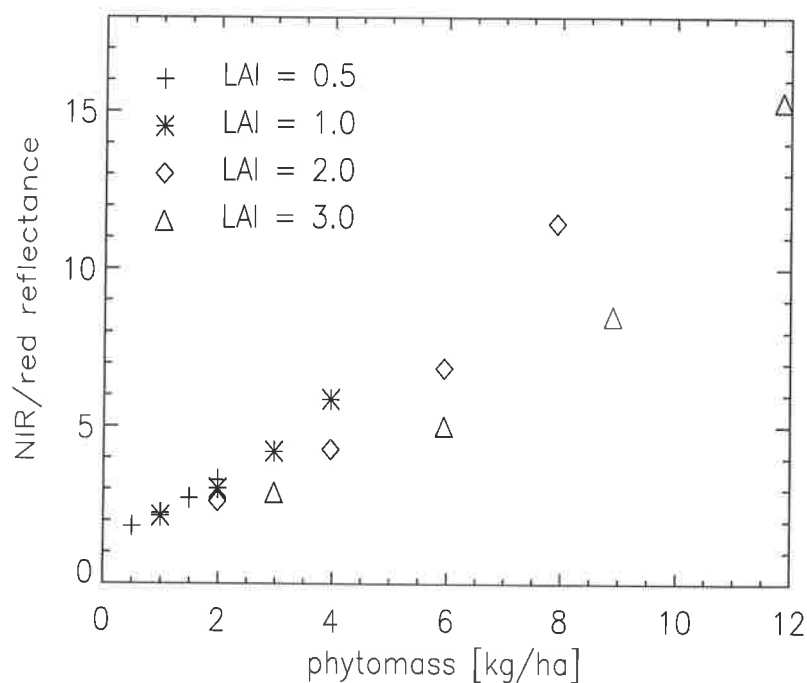


Figure 4.2: Ratio of the reflectances between near-infrared and red, simulated with the bidirectional reflectance model for soil and vegetation, NADIWAS, with erectophile leaf-angle distribution (Gobron et al. 1997) for different values of LAI and fractional cover (25, 50, 75 and 100%). Solar zenith angle is 45° , view zenith 30° and the view azimuth 90° relative to the direction of the sun. All other variables correspond to the standard values for cereals and a wet, medium-light soil. The graph is meant to illustrate the principle of 'spectral mapping' of vegetation amount and is based on a conversion from LAI to green phytomass using 25.3 m^2 per kg leaf mass (Schulze et al. 1994, for cereals).

high frequency of observations also allows the large-scale monitoring of seasonal and interannual variations that would otherwise be impossible. With those advantages, satellite data constitute a unique and irreplaceable source of information.

At a closer look, however, it turns out that there are a number of severe problems. They result from the fact that the spectral information measured by the satellite does not only depend on the variables of interest, that is on the amount of vegetation, but also in a complicated manner on a number of perturbing factors: solar position and observation angles (Pinty and Verstraete 1991, Meyer et al. 1995), soil background (Huete and Jackson 1988, Leprieur et al. 1994), snow (Dozier 1989), non-green plant parts (Sellers 1985), size, orientation and optical properties of leaves and needles (Verstraete 1987, Jacquemoud 1993, Myneni et al. 1995), the ratio of LAI to fractional cover (Asrar et al. 1992), aerosol, water vapour and ozone content of the atmosphere (Kaufman 1989), sub-pixel clouds (Kaufman

1989) and changes in the calibration of the on-board instrument (Kaufman and Holben 1993, Koslowsky 1996).

The strategies to avoid those perturbations that have so far been developed can be summarised as follows:

- (1) Both the measurement technique and the quantity measured are adapted to the problem. This applies to the selection of the characteristic wavelengths in the red and NIR, but also to the choice of FPAR instead of LAI for quantifying vegetation cover (Asrar et al. 1992, Goel and Qin 1994).
- (2) The quantities that characterise the perturbation are determined from other sources and the signal is normalised to some standard condition. This requires not only that the dependence of the signal on the quantity of interest and the perturbing factor is known, but also that this dependence is invariant against other, still unknown perturbations. The most important example for this method is the correction of satellite data for atmospheric effects with the help of rather well established models of radiative transfer within the atmosphere. A still unknown perturbation is here given by the anisotropy of the surface reflection, determined to a large degree by vegetation cover. It influences the atmospheric effect mainly in the backscatter region (with the sun in the back of the sensor) and can otherwise be neglected (Lee and Kaufman 1986).
- (3) A further strategy consists of forming combinations of the reflectances in different channels, so-called vegetation indices, that are as robust as possible against unknown quantities, and at the same time as sensitive as possible against the variables of interest (Verstraete and Pinty 1996, Pinty et al. 1993, Leprieur et al. 1994). Such indices are used especially to identify vegetation, since here the problem is still relatively simple because of the marked contrast in reflectance around $0.7 \mu\text{m}$ (see above). Improved indices make use of the so-called soil line (Kauth and Thomas 1976, Richardson and Wiegand 1977), a line on a red/NIR reflectance diagram close to which most occurring soils fall, irrespective of wetness (e.g. SAVI, Huete 1988). When the Global Environmental Monitoring Index (GEMI, Pinty and Verstraete 1992a) was developed, this robustness against changes in the soil colour was retained and at the same time a standard atmospheric correction was included into the definition of the index (Verstraete and Pinty 1996). As a result, GEMI responds much less to variations in atmospheric conditions than the NDVI, as Flasse and Verstraete (1994) show for AVHRR data from Africa. A test of the performance of the indices NDVI, GEMI and SAVI by measuring their signal-to-noise ratios can be found in Leprieur et al. (1994).
- (4) The last strategy to suppress perturbations to be mentioned here is simply given by their identification and avoidance. It is applied in particular to clouds and snow; in fact, cloud screening belongs to the standard pre-processing techniques in remote

sensing technology. To avoid clouds that are smaller than the resolution of the satellite image and are therefore difficult to identify, one maximum value is usually selected out of a period ranging from one week to one month (Holben 1986). A quantitative estimate for the effect of this method, which is favoured by the one-day repeat cycle of the AVHRR, is given by Kaufman (1989).

It must be said that all those strategies lead to their own specific problems. For method (2), they usually consist of a lack of reliability of the additional information. Apart from atmospheric correction, this problem is known to exist for the correction of sensor degradation as well, where different authors have found solutions that diverge significantly (Koslowsky 1996). The case is different for solar and viewing angles: given appropriate archiving, these are well known. However, correction of the signal by normalising it to some standard condition is often impeded by the complexity of the angular dependence of reflectance; suitable models are still under development (Pinty and Verstraete 1991, Pinty and Verstraete 1992b, Myneni et al. 1995). Also, method (3) does not offer a definite solution to the problem of perturbation, since such indices always constitute a compromise between various factors. Eventually, method (4) has the problem of introducing a certain bias into the measurements towards certain viewing conditions and solar positions, which makes the selection itself dependent on the weather situation.

It is important to stress that all problems mentioned so far have implications for the further strategy of this study – besides this, the above overview is intended to give an impression of how much quantitative interpretation of satellite data is made difficult by considerable perturbations whose effect is often unknown. One of the consequences is that until now, using AVHRR for capturing interannual changes in vegetation cover in a quantitative way can only be performed with great difficulty, if it is not even impossible (Koslowsky 1996). Similar problems of incompatibility between scenes taken at different times are known for the traditional qualitative interpretation of satellite data (Duda and Hart 1973, Wharton 1989), with the vegetation map by DeFries and Townshend (1994) as an example of a global application (used here as one of several vegetation maps, cf. Section 2.4).

Conclusions and further strategy

The preceding discussion might have given the impression that the advantages of satellite remote sensing presented briefly at the beginning, i.e. consistency and global completeness, would by far be outweighed by the problems explained afterwards. In fact, projects that try to derive biophysical quantities globally with the aid of AVHRR data have to make considerable use of other sources of information (Los et al. 1994, Sellers et al. 1994). In the study cited, a correction is applied to the NDVI that depends on vegetation type, a piece of information usually derived from the NDVI itself. The data set by Los et al. and Sellers et al. is certainly of great use for realistic characterisation of the global vegetation cover, for

example in climate models. It is, however, inappropriate when dealing with the question of this study, whether satellite data contain useful information for global biogeochemical modelling.

For this reason, a different strategy will be pursued that allows a clear distinction between different sources of information, on the one hand the satellite data and on the other hand vegetation, climate and soils maps. The first part of that strategy consists of the prognostic calculation of the spatial and temporal distribution of global land vegetation described in the Chapters 2 and 3. In the second part, the results of different prognostic model versions are compared to satellite data, in the form of the vegetation index GEMI. This index is chosen because it has, in most cases, a clearly superior signal-to-noise ratio than other indices (Leprieur et al. 1994) and is at same time a good cloud detector (Flasse and Verstraete 1994). This procedure is first done in Section 4.4 simply by comparing the simulated LAI directly with the measured GEMI. A quantitative comparison is then given in Section 4.5, where GEMI is simulated with a remote-sensing model. Such a comparison on the level of the signal has first been tried by Knorr et al. (1995), and only this method allows an objective judgment of the possibilities of satellite measurements for model validation. Finally, as a third step, satellite data are used in Chapter 5 as an additional constraint of the vegetation model. For reasons of computational efficiency, this is done via the quantity FPAR, which, on the one hand, is derived from satellite data and, on the other hand, has to be reproduced by the vegetation model.

As an illustration of vegetation monitoring with vegetation indices, Fig. 4.3 shows the influence of the soil background on the dependence of three such indices on vegetation cover. The calculation is based on a simple linear mixture of the reflectances of dense vegetation (0.02/0.40) with those of various soils, following the soil line by Price and Bausch (1995) and classified according to Table 2.4 of Section 2.5 (wet/dark, wet/medium, dry/medium, and dry/light). It can be clearly seen that both NDVI and SR depend strongly on soil background in the middle range of vegetation cover, where the influence is even stronger than in the case of bare ground. A near-linear dependence on vegetation cover only exists for the NDVI if the soil is relatively light, and both indices increase when going from light to dark soils. GEMI, by comparison, shows a much reduced dependence on the soil background, with the largest impact at the lower end of vegetation cover fraction. The index initially increase when the soil albedo is increased up to about 20%, then decreases again and reaches even negative values for some very bright desert soils (Flasse and Verstraete 1994).

4.2 Data collection and processing

The remote sensing data used in this study come from the GVI product by NOAA (see above) from 1989 and 1990 in a reprocessed version by Berthelot et al. (1994) of the *Centre d'Etudes Spatiales de la Biosphère* (CESBIO) in Toulouse, France. In this section, the most

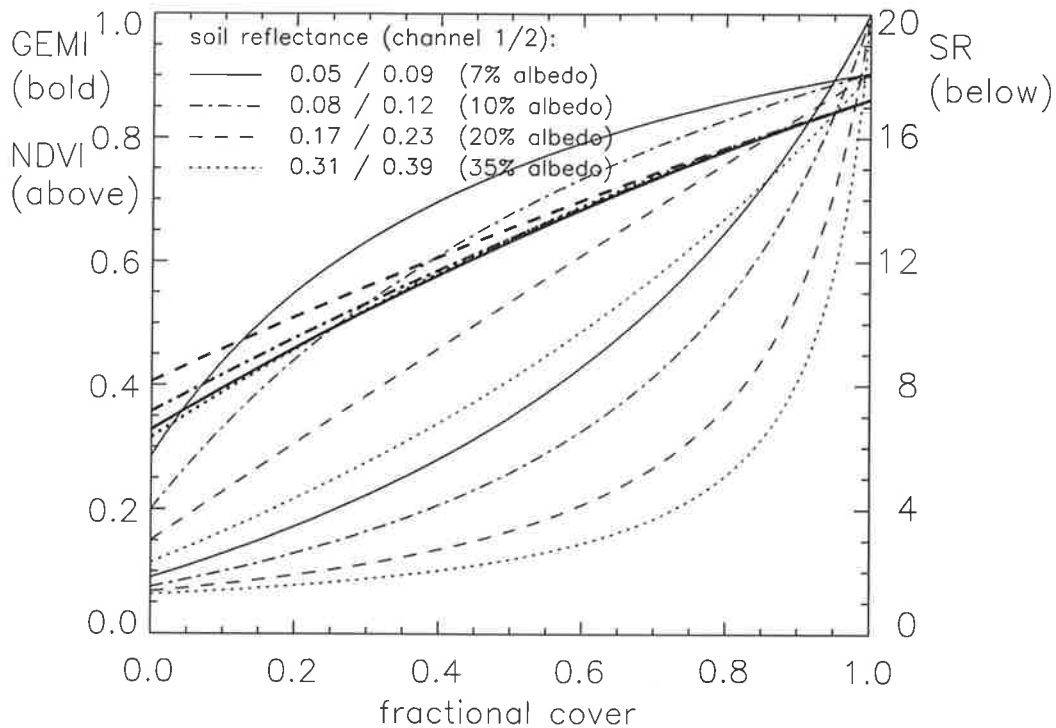


Figure 4.3: Dependence of the vegetation indices GEMI, NDVI and SR on fractional cover for some characteristic values for the reflectances of soil and dense vegetation.

important characteristics of the NOAA-11 satellite, operational from 8 November 1988 until 11 April 1995, the GVI and the processing chain developed here will be explained.

The NOAA-11 satellite and the AVHRR instrument

This satellite has a nearly sun-synchronous orbit between 833 and 870 km altitude that is rotated by 8.8° away from the poles. Because of the non-spherical shape of the earth, a slow shift in space of the satellite's orbital plane is generated that compensates for the movement of the earth around the sun, which explains the term "sun-synchronous". Immediately after launch, the satellite passed the equator at 14:30 h solar time at the satellite's geographic position in south-north direction, and at 2:30 h when going north-south; through small deviations from the ideal orbit, the time has, until March 1995, shifted to 17:23 h and 5:23 h, respectively.

With an orbital period of approximately 102 minutes, NOAA-11 completes every day $14\frac{1}{9}$ cycles and, with a width of 2800 km of the area covered by the AVHRR, is able to observe nearly every point of the earth daily. Every 9 days, the same area is observed again from the same angle; this area has a circular shape of 1.1 km diameter for nadir viewing. This resolution decreases to an ellipse of up to 2.4 by 6.9 km at a view zenith angle of over

Table 4.1: Channels of the AVHRR instrument on Board NOAA-11 with their spectral ranges and their significance for the remote sensing of land surfaces.

| channel | wavelength [μm] | remote sensing of |
|---------|---------------------------------|---------------------|
| 1 | 0.572-0.698 | par absorption |
| 2 | 0.716-0.985 | vegetation cover |
| 3 | 3.536-3.935 | fire |
| 4 | 10.338-11.287 | surface temperature |
| 5 | 11.408-12.386 | surface temperature |

70°. Since from 60° onwards, atmospheric scattering and absorption begin to dominate the signal (Kaufman 1989), a large part of the data recorded are useless for capturing properties of the surface.

The AVHRR has a total of 5 channels, in which the spectral flux density emerging from the observed area is measured and stored with an accuracy of 10 bit ($\approx 0.1\%$, hence the term “Very High Resolution”). One of the channels is in the red spectral region, one in the near-infrared, one in the middle and two in the thermal infrared (see Table 4.1). The high data rate of 122,880 bits per second and channel is transmitted to the surface and is not stored on-board entirely, so that a global coverage with the full resolution cannot be achieved with one receiving station only. (It is possible with a global network as demonstrated by the IGBP; Eidenshink and Faundeen 1994; see above). In order to capture all of the earth’s land surfaces, only a selection of the measurements is recorded on tape by the sensor and is later transmitted as the “Global Area Coverage” (GAC). This data subset is formed by only selecting every third row (of 2048 pixels) and then taking an average of 4 adjacent pixels of every 5. The mean of those four pixels thus represents a section of three by five pixels, so that a data reduction from 500 million measurements per day and channel to 15 million is achieved, which still amounts to around 220 megabytes per day.

The GVI product

The GVI data, which exist as long-term archives and will be used here, constitute yet another subset of the GAC data sets; a detailed discussion can be found in Goward et al. (1993). Since April 1985, GVI archiving is performed by subsampling the GAC data to a grid with constant angular distances of $1/7^\circ$ longitude and latitude, with only one GAC measurement per GVI pixel. The scenes consists of 2500 times 904 pixels and comprise all land surfaces from 75°N to 55°S. The strategy for selecting the GAC pixel that has been applied since March 1983 simply consists of taking the last measurement on tape that falls within the GVI sampling region. This method leads to a preference of easterly viewing directions with large zenith angles and a late solar time at the point of observa-

tion. The temporal resolution is also reduced from daily to weekly by selecting the weekly measurement that has the highest brightness contrast between channel 1 and 2, expressed as raw digital counts. The result is that observations with large atmospheric backscatter are preferred even more; this and the effect of the directional bias result in a significant contamination of the measurement of surface reflectance.

The raw digital counts of the GVI data set have been converted to reflectances by CESBIO using the coefficients by Kaufman and Holben (1993). During the process, some data with apparent reflectances greater than 1 or less than 0 have been deleted, along with those with a solar zenith angle of more than 85° . Those top-of-atmosphere (TOA) reflectances have then been converted to surface or top-of-canopy (TOC) reflectances by the fast parametrised atmospheric transfer model SMAC (Rahman and Dedieu 1994). Input data to this calculation are water vapour according to Oort (1983) and ozone content from TOMS satellite data, while aerosol content has been parametrised as a function of latitude (cf. Berthelot et al. 1994). Those data are part of the LASUR data set issued by CESBIO. Further processing steps by the authors Berthelot et al., as for example further screening and cloud detection algorithms, have been replaced by other methods developed in this study.

Further data screening

The LASUR data are first screened according to several criteria in order to remove unreliable measurements. Two products come out of this process: one monthly maximum composite (code: 'max') and one composite, for which the mean of all weekly values considered cloud-free is computed (code: 'cmp'). These are the processing steps in detail:

1. Measurements with a view or sun zenith angle of larger than 60° are removed. The same is true for so-called "hot-spot" conditions, where the view and solar directions nearly coincide. The criterion is

$$G_f(\theta_s, \theta, \Delta\phi) = \sqrt{\tan^2 \theta_s + \tan^2 \theta - 2 \tan \theta_s \tan \theta \cos \Delta\phi} < 0.25 \quad (1)$$

θ_s and θ are solar and sensor zenith angle, respectively, $\Delta\phi$ the relative azimuth and G_f a geometrical factor that is a good indicator of hot-spot conditions (Verstraete et al. 1990).

2. The vegetation indices NDVI and GEMI are computed according to

$$\text{NDVI} = \frac{\rho_n - \rho_r}{\rho_n + \rho_r} \quad \text{and} \quad (2a)$$

$$\text{GEMI} = \eta(1 - 0.25\eta) - \frac{\rho_r - 0.125}{1 - \rho_r} \quad \text{with} \quad (2b)$$

$$\eta = \frac{2(\rho_n^2 - \rho_r^2) + 15\rho_n + 0.5\rho_r}{\rho_n + \rho_r + 0.5}$$

where ρ_r and ρ_n are the red and near-infrared reflectances, respectively.

3. The weekly time series of GEMI is smoothed by a Fourier filter and all measurements that have a lower GEMI than the smoothed curve by more than 0.2 are considered cloudy. Before the filtering, negative GEMI values are set to zero. This method exploits the fact that GEMI can have large negative values for clouds and snow. By choosing a 4-week wide Gaussian filter characteristic, many long-persisting low-GEMI conditions are kept within the data set; these usually indicate snow or very bright soils. The remaining data of each month are averaged, which yields the mean-composite product, 'cmp'.
4. To produce the 'max' data set, the measurements with the highest GEMI are selected within one month, without the Fourier-filtering.

An example scene

Fig. 4.4 shows some example scenes of the monthly mean ('cmp') of GEMI from April 1989, globally and for selected areas in Europe and around Hamburg. Values below zero or without valid data appear white. On the global scene, the major vegetation zones, the tropical ones in particular, and the great deserts of Africa and Central Asia are clearly discernible. In the deserts, especially in the Sahara, there are some extensive areas with extremely light soils ($GEMI \leq 0$). By contrast, the low values in parts of Canada and northern Eurasia are caused by snow.

In the Europe section, snow-covered areas can be found in the Alps and for much of Scandinavia. Further, there is a clear gradient of vegetation cover from south-west to north-east caused by later spring onset in an increasingly continental climate. On a smaller scale, some fertile plains can also be distinguished, such as north, south and east of the Alps, or north of the Erzgebirge in Saxony. However, a closer look at the Hamburg section reveals that the spatial "noise" is generally high. As a result, it is difficult to judge whether those high values for Schleswig-Holstein, just north of Hamburg, are the result of a particularly early spring onset, or whether the reason lies in a usually clear and cloud-free weather during that month.

The average GEMI for this section is plotted on the left graph below for all months of 1989 (solid line), except for those where no data are left after reprocessing. For comparison, the dotted line shows the original weekly LASUR-GVI data. It turns out that the weekly variations, to a large degree the result of angular effects, are much reduced by the monthly reprocessing.

To the right, a time series for only one pixel slightly north of Hamburg is plotted. As it would be expected, the variability in the weekly data is higher than for the regional average. There are two downward peaks identified as clouds that have apparently been taken out of the monthly averaging. Other variations, like the ones in July and August, seem to be of angular origin. A comparison with the regional mean on the left shows that most of the angular variation could not be suppressed by regional averaging. An interesting feature of

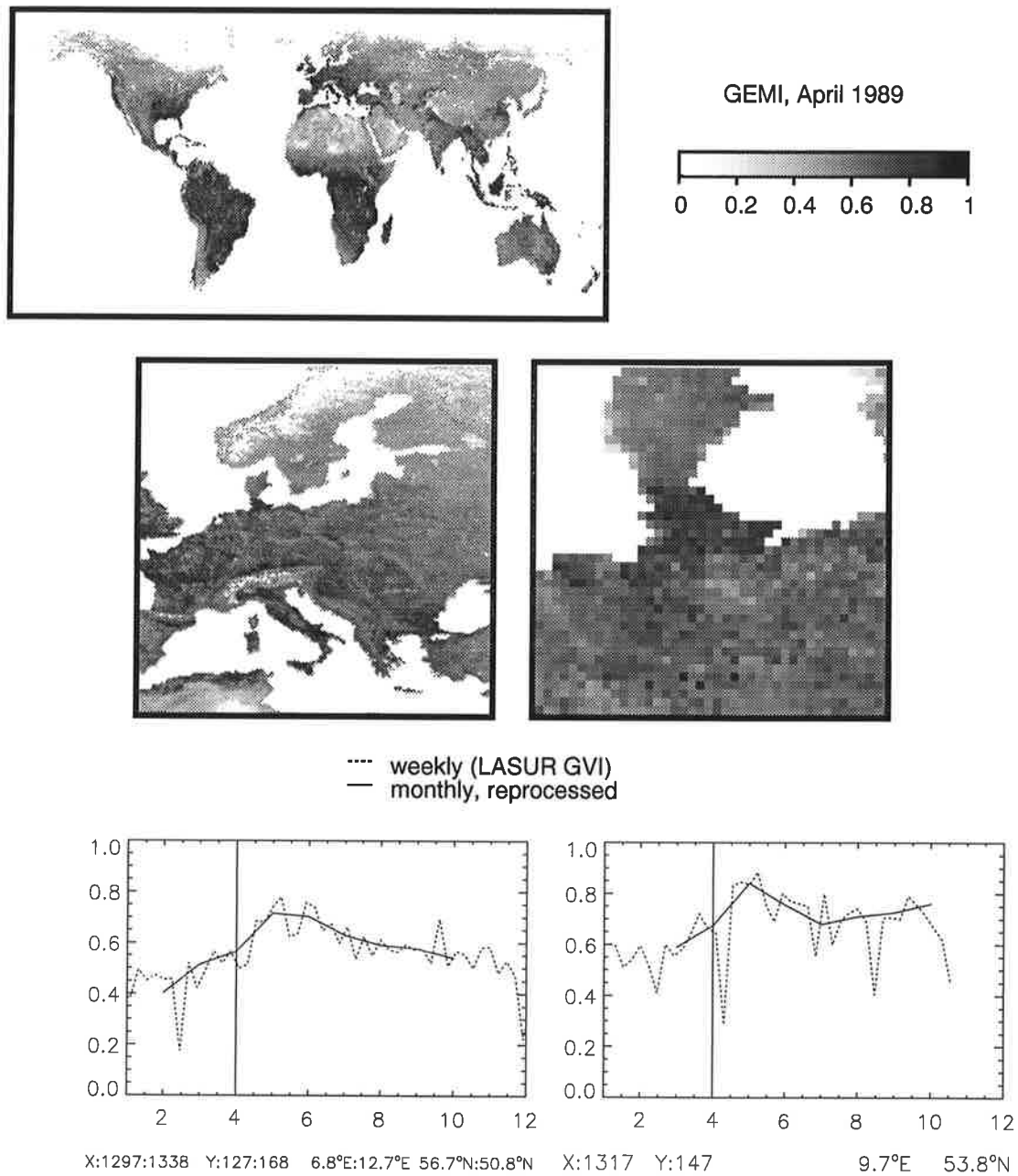


Figure 4.4: Example of GEMI from Hamburg and the rest of the world. The vertical line marks the time of the scene within the plotted time series. See text for further explanations.

Table 4.2: Description of some additional variants of the vegetation model BETHY.

| Code | Description |
|------|---|
| 0++ | Standard daily course every 10 days, up to 3 vegetation types per pixel |
| x0 | as 0++, but rooting depth for vegetation type 1 sufficient for closed vegetation cover ($LAI = 0.9\hat{\Lambda}$); for grasses in savannas 2 m instead of 1 m |
| D++ | as x0, but rooting depth increased also for type 2 (maximum monthly $LAI \geq 0.9\hat{\Lambda}$) |
| xT+ | as x0, but T and \hat{T} reduced by 2°C (cf. T+) |
| xT- | as x0, but T and \hat{T} increased by 2°C (cf. T-) |

the weekly time series are the large variations in May and June that later decrease until they reappear in September. This seems to be the result of an inference between the 7-day maximisation period of the original GVI data and the 9-day repeat cycle of the view angles of the AVHRR. Because of the peculiar selection process during GVI processing, this effect tends to be regionally rather uniform.

No such effect is found in monthly composites (cf. Goward et al. 1993, Meyer et al. 1995), although angles still seem to play an important role. Taking for example the one-pixel time series in Fig. 4.4 (bottom right), it is impossible to say whether a rise in GEMI, as the one from July to October, is the result of variations in the viewing geometry or caused by changes in cloud cover. This is another example to demonstrate that a certain temporal and spatial averaging is necessary for the interpretation of the GVI data as an indicator of changes in vegetation cover.

4.3 Versions of the vegetation model BETHY

In the preceding chapter it has turned out that the model versions used there all show a remarkably low NPP in relatively extended parts of the tropical evergreen rainforest. This is probably the result of insufficient soil water storage represented in the model, an interpretation supported by a study on rooting depth at various places in the Amazon rainforest by Nepstad et al. (1994). They found that during a dry period of up to five months, large sections of the area depended on deep roots for their water supply, some extending down to at least 18 m. The area marked by the authors roughly coincides with the area of low NPP in Fig. 3.4.

In order to take those results into account, further model versions are defined in this chapter that allow, in principle, an estimate of the rooting depth in tropical evergreen and drought-seasonal forests. This is achieved through increasing the rooting depth for vegetation type 1 (tropical evergreen trees) by steps of 1 m until the sustained LAI is at

least $0.9\hat{\Lambda}$, i.e. 4.5 (version 'x0'). In a further variant ('D++'), the same is done for type 2 (tropical drought-seasonal trees), except that the highest monthly mean is taken for the LAI criterion. For each value of the rooting depth, the model is re-run for another 5 years with stochastic rainfall simulation. These model versions are variations of '0++', which has already been introduced in the preceding chapter and which requires a recalculation of the daily cycle of energy balance and photosynthesis only every 10 days. Version 'x0' thus becomes the new standard version, which is listed in Table 4.2 along with further variants.

4.4 First comparison: LAI-GEMI

Before going into a more elaborate comparison of the model results with satellite data through the generation of a synthetic vegetation index, it will simply be checked whether the distribution of vegetation roughly coincides between model and observations. This section rather serves as an illustration and a quality check of the satellite data than as a final validation.

Fig. 4.6 shows GEMI in the form of monthly means ('cmp') for July 1989, both for non-vegetated (LAI=0) and fully covered areas (LAI \geq 4) according to model predictions. The version is 'x0', which can be recognised by the closed Amazon forest reaching far south-east ($\approx 15^\circ\text{S}$ and 52°W , lower map). This is the largest continuous vegetation formation simulated by the model.

It will now be assumed that this is in fact closed vegetation, so that GEMI should be 0.8 or more everywhere (cf. Fig. 4.3). For the actual measured values, however, this is only the case for the southern and south-western Amazon, while the value is only around 0.58 for the central Amazon. To understand this discrepancy, it should be remembered that in South America in July, the zone of maximum rainfall and cloudiness lies slightly north of the equator, so that the southern portions of the area are in the dry season. Hence, the data from those areas are largely unaffected by clouds, which explains the relatively high values of GEMI.

A different picture is found in Africa, where at this time the rainfall zone lies further to the north. Here, the maximum GEMI roughly coincides with the maximum precipitation. This difference between the two equatorial rainforest areas is illustrated by Fig. 4.5. In the Amazon, rainfall is much higher and is in opposite phase with the GEMI curve, with a rise of GEMI during the slightly developed dry season. By contrast, in the Congo region GEMI follows the seasonal course of precipitation quite closely, with two maxima corresponding to the two dates with the sun at zenith.

It is likely that in the first case, the seasonal course of GEMI is caused by perturbations of the measurement process during the rainy season, while in reality this is a truly evergreen forest with no seasonal variation of LAI. In the second case, it is a rainforest with some clearly developed seasonality, i.e. there is partial leaf shedding during the two dry periods. Precipitation rate and cloudiness are not high enough to perturb the satellite measurements

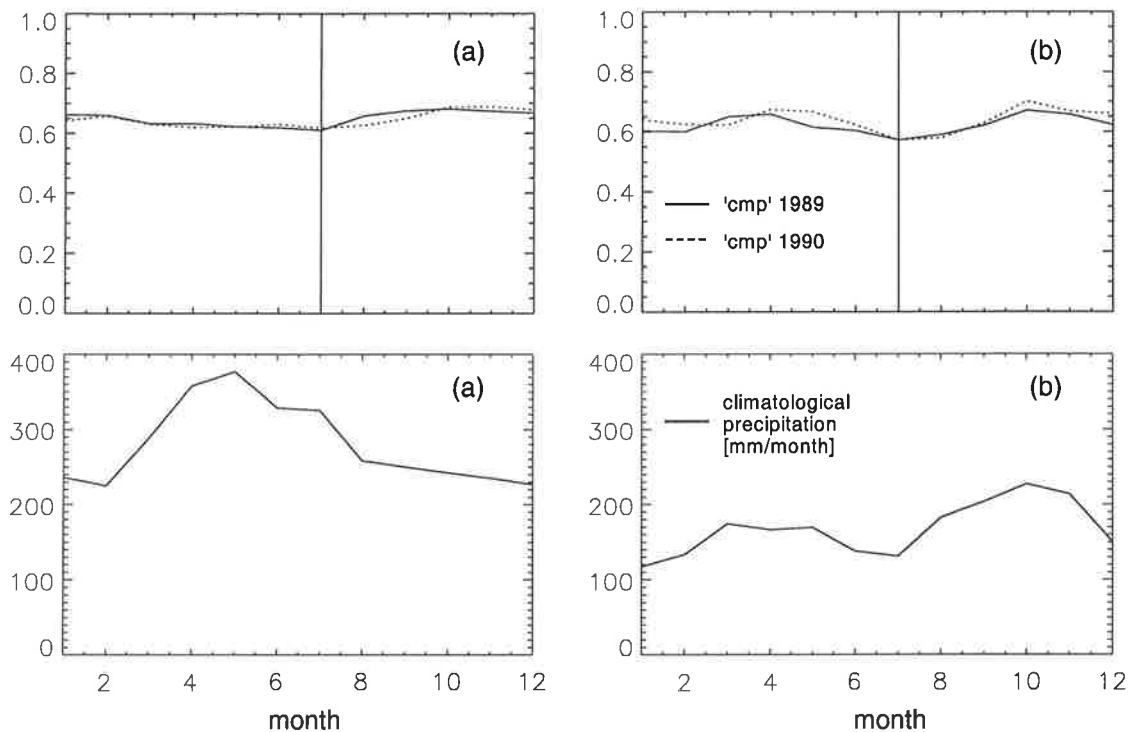


Figure 4.5: Monthly time series of GEMI for 1989 and 1990 (version 'cmp') averaged over a 24×24 pixel section over the equator and long-term average precipitation; (a) for the central Amazon region; (b) for the rainforest of the Congo Basin.

to a degree that changes their seasonal course.

In the northern temperate latitudes, with the exception of the broadleaf forests of the US South-East, the zones of closed vegetation are dominated by the needleleaf forests of Canada, Scandinavia, northern Russia and Siberia, whereas the highly agricultural areas of the USA, Europe and China are left out. High values of GEMI are measured in most cases, although with some important exceptions, in particular the northern part of the zone in eastern Canada and Scandinavia with only 0.54 and 0.57, respectively. The similarity of those values with the ones of the central Amazon underlines how difficult it is to state definitely whether the reason lies in perturbations of the satellite data or in the actual conditions on the ground, i.e. low vegetation cover fraction.

The largest vegetation-free areas of the model simulation (upper map) are the desert belt from Sahara to Gobi and the northern Arctic. GEMI values in the Saharan-Arabic desert are generally below a threshold of around 0.37 (cf. Fig. 4.3), as well as those of the Greenland glacier and the largest part of the deserts of Iran and Kazakhstan, the Gobi desert, Baffin Island (northern Canada) and Novaya-Semlya (north-west Siberia). Above this value, there are large parts of the northern Canadian Arctic, Siberia and Tibet. It appears that here, the vegetation, though sparse, is not predicted correctly by the model, probably because the relatively simple temperature part of the phenology scheme cannot

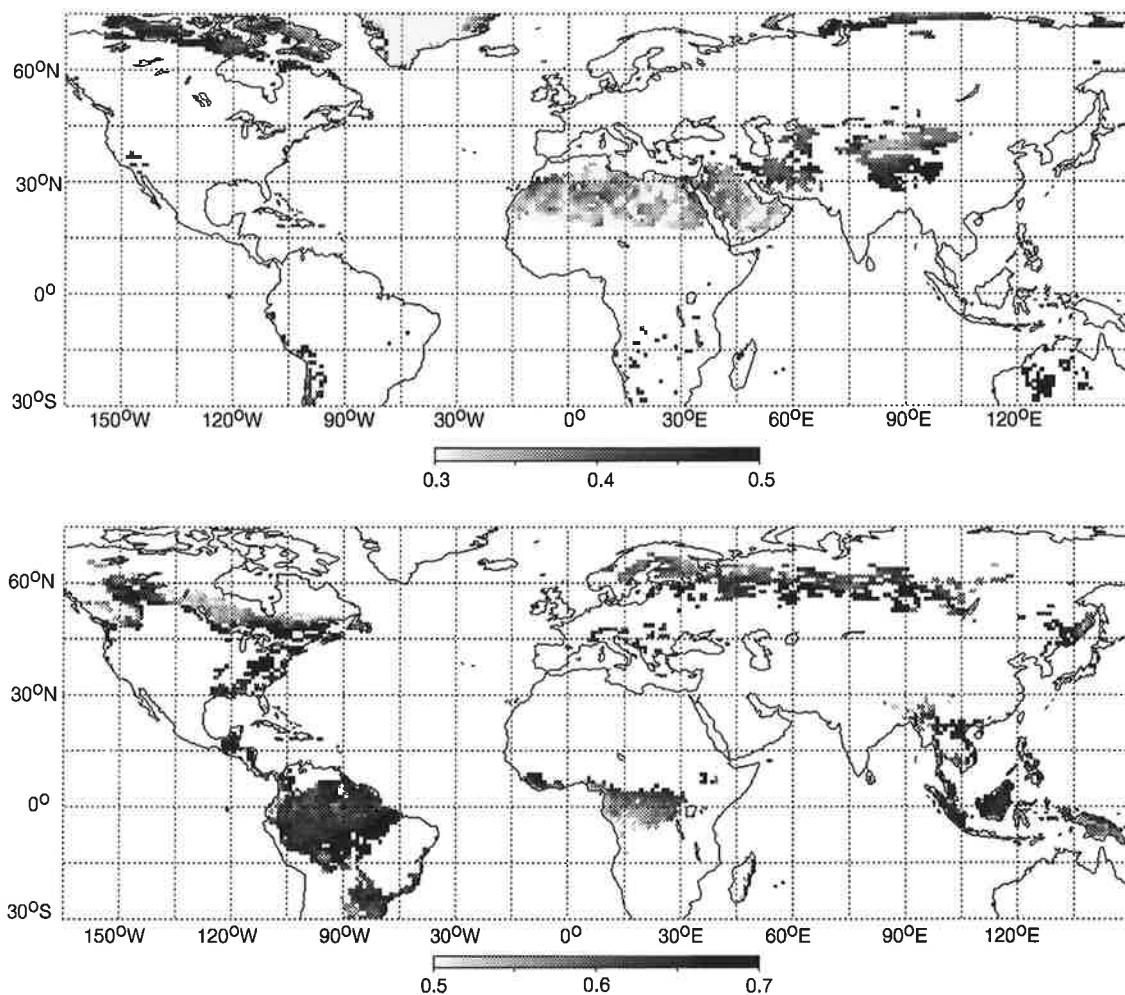


Figure 4.6: Measured GEMI for July 1989 (version 'cmp') for areas with a model-predicted LAI of 0 (above) or ≥ 4 (below). Model version is 'x0'. Areas where the respective condition is not met appear white.

always be applied to the tundra. Considerable deviations are also found for some areas of central Australia and for single pixels in southern Africa. The scattered distribution of these pixels is mainly the result of the stochastic rainfall simulation.

As an addition to Fig. 4.6, the latitudinal average of the above areas is plotted in Fig. 4.7. When interpreting the graph, it should be noted that the number of pixels over which the average has been taken can vary considerably, from only a few (southern Africa with $\text{LAI} \geq 4$) to around 30 or 50 (Amazon rainforest, Sahara). Ideally, the values of the two categories should fall into two narrow regions of GEMI, which is often the case where averaging is over larger sections. If however the two overlap, the average is usually taken over only a few points, as a comparison with Fig. 4.6 reveals. The most important exceptions have already been discussed: the tundra ($\text{LAI}=0$), the boreal forests ($\text{LAI} \geq 4$), southern Africa, and Australia ($\text{LAI}=0$). Another case that has not yet been mentioned is the subtropical to

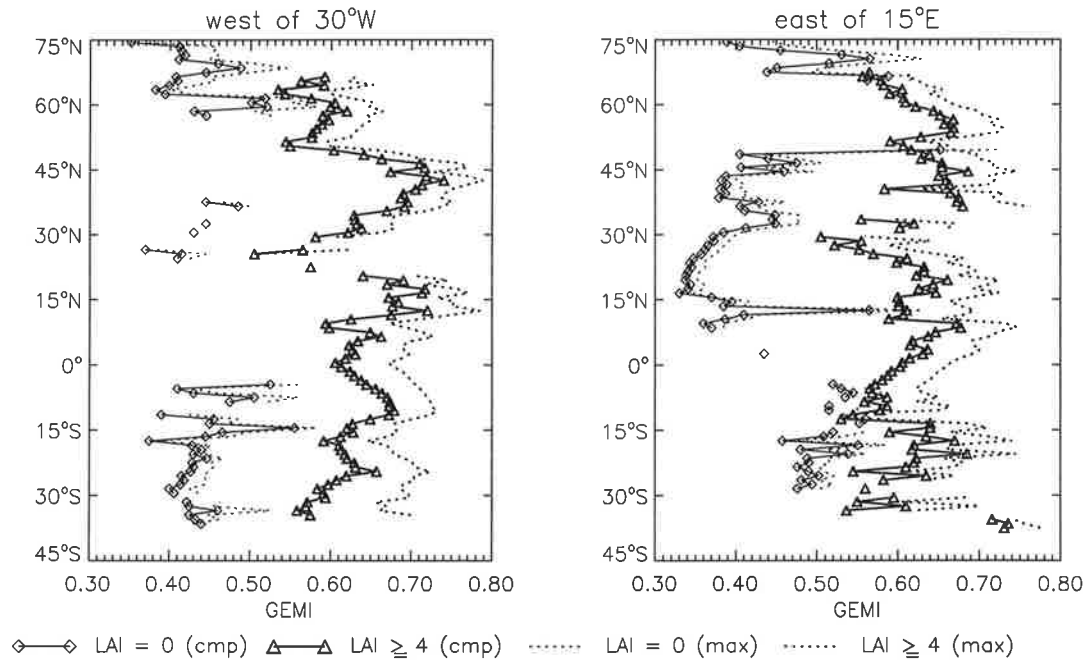


Figure 4.7: Latitudinal average of the areas of the preceding figure, separated into North and South America (left) and Eurasia-Africa-Australia (right). Greenland has been excluded. For comparison with the monthly means of GEMI for July 1989 (version 'cmp'), the monthly maxima ('max') are also plotted. Note that this graph has been extended southwards beyond 30°S.

temperate zone of South America with a continuous decrease in GEMI southwards, probably as a result of the winter senescence in the Argentine Pampas despite the relatively mild climate. The highest GEMI values are measured for the US East, the subtropical rainforests of Central America, and for New Zealand, while for the equatorial rainforests, the same picture is found as in the Fig. 4.6: a maximum south of the equator in the western part, and north of the equator in the eastern part.

For comparison with the monthly mean composites ('cmp'), the monthly maxima ('max') are also shown in Fig. 4.7. As explained earlier, the purpose of the maximisation is to minimise the effect of clouds on the satellite data by choosing the clearest days possible (Kaufman 1989). However, this technique has also a clear disadvantage leading to a systematic preference of certain viewing conditions (Meyer et al. 1995), which has been the motivation for introducing the processing method 'cmp'. The comparison reveals that the 'max' values follow the 'cmp' almost linearly. The only exception is the zone south of 30°S (LAI \geq 4, western part). The relatively high 'max' value is probably a consequence of a further disadvantage of this technique: if the month considered lies at the beginning of the growth period, there is a tendency for selecting a later date (or vice versa). Thus, a non-representative monthly value is selected and the length of the growing season appears

exaggerated. Apart from such effects, which are unfavourable for the maximisation technique, the variations within a month are dominated by changes in the viewing geometry. Consequently, atmospheric perturbations not captured by the screening method in 'cmp' also escape the monthly-maximum selection process.

What do these considerations imply for the usefulness of satellite data as a check on vegetation models? First, the minimum condition is fulfilled that satellite data roughly repeat the vegetation distribution as computed by the model. It has also turned out that the model can identify probable model deficits, such as too little vegetation in the tundra or too much in the boreal forests. On the technical side, it can also be demonstrated that the selection of monthly maxima does not offer significant advantages over the screening and averaging technique developed here, while it has some important known disadvantages. Eventually, the difficulty remains that areas that are almost certainly covered with dense vegetation can have measured GEMI values ranging from 0.58 to 0.74. This is almost half of the range that can be assigned to any at least partially vegetated area.

As a consequence, the question has to be asked whether the data used here do at all contain quantitative information on vegetation cover, i.e. more than simply "vegetated vs. non-vegetated". As discussed earlier, the strategy for answering this question consists of first simulating the signal and then comparing it with measurements. However, in this case a simple comparison of vegetation distribution is not sufficient and the vegetation index itself has to be predicted. This is the topic of the following section.

4.5 The method of model validation

After this simple, more qualitative comparison of modelled vegetation distribution with satellite data, in this section the satellite derived GEMI is compared to a GEMI computed on the basis of the model predictions and under the viewing conditions of the GVI data. The necessary steps are illustrated by Fig. 4.8:

- (1) The *vegetation model* BETHY is run using prescribed data sets of climate, soils, and vegetation type. It predicts the spatial and temporal distribution of LAI and fractional cover, and computes FPAR and carbon and water fluxes.
- (2) Atmospherically corrected remote sensing data are *screened* for clouds, snow and unfavourable viewing conditions.
- (3) A *remote-sensing simulator*, i.e. a model describing the bidirectional reflectance of the vegetation canopy coupled to a soil reflectance model, computes top-of-canopy reflectances at the angles and dates of the data selected in step (2).
- (4) The vegetation index GEMI is formed from the simulated and observed reflectances, and both values are *compared*.

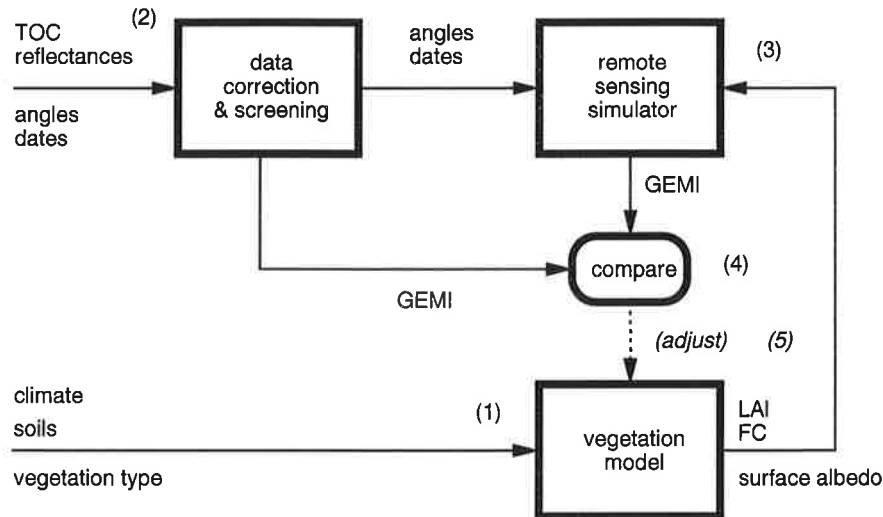


Figure 4.8: A diagram illustrating the proposed logic for using remote sensing data as a check on vegetation models. The numbers refer to the points in the text. An extension of the scheme indicated by the dashed arrow leads to a model constraint.

- (5) Parameters within the vegetation model are *adjusted* until simulated and measured vegetation indices agree with a pre-defined degree of accuracy.

Steps (1) to (4) constitute a partial model *validation*, while adding step (5) leads to a procedure of model *constraint*. The remainder of this chapter follows the first possibility, while the second, in a modified form, will be the topic of the next chapter.

The monthly maxima (version 'max', see previous section) of the reprocessed LASUR-GVI data are used as satellite data according to step (2). 'cmp' is not chosen because with the 'max' data it is possible to assign a definite set of viewing and solar angles to the monthly values. When simulating the satellite data (3), the date of the satellite measurement is taken into account by linear interpolation of the monthly vegetation model output.

The number of measurements with $GEMI > 0.35$ for the 'max' data set ranges from 365,820 for December to 666,576 for August (both 1990). Since the required computing time for the simulation of only one measurement is in the range of one second, only a small selection can be simulated. Therefore, one measurement is chosen for each of the 11,069 pixels of the equal-area one-degree grid used by the vegetation model. A value close to the grid cell centre is selected, so that no angular conditions or measured values are preferred.

The remote sensing simulator

The generation of synthetic remote-sensing data according to step (3) is done with the model NADIWAS (New Advanced Discrete model With Anisotropic Soil; Gobron et al. 1997). It computes the bidirectional reflectance factor of the coupled system canopy-soil, i.e. the top-of-canopy reflectance. "Bidirectional" stands for the two directions from the ground scene

Table 4.3: Common parameters used for the calculation of synthetic satellite data.

| Symbol | Description | Value | Source |
|-----------------|----------------------|-------|---------------------|
| Canopy (leaves) | | | |
| τ_L^{red} | transmissivity (red) | 0.05 | Asrar et al. (1992) |
| ρ_L^{red} | reflectivity (red) | 0.07 | " |
| τ_L^{NIR} | transmissivity (NIR) | 0.45 | " |
| ρ_L^{NIR} | reflectivity (NIR) | 0.45 | " |
| Soil | | | |
| Θ_s | asymmetry factor | -0.2 | Pinty et al. (1989) |
| h_s | hot-spot parameter | 0.2 | " |

to the positions of the sun and sensor. The reflectance of the soil background is computed according to Pinty et al. (1989), while the radiation transfer within the canopy is modelled by a semi-discrete approach by a new combination of formerly separate concepts: on the one hand, the position and orientation of leaves of fixed size is described statistically, on the other hand, the optical properties of the scatterers are characterised as a turbid medium. The statistical approach (Verstraete et al. 1990) is applied to unscattered ray transfer (one reflection by the soil, none by the canopy) and to single scattering (by the canopy), while the turbid-medium approach is used for scattering of higher order, with the scattering elements considered infinitely small and homogeneously distributed (Chandrasekhar 1960).

Since anisotropic soil reflectance is assumed, the single-scattering albedo of the soil has to be chosen in such a way that the hemispherical integral over the bidirectional reflectance factor is equal to the soil albedo used in the vegetation model. The translation from albedo to single-scattering albedo is precomputing with a solar zenith angle of 60° , which is exactly the mean over the sunlit hemisphere. Taking diffuse skylight instead would lead to very similar results. At first, however, the surface albedo, ρ_S , imported from the vegetation model, has to be split into a PAR (red) and a NIR portion corresponding to channels 1 and 2, respectively. If ρ_S is less than 0.5, the following linear equations for soils are used:

$$\begin{aligned}\rho_s^{red} &= 0.92\rho_S - 0.015 \\ \rho_s^{NIR} &= 1.08\rho_S + 0.015\end{aligned}$$

For values great than 0.5, snow cover is assumed and the values are set according to:

$$\begin{aligned}\rho_s^{red} &= \min\{1.059\rho_S; 0.98\} \\ \rho_s^{NIR} &= \rho_s^{red}/1.125\end{aligned}$$

The first set of equations is based on the soil line by Price and Bausch (1995, cf. Equ. 122 in Section 2.6), while the second has been estimated from data found in Bowker et al. (1985).

The parameters for the calculation of synthetic satellite data are listed in Tables 4.3 and 4.4. The expressions "planophile" and "erectophile" signify a preference of horizontal

Table 4.4: Size parameters (vegetation height and leaf diameter in m) and leaf angle distribution (LAD) of vegetation for the calculation of synthetic satellite data. Pl: planophile; Er: erectophile; Un: uniform (see text).

| | | | | | | | | |
|-------|-------|-------|-------|-------|-------|-------|-------|-------|
| Typ | 1 | 2 | 3 | 4 | 5 | 6 | 7 | 8 |
| h_v | 30.0 | 15.0 | 15.0 | 15.0 | 15.0 | 15.0 | 1.0 | 1.0 |
| d_l | 0.300 | 0.100 | 0.100 | 0.050 | 0.005 | 0.005 | 0.005 | 0.050 |
| LAD | Pl | Pl | Pl | Pl | Un | Un | Un | Pl |

| | | | | | | | | | |
|-------|-------|-------|-------|-------|-------|-------|-------|-------|-------|
| Typ | 9,11 | 10,12 | 13 | 14 | 15,16 | 17-19 | 20,21 | 22 | 23 |
| h_v | 0.3 | 0.3 | 0.3 | 0.3 | 0.6 | 2.0 | 2.0 | 0.3 | 1.0 |
| d_l | 0.010 | 0.050 | 0.005 | 0.010 | 0.010 | 0.050 | 0.050 | 0.010 | 0.050 |
| LAD | Er | Er | Un | Un | Er | Pl | Er | Er | Un |

or vertical leaf orientation, respectively, following a mathematical description by Bunnik (1978; see also Ross 1981). For reasons of computational speed, only the most common vegetation type is selected and the parameters of Table 4.4 are assigned accordingly. As optical properties of the leaves, fixed values of a different study are chosen (Asrar et al. 1992) that are consistent with the single-scattering albedo, ω , of the light-absorption calculation for photosynthesis (cf. Section 2.6 “light absorption”). The relevant relationship is $\omega = \tau_L^{red} + \rho_L^{red}$, with typical values for developed leaves and needles. A comparison with other modelling studies (Bégué 1992, Myneni et al. 1992, Goel and Qin 1994, Myneni et al. 1995, Gobron et al. 1997) shows that the NIR single-scattering albedo, in particular, (i.e. the sum of τ_L^{NIR} and ρ_L^{NIR}) does not differ much from the value assumed here. However, the value in the red or photosynthetically active part of the spectrum varies much more, depending on leaf chlorophyll content (Jacquemoud and Baret 1990), and typically lies between 0.08 (mainly crops, fertilised) and 0.15 (natural vegetation, low nitrogen). The effect of this and other uncertainties will be discussed in the next chapter when computing a relationship between vegetation indices and FPAR. One of the results is that through multiple scattering, larger changes in ω lead only to relatively small changes in FPAR, which justifies the use of standard values according to Table 4.3.

4.6 Comparison of simulated and measured vegetation indices

The results of the simulations for the months of March and July 1989 are shown in Fig. 4.9 and 4.10, together with the corresponding measurements of GEMI taken from the ‘max’ data set. For each model grid point (1° equal-area), there is one simulation and one measurement with identical sun and viewing geometries. The results with the satellite data

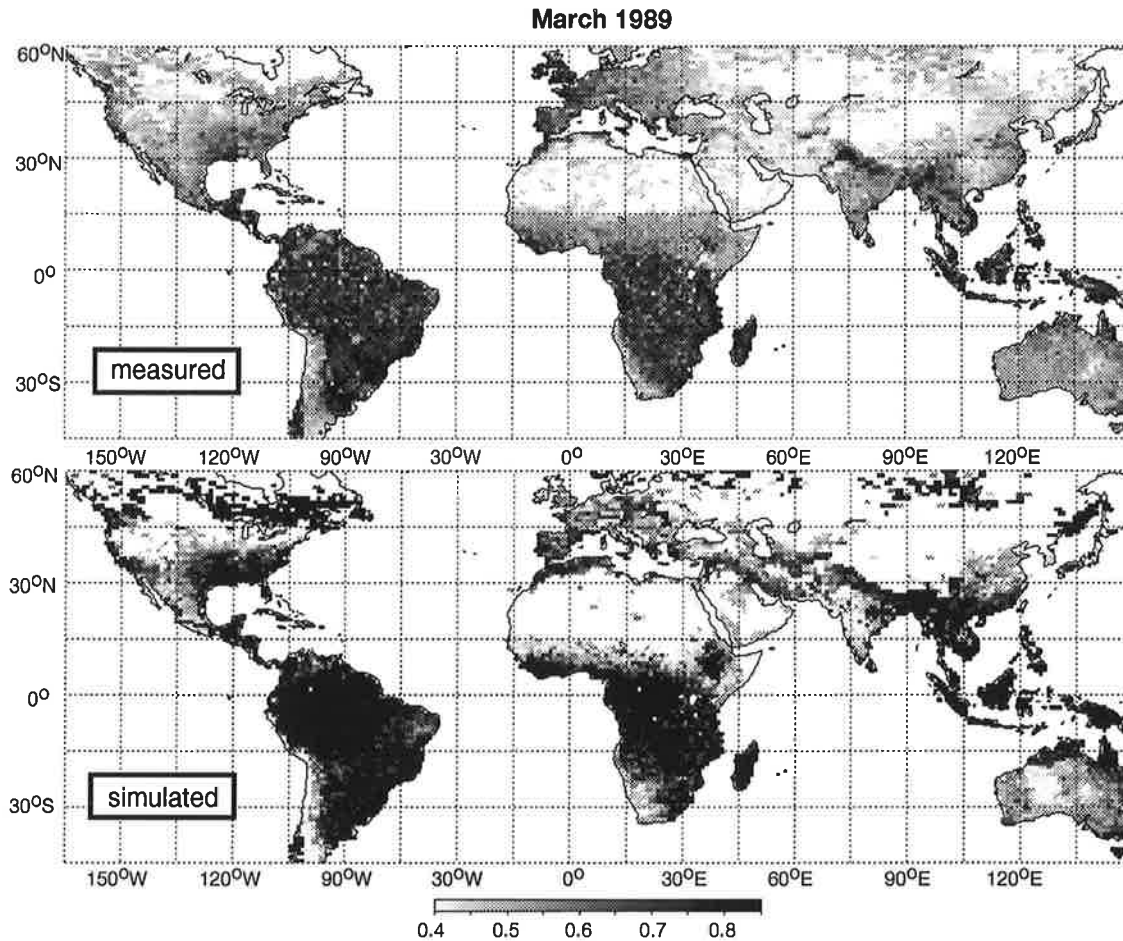


Figure 4.9: Measured and simulated values of the vegetation index GEMI for March 1989. These are monthly maxima and simulations on the basis of the vegetation model, version 'x0', with long-term mean climate and for the same week and viewing conditions as the measurements.

of 1990 differ only slightly from those shown here (see Appendix and Fig. 4.12 and 4.13). The comparison of the two sets of GEMI data can be summarised as follows:

- (1) The simulations have generally higher values.
- (2) The spatial variability in arid regions is higher in the simulations.
- (3) The outlines of many biomes and vegetation formations coincide to a high degree.
- (4) The contrast between wet and arid areas, as well as between boreal forests and tundra is more pronounced in the simulations.
- (5) The difference between the two years considered is small.

Point (1) indicates that during the correction of the satellite data, the effect of atmospheric perturbations has been underestimated so that measurements have not exactly been brought

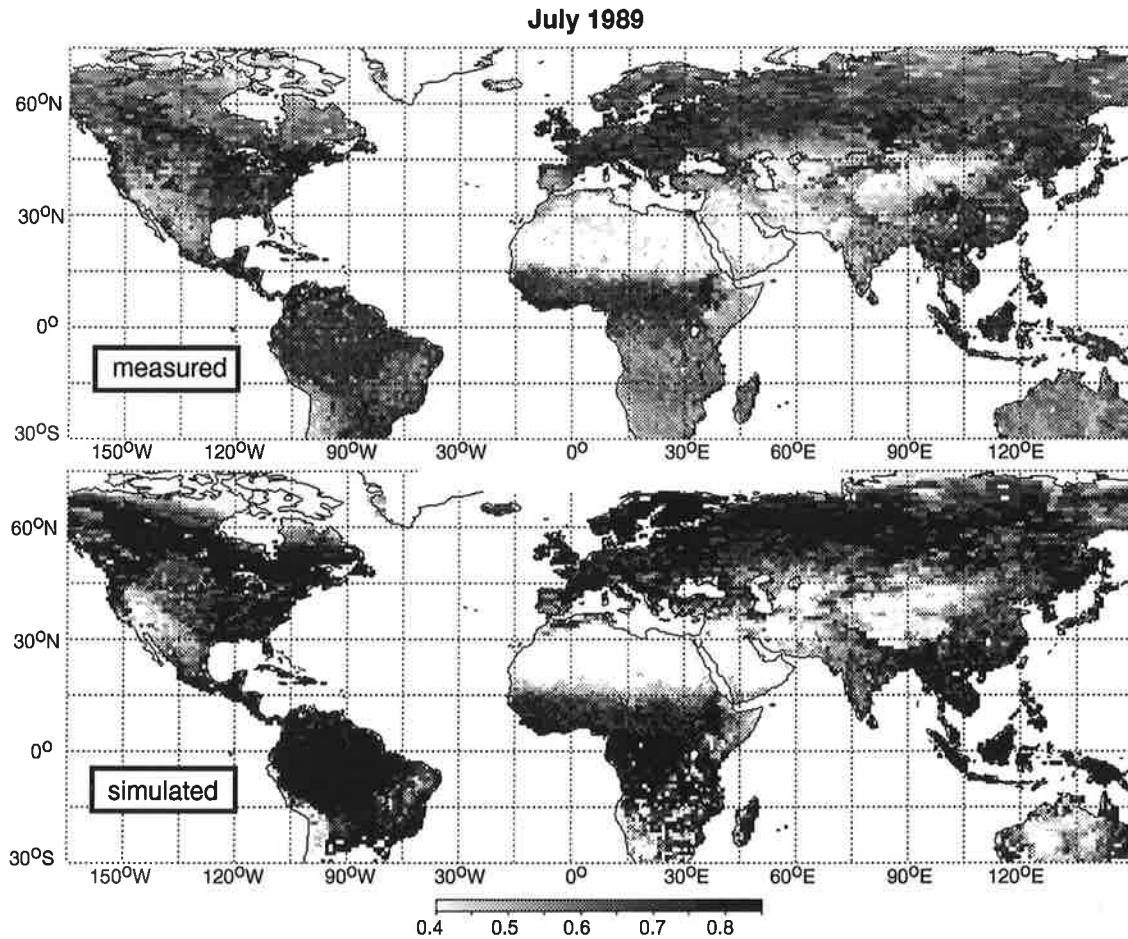


Figure 4.10: As the preceding figure, but for July.

to TOC level. Point (2), however, was expected, because the stochastic precipitation is generated independently of neighbouring pixels in the model, whereas in reality there is a high degree of spatial correlation.

For point (3), a range of examples can be given, for example from north to south:

The forest/tundra transition in Labrador in March.

The partially snow covered continental steppes of North America and northern Asia with the border to forested areas in the north and, in Central Asia, to the fertile mountain fringes in the south-east.

The extent of the Saharan-Arabic and the Iranian-Central Asian deserts with interspersed oases.

The agricultural areas at Ganges and Indus (especially in March).

The tropical rainforest in South America and its border to the Llanos of Venezuela and Columbia as well as to the north-east Brazilian Cerrados, which also turn green in March.

The Sahel, the fertile Ethiopian highlands and the semi-arid savannas of East Africa.

The summer-rain areas of northern Australia.

The humid/arid transition in southern Africa from north-east to south-west.

The transition from the fertile grasslands of the Pampas and southern Brazil to the arid steppes of Patagonia.

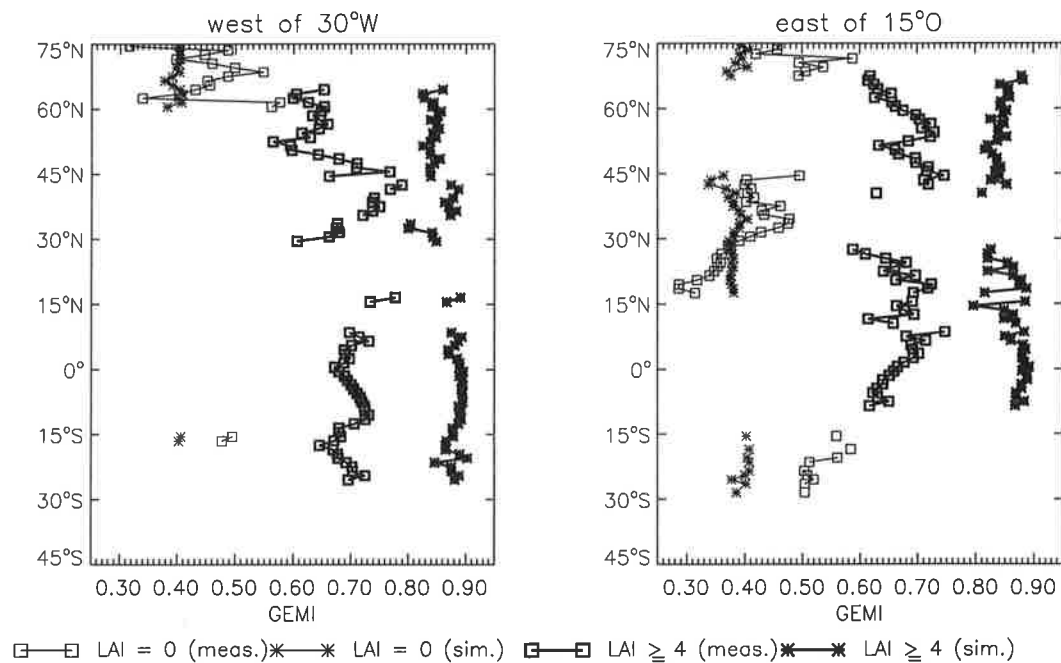


Figure 4.11: Latitudinal average of measured and simulated monthly maxima of GEMI (version 'max') for July 1989 over areas with LAI = 0 and LAI \geq 4 according to model version 'x0'. Only averages over at least five pixels are shown.

As far as the boreal-arctic transition is concerned, point (4) repeats the results of the preceding section. However, the apparent overestimate of the contrast between humid and arid environments and seasons only becomes visible through the quantitative approach developed here. The reason for these discrepancies is probably that the model underestimates the ability of vegetation formations to adapt to the prevailing climate. It is thus indicated how, through comparison of model simulations with remote-sensing data, insights into geo-ecological functioning can be gained.

Eventually, point (5) indicates that the generally good agreement has not been achieved by chance, but that the year-to-year differences are small compared to the uncertainties during modelling of vegetation distribution. The use of a mean climate can therefore be justified.

Before a further interpretation, the results are presented again as latitudinal averages. Fig. 4.11 shows, in addition to Fig. 4.7, the simulated and measured GEMI for non-vegetated and fully vegetated areas according to model version 'x0'. On the one hand, it can be seen that many areas simulated as LAI=0 probably have some sparse, but highly drought-resistant vegetation growth. On the other hand, the areas with LAI \geq 4, as for example the Amazon rainforest, are quite certainly densely vegetated in actuality. In this case, the overestimate of GEMI is, as observed before, the result of insufficient atmospheric correction.

Within the simulations with 'x0', there are 3463 cases where the vegetation model calculates an LAI of 5. For those pixels, the mean of the simulated GEMI is 0.89, while measured values of dense vegetation are around 0.76, apart from the higher values in the US East and the lower ones over rainforests when precipitation is high (cf. above). By contrast, simulations for non-vegetated areas are around 0.38 and correspond roughly to measured values.

How can this obvious deficiency of the atmospheric correction be explained? As noted in Section 4.2 during the description of the GVI product, the criterion for selecting weekly data used by NOAA has been the maximum difference between the channels 1 and 2, leading to a preference of situations with high atmospheric backscatter. This might be an explanation for the fact that the atmospheric data used by Berthelot et al. (1994) do not represent the actual situation in an appropriate way.

To correct for the remaining influence of the atmosphere, a common principle in remote sensing will be applied here: the data are recalibrated against "ground truth". Here, the simulation result of 0.89 serves as a "true" value for dense vegetation, while 0.76 is assumed as a typical value for the measurements. For non-vegetated areas, a value of 0.38 is taken for both simulations and measurements, with a linear interpolation for the intermediate range:

$$\text{GEMI}' = (\text{GEMI} - 0.38) \frac{0.89 - 0.38}{0.76 - 0.38} + 0.38$$

Values less than 0.38 indicate special conditions (very bright soils, snow) and are ignored in the following considerations.

In principle, this correction is only valid for 1989 and the 'max' version of the monthly satellite data. A comparison of the two years shows that the average of all measured values of 1990 is by about 1.7% higher than for 1989. For the simulations, the figure is only 0.7%. This difference between 1989 and 1990 is mainly the result of a larger solar zenith angle during observations resulting from the shift of the overpass time into the evening: while in 1989 the mean angle was 40.8°, it was already 43.6° in 1990. The fact that the difference is smaller in the simulations might be the result of insufficient correction of sensor degradation for the data, or of real differences between the model and the actual situation. For lack of a definite answer, the above correction will be taken also for 1990. Nevertheless, these comparisons show that one has to be cautious when interpreting year-to-year variations in satellite data. Besides, it is demonstrated that the remote-sensing simulator can represent trends caused only by angular effects.

A comparison using the recalibrated values is shown in Fig. 4.12 and 4.13 as a latitudinal mean for different versions of the vegetation model according to Table 4.2. The average has only been taken over those pixels where both measurement and simulation are valid, while values below 0.38 have been set to 0.38. There is generally a good agreement, with the exception of some important deviations. For example, simulations are well above measurements in northern latitudes, at about 35°N and around the equator, while the satellite signal is underestimated around 40°N, 15°N and 30°S. Exceptions are the versions 'xT+'

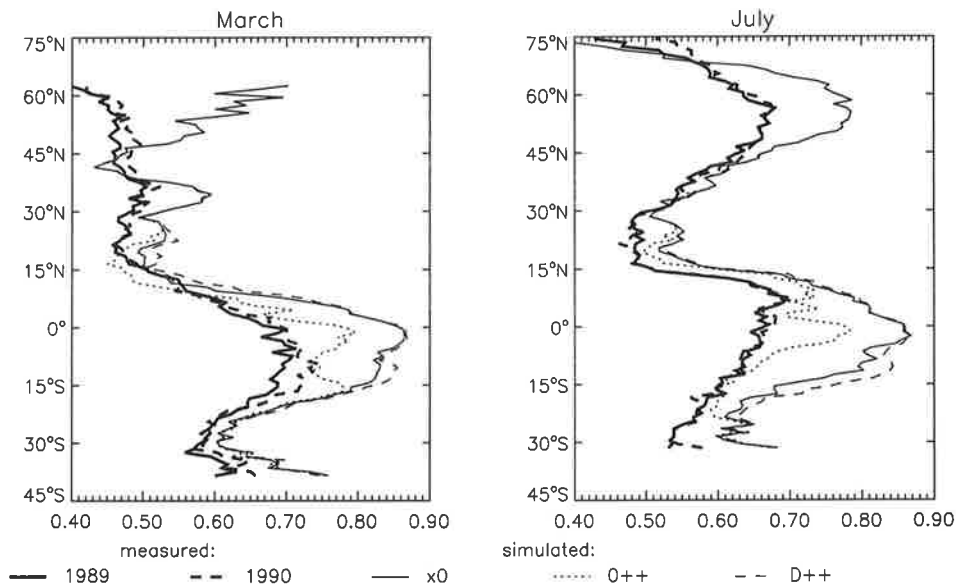


Figure 4.12: Latitudinal average of measured and simulated monthly maxima of GEMI with various versions that differ in the water balance of tropical vegetation. Simulations under the viewing conditions of the 1989 data, measured values recalibrated (see text).

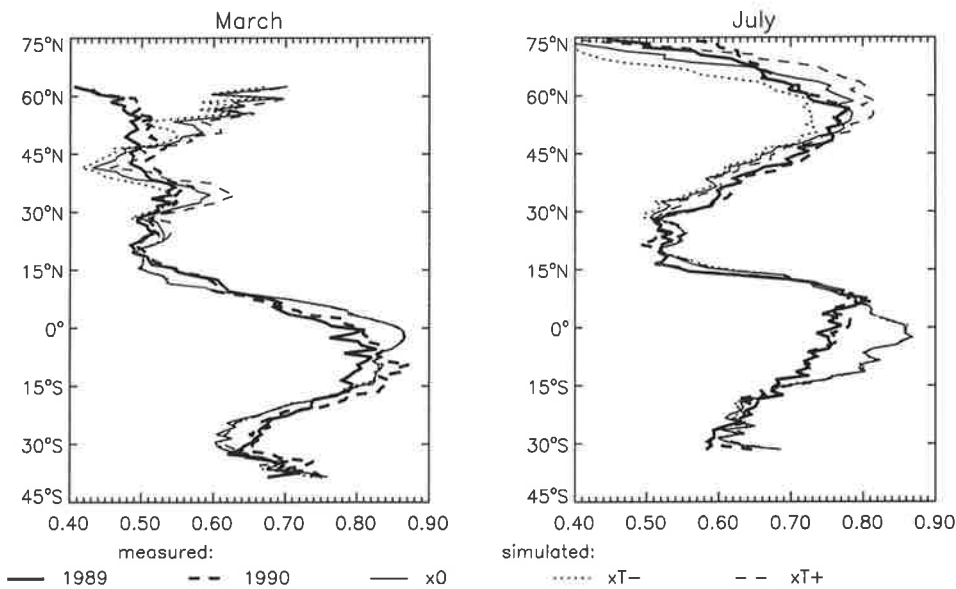


Figure 4.13: As previous figure, with further variants of the vegetation model: growing season length in cold climates shortened ('xT-') or lengthened ('xT+').

around 40°N, 'xT-' around 35°N and '0++' at the equator. An important result of this comparison that applies to all versions is that in the satellite data, GEMI is reduced to a larger degree by snow cover than in the simulations, possibly because much snow is visible also on top of the boreal forest. In the model, the assumption is that the snow remains below the canopy so that it is hidden below evergreen coniferous forests. In some cases, e.g. south of that region, the model can be adapted to the measurements by varying parameters, in this case by modifying T_ϕ ('T+/-'). To some extent, this is also true for version 'D++', where the agreement between 10 and 15°N is improved compared to the standard. Otherwise, an earlier observation referring to Fig. 4.9 and 4.10 is repeated here: Water limitation in many arid areas is too pronounced, because either soil water storage or adaptability to drought is underestimated. Besides, the strong residual perturbation by clouds (see Section 4.4) should play a role in the wet tropics, and in fact the simulated signal is always higher around the equator, except for version '0++' without deep roots.

For July, there is a good agreement also for the northern latitudes, with a slight underestimate between 30°N and 50°N for all versions considered here. Further to the north, it is the standard version that fits the data best, except for the arctic where simulated vegetation is too sparse, as already observed in Section 4.4. Here, version 'xT+' achieves a better fit to the data. Around the equator the satellite signal is overestimated even further for July compared to March, again with the exception of version '0++'.

For a better interpretation of the previous comparisons, Fig. 4.14 shows, again for the standard version 'x0', those areas where the deviation from the satellite signal is at least 0.10. It reveals some clear regional differences that are invisible on a latitudinal average. For example, the transition in March from positive to negative deviation comes from a combination of an already observed overestimate for the boreal forests and an underestimate for Western Europe. Evidently too "green" are also the South-East of the USA and China. Both regions have a particularly mild winter climate, but with a high number of frost events compared to Western Europe, so that the actual vegetation is not as developed. The phenology scheme, more adapted to the European situation, would have to be modified here. On a latitudinal average, this is partly compensated by negative deviations in Mexico and India. Contrary to the previous underestimate, in some regions (Algeria, Syria, Iran), this appears to be the result of soil erosion not taken into account by the vegetation model. Considering the aridity of those areas, a suppressed satellite signal, as near the Gulf of Guinea (equatorial Africa) or in the central Amazon Basin, seems highly improbable. Eventually, in the Sahel, and around the tropic of Capricorn in southern Africa and Australia, it becomes again evident that the model underestimates the vegetation's ability to adapt to arid conditions.

The map for July shows again an unambiguous negative deviation from the measured GEMI for the boreal coniferous forests. Probably, the tree fraction of those regions, some of which can be characterised as transitional formations to the tundra, is assumed too high. Moreover, the Sahel appears to extend too far north in the model for this month,

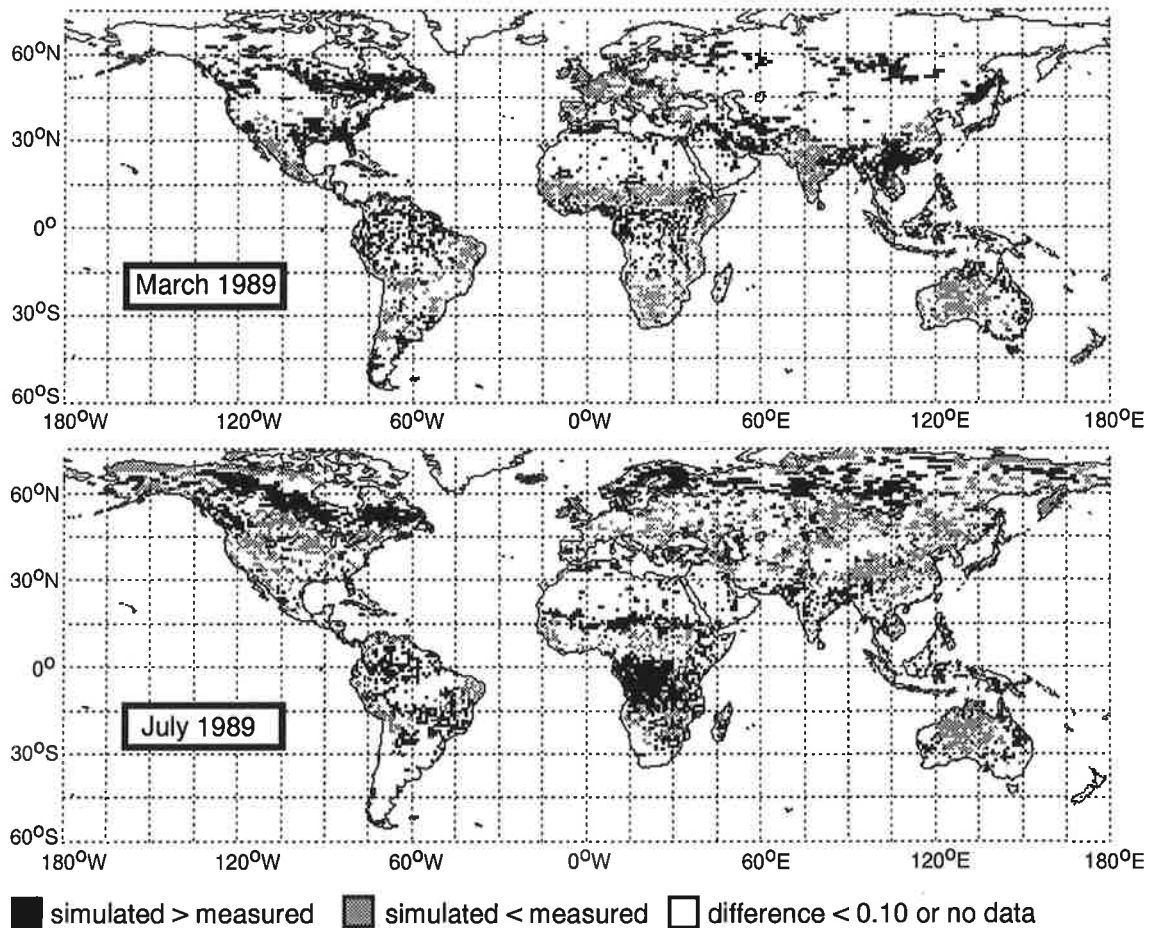


Figure 4.14: Check of the simulated GEMI against the satellite derived value, taken from monthly maxima ('max') of 1989, for version 'x0' of the vegetation model. Satellite data have been recalibrated (see text).

which also shows up in the same comparison for 1990 (see Appendix). This seems to be a real model deficit, even though the rainfall variability in that region might be so large that two years are not enough for a definite statement. Further to the south, around the equator in South America and Southeast Asia, the known signal perturbation becomes apparent, while in Africa south of the equator, the model overestimates the signal, even though the area is undergoing a dry season. It thus appears that the dry season in the drought-deciduous forests and savannas south of the central Congo Basin is much more pronounced in reality than in the model. This also explains the large difference between measurement and simulation just south of the equator in Fig. 4.12 and 4.13.

Eventually, Fig. 4.15 again demonstrates the deficit of model version '0++' in the south-eastern part of the Amazon rainforest and in central Africa just north of the equator. This and the previous comparisons are evidence of the satellite data's capacity for checking vegetation models. However, the comparison for the central Amazon Basin also shows that a check on the basis of remote sensing data alone is often not possible, but that additional

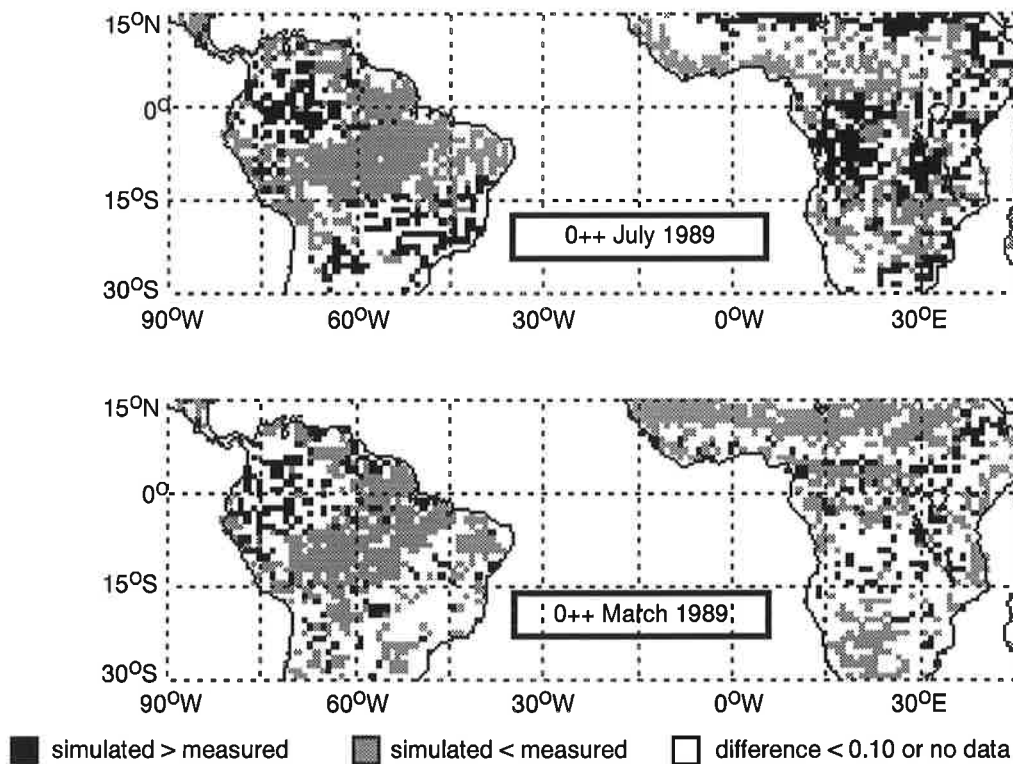


Figure 4.15: As the previous figure, but for version '0++', without deep roots for the evergreen tropical rainforest.

“expert knowledge” is required in most cases.

Taking for example an uncertainty of 0.10 for the satellite measurements, Fig. 4.14 and 4.15 amount to a first check of the vegetation model that is not valid for some areas because the quality of the satellite signal is affected to a larger degree than this particular value. A consistent and at the same time unsupervised method for deciding, in which cases there is a model deficit, and in which a deficit of the satellite measurement, could be devised in the following way: The model is varied within “reasonable” bounds until – within an assumed degree of accuracy – agreement is achieved with the satellite data. If this is not possible, e.g. because all model versions predict a closed forest in central Amazonia, then the measurements have to be considered in error. Such an approach will at least be necessary as long as there is no clearly defined quality check available for the satellite data.

4.7 Conclusions

In the present section, a consistent method has been introduced that allows a validation of certain aspects of mechanistic vegetation models on a global scale, and in this way to gain insight into ecophysiological processes on large spatial scales. Because of the quality of the presently available global satellite data, an automatic, unsupervised check is not yet

possible and some “expert” judgment is required. However, considering the large scatter in the results of present terrestrial vegetation models that is mentioned in Chapter 1, the relatively coarse comparisons between model predictions and satellite data presented here are still of substantial value because they constitute a much needed source of empirical data for their validation.

Chapter 5

Model Constraint with Remote Sensing Data

5.1 The method of model constraint

In the preceding chapter, a method has been developed that consists of checking various prognostic model versions of BETHY within a predefined range of parameter settings with the help of satellite data. This method will now be extended to a “diagnostic” model simulation based on satellite observations. Such a possibility has already been indicated by point (5) of the scheme introduced in Section 4.5 (cf. Fig. 4.8). By this method, it is required that predicted and measured satellite data agree as well as possible, but also, that the choice of model parameters does not deviate too far from the standard setting, assumed to be most probable.

In principle, it would be possible to demand an agreement at the level of GEMI as illustrated in Fig. 4.8. Because the required computer time for the remote sensing simulation would be extremely high, a method is developed that allows the use of all satellite measurements within a model grid box, instead of only one sample as before. As shown in Section 4.2, a certain spatial averaging can reduce variations in the satellite data caused by bidirectional effects. The following scheme is therefore based on a measurement of the variable FPAR (cf. Fig. 5.1):

- (1) The vegetation model BETHY computes the internal prognostic variable FPAR under remote sensing conditions, that is for 100% direct incoming radiation at a solar time of 15:30 h.
- (2) The processing scheme for satellite data is extended by a general relationship of the form $FPAR = f(\text{GEMI})$. Remote sensing simulation and angular data are not needed any more.
- (3) The model-inherent value of FPAR is compared to its satellite-derived analogue.

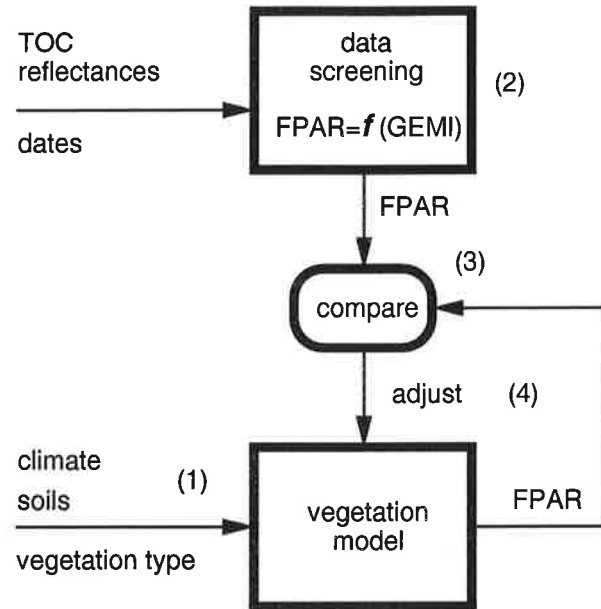


Figure 5.1: A diagram illustrating the proposed logic for using remote sensing data as a constraint for vegetation models. The numbers refer to the points in the text. FPAR is the fraction of photosynthetically active radiation absorbed by the vegetation.

- (4) Parameters of BETHY are corrected and FPAR is recomputed. This and the preceding steps are repeated until an agreement within a predefined degree of accuracy is reached.

5.2 Computed FPAR-vegetation index relationships

Before this scheme is implemented, it is necessary to investigate how FPAR can be estimated from vegetation indices, and whether GEMI is in fact the most suitable index for the purpose. Some detailed studies on the topic have so far been published: Asrar et al. (1992) have used a three-dimensional radiative transfer model to develop a linear function of FPAR depending on NDVI. It is reasonably accurate for a medium-bright soil type and viewing angles not too far from nadir. An important statement is also that the determination of LAI is largely impossible when the fractional cover (FC) is unknown. In a similar study, Goel and Qin (1994) have tested a range of proposed vegetation indices for their ability to determine the variables LAI and FPAR under the presence of several perturbing factors. As far as the LAI is concerned, the authors come to a similar conclusion as Asrar et al.; for the determination of FPAR, they state that all newly developed indices are almost always superior to the traditional NDVI. GEMI is found among the three most suitable indices, and it is also important to note that one of the other two requires additional information on soil reflectance (WDVI), and the other a second measurement at a prescribed view zenith angle (NLI2). The authors also find a considerable dependence of the indices on leaf angle

Table 5.1: Parameters, correlation coefficient and standard error of the linear regression of FPAR against GEMI, NDVI and SR in the form $y = a + bx$. Simulations are with vegetation model 'x0'. Only snow-free cases, with $n = 1951; 1883$ (1989; 1990) for 'max', and $n = 1762; 1762$ (1989; 1990) for 'cmp'.

| index | year | 'max' | | | | 'cmp' | | | |
|-------|------|--------|-------|-------|-------|--------|-------|-------|-------|
| | | a | b | r^2 | error | a | b | r^2 | error |
| GEMI | 1989 | -0.645 | 1.685 | 0.954 | 0.060 | -0.647 | 1.713 | 0.950 | 0.062 |
| | 1990 | -0.629 | 1.664 | 0.951 | 0.063 | -0.637 | 1.698 | 0.947 | 0.065 |
| NDVI | 1989 | -0.198 | 1.217 | 0.941 | 0.068 | -0.197 | 1.207 | 0.937 | 0.070 |
| | 1990 | -0.195 | 1.221 | 0.943 | 0.067 | -0.199 | 1.214 | 0.935 | 0.071 |
| SR | 1989 | 0.089 | 0.075 | 0.890 | 0.092 | 0.104 | 0.070 | 0.873 | 0.100 |
| | 1990 | 0.095 | 0.074 | 0.884 | 0.090 | 0.111 | 0.069 | 0.863 | 0.104 |

distribution (LAD) and leaf single-scattering albedo (ω).

The most important difference between the approach followed in this study and the ones cited is the large spatial scale and its application to the observation conditions of actual remote sensing data. Instead, those previous studies have used an arbitrary choice of viewing conditions. It is likely that the significance of variations in LAD and ω is greatly reduced for an average over a large area, because their regional averages vary much less. Therefore, a new simulation is presented here to investigate various relationships between FPAR and the indices GEMI, NDVI and SR and their robustness against changes in the choice of certain parameters. In this case, the variable FPAR is not calculated by the 2-flux scheme as in the vegetation model, but, as the indices, by the anisotropic, semi-discrete model NADIWAS (cf. Section 4.5).

In addition to GEMI, the indices NDVI and SR are chosen, because they have already been used in other studies to derive FPAR on a global scale, SR by Heimann et al. (1989) and Potter et al. (1993) and NDVI by Ruimy et al. (1994, 1996) and Knorr and Heimann (1995). Besides, Sellers (1985) and Sellers et al. (1992) have concluded, on the basis of some calculations with the 2-flux scheme, that there should be an almost linear relationship between FPAR and SR. This relationship has also been proposed for routine applications to determine FPAR on a global scale (Sellers et al. 1994).

Since computer time for calculating FPAR is again 10 times that for calculating the bidirectional reflectance factor, this variable is only computed for every 40th pixel during the remote sensing simulations (cf. Section 4.5). In this way, a random selection of observation conditions (viewing and solar angles, soil brightness, LAI, FC, LAD, ω , etc.) is achieved that represents the conditions of actual global measurements. The calculations follow the standard setup of NADIWAS (further ones see below) with angles and dates of the monthly maxima ('max') and the version 'x0' of the vegetation model. Cases with snow cover are excluded.

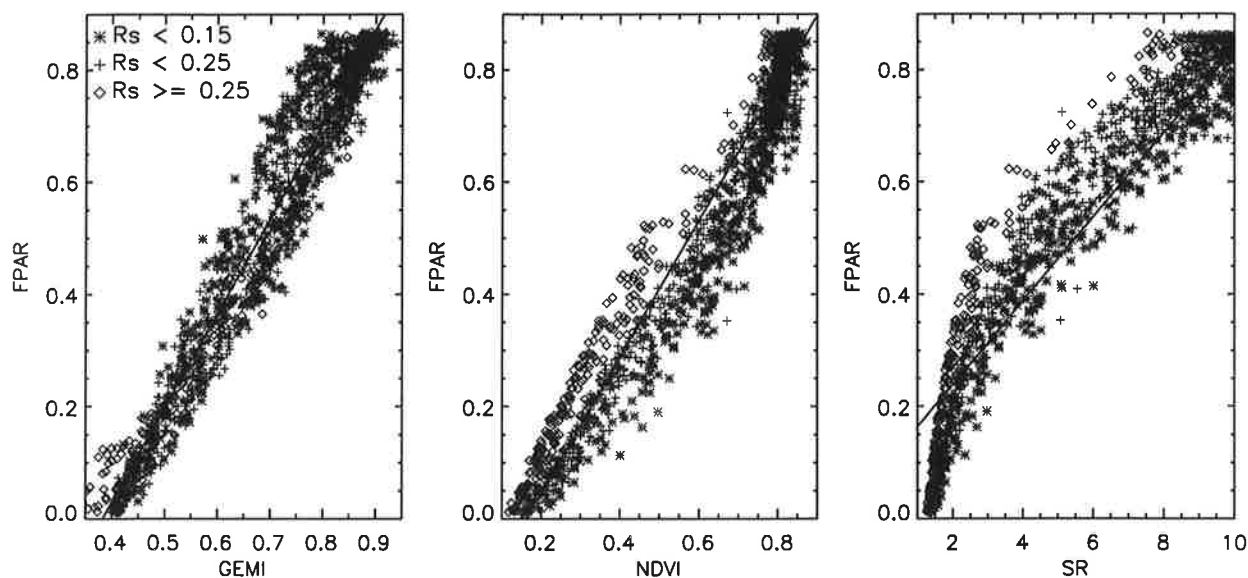


Figure 5.2: Relationship between FPAR and various vegetation indices calculated with NADIWAS, for three ranges of soil reflectance (R_s). The solid line stands for a linear regression of all data points.

The result is shown in Fig. 5.2, differentiated by soil brightness. It turns out that GEMI offers the best linear relationship with FPAR. Contrary to the other two indices and with the exception of very bright soils with low FPAR values, there are no systematic variations caused by the brightness of the soil background. By comparison, the NDVI shows a certain downward curvature for medium and dark soils, and SR a clearly non-linear relationship in all cases (cf. Fig. 4.3). As shown in Table 5.1, the correlation and the standard error for NDVI is almost as good as for GEMI. However, the variations in GEMI are caused more by angular than by soil background effects, a perturbation that can be minimised reasonably well by averaging over a large number of measurements. (The index has been designed to be sensitive towards angles as a usually well known variable, see Verstraete and Pinty 1996.) Consequently, the variations are particularly large at high values of FPAR, where the influence of the soil background is small. The results with the data set using monthly averaging and screening ('cmp') differ only little from those using the angular conditions of the monthly maxima ('max'). In this case, the angles of each mid month measurement are used for the simulation.

The assumption of a linear dependence between SR and FPAR, as proposed by Sellers et al. (1994) for global applications, is not supported by the results of these simulations. As a test for the applicability of this assumption for the conditions of global observations, the method used here seems more appropriate, because the original derivation from the 2-flux scheme by Sellers (1985) could not take account of the influence of the viewing geometry, and was confined to some special conditions.

The next two equations are therefore shown as a result and a recommendation for future applications for estimating FPAR from satellite data (mean of the simulations for 1989 and 1990 of the standard version with 'x0'). The first one is for monthly maximum composites:

$$\text{FPAR} = -0.637 + 1.674 \text{ GEMI} \quad (1a)$$

the second for screened monthly averages as first proposed by Meyer et al. (1995), and according to the present work:

$$\text{FPAR} = -0.642 + 1.704 \text{ GEMI} \quad (1b)$$

Values of FPAR less than 0 or great than 1 have to be set to 0 or 1, respectively. The difference between the two relationships comes from a tendency towards angles with a large GEMI for the monthly maxima, an effect that is not independent of atmospheric perturbations.

The robustness of the relationship in Equ. 1a for monthly maxima is tested by several variants of NADIWAS. The simulations have again been computed with version 'x0' of the vegetation model. One test takes account of some of the chlorophyll-dependent variation in leaf transmissivity for PAR, as mentioned in Section 4.5 ($\tau_L^{red} = 0.03$ according to Myneni et al. 1992), while two others concern aspects of length scale. The first one assumes a uniform LAD for all vegetation types, something that could be more representative for larger areas; in the second test, it is assumed that ground scenes with incomplete vegetation cover are never composed of $FC \approx 1$ with a low LAI, as it would be possible in the vegetation model, but that all scenes are a mixture of dense vegetation with varying degrees of FC (cf. Fig. 4.3). Therefore, the FC for the NADIWAS simulation is not imported directly from the vegetation model, but it is computed independently according to the following equation:

$$f_c = \begin{cases} f_{c,max} \Lambda / \Lambda_0 & \text{for } \Lambda < \Lambda_0 \\ f_{c,max} & \text{for } \Lambda \geq \Lambda_0 \end{cases} \quad (2)$$

(Instead of the maximum annual LAI, $\hat{\Lambda}$, the current value, Λ , is taken; $f_{c,max}$ and Λ_0 are from Table 3.1, Section 3.1.)

The results are shown in Table 5.2, either with FPAR and GEMI according to the corresponding test variant, or with FPAR according to the standard version, so that only changes in GEMI are documented. The systematic deviation of the value according to Equ. 1a from the simulated FPAR is only small, with a standard, unsystematic error of around 0.06. It is remarkable that the smallest error is found for a heterogeneous model of vegetation distribution (cf. Equ. 2). In fact, this is the type of distribution on which the development of GEMI has been based (Verstraete and Pinty 1996).

When choosing a leaf transmissivity reduced by 0.02 (Tab. 5.2), it turns out that the resulting increase in the simulated GEMI has an FPAR equivalent of only 0.005 (column 3, according to the linear relationship). This increase corresponds with a high degree of accuracy to the increase in the directly computed FPAR, so that the linear equation is still

Table 5.2: Test of the linear relationship between FPAR and GEMI for monthly maxima, FPAR(GEMI). On the one hand, FPAR is computed directly with NADIWAS (with angles from 1989), on the other hand, it is derived from the simulated GEMI through the linear relationship to be tested. The systematic deviation and the standard error, defined as the root mean squared deviation, are shown ($n = 1918$). In the last two columns, only GEMI is computed with the test variant of NADIWAS, while FPAR is taken from the standard case.

| test | FPAR(GEMI)-FPAR | error | FPAR(GEMI)-FPAR | error |
|--|-----------------|--------|-------------------------|--------|
| | | | FPAR from standard case | |
| standard | 0.0001 | 0.0592 | | |
| $\tau_L^{red} = 0.03$ | 0.0004 | 0.0597 | 0.0050 | 0.0609 |
| uniform LAD | -0.0119 | 0.0636 | -0.0161 | 0.0702 |
| heterogeneous vegetation distribution (see text) | 0.0023 | 0.0533 | | |

valid (column 1). This result shows that the choice of a uniform leaf transmissivity leads only to small errors in the computation of FPAR, through compensating effects during multiple-scattering processes.

As far as the sensitivity of the result to changes in the LAD is concerned, a relatively strong impact on GEMI is found (column 3), an effect that is compensated by only around a third through corresponding changes in FPAR (column 1). However, as the largest systematic effect, it creates an error of still little more than 0.01 in FPAR and thus lies well below other perturbation, such as atmospheric influences. The difference between a more even and a more heterogeneous vegetation distribution is largely compensated (only 0.002 for the systematic deviation), a result that supports the findings by Asrar et al. (1992).

Because variations in the GEMI-FPAR relationship are, as explained earlier, to a large extent caused by angular effects, the estimated (unsystematic) error of 0.06 to 0.07 can be reduced by averaging over a large number of angular conditions. This is not the case for NDVI and SR, since soil background colour leads to mostly systematic deviations. When averaging GEMI from the GVI data set (1/7 degree resolution) to 1 degree latitude by longitude, the error is thus reduced to about 0.01, provided there are no systematic preferences of certain angles. Since this might be the case for the GVI, the figure could be somewhat higher for this particular data set.

This error, however, is still small compared to signal contamination by unresolved clouds and other perturbations not captured by the atmospheric correction algorithm. A typical value for GEMI over dense vegetation is 0.72 for 'cmp' and 0.76 for 'max' (see Fig. 4.7). According to the calculations with NADIWAS, this corresponds to a FPAR of only 0.60. It also appears that the residual contamination increases with increasing FPAR, since for $FPAR \approx 0$, both simulations and satellite data assume a typical value of around 0.38. A pos-

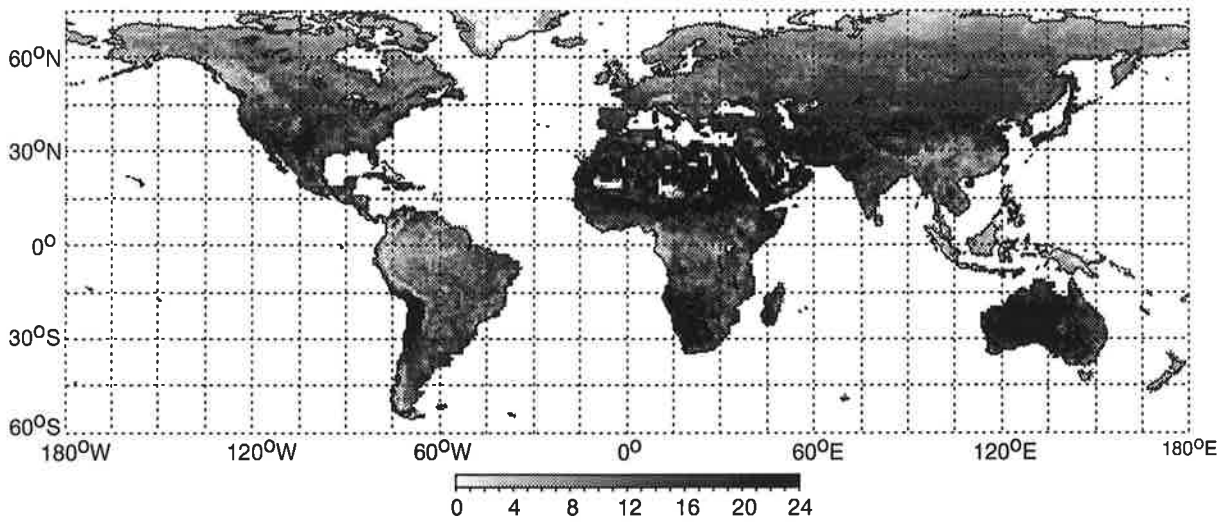


Figure 5.3: Number of valid monthly GEMI measurements ('cmp') of the years 1989 and 1990, after averaging over 1 degree latitude by longitude and removing data with $\text{GEMI}(\text{'max'})/\text{GEMI}(\text{'cmp'}) > 1.10$.

sible linear correction has been applied to the satellite data in Section 4.5 for monthly maxima. Its application to the FPAR-GEMI relationship, Equ. 1b, yields, with $\text{FPAR}(0.38) = 0$ and $\text{FPAR}(0.72) = 1$:

$$\text{FPAR} = -1.12 + 2.94\text{GEMI} \quad (3a)$$

Since the perturbations are particularly small over areas with little or medium vegetation cover (arctic and arid regions), it seems appropriate to introduce an additional constraint, which requires that the slope of the theoretically derived FPAR-GEMI relationship is preserved at $\text{GEMI} = 0.38$, i.e. $d\text{FPAR}/d\text{GEMI}(0.38) = 1.704$. This leads to the following quadratic expression:

$$\text{FPAR} = -0.122 - 1.061\text{GEMI} + 3.639\text{GEMI}^2 \quad (3b)$$

The difference in FPAR between the two relationships is around 0.1 for medium vegetation cover, and 0 for a FPAR of 0 or 1.

5.3 The strategy of model constraint

Despite the serious limitations discussed above, a fit of the vegetation model to match the satellite data will be tried next. To do so, it is necessary to remove data with a particularly high degree of contamination. Therefore, the GEMI data of 1989 and 1990 are averaged to 1 degree latitude by longitude after which those entries are removed, where the ratio 'max'/'cmp' is greater than 1.10. Such values are reached especially over tropical rainforests (cf. Section 4.4). The total number of monthly data remaining after this and the previous

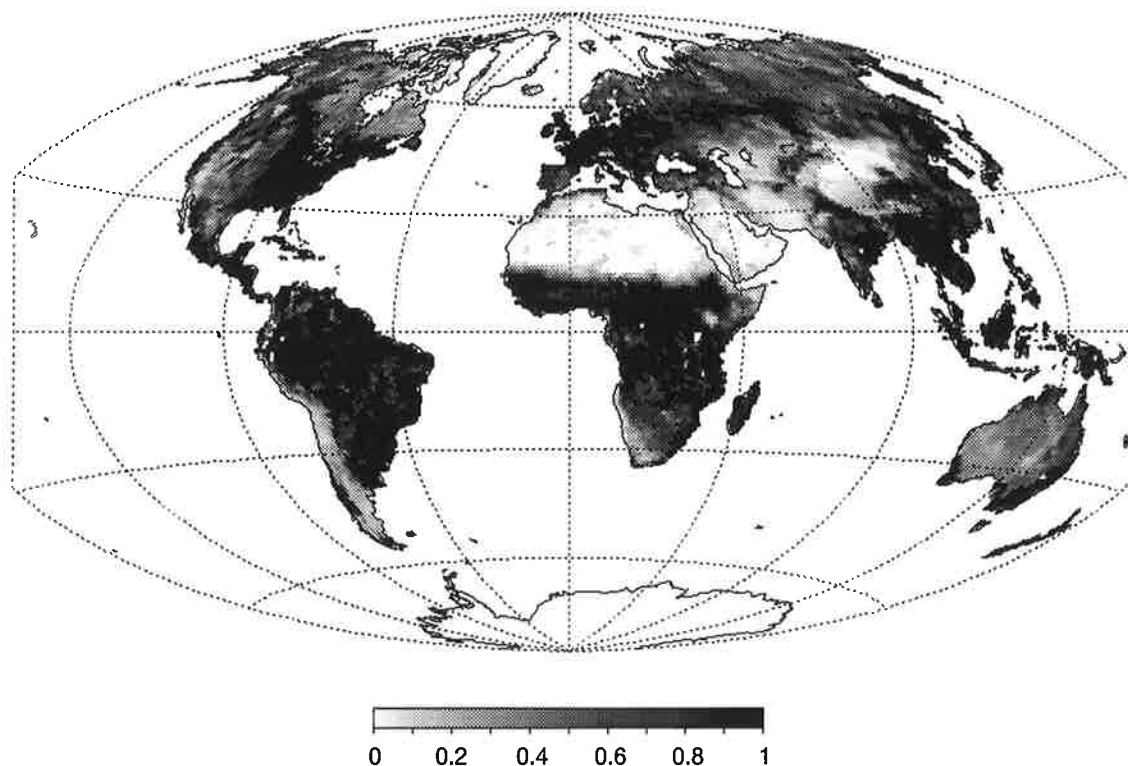


Figure 5.4: The fractional cover, f'_c , assumed for the diagnostic simulation with $\hat{\Lambda} = 5$ (equal-area projection). Some white pixels stand for areas with no valid data.

screening process in Section 4.2 is shown in Fig. 5.3. From those data, averages of the months January to December are formed, and then gaps of only one month are filled by linear interpolation. This increases the number of valid data points on the 1-degree equal-area grid from 89,780 or 67.6% to 99,389 or 74.8%. This reprocessed data set is eventually used to compute FPAR according to the scheme in Fig. 5.1.

The task is now to constrain the range of model versions from Chapter 3, all of which conform to our knowledge of vegetation physiology and are in agreement with input data as known *a priori*. The constrained version is then required to agree also with the satellite data within their degree of accuracy. In a highly complex model as the one developed here, there are a great number of parameters that could in principle be adapted. However, all those possibilities cannot be explored with reasonable computational effort. For this reason, it appears to be an acceptable solution to modify parameters that are directly linked to FPAR, such as the LAI or the phenological temperature T_ϕ . In general, it has to be made sure that the consistency of the modelling principle is not violated, e.g. when assuming a LAI greater than the maximum allowed by the water balance; a “sensible” compromise

between simplicity of the parameter adjustment, and the adherence to the original model concept is therefore required.

The following strategy has turned out to be an adequate compromise of this sort:

- (1) The revised fractional cover, f'_c , is computed from the maximum of the monthly measured FPAR values, f_{PAR}^{max} , according to

$$\begin{aligned} f_{c,0} &= \frac{f_{PAR}^{max}}{1 - e^{-0.5\hat{\Lambda}_{c,max}}} \\ f'_c &= \min \{f_{c,0}; f_{c,max}\} \end{aligned} \quad (4)$$

with $\hat{\Lambda}_{c,max} = \hat{\Lambda}/f_{c,max}$ (see Fig. 5.4). This equation replaces Equ. 137 of Section 2.8, if f_{PAR}^{max} exists. The temperature limit of LAI, Λ'_T , is then adapted to the new fractional cover by

$$\Lambda'_T = \Lambda_T \frac{f'_c}{f_{c,max}} \quad (5)$$

(cf. Equ. 134, Section 2.8).

- (2) To assure that in arctic regions, the remote sensing derived fractional is actually reached, T_ϕ is modified to T'_ϕ according to

$$f_c \hat{\Lambda}_{c,max} = \hat{\Lambda} \left[1 - \left(\frac{\hat{T}_\phi - T_{0.5max}}{\hat{T}_\phi - T'_\phi} \right)^2 \right] \quad (6)$$

where T'_ϕ is constrained to the range from 0°C to \hat{T}_ϕ . $T_{0.5max}$ is the annual maximum of the 0.5 m soil temperature (Equ. 85, Section 2.5).

- (3) In certain cases, the temperature limited LAI, Λ_T , is replaced by a diagnostic LAI limit, Λ_D . To do so, the evergreen portion assumed in the model, i.e.

$$f_{PAR,e} = e_v f_c \left(1 - e^{-0.5\hat{\Lambda}_{c,max}} \right) \quad (7)$$

is first subtracted from the measured FPAR. e_v is the evergreen vegetation fraction as derived from the vegetation map used. If the remainder is less or equal to zero, $\Lambda_D = 0$ is assumed, otherwise Λ_D is set according to the condition

$$(1 - e_v) f_c \left[1 - \exp \left(-0.5 \frac{\Lambda_D}{(1 - e_v) f_c} \right) \right] = f_{PAR} - f_{PAR,e} \quad (8)$$

This modification is only done for grasses and dry-seasonal vegetation, and only if there are valid FPAR measurements and the monthly mean temperature is greater than 5°C, in order to avoid snow influence.

- (4) To adapt the water balance to the satellite data, the rooting depth, d_r , is increased in steps of 2 m until the maximum monthly LAI, Λ_{max} starts to fill up the fractional cover, f'_c . This is expressed by the condition

$$\Lambda_{max}/f'_c \geq 0.8\hat{\Lambda}_{c,max} \quad (9)$$

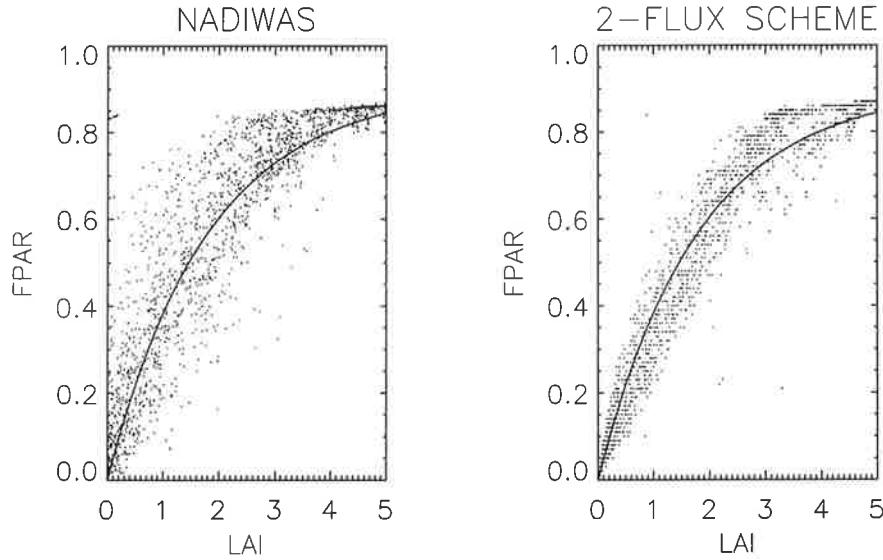


Figure 5.5: Relationship between FPAR and LAI calculated with NADIWAS (left) and with the 2-flux scheme of the vegetation model (right) for 100% direct insolation and at the time of satellite observation ($n = 1952$). The solid line denotes a simple exponential relationship (see text).

There is a limit of 10 m for tropical and evergreen-temperate trees, of 0.5 m for field crops and tundra vegetation, and of 4 m for other types. d_r is set uniformly to 0.5 m at programme start and to 2 m in savannas. During the calculation of the soil water holding capacity, $W_{s,max}$, the depth of the lowest horizon is extended to d_r after the first model run.

Further use of the remote sensing data, e.g. for determining the evergreen fraction, e_v , has not been successful. One reason is that many data are missing or are unreliable, especially in spring and autumn or during the rainy season, another that the standard vegetation map by Wilson and Henderson-Sellers is already quite accurate. The strategy chosen rests on the assumption that the best measure for the fractional cover, f_c , is the annual maximum of the monthly GEMI values. Within this fractional area, densely covered by vegetation for at least one month within a year, a closed vegetation cover at the maximum annual LAI is assumed, with a local LAI of $\hat{\Lambda}_{c,max} = \hat{\Lambda}/f_{c,max}$ as in the prognostic case. Conversion from LAI to FPAR is done with a simple exponential approximation as plotted in Fig. 5.5. This fixed LAI-FPAR relationship assumed here is meant only as an approximation within the accuracy of the FPAR measurements. A possible error of ± 1 LAI is taken into account by the sensitivity test 'L+/-', and to some degree by 'T+/-' (cf. next section).

There is another result at the side that follows from the same figure: By comparison with the more realistic semi-discrete radiative transfer model, the 2-flux scheme underestimates FPAR by around 5 to 10% in the range of low LAI. Considering this, the simple exponential

relationship appears to be sufficient for most applications, at least when all of the incoming radiation is direct. The use of the 2-flux scheme, however, can still be justified on the grounds that photosynthesis depends to a large portion on diffuse light under cloud cover.

This result is of relatively small importance for the quality of the model fit to FPAR, because the LAI is simply increased somewhat more to balance the 2-flux scheme's slight underestimate.

5.4 Results

The strategy used to find an answer to the question, whether optical satellite data contain useful information for global vegetation modelling now consists of comparing the results of the prognostic and diagnostic simulations. The diagnostic model versions correspond in all remaining parameter settings to the definitions of Table 3.2 and are denoted by a preceding letter 'd'. One difference to the prognostic versions listed there is that the diurnal calculations are repeated only every 10 days. These are, however, not taken as prognostic counterparts, because they suffer from the already discussed deficit of insufficient water storage in tropical rainforests. Instead, the versions of Chapter 4 are chosen, denoted by a preceding 'x', with rooting depth of tropical-evergreen trees adapted to the prevailing precipitation conditions (cf. Table 4.2). It is important to note that the information needed is derived solely from vegetation maps, and not from satellite data.

Whether the model adjustment has had an effect on the agreement with the satellite data can be checked from Fig. 5.6. It shows that the squared difference of FPAR as calculated in the vegetation model and from the satellite-based measurements, summed over the months with valid data (cf. Fig. 5.3) and divided by their number. From a value of 0.1 on, simulations and measurements can be considered to be in clear disagreement. After fitting to the satellite data, this case occurs only for parts of the arctic and the North American prairies, for large irrigated areas (India in particular) and for the arid regions of Australia and the Brazilian Northeast. For the northern areas, the reason probably lies in the 5°C criterion when determining Λ_D , in the case of irrigation it is inappropriate representation in the models, and for arid environments, deficiencies of either the precipitation data or of the soil hydrology scheme. In central Australia, the evergreen fraction of vegetation is also overestimated. In total, however, the agreement has been improved considerably.

An improved agreement with satellite data does not imply, that the agreement with field measurements of net primary productivity (NPP) is improved. This is demonstrated by Fig. 5.7, which also shows the simulated values of the first prognostic version of Chapter 3, as in Fig. 3.18. The differences between the two simulations are much smaller than the difference to the measurements. The only exception is given by the tropical rainforest sites, for which the correction of rooting depth has clearly increased the agreement. Although there is a slight reduction in the difference to measurements for C3 grasses and savannas, the large overestimate for savannas and C4 grasses is maintained. This indicates that the

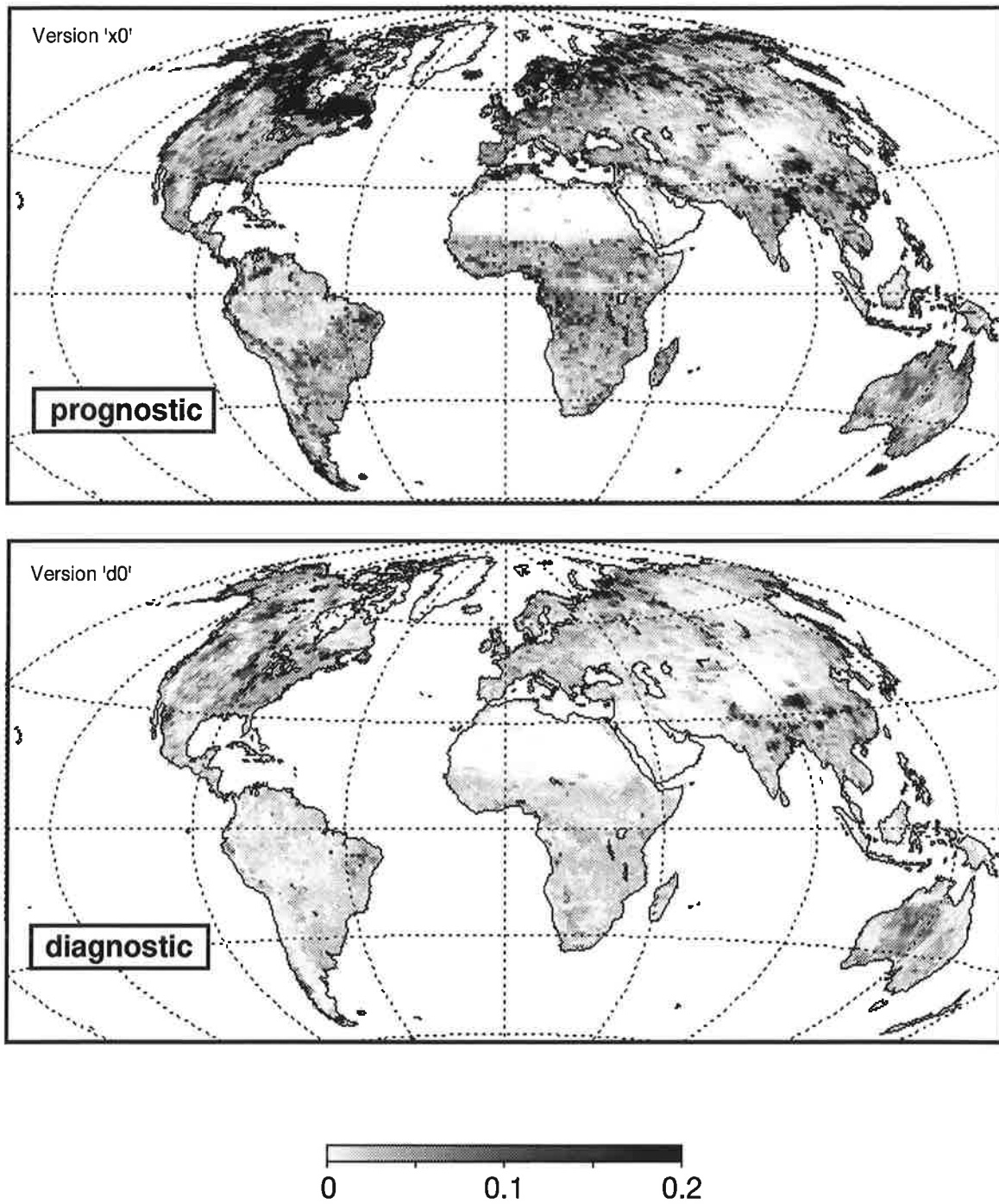


Figure 5.6: Mean squared deviation of simulated from remote sensing derived FPAR without (“prognostic”) and with (“diagnostic”) adaptation to the satellite data.

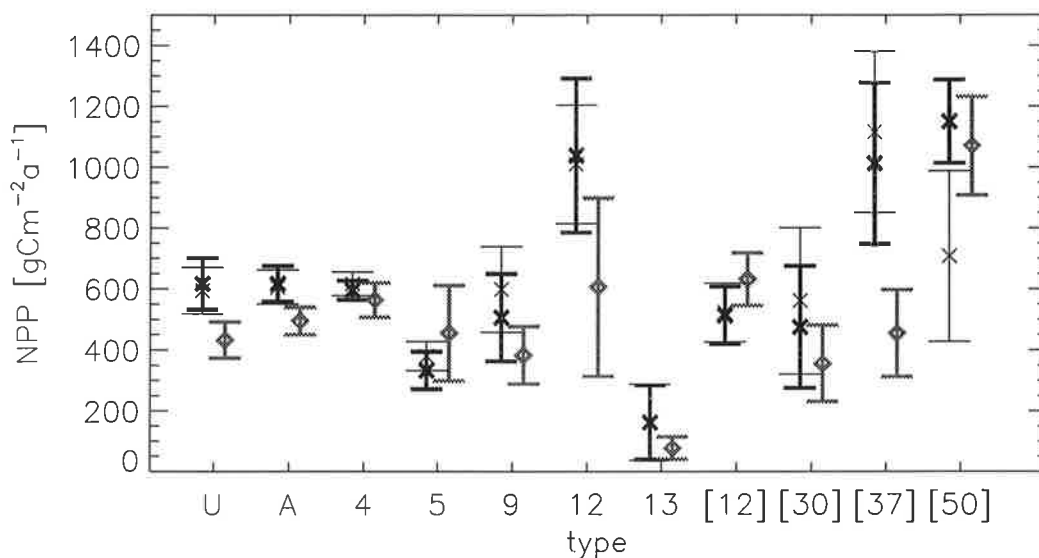


Figure 5.7: Means and 90% confidence ranges of simulated NPP with the diagnostic version ‘d0’ (black, bold) and the prognostic version ‘0’ (thin) compared to field measurements (grey). ‘U’ unknown type, $n = 78$; ‘A’ all cases with known type, $n = 178$; ‘4’: broadleaf deciduous trees, $n = 30$; ‘5’: conifers, $n = 17$; ‘9’: C3 grass, $n = 18$; ‘13’: tundra, $n = 10$; [12] mixed forest, $n = 12$; [30] C3/C4 grasses, $n = 11$; [37] savanna, $n = 19$; [50] tropical rainforest, $n = 12$.

differences between simulations and field studies are not a result of errors in the vegetation cover within the model, but probably come from fundamental uncertainties, both of field measurements and of simulations.

Relatively small differences between prognostic and diagnostic simulations are also displayed by Table 5.3, at least when using the Farquhar model of photosynthesis. Most remarkably, the global total has hardly changed. There is a significant productivity increase only for tropical-deciduous trees (type 2) and a clear decrease for conifers (type 5) after including the satellite data. For grasses, there is a much less pronounced decrease of ca. 12% (9-12).

With the Ruimy-Monteith photosynthesis scheme, there is a decrease in NPP in all cases, so that global NPP for version ‘Pm’ is significantly less than for ‘0’ after adjustment, with an opposite difference as before. It is remarkable that the absolute difference has remained at about 6 GtC a^{-1} . There are significant changes especially for deciduous trees and shrubs in dry-seasonal climates (types 2 and 8). While for the Monteith scheme, an increase in the absorbed PAR at a higher LAI always leads to an increase in NPP, the same can have the opposite effect in the case of the Farquhar model because of higher plant respiration rates. Recalling the high degree of uncertainty concerning respiration costs, it is difficult to judge

Table 5.3: Prognostic and diagnostic NPP calculated with the photosynthesis model by Farquhar (versions 'x0/d0') and according to the Monteith model (versions 'xPm/dPm'), sorted by vegetation type. Areal totals are in GtC a⁻¹ and means in gC m⁻²a⁻¹.

| type | Version '0' | | | | Version 'Pm' | | | |
|-------|-------------|------|------------|------|--------------|------|------------|------|
| | prognostic | | diagnostic | | prognostic | | diagnostic | |
| | total | mean | total | mean | total | Mean | total | mean |
| 1 | 15.54 | 1153 | 15.43 | 1146 | 10.68 | 793 | 10.05 | 746 |
| 2 | 6.96 | 958 | 9.39 | 1291 | 8.00 | 1101 | 6.10 | 839 |
| 3 | 0.27 | 616 | 0.22 | 498 | 0.24 | 543 | 0.15 | 337 |
| 4 | 2.14 | 553 | 2.07 | 534 | 2.23 | 578 | 1.97 | 510 |
| 5 | 3.18 | 342 | 2.72 | 292 | 6.28 | 675 | 4.01 | 432 |
| 6 | 0.70 | 349 | 0.74 | 367 | 0.68 | 338 | 0.60 | 301 |
| 7 | 0.20 | 9 | 0.25 | 11 | 0.23 | 10 | 0.29 | 13 |
| 8 | 0.79 | 229 | 0.99 | 288 | 1.03 | 300 | 0.91 | 263 |
| 9 | 9.45 | 553 | 8.25 | 483 | 7.31 | 428 | 6.18 | 362 |
| 10 | 4.85 | 858 | 4.66 | 826 | 5.02 | 889 | 4.14 | 733 |
| 11 | 5.85 | 769 | 5.05 | 663 | 5.40 | 709 | 4.30 | 565 |
| 12 | 17.38 | 898 | 15.05 | 778 | 16.48 | 851 | 13.10 | 677 |
| 13 | 1.87 | 189 | 0.93 | 94 | 0.92 | 93 | 0.51 | 51 |
| 14 | 0.71 | 541 | 0.50 | 384 | 0.82 | 624 | 0.59 | 447 |
| 15-23 | 6.24 | 551 | 7.36 | 651 | 16.38 | 1448 | 14.21 | 1255 |
| 1-23 | 76.13 | 565 | 73.61 | 546 | 81.70 | 606 | 67.11 | 498 |

which of the two is closer to the actual situation

However, a general decrease in FPAR for both model versions after using the satellite data is in agreement with the idea that the prognostic vegetation amount is a potential one, computed under the conditions of temperature and water limitations, only. This will naturally tend to be less than the actual value. The use of satellite data thus amounts to a method that is able to take effects into account that cannot easily be modelled. For example, grazing pressure, either natural or caused by human use, will play a significant role for most grasslands and savannas, and there are certain growth limitations in boreal forests that are not considered in the model. Thus, for slowly growing vegetation, the vegetation cover depends to a major degree on stand age, the regional average of which is determined primarily by the frequency of forest fires and other disturbances (Kurz and Apps 1994).

The spatial distribution of the diagnostic NPP of version 'd0' and its difference to the prognostic version, 'x0', is shown by Fig. 5.8. Compared to Fig. 3.4 in Chapter 3, the spatial variability, generated to a major degree by the stochastic rainfall simulation, has been reduced significantly by the adjustment to the satellite data. This is true in particular for the savannas and shrublands of Africa and Australia. As a result, there is a pronounced

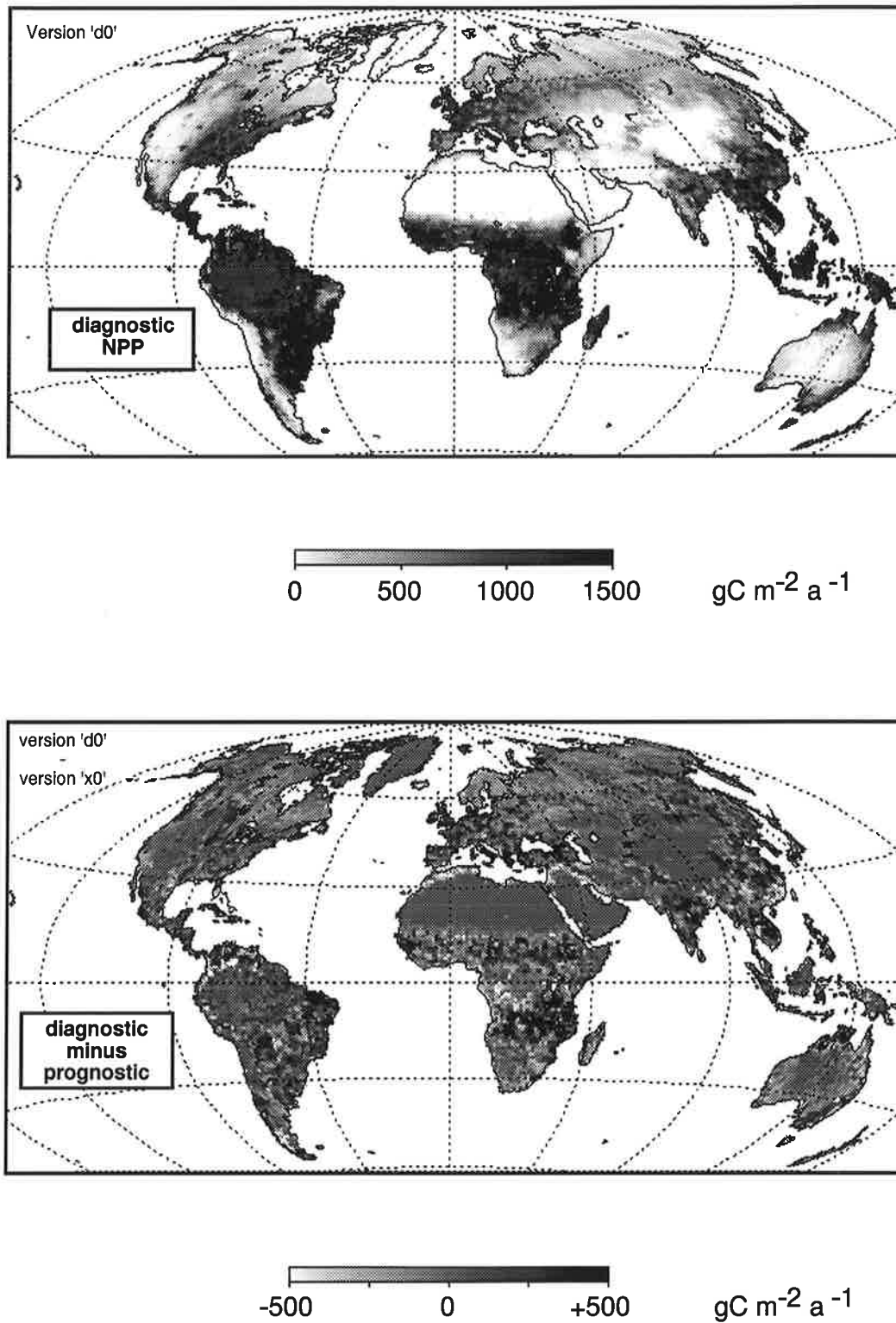


Figure 5.8: Diagnostically computed annual NPP according to version 'd0' of the vegetation model BETHY and the difference to the corresponding prognostic version 'x0'.

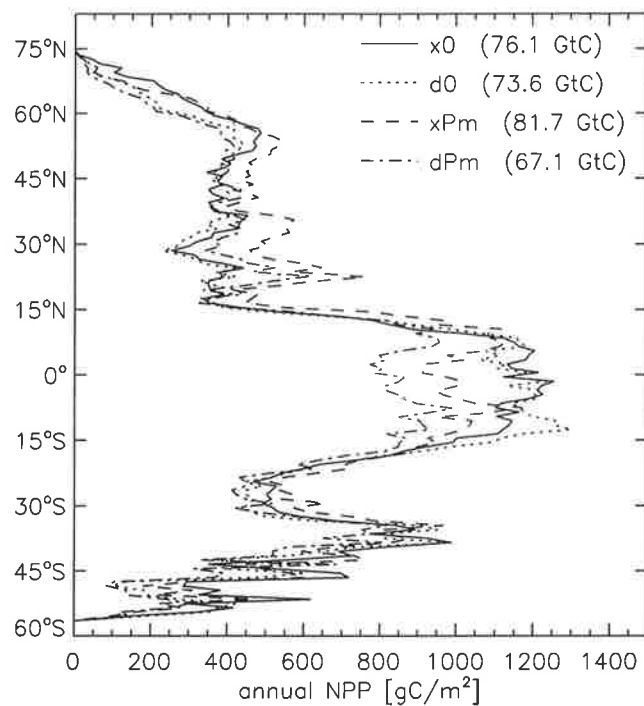


Figure 5.9: Latitudinal average of the NPP of the prognostic ('x') and diagnostic ('d') model versions with photosynthesis according to Farquhar ('0') and Monteith ('Pm').

spatial "noise" in the difference between the two simulations. Nevertheless, in areas of medium productivity, there is often a clear change in one or the other direction, while the difference is small for deserts and for areas of constantly closed vegetation. Here, the satellite data cannot deliver much additional information.

The most important changes are found for the water limited tropics, in particular southern Africa, the savannas of Brazil, the Sahel and India. Here, increased rooting depth results in a strong productivity rise. For northern latitudes, there is a less significant increase in Western Europe and a decrease in Canada, North and Southeast Europe and Siberia. An interesting detail is also a pronounced productivity decrease for the heavily populated areas of North Africa and the Middle East. Here, fertility is much reduced by soil erosion and land use, so that the productivity is far below its potential.

Fig. 5.9 shows the latitudinal average of the NPP of the four model versions occurring in Table 5.3. North of approximately 50°N, both diagnostic versions agree well and differ clearly from the two versions without reference to satellite data. By comparison, for the tropics and subtropics, the differences are more pronounced between the two photosynthesis models.

This already indicates that the additional constraint delivered by the remote sensing data has only a relatively small effect for the modelling of CO₂ fluxes compared to the

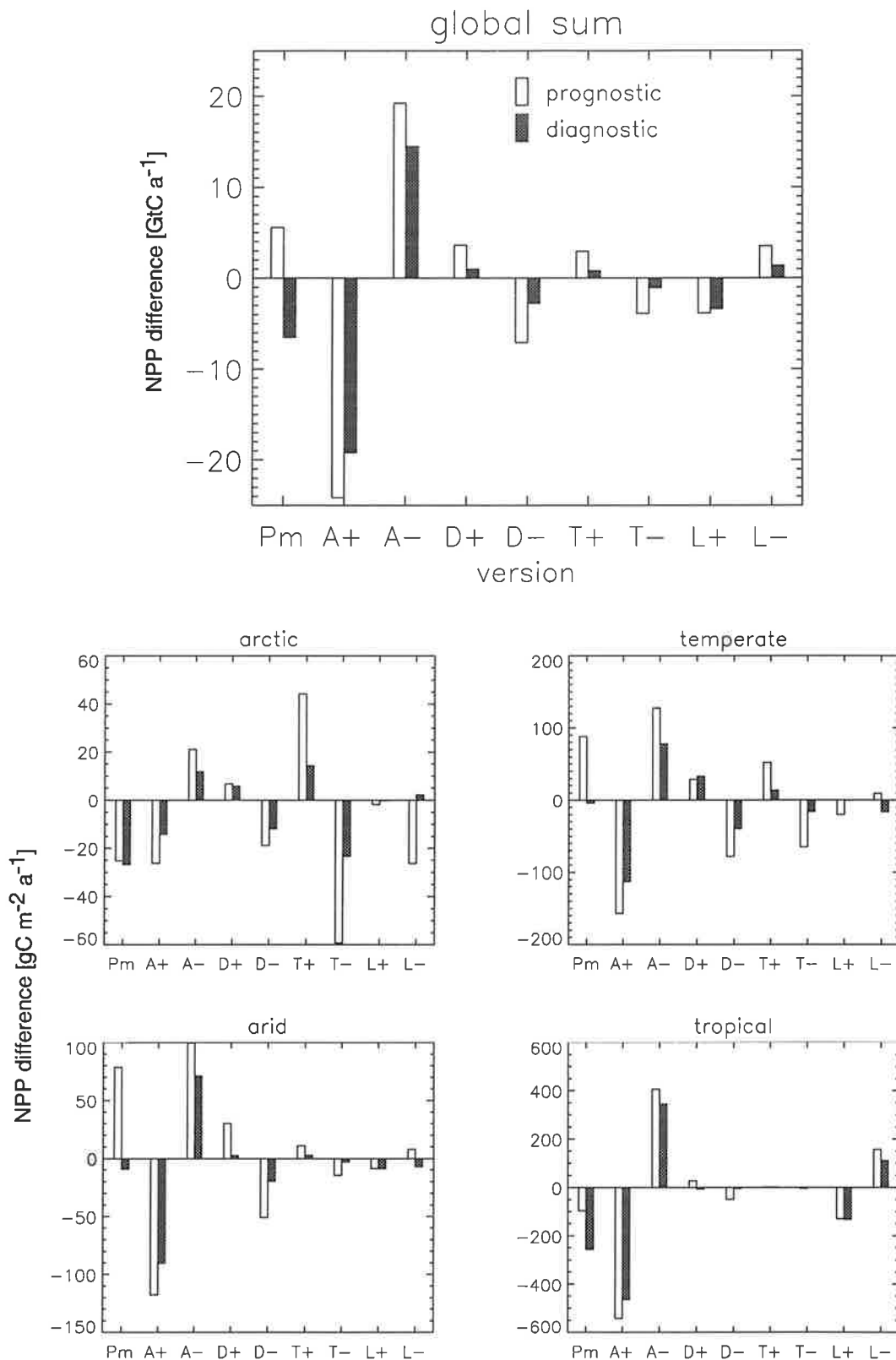


Figure 5.10: Sensitivity of the prognostic and diagnostic model versions against various uncertainties in model parameters. Climate zones and sensitivity tests are defined in Section 3.1.

uncertainties discussed in Section 3.3. A new set of sensitivity tests of the vegetation model against the most important uncertainties found there is shown in Fig. 5.10. The same definitions of Table 3.2 apply, with the only difference that the two groups of model versions are now 'x' and 'd' (see above). As far as the rooting depth is concerned, it has to be taken into account that for 'd', this parameter is set to only half of the value of the 'x' versions before the adjustment to satellite data starts. For that reason, the variation in NPP is in some cases (arctic and temperate, 'D+') higher in the diagnostic than in the prognostic version. Note that the upper bounds of rooting depth have not been altered.

As expected, the variation coming from the temperature controlled phenology ('T+/-') and the rooting depth ('D+/-') is reduced most by remote sensing, as far as the global integrals are concerned. It is remarkable, though, that those data are also capable of reducing the largest source of uncertainty, i.e. that coming from the parametrisation of respiration costs, even if the reduction is still relatively small, ranging from 1/10 to 1/3 of that in the prognostic case when going from cold to warm climates. As a result, the same uncertainties also dominate the diagnostic calculations.

This is true for all climate zones of Fig. 5.10, with the exception of the arctic, where the phenology (sensitivity tests 'T' and 'L') contributes most to uncertainties; this particular source can be reduced well by remote sensing data. Naturally, the satellite data can also refine the phenology well in the temperate zone, but here the respiration costs already dominate. For arid regions, it is evidently the rooting depth where the largest gains are made in terms of reducing uncertainty in NPP calculations, whereas for the wet tropics, this parameter turns out to have only minor importance. This last result demonstrates that for the 'x' versions, plant available soil water is already modelled rather well, with the remaining uncertainties almost entirely removed.

5.5 Error analysis

It appears to be an appropriate method to summarise the sensitivity tests of BETHY described in the previous section and in Section 3.3 by an error calculation for each grid point. To do so, the mean and the sum of the squared deviation from the mean are calculated with version '0' plus the nine versions shown in Fig. 5.10, with pairs of opposite sensitivity tests weighted by only 0.5. The estimated error is then the square root of this number. It is important to note, however, that this is only a first attempt at a consistent error analysis during global vegetation modelling, in which some minor factors from Section 3.3 are left out, such as climate, net radiation and day-to-day variability.

While excluding those factors might lead to an underestimate, the assumption that different sources of error add up made in the above calculation might result in an overestimate of the overall error. For example, the assumption means that by a combination of 'xA+', 'xD-' and 'xT-' according to Fig. 5.10, the global sum of NPP would be reduced by 35 GtC a⁻¹. A test run of the model where all three sets of parameters have been modi-

Table 5.4: Mean and estimated error of the annual NPP in GtC a⁻¹ for different climate zones and globally.

| zone | prognostic | diagnostic |
|-----------|---------------|---------------|
| arctic | 3.40 ± 3.00 | 2.22 ± 1.21 |
| temperate | 17.93 ± 10.93 | 16.67 ± 7.61 |
| arid | 30.17 ± 21.06 | 29.20 ± 14.74 |
| tropical | 24.75 ± 14.71 | 23.70 ± 13.33 |
| Global | 76.25 ± 49.70 | 71.80 ± 36.89 |

fied simultaneously produces an actual change of 32 GtC a⁻¹, which shows that the error behaves almost linearly with respect to those parameter changes. A more accurate Monte Carlo method (Binder 1986) for exploring the complete range of likely model configurations by random selection of parameters seems not appropriate for the present analysis. On the one hand, the method is computationally expensive, since it requires at least 100 model runs for 10% accuracy, on the other hand, the definition of uncertainties in the parameters is still rather arbitrary so that the gain in accuracy would not be justified by the additional effort. The simple method followed here has also the advantage that it is more transparent, a fact that seems more important than accuracy considering that this is the first systematic study of the kind (see Chapter 1).

The calculated error range of regional and global annual NPP is shown in Table 5.4. This range is large in all cases, larger in fact than the range of values by other authors cited in Section 3.1. In particular, with more than 100 GtC, the upper bound lies well above most previously cited values. However, at the 1995 NPP intercomparison workshop in Potsdam (Kicklighter et al. 1997), results were presented that still lay between 39.9 and 80.5 GtC. This range is a little more than half of what is found here for the diagnostic case.

A spatially resolved picture is offered by Fig. 5.11. Here, the total range from the lower to the upper bound is displayed, which in some cases, as in Table 5.5 below, is larger than the mean. As it has been found already, the reduction in the error is largest for the temperature limited areas of the north and for some water limited regions, in particular Brazil (North-East and South), southern Africa and Australia. By comparison, the effect is small for the evergreen tropical rainforest, which is easy to understand, since it is already known without satellite data that those areas are evergreen. The reduction of the error in Table 5.4 can largely be explained by the fact that part of the vegetation in the defined wet-tropical zone consists of drought-deciduous species. Eventually, the error reduction for some areas is low for other reasons: here, as Fig. 5.6 demonstrates, the adjustment to satellite data is only partially successful. The areas in question, in the US Mid West, the Ganges valley in India and the densely populated part of China, are likely to contain much irrigated agriculture.

As a last way of presenting the results, Table 5.5 shows, similar to Table 3.4 in Chapter

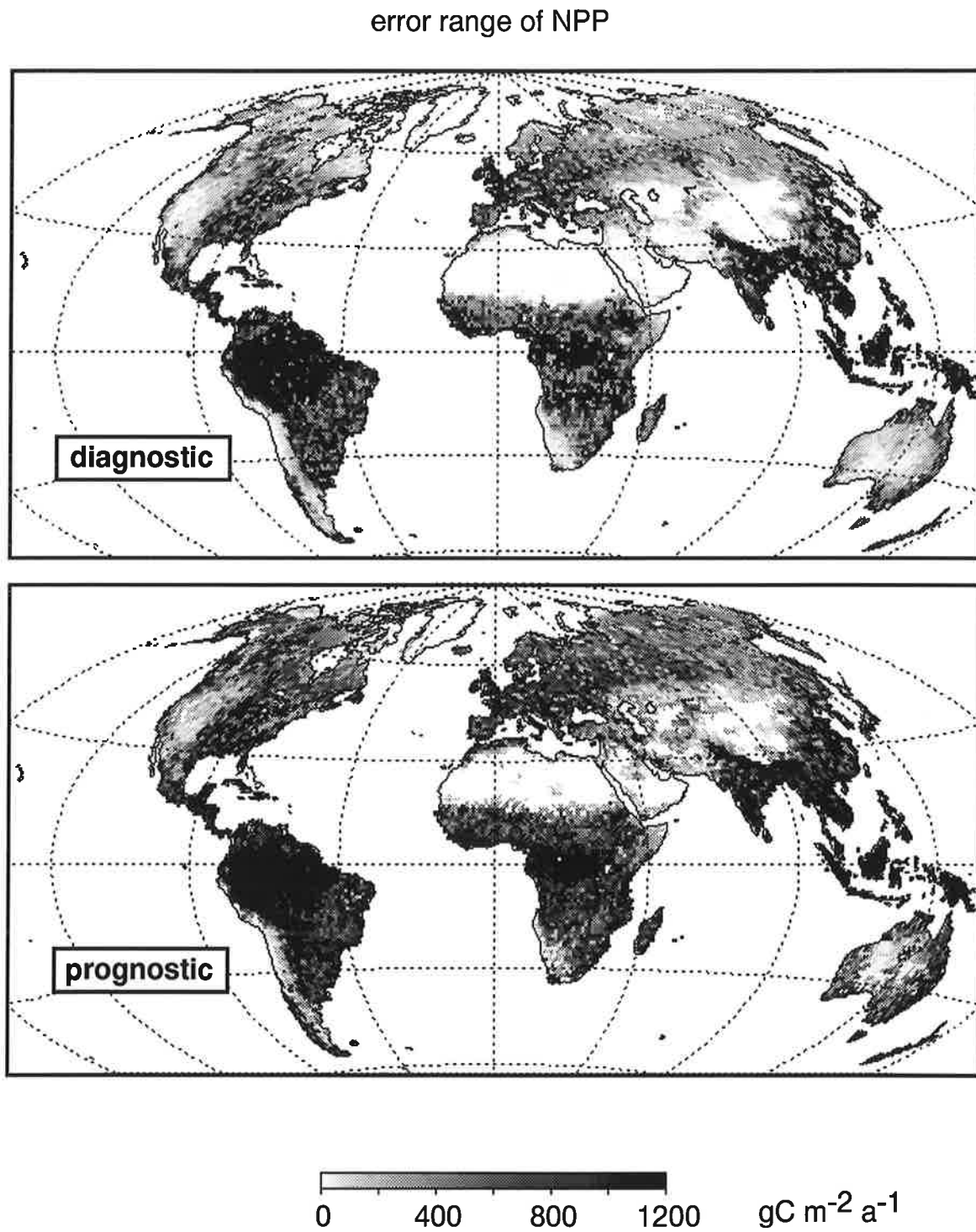


Figure 5.11: Estimated error of the NPP of the prognostic and diagnostic model versions.

Table 5.5: Mean and estimated error of the annual NPP by vegetation type, as totals in GtC a⁻¹ and as spatial means in gC m⁻² a⁻¹.

| type | prognostic | | diagnostic | |
|-------|--------------|------------|--------------|------------|
| | total NPP | mean NPP | total NPP | mean NPP |
| 1 | 14.63 ± 9.48 | 1085 ± 703 | 14.33 ± 9.11 | 1064 ± 676 |
| 2 | 7.17 ± 4.19 | 986 ± 576 | 8.76 ± 4.63 | 1205 ± 636 |
| 3 | 0.26 ± 0.25 | 586 ± 562 | 0.21 ± 0.16 | 477 ± 350 |
| 4 | 2.18 ± 0.98 | 563 ± 252 | 2.06 ± 0.71 | 533 ± 183 |
| 5 | 3.75 ± 3.19 | 403 ± 343 | 2.92 ± 1.90 | 314 ± 204 |
| 6 | 0.68 ± 0.37 | 339 ± 184 | 0.71 ± 0.25 | 353 ± 123 |
| 7 | 0.40 ± 1.32 | 17 ± 58 | 0.26 ± 0.37 | 11 ± 16 |
| 8 | 0.90 ± 1.11 | 260 ± 321 | 0.98 ± 0.73 | 285 ± 212 |
| 9 | 8.76 ± 4.59 | 512 ± 268 | 7.84 ± 2.97 | 458 ± 173 |
| 10 | 4.82 ± 2.03 | 854 ± 358 | 4.48 ± 1.49 | 792 ± 264 |
| 11 | 5.61 ± 2.51 | 736 ± 329 | 4.87 ± 1.49 | 639 ± 195 |
| 12 | 16.74 ± 7.00 | 864 ± 361 | 14.54 ± 4.17 | 751 ± 215 |
| 13 | 1.59 ± 1.42 | 161 ± 143 | 0.84 ± 0.57 | 84 ± 57 |
| 14 | 0.72 ± 0.31 | 547 ± 235 | 0.51 ± 0.17 | 391 ± 127 |
| 15-23 | 8.05 ± 10.95 | 711 ± 967 | 8.48 ± 8.17 | 749 ± 722 |

3, mean and error range of the annual NPP sorted by vegetation type. The first thing to be noted here is that the error is again large, and that in some cases the lower bound is negative. The reason for this again lies in the non-linearity of the effect of the underlying uncertainties, i.e. in the fact that different errors do not exactly add up. In some cases, where the number of pixels for the specific vegetation type is small, there is an additional noise from the stochastic simulation of precipitation, which should normally not be added to the error calculations (especially type 3). However, this effect should be small in most cases.

As it has already been found when considering Fig. 5.11, the satellites do not deliver any additional constraint for the NPP calculation of evergreen tropical trees (type 1). The additional constraint is also small for deciduous trees of the tropics (2). The largest effect is found for evergreen conifers (5), C3 grasses of the temperate latitudes (9), and C4 grasses of the tropics (12). By comparison, the added constraint for deciduous conifers (6) is only small because of the difficulties in defining the growing season length from satellite data. A remarkable effect is found for evergreen shrubs (7): despite their very low productivity per area, the additional constraint amounts to as much as 1 GtC globally. For those, and for the tropical grasses (12), the satellite data deliver the largest gain, as for arid regions in general (see above). The fact that this gain is also large for the tundra (13) – again a total of ca. 1 GtC – comes from the difficulties the model has in its prognostic variant to

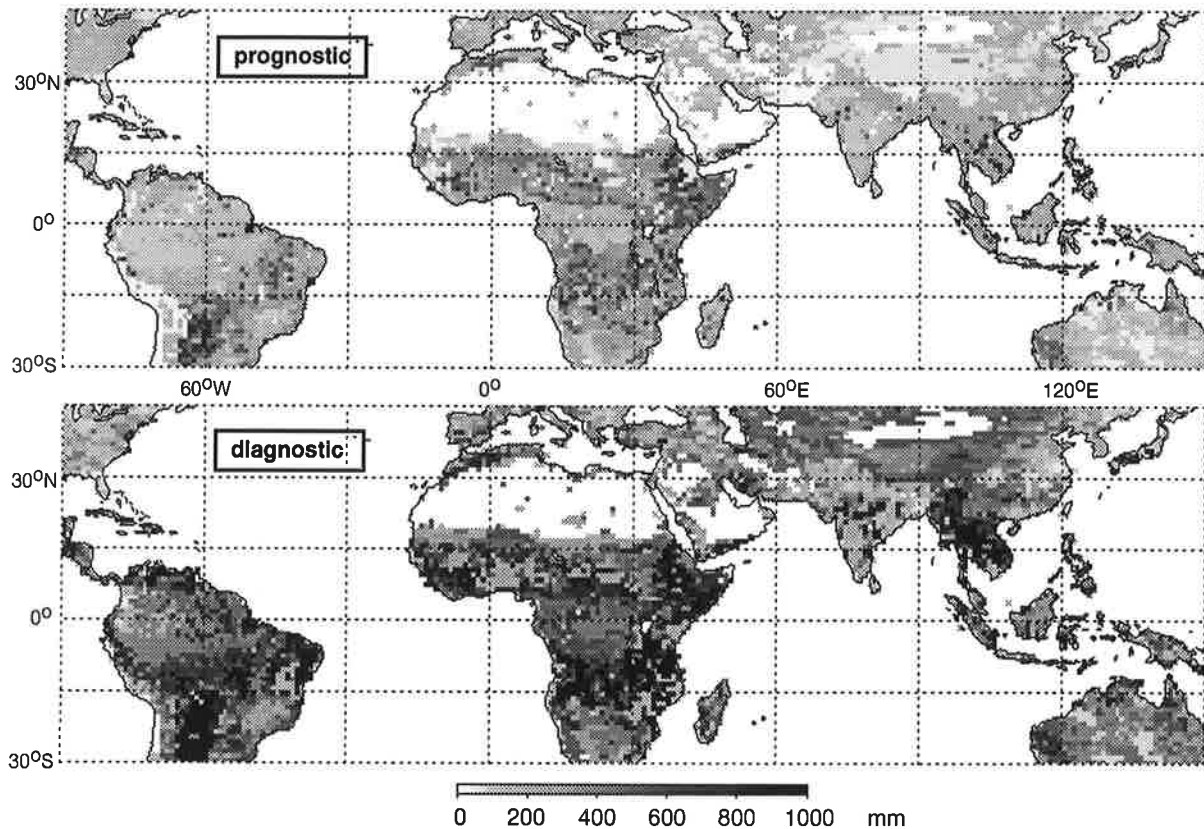


Figure 5.12: Maximum water content available for plants calculated by version ‘0’ before (“prognostic”) and after (“diagnostic”) adjustment to the satellite data.

accurately represent the limiting factors of this vegetation type, as discussed earlier.

A comparison with Table 3.4 of Chapter 3 also delivers some interesting results: for the evergreen rainforest (type 1), the NPP of version ‘0’ has increased by about 6 GtC annually through the assumption of deep roots. For type 2, deciduous tropical trees, there is still an increase by ca. 1.5 GtC after including the satellite data (“diagnostic” in Table 5.5). A similar result has been found by Kleidon and Heimann (1997). Apart from a 10% increase in global NPP, a rooting depth previously not considered in vegetation models could also have consequences for the calculation of carbon turnover in roots and soils.

Fig. 5.12 shows the value of $W_{s,max}$, i.e. the maximum of the plant available soil water content, before and after adjustment to the satellite data. There are considerable changes for all of the tropics, with particularly high values for some regions. These are the areas outlined by Nepstad et al. (1994) in Amazonia, the monsoon rainforests from Myanmar (Burma) to Vietnam, and the savannas of southern Africa and the Brazilian Northeast. There are also rather high values for the Sahel and for parts of India, while the general distribution resembles the one found by Kleidon and Heimann (1997). It is remarkable that a value of 1000 mm, often found for the maximum plant available soil water content, clearly contrasts with values normally used in models of atmospheric circulation. For example, in

the climate model ECHAM3 (DKRZ 1992), a uniform value of 160 mm is used, which is the plant available portion of 200 m total soil water holding capacity. However, the fact that the values are generally higher in the diagnostic case than in the prognostic simulation should not be over-interpreted (typically 300 to 400 mm instead of only 200). Especially for northern latitudes and for not too arid regions, the model is not very sensitive to such changes in rooting depth and the results are bound to contain a large degree of error (which is consequently larger for the soil water holding capacity than for the NPP).

5.6 Summary and conclusions

In this chapter, despite significant problems of data quality, the range of possible model configurations of a complex mechanistic model of global vegetation activity has been constrained further with the help of satellite data. During the process, model parameters could be modified for most areas such that model predictions and satellite measurements match within their inherent degree of accuracy.

To facilitate this additional constraint, a method is presented by which the global distribution of vegetation can be captured on the basis of satellite data through the variable FPAR. This is done by averaging a larger number of measurements expressed by an improved vegetation index, GEMI. The method can easily be extended to future instruments and satellite platforms, for which it is expected that the problems of calibration and signal contamination are reduced considerably. There is also a recommendation for future operational applications that comes out of this study: screening for clouds and other perturbations should happen as early as possible within the processing chain; otherwise there is the danger that also with much improved instruments, there will be residual, unresolved contamination in the data. For further archiving, however, a spatial averaging over larger areas, for example 0.5 degree latitude by longitude, would be sufficient for the need of global carbon cycle studies.

As far as model simulations of the global carbon cycle are concerned, the most important result is that the inclusion of satellite data has reduced the sensitivity of the model against the most important parameters. This effect is less important globally than regionally. An error analysis shows that the possible range of NPP estimates, on the basis of climate, soils and vegetation data, is still large even when agreement with the satellite data is assured. For that reason, the greatest significance of those data lies in the more regional validation and improvement of vegetation models, in particular for arid environments.

Finally, it is shown that the difference between prognostic NPP, limited only by water, light and temperature, and the value after correction with satellite measurements can in some cases be used as an indicator of large-scale human-induced changes. The most likely such changes come from irrigation and from soil erosion.

Chapter 6

A Consistency Check with CO₂ Measurements

6.1 Method and model versions

After a demonstration of how optical satellite data can be used for partial validation and further constraint of global vegetation models presented in the preceding chapters, those results will now be checked for consistency with measurements of CO₂ in the free atmosphere. The method is based on the fact that the seasonal cycle of atmospheric CO₂, an important component of the global carbon cycle by itself, reflects the activity of the terrestrial biosphere over wider regions in a unique way (Heimann et al. 1989)

Naturally, a comprehensive model of the global carbon cycle should be capable of reproducing the concentration and the temporal changes of the CO₂ content of the atmosphere at any place and time. However, there is still little known about many of the more long-term fluxes within the system (Schimel 1995). Consequently, as explained in Chapter 1, the present comparison is restricted to the diagnosis of variations on shorter time scales.

As said, the method presented for checking the previously calculated fluxes between the land biosphere and the atmosphere uses only the seasonal cycle of measured CO₂ concentrations. The assumption that these are mainly caused by biological activity of land plants has been shown through the analysis of the isotopic ratio ¹³CO₂/¹²CO₂ (Heimann et al. 1989, Nakazawa et al. 1993). Contrary to measurements in the field, the advantage of CO₂ measurements in the free atmosphere is that they “see” the integrated effect of a large part of the terrestrial biosphere. Such a model check with the annual CO₂ cycle has first been developed by Fung et al. (1987) and Heimann and Keeling (1989) for very simple models, and has later been applied also to complex ecosystem models (Kaduk 1996, Heimann et al. 1997).

Even though the simulation is restricted to the seasonal cycle, further components of the global carbon cycle have to be taken into account: the transport of CO₂ within the atmosphere, the seasonal cycle of the air-sea exchange and the emission of fossil fuels. The last

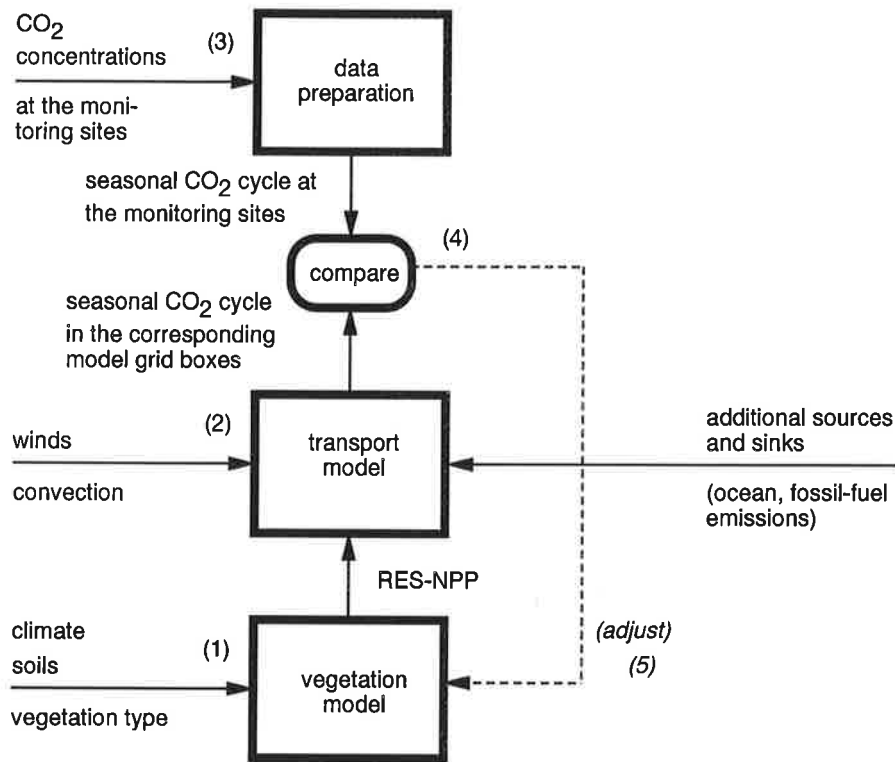


Figure 6.1: Diagram illustrating the information fluxes during model validation with measurements of the atmospheric CO₂ concentration. A possible extension to a method of model constraint is shown by the dashed arrow. The numbers refer to the points in the text.

component causes a certain seasonal cycle in areas of seasonally varying interhemispheric transport (monsoon) by raising the CO₂ content of the northern hemisphere (Heimann et al. 1989).

The scheme for model validation and constraint with CO₂ data illustrated by Fig. 6.1 and resembles the one for the use of satellite data (Fig. 4.8). Apart from the model to be validated, there is again a second model for the translation of model predictions into values analogous to the measurements. Similar to the remote sensing simulator, which translates vegetation cover into satellite measurements, a model of the atmospheric transport establishes a link between the size of sources and sinks at the surface with the seasonal cycle of CO₂ and various measurement stations. This model receives values of the monthly net CO₂ flux from the vegetation model and requires additional boundary conditions independent of land vegetation, such as additional fluxes and information on atmospheric transport. On the side of the measurements, there is again some data pre-processing, in which long-term trends are removed and the mean seasonal cycle and its variance are computed.

Following is a detailed description of the steps (with numbers according to Fig. 6.1):

- (1) The *vegetation model* BETHY is driven with data on climate, soil properties and

vegetation type and computes the net CO₂ exchange with the atmosphere as the difference of soil respiration (RES) and net primary productivity (NPP).

- (2) The tracer *transport model* of the atmosphere TM2 (Heimann 1995) uses RES-NPP and additional sources and sinks from oceans and fossil-fuel emissions to compute the transport of CO₂ to the model grid boxes corresponding to the positions of the monitoring stations. The oceanic exchange is taken from a calculation with the oceanic circulation and plankton model by Six and Maier-Reimer (1996), while the fossil fuel emissions are prescribed as in Heimann and Keeling (1989), with the annual emission of 1987 (CDIAC 1991). All surface fluxes are aggregated to the TM2 grid and are kept constant over one month. The TM2 has a resolution of 7.83° latitude by 10° longitude with 9 layers in the vertical and is executed with a basic time step of 6 hours. It is driven with wind data of reanalyses from the ECMWF weather forecast model for the years 1986 and 1987 and is initially run for 3 years after which a nearly stationary state is reached. The calculated concentrations, denoted c_i , are then taken as monthly means from the fourth model year, after subtracting a linear trend in the concentrations such that the mean annual concentration is zero.
- (3) As observed CO₂ concentrations, samples from the flask sampling programme of the NOAA Climate Monitoring and Diagnostic Laboratory are taken (Conway and Tans 1990, CDIAC 1991). By an appropriate *data preparation*, the mean seasonal cycle, $c_{i,obs}$, and its variance, σ_i^2 , of the years 1980 to 1990 are computed, as far as measurements are available. This is done by fitting a long-term trend to the annual means with cubic Hermite polynomials and subtracting this from the monthly means of the CDIAC data set.
- (4) Measured CO₂ concentrations at the monitoring stations are *compared* to simulated values of the corresponding TM2 grid boxes. The following value is used to measure similarity:

$$j^2 = \frac{1}{12n_{st}} \sum_{i=1}^{12n_{st}} \frac{(c_{i,obs} - c_i)^2}{\sigma_i^2} \quad (1)$$

The index i runs over 12 months times the number of selected stations, n_{st} .

- (5) The additional possibility of adjusting the vegetation model is discussed in Section 6.3.

One factor that has been neglected here is a possible local disequilibrium between NPP and RES (see below). A possible net sink within the global land vegetation, mostly in the north, of 0.5 to 2 GtC per year (cf. Section 1.3) would lead to a reduction in the north-south gradient of the CO₂ concentration that is caused by fossil fuel emissions (Heimann and Keeling 1989), but has only little impact on the seasonal cycle (Heimann et al. 1989). In any case, the sink is only small compared to the uncertainties in the global calculations of NPP (Chapter 3).

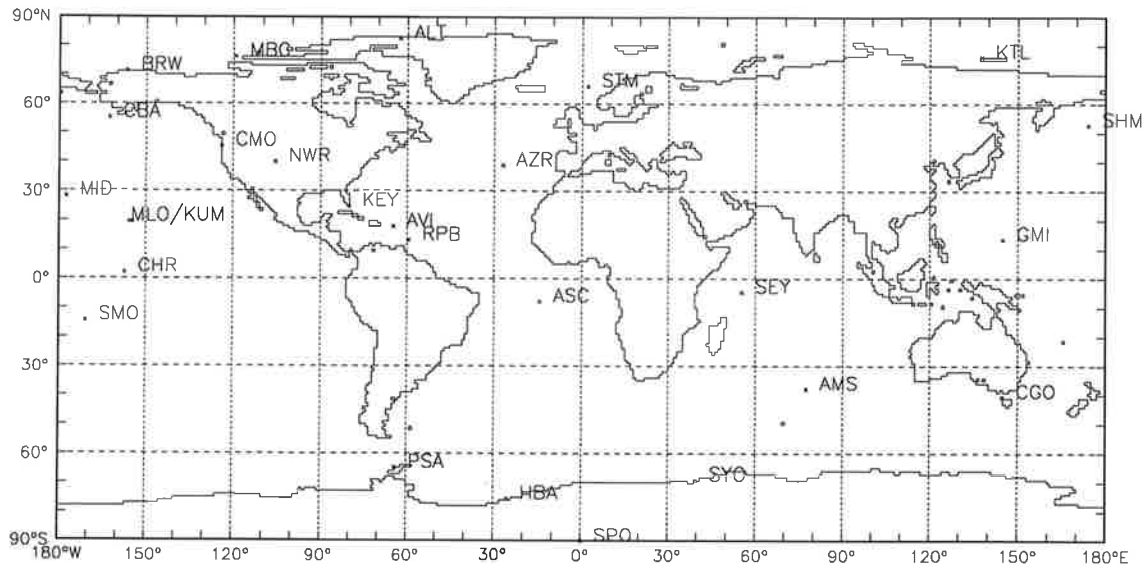


Figure 6.2: Position of the CO₂ monitoring stations.

Fig. 6.2 shows the position of 26 stations belonging to the NOAA monitoring network, plus the Russian station KTL. Since tracer transport is linear, it can be expressed as a matrix equation of the 12 monthly sources and sinks as the first dimension ($24 \times 36 \times 12$ columns) and the 12 monthly concentrations at the 27 stations as the second (27×12 rows). This matrix has been computed by Thomas Kaminski with an adjoint of the TM2 model for the wind fields of 1986 and 1987 (Kaminski et al. 1997). With this matrix, different versions of the vegetation model can be tested in a fast and efficient way.

One important component that has evidently been omitted during validation of the vegetation model by satellite data described in Chapter 4 is the soil respiration (RES), since it cannot be observed from space. Its formulation, used in the standard version (Chapter 2, Equ. 132) and derived from the combined observations by Raich and Potter (1995) and Meentemeyer (1978), is clearly not the only possible way of describing this process. As an example, Bonan (1991) and Norman et al. (1992) use soil moisture multiplied by an exponential function of soil temperature, while the moisture dependence in Raich and Potter (1995) is approximated by the rate of precipitation. Therefore, additional test versions of the vegetation model differing in their formulation of soil respiration are defined in this chapter.

As far as the CO₂ flux during the winter months is concerned, Bonan refers to various field studies (Vogt et al. 1980, Moore 1983, Stohlgren 1988, Taylor and Jones 1990) when assuming that the exponential dependence can also be extrapolated to very low temperatures, at which at least part of the soil is frozen. In fact, in the study by Moore the heat

Table 6.1: Test variants of the vegetation model BETHY concerning soil respiration (RES).

| Code | Description |
|------|---|
| R- | $Q_{10} = 1.4$ |
| R+ | $Q_{10} = 1.8$ |
| Rw | warmer soil than air temperature at freezing ($T \geq -5^{\circ}\text{C}$ when calculating RES) |
| Rp | “Model B, All Data” from Raich and Potter (1995) (precipitation rate as humidity multiplier) |
| R0 | no humidity multiplier |

insulating properties of the snow left soil temperatures in the range of 0 to 3°C, compared to air temperatures down to -35°C. Also, the snow cover does not seem to seriously impede the efflux of carbon dioxide to the atmosphere. Although Solomon and Cerling (1987) found very high CO₂ concentrations in a dense snow pack in a montane environment in Utah (up to 12000 ppm), the effect of the snow cover only consisted in a time shift of the CO₂ emission to the atmosphere.

Based on those observations, it will be assumed here that soil respiration continues down to very low temperatures, with a dependence of air temperature as in Raich and Potter's work. With respect to the study by Moore, it could even be assumed that the evolution of CO₂ in the soil is higher than according to those calculations based on air temperature. While the studies mentioned above all lie in snow-rich areas with cold winters, later work done within the US-Canadian BOREAS project has also shown CO₂ emissions from soils and through the snow cover at very low temperatures (Winston et al. 1995). In this case, the measurements are from an environment with relatively little snowfall, conditions more typical of the large continental areas of Siberia and North America.

The test variants of BETHY for the soil respiration are listed in Table 6.1. The above observation of relatively high rates at severe frost are accounted for by version 'Rw', while 'R-' takes the lower Q_{10} value found by Raich and Potter (1995). An older such review of field studies, where seasonal changes of the respiration rate at one place have been analysed (Raich and Schlesinger 1992), indicates a rather conventional value of 2.0, which is used also in some global models (Raich et al. 1991, Potter et al. 1993, Bonan 1995). Therefore, the average of this value and 1.6, the higher one found by Raich and Potter, is taken here for 'R+' as an upper bound. As a further variant, 'Rp' adapts the model by Raich and Potter directly – Q_{10} function times precipitation as a moisture indicator – and in version 'R0' it is assumed that the influence of moisture on soil respiration can be neglected. This corresponds to the simple models by Fung et al. (1987) and Heimann and Keeling (1989) and is also suggested by the fact that in the review by Raich and Potter, precipitation correlates much less with the respiration rate than temperature.

Apart from the variants just described, the check with CO₂ data is done especially with

Table 6.2: CO₂ monitoring sites, from north to south.

| Code | Name | Country | Latitude | Longitude | Height [m] | Period |
|------|-----------------------|------------|----------|-----------|------------|-----------|
| ALT | Alert, N.W.T. | Canada | 82°27'N | 62°31'W | 210 | 1986-1990 |
| BRW | Point Barrow, Alaska | U.S.A. | 71°19'N | 156°36'W | 11 | 1980-1990 |
| AZR | Azores (Terceira Is.) | Portugal | 38°45'N | 27°05'W | 30 | 1980-1990 |
| NWR | Niwot Ridge, Colorado | U.S.A. | 40°03'N | 105°38'W | 3749 | 1980-1990 |
| MLO | Mauna Loa, Hawaii | U.S.A. | 19°32'N | 155°35'W | 3397 | 1980-1990 |
| KUM | Cape Kumukahi, Hawaii | U.S.A. | 19°31'N | 154°49'W | 3 | 1980-1990 |
| GMI | Guam | U.S.A. | 13°26'N | 144°47'E | 2 | 1980-1990 |
| SEY | Seychelles (Mahe Is.) | Seychelles | 4°40'S | 55°10'E | 3 | 1980-1990 |
| ASC | Ascension Island | U.K. | 7°55'S | 14°25'W | 54 | 1980-1990 |
| AMS | Amsterdam Island | France | 37°57'S | 77°32'E | 150 | 1983-1989 |
| CGO | Cape Grim, Tasmania | Australia | 40°41'S | 144°41'E | 94 | 1985-1990 |
| SPO | South Pole | Antarctica | 89°59'S | 24°48'W | 2810 | 1980-1990 |

those used for the error calculation of the preceding chapter (Fig. 5.10). Thus, the estimated error ranges of both the prognostic and diagnostic versions will be reproduced as simulated seasonal cycles of CO₂. The difficulty is that during the error analysis, the squares of the annual NPP values are added, while with the CO₂ data it is rather the monthly changes that are captured. Therefore, the error analysis is repeated for the simulated annual cycles, with the mean value, \bar{c}_i , and its standard error, s_i , calculated for each month according to:

$$\bar{c}_i = \frac{\sum_{v=1}^{10} w_v c_{i,v}}{\sum_{v=1}^{10} w_v} \quad (2)$$

$$s_i^2 = \sum_{v=1}^{10} w_v (c_{i,v} - \bar{c}_i)^2 \quad (3)$$

The index, v , runs over the 10 model versions '0', 'Pm', 'A+/-', 'D+/-', 'T+/-' and 'L+/-', with $w_v = 1$ for the first two, and 0.5 for the remaining ones (as in the previous chapter, opposite pairs count as one half each version). The assumption is here that errors in the seasonal cycle are additive. To test this assumption, an additional model version is defined, with combined parameter changes against '0' of the model versions 'A-', 'D+' and 'T+'. This version, named 'ADT+', has also an opposite variant denoted 'ADT-', combining just the opposites of the first.

6.2 Results

Fig. 6.3 shows the simulated seasonal cycle of the CO₂ concentration at 12 selected monitoring sites listed in Table 6.2 for the two versions of BETHY that are expected to be the most realistic, from parametrisation and agreement with satellite data. For comparison, the measurements, c_i , and their standard deviations, σ_i , for the periods listed in Table 6.2, and the contributions from oceans and fossil fuel burning alone are also displayed. The wind

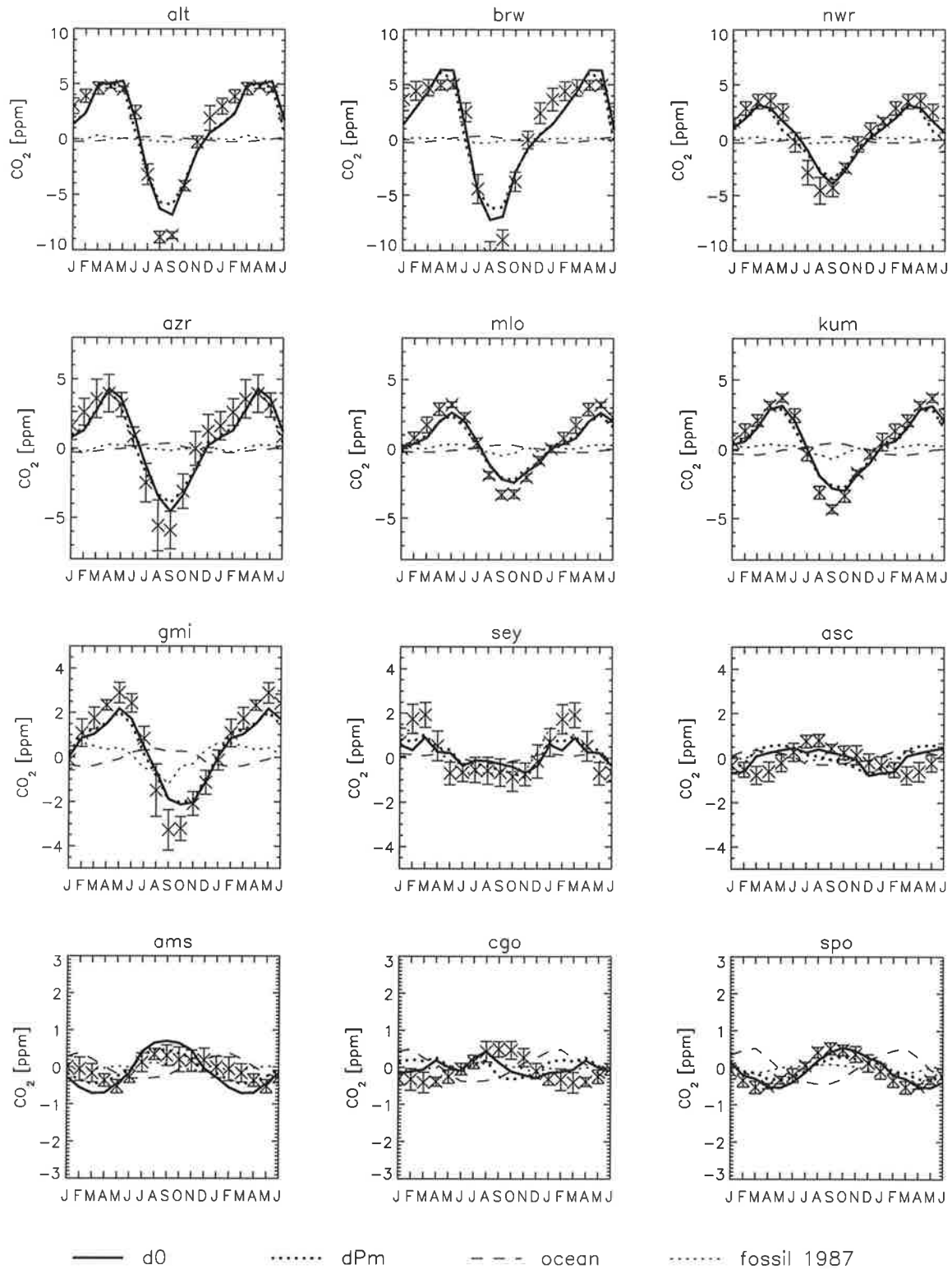


Figure 6.3: Observed seasonal cycle of CO₂ concentrations (×) and simulations for oceanic fluxes, fossil fuels and the sum of the two plus the fluxes from the vegetation model (in 2 versions).

and convection fields used for the transport simulation for this and the following figures are from 1987.

The first thing to notice is a strong decline in the amplitude from north to south, until south of the tropics the oceanic contribution has about the same amplitude as the total signal. The agreement between simulations and observations is generally good. For further examination, however, it should be borne in mind that the transport model only has a spatial resolution of approximately 8 by 10 degrees, so that local effects cannot be reproduced. This is also the reason for selecting sites that are usually on remote islands or high mountains. Local effects might cause the more pronounced downward peak in the observed CO₂ concentrations in late summer for most northern stations. For the southern station 'cgo', there is also a special problem that has to do with a specific selection of wind directions before measurements. If this effect is taken into account (Ramonet 1994), there is a certain shift in the phase of the simulated signal, while the amplitude stays about constant.

In general, a certain degree of uncertainty coming from the oceanic fluxes has to be accounted for at the southern stations, because these have so far only been validated by a few measurements of the atmospheric O₂/N₂ ratio (Six and Maier-Reimer 1996). At 'sey' and to some degree also at 'gmi', there is also a significant contribution from fossil fuel burning caused by the monsoon cycle. This circulation pattern might not be resolved as well as in the original ECMWF input data with this coarse resolution version of TM2.

At the station 'asc', savanna fires from southern Africa have an additional effect that is not simulated here. The reason for having excluded this effect lies in the great difficulties of estimating the exact CO₂ amounts emitted, either from statistics (Hao et al. 1988) or with satellite data (Kaufman et al. 1988). From calculations by Iacobellis et al. (1994), who have used the data by Hao et al. and an earlier, modified version of TM2, those fires generate an amplitude of approximately 1 ppm at a position over the Atlantic slightly northeast of 'asc', with a peak in August and a trough in April. Such an additional signal would in fact improve the agreement between simulations and measurements at that station. This is especially important if one considers that the low biological activity in this region causes the oceanic fluxes to be controlled mainly by temperature, which reduces the uncertainty of the calculated fluxes, in particular as far as their phase is concerned.

Despite the admitted lack of accuracy of the assumed oceanic contribution, a comparison of amplitudes at the southern stations is of great value for testing the vegetation model. Thus, it turns out that the simulated amplitude is possibly a little too large at the Indian Ocean station 'ams'. Since the signal at this site mainly comes from South America (Kaminski et al. 1996), the reason might lie in a seasonal contrast of NPP of the grasslands in that region that is too large in the simulations (more in Section 6.3).

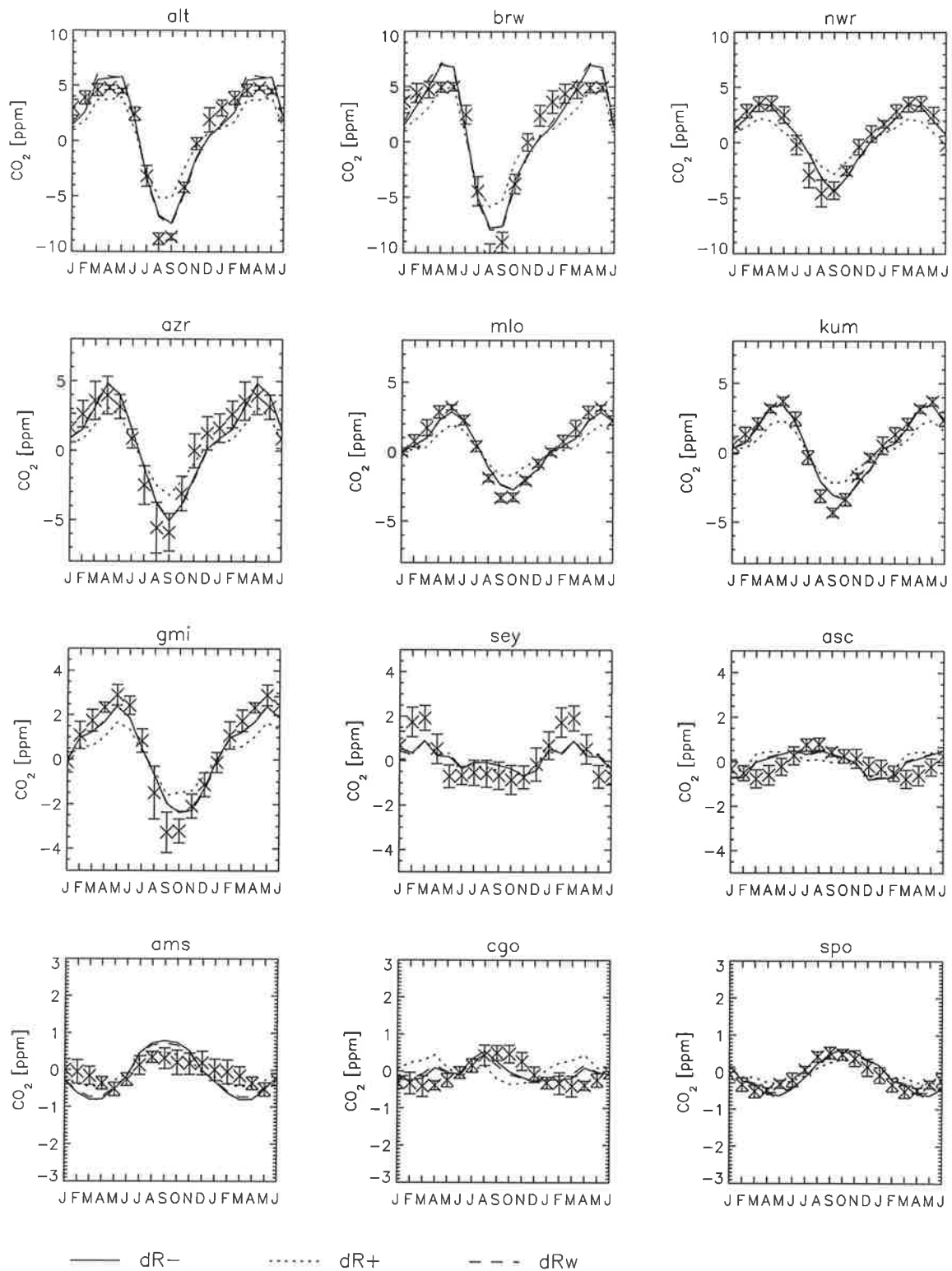


Figure 6.4: Observed (×) and simulated CO₂ concentrations for three test variants of soil respiration.

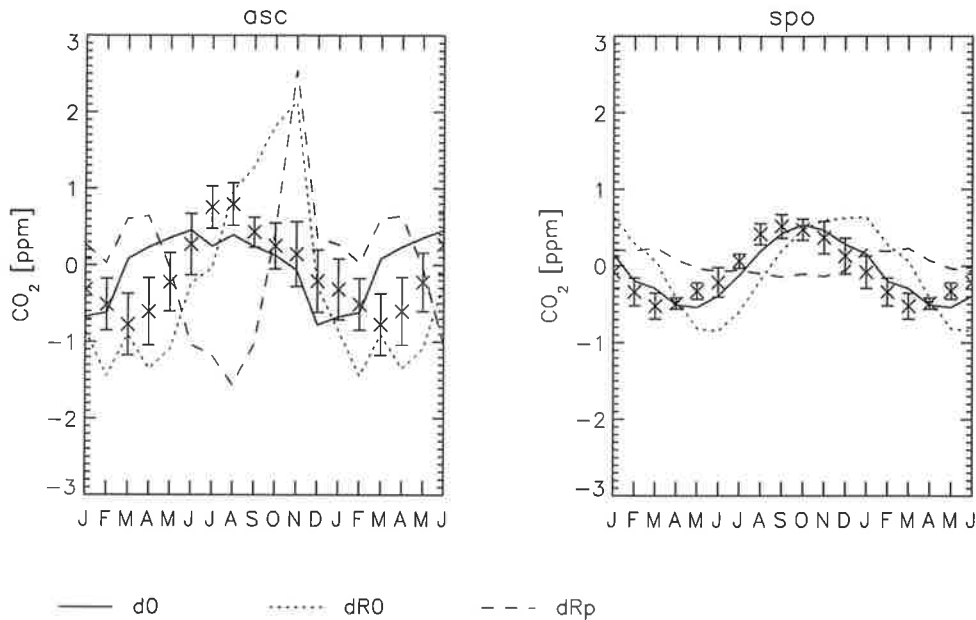


Figure 6.5: Observed (\times) and simulated seasonal cycle for two more test variants of soil respiration.

Soil respiration

Before the general error range that comes from vegetation modelling is discussed, an impression of the possible sources of error during calculation of soil respiration will be given here. This is done with the model versions of BETHY according to Table 6.1, each computed in its diagnostic variant (denoted 'd'). contributions – are shown in Fig. 6.4 for the first three versions. The agreement is a little better for a lower value of Q_{10} (R-) or for an increased source in the winter (Rw), and a little less satisfactory for a higher Q_{10} (R+). In total, considering the various influences not accounted for (local, circulation, fire etc.), the agreement is still remarkably good.

By comparison, Fig. 6.5 demonstrates how strongly changes in the moisture dependence of soil respiration affect the simulated cycle in the southern hemisphere. While at the south pole ('spo'), the simulated amplitude is not increased so that agreement with observations would still be possible with different oceanic fluxes, there is a pronounced peak of the concentration at 'asc' during November which clearly contradicts observations. As already mentioned, this station receives its signal mostly from southern Africa, an area of extended dry-seasonal savannas. If moisture dependence of soil respiration is neglected altogether ('R0'), the seasonal signal is determined solely by the dry/wet rate of photosynthesis, an assumption that does not appear to be realistic. Another observation is here, that the use of precipitation ('Rp') instead of soil moisture or actual evapotranspiration, as proposed by Raich and Potter (1995), leads to an unrealistic phase difference between the fluxes NPP and RES. Therefore, this formulation does not seem to be suitable for simulating the

Table 6.3: Mean normalised deviation, j^2 , for the diagnostic standard version and the test variants of soil respiration.

| transport | d0 | dR- | dR+ | dRw | dR0 | dRp |
|-----------|------|------|------|------|------|------|
| 1986 | 3.63 | 3.60 | 7.00 | 3.80 | 4.87 | 9.41 |
| 1987 | 2.86 | 2.73 | 6.43 | 2.79 | 4.44 | 8.88 |

seasonal course of CO₂ fluxes.

A quantitative expression of the foregoing comparisons is offered by the above defined value j^2 listed in Table 6.3, i.e. the mean squared deviation from the observations normalised by the variance of the observations (Equ. 1). The sum is executed over the 12 stations of Table 6.2 or Fig. 6.4. As it can also be seen on Fig. 6.4, the best agreement is found for the lowest Q_{10} ('R-') or for increased winter respiration ('Rw'). The two last versions, 'R0' and 'Rp', have to be rejected on the basis of the comparisons at station 'asc'. For 'R0', this discrepancy is not reflected by the value in Table 6.3, which shows that considering the mean deviation alone is not sufficient for a comprehensive interpretation.

The differences in transport between 1986 and 1987 are not as dramatic as those between model variants, and they are fairly evenly distributed across all stations. For that reason, the j^2 values give a correct impression of the effect of interannual variability in the atmospheric transport. The agreement for 1986 is inferior by about 0.5 to 1.0 compared to 1987, while the ranking of the different model versions does not change. Hence, such differences in transport seem to be small enough for a check of the vegetation model with only one year of wind data. Another fact that is also demonstrated here is that small differences between simulations should not be overestimated. In general, a value of up to $j^2 \approx 5$ appears to be in good agreement with observations.

Model error and CO₂ measurements

Fig. 6.6 shows the error range of the diagnostic model versions, i.e. $\bar{c}_i \pm s_i$ according to Equ. 2 and 3, and the previously defined extreme model versions 'ADT-' and 'ADT+'. These combine those three variants included into the error analysis that always lead to either a lower or a higher NPP value. Despite the considerable uncertainty for the global value of NPP, the agreement is still rather good for the complete simulated range.

Before a further consideration of the computed error range, a brief look is appropriate at whether this is in fact the correct way of mapping the vegetation model's uncertainties onto the CO₂ simulations. Comparing the complete error range with the simulations of versions 'ADT+/-' reveals that these two extreme versions have a somewhat larger amplitude than what is computed from Equ. 2 and 3. Here, it has to be taken into account that from the logic of the error analysis, the probability of a case combining three deviations is only $1/\sqrt{3}$, with the result that the combined error is less than the simple combination of the three

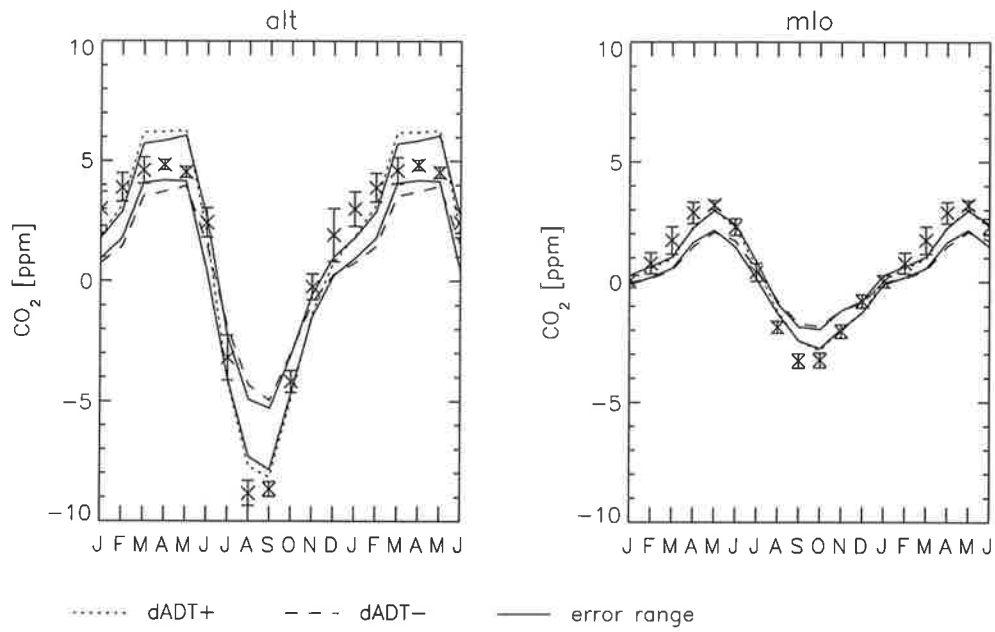


Figure 6.6: Comparison of the error range of the diagnostic versions in the simulated CO₂ cycle with two extreme variants of the vegetation model.

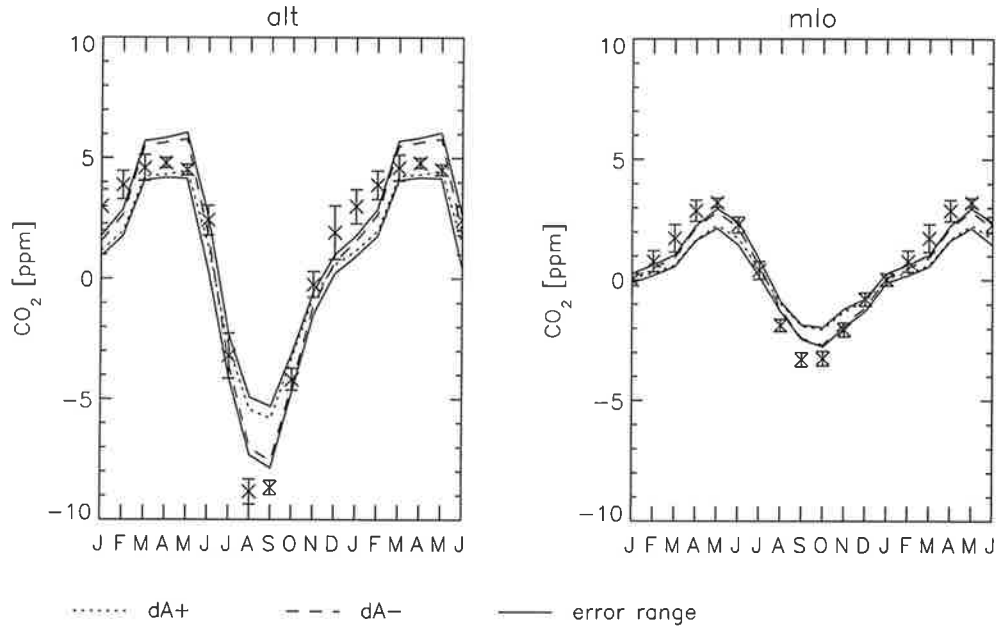


Figure 6.7: Sensitivity of the seasonal cycle of CO₂ against plant respiration.

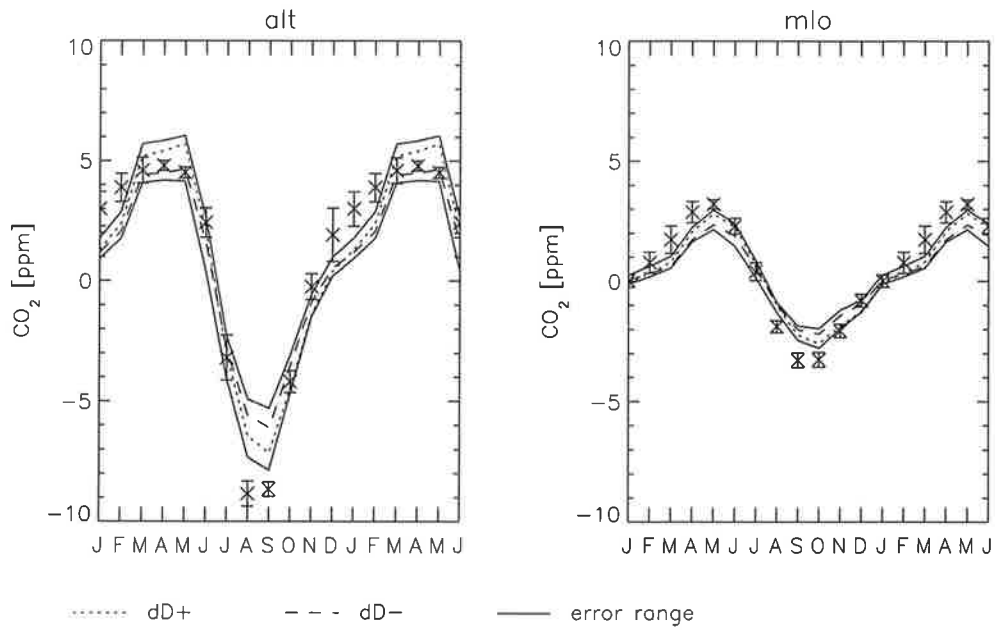


Figure 6.8: Sensitivity of the seasonal cycle of CO₂ against rooting depth.

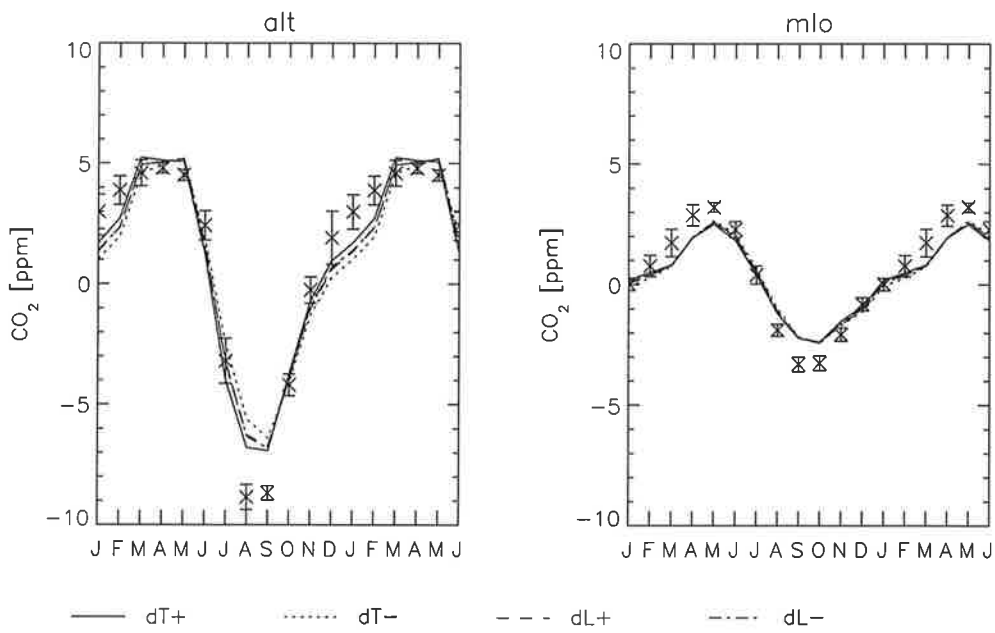


Figure 6.9: Sensitivity of the seasonal cycle of CO₂ for different parametrisations of phenology.

Table 6.4: Mean deviation, j^2 , over 12 stations and 12 months of the average prognostic and diagnostic simulations with BETHY from the observed CO₂ seasonal cycle; and the averaged deviation over all possible error configurations, J^2 , assuming normal distribution.

| version | transport | average simul. | integral |
|------------|-----------|----------------|----------|
| | | j^2 | J^2 |
| prognostic | 1986 | 6.22 | 9.96 |
| | 1987 | 4.94 | 8.53 |
| diagnostic | 1986 | 4.46 | 5.85 |
| | 1987 | 3.69 | 5.03 |

influences. As Fig. 6.7 shows, plant or “autotroph” respiration already accounts for most of this range. The rest comes largely from rooting depth (Fig. 6.8), while uncertainties in the phenology have only little influence on the seasonal cycle of CO₂ (Fig. 6.9). In particular, for the assumed error in LAI (‘L+/-’), which according to Fig. 5.10 has a greater global effect than that related to temperature (‘T+/-’), the impact in different areas compensate such that the two curves in Fig. 6.9 are hardly discernible. These comparisons are meant to demonstrate that a considerable error range of the NPP calculations has only a relatively limited impact on the simulated seasonal cycles of CO₂, and that the error analysis in the picture of the CO₂ concentrations described above correctly reflects the vegetation model’s sensitivity against defined uncertainties.

Prognostic and diagnostic versions

Fig. 6.10 and 6.11 show the mean and the error range of the simulated seasonal cycle for the prognostic and diagnostic versions of BETHY compared to the measurements. The simulations again include the oceanic and fossil fuel fluxes and are driven with wind fields of 1987. The agreement, especially for the diagnostic versions, is at almost all stations about as good as for the various formulations of soil respiration in Fig. 6.4. Only for the tropical stations, the variation is smaller in Fig. 6.4 after rejection of versions ‘R0’ and ‘Rp’. Some uncertainty in the moisture dependence of RES, however, should still be expected.

Naturally, the greatest uncertainty, amounting to several ppm, is found where the amplitude is also greatest, i.e. at the arctic stations. For the prognostic case, these are also the stations with the clearest deviation from the measurements. For most stations, however, even the prognostic simulations lie within a range that is consistent with observations.

The only exception seems to be station ‘ams’ in the southern Indian Ocean, receiving its signal largely from southern South America. Here, the amplitude of the upper bound appears to be too large in both cases (cf. above).

The mean normalised deviation over the stations in Fig. 6.10 or 6.11 is again taken as a quantitative criterion for a comparison with measurements. Here, not only the value j^2 for

the average simulation is considered, but also the mean, J^2 , of this value over all possible deviations within the error range. To calculate J^2 , it is assumed that the possible values of c_i have a normal distribution around the average, \bar{c}_i , with a standard deviation equal to the estimated error, s_i :

$$\begin{aligned} J^2 &= \sum_{i=1}^{12n_{st}} \frac{1}{12n_{st}} \int_{-\infty}^{+\infty} \frac{(c_{i,obs} - c_i)^2}{\sqrt{2\pi s_i} \sigma_i^2} e^{-(c_i - \bar{c}_i)^2 / s_i^2} dc_i \\ &= j^2 + \sum_{i=1}^{12n_{st}} \frac{1}{12n_{st}} \frac{s_i^2}{\sigma_i^2} \end{aligned} \quad (4)$$

The values calculated in this way are shown in Table 6.4 for two different years of wind fields. It does not only become evident that averaged over the range of variations, the diagnostic simulations are more consistent with observations than the prognostic ones (J^2), but also that the mean seasonal cycles, \bar{c}_i , lie closer to the observations in the diagnostic case (j^2). While after including the satellite data, the simulations fall rather well into the above mentioned range of up to ≈ 5 , without that additional source of information, some of the model configurations lie clearly above that value when compared to CO₂ observations. This consistency check of the vegetation model can therefore be considered successful in its form constrained by satellite data, while without those data, some model configurations will necessarily conflict with observed CO₂ measurements.

6.3 CO₂ data for model constraint

In the previous section, it has turned out that the additional information contained in the satellite data can be used to constrain the vegetation model BETHY just far enough to make simulations within the range of general uncertainties consistent with CO₂ measurements, and this despite of remaining large uncertainties in the global NPP. If the CO₂ data were now taken instead of the satellite data as a constraint for the vegetation model, then all calculated diagnostic model versions of the previous chapter would be possible realisations of this condition. It should therefore be asked, what the additional constraint is that measurements of the atmospheric CO₂ content can deliver.

Table 5.5 in Chapter 5 shows for which vegetation types the information content of the satellite data leads to a refinement of the NPP calculations. For example, since for tropical rainforests, the monthly values of FPAR are already known rather well (close to 1), those data have no value for this type of vegetation (as far as modelling of a monthly mean NPP is concerned). Fig. 6.12 allows a similar evaluation of the CO₂ data, showing the relative contributions of different vegetation types to the simulated seasonal cycle, c_i . Calculations are with version 'd0' and the transport of 1987, with the stations corresponding to those in Fig. 6.2. The contributions, a_t , are defined as the normalised scalar product of the single

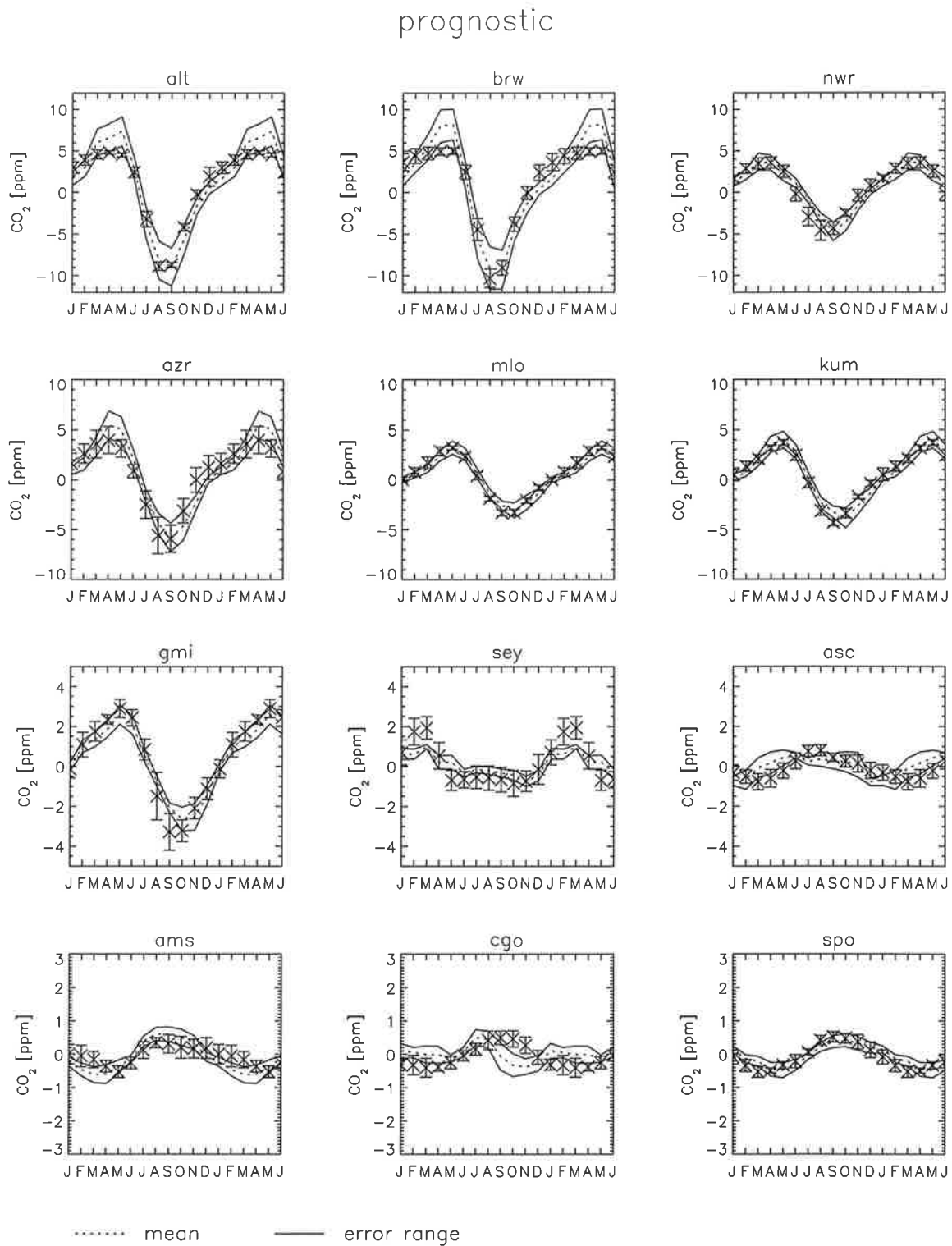


Figure 6.10: Mean and error range of the simulated seasonal cycle of CO₂ for the prognostic versions of BETHY.

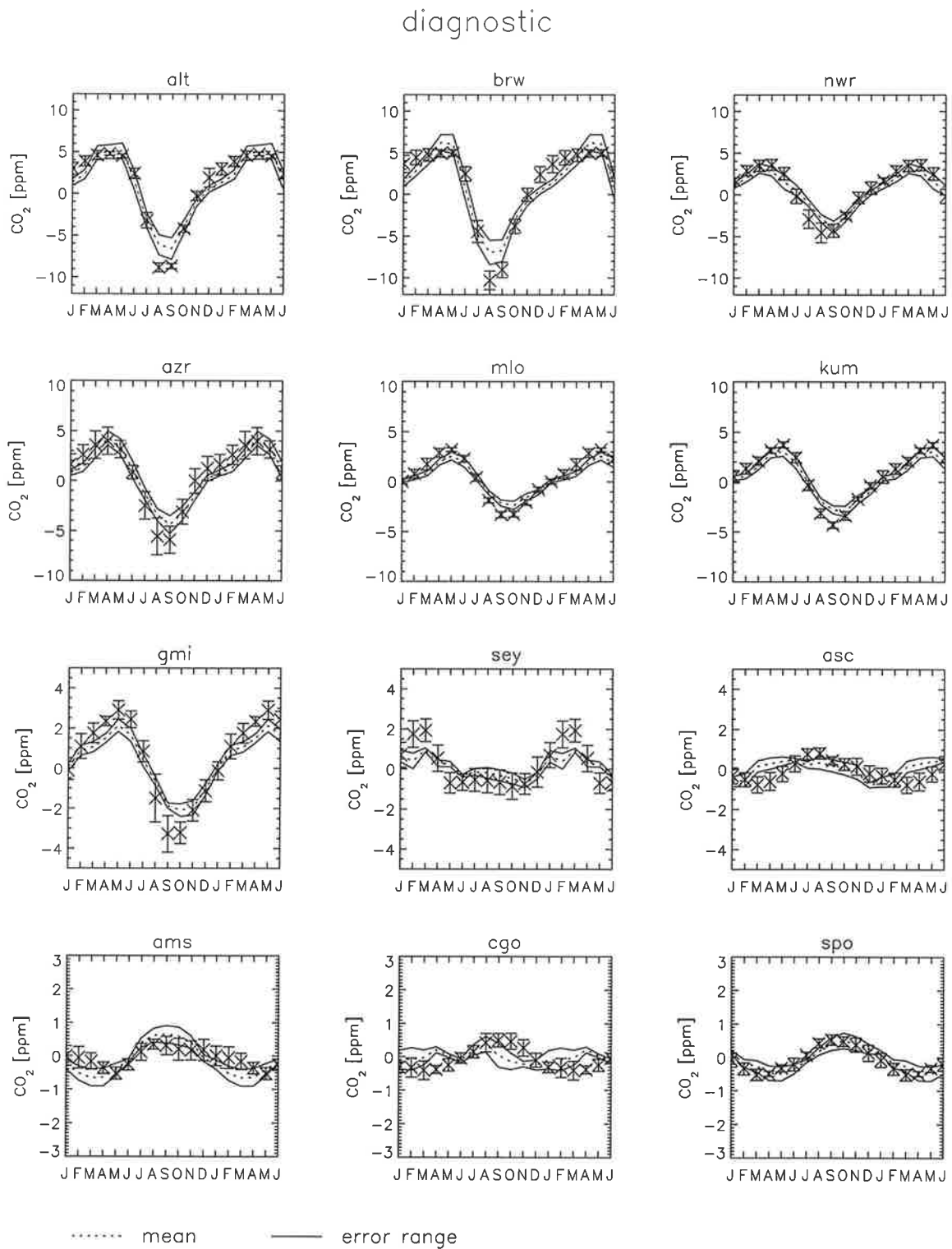


Figure 6.11: Mean and error range of the simulated seasonal cycle of CO₂ for the diagnostic versions of BETHY.

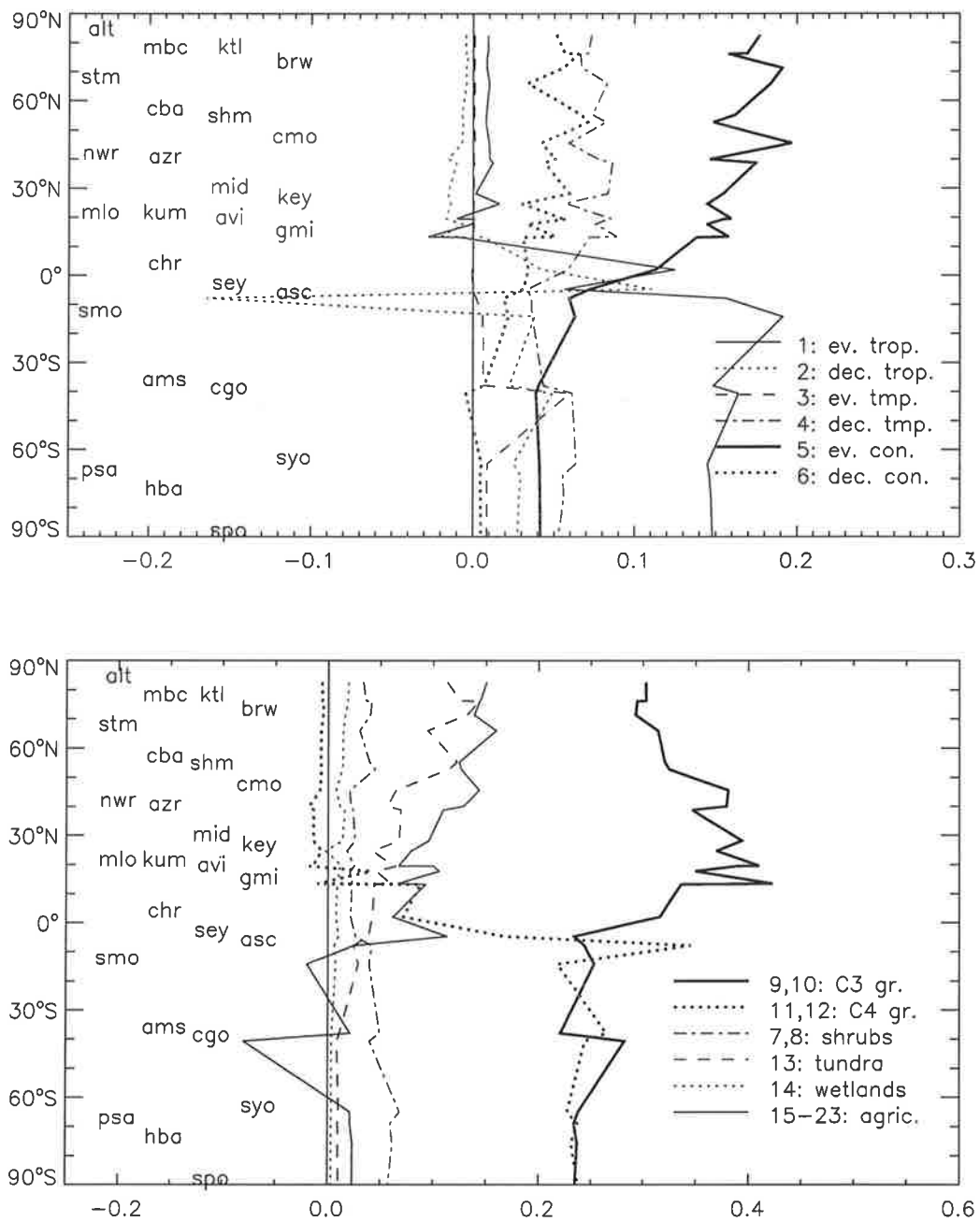


Figure 6.12: The contribution of various trees (above) and other vegetation types (below) to the seasonal cycle at different stations, simulated with version 'd0'.

contributions, $c_{i,t}$, of type t with the concentration derived from the fluxes of all vegetation:

$$a_i = \frac{\sum_{t=1}^{12} c_{i,t} c_i}{\sum_{i=1}^{12} c_i^2} \quad (5)$$

It turns out that in the northern hemisphere, the signal comes primarily from C3 grasses and conifers, while the smaller signal in the southern hemisphere is caused mainly by C3 and C4 grasses, and to a smaller degree by evergreen tropical trees.

Since there is a strong seasonal cycle only at the northern stations, the consistency check of the previous section mainly concerns C3 grasses and conifers with a total of 0.55 (types 9, 10 and 5, 6). Errors in the modelling of e.g. broadleaf trees cannot be checked with this method. Also, if signals of opposite phase compensate each other, such as at the important station 'asc' for types 1 and 2, it could mean that two errors actually cancel. Thus, a more accurate determination of the NPP of those two important vegetation types is possible neither with CO₂ nor with satellite data.

This leads to the conclusion that it is mainly conifers and C3 grasses whose error range can be reduced with the help of the CO₂ data. The fact that these are just two of the three major vegetation types for which in Section 5.5 satellite data contain useful information might explain that constraining the vegetation model to the satellite measurements leads to a clear improvement as far as the CO₂ signal is concerned. In most other cases, however, the significance of the satellite data is clearly higher: For example, while according to Table 5.5 the productivity of C4 grasses can be constrained most, this effect cannot be checked with the CO₂ signal because of the small amplitude at southern latitudes.

A possible exception is the station 'ams', where the amplitude of the upper error range has earlier been found to be too pronounced. As Fig. 6.12 shows, this signal comes mainly from grasses. Here, a further model constraint would be possible, although with ca. 1.5 ppm, the amplitude is smaller by a factor of 10 compared to the important arctic stations, and hence only a relatively small part of the global net CO₂ flux is concerned here.

It can therefore be stated that the satellite data have a clearly higher information content for determining global NPP than measurements of the atmospheric CO₂ content. That means that, despite or just because of large remaining inaccuracies, they constitute the most important global data set for validating and improving global vegetation models.

Nonetheless, the importance of the CO₂ data lies in the fact that they allow an additional check of the difference between NPP and the soil respiration, RES, that cannot be captured with optical remote sensing data.

6.4 First concluding remarks

A final remark about the value of the consistency check with CO₂ data seems appropriate. It is possible that with other vegetation models than BETHY, the deviations from the observed CO₂ seasonal cycle are found to be much larger. In this case, those measurements

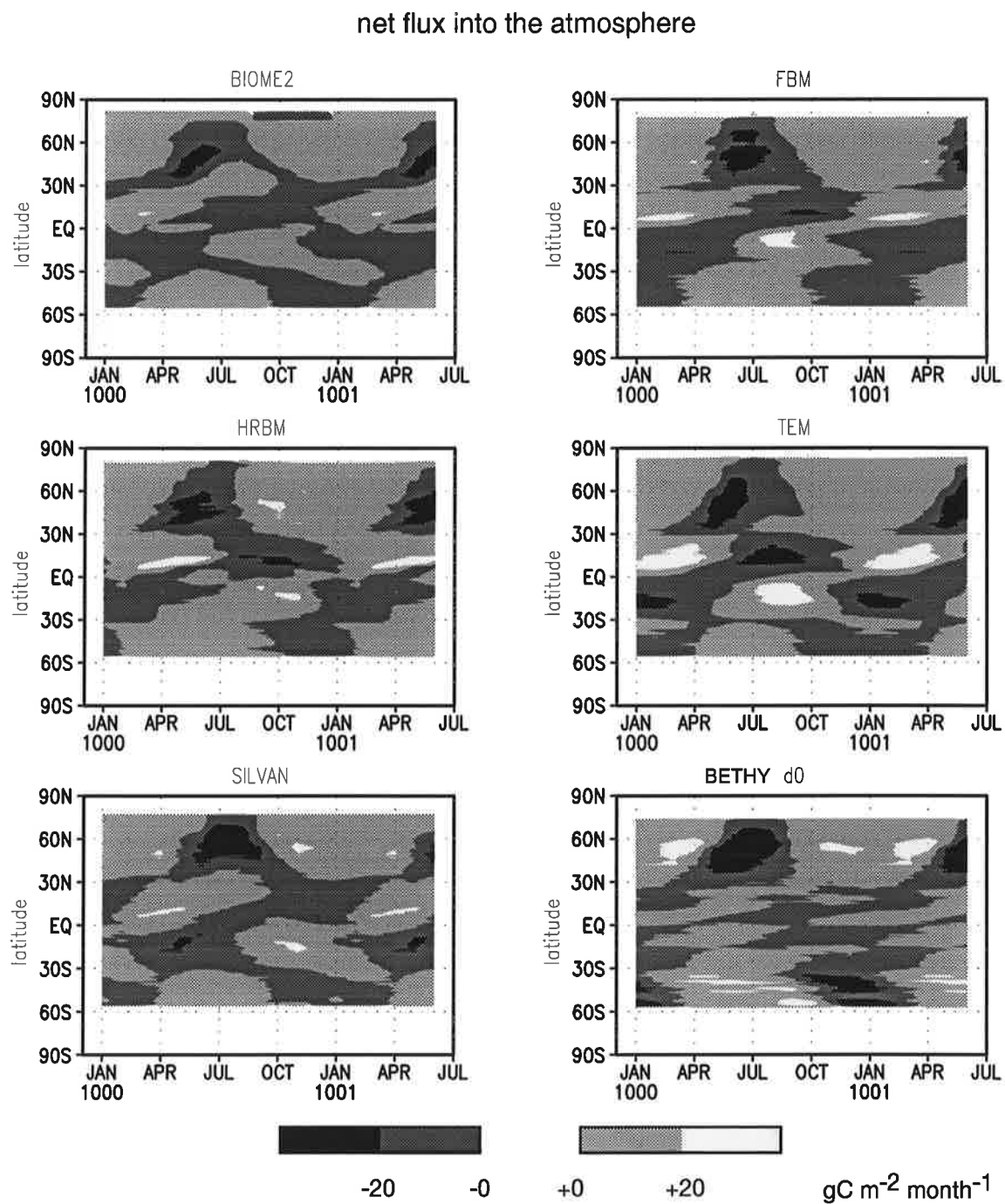


Figure 6.13: Latitudinal average of the net flux RES - NPP and its annual course for five complex vegetation models and the diagnostic standard version 'd0' of BETHY.

constitute an important and necessary condition for the reconstruction of the biosphere's present state. Such a test of five different complex models is presented in a study by Heimann et al. (1997), from which Fig. 6.13 has been adopted. It shows the seasonal cycle of the net flux into the atmosphere by latitude, calculated by the different models and the diagnostic standard version, 'd0' (not included in Heimann et al.).

The most conspicuous feature of this comparison is the large difference between the models, in particular for the tropics. Most of them simulate a marked contrast in the net flux between the dry and wet seasons, which is also simulated by other modelling studies, e.g. by Potter et al. (1993). In fact, Heimann et al. find an amplitude of the seasonal cycle at station 'asc' that is similar to version 'R0' in Fig. 6.5 and therefore too large. Hence, one of the results of this study is an observation not taken account of in most biosphere models: The seasonal cycle of CO₂ exchange in the tropics is largely suppressed, because NPP and RES follow the change from dry to wet season with almost coinciding phases.

Apart from this, the large uncertainty in vegetation modelling mentioned in Chapter 1 is again illustrated, which is not only reproduced by the model developed here, but also shows up during such a model intercomparison. Therefore, the significance of this study also lies in the consistent reproduction of this uncertainty range within one model alone. Only in this way it becomes possible to distinguish important from unimportant sources of error and to evaluate the usefulness of global observational data, an important necessity considering the need for improving the accuracy of vegetation models. Such an evaluation has been tried here for two different truly global data sets; a possible application of the method to other data is discussed in the following chapter.

Chapter 7

Summary and Further Applications

7.1 Summary of results

The results of the three preceding chapters can be grouped into three topics, concerning the global carbon cycle, vegetation modelling, and satellite remote sensing technology:

Carbon cycle: The net primary production of the land vegetation amounts to approximately 70 ± 35 GtC per year; this considerable error range is for models satisfying the vegetation distribution measured from satellites. The accuracy of this result can not be improved with the help of CO₂ measurements in the free atmosphere.

It is again made evident that the seasonal cycle of atmospheric CO₂ is caused largely by the photosynthesis of land vegetation. A pronounced annual cycle in the tropics, as calculated by various models, is not reproduced. Instead, plant activity and soil respiration seem to depend on moisture in a similar way, which largely suppresses the seasonality of the net fluxes in warm-arid regions.

The soil water reservoir available for plant use appears to be much larger in extended parts of the tropics than previously assumed. This has important consequences for global net primary productivity and possibly, because of the necessary rooting depth, also for the amount of carbon cycled in the soils.

The difference between potential productivity at a potential vegetation distribution and actual productivity is far smaller than the uncertainties involved in computing those quantities. As a consequence, human impact on global net primary productivity can neither be determined by modelling studies, nor through the use of satellite data.

Modelling: Remaining uncertainties regarding the extrapolation of field study results to large regions have important consequences for the possibility of modelling vegetation activity globally.

An improved understanding of the factors controlling respiration costs and plant growth is clearly necessary for projecting the current state of the land biosphere into the future.

Some factors so far neglected in global vegetation models have a rather large impact on productivity. Among these are albedo and net radiation at the surface, day-to-day variability of precipitation, temperature amplitude and radiation, and accessibility of soil water resources so far neglected.

Less important factors appear to be the control of stomata and the aerodynamic exchange coefficient for heat and water vapour. It is also relatively unimportant for large-scale calculations whether to use traditional or satellite derived vegetation maps.

Remote sensing: The method developed here, which consists of first simulating satellite data and then comparing this to actual measurements, has some considerable advantages for both the qualitative and the quantitative interpretation of such data compared to a direct translation into biophysical quantities. Even after an “ideal” correction for atmospheric and soil background perturbations, the optical signal depends on a range of physiological and micrometeorological factors. Therefore, a quantitative interpretation will always require a synthesis of measurements and model calculations.

Some new methods are added to the technique of satellite based vegetation monitoring. One of them is the determination of the fraction of absorbed photosynthetically active radiation with the help of the modern vegetation index GEMI and a time averaging technique, also on the basis of GEMI, that avoids the selection of maximum vegetation index values and the various distortions brought about by this traditional method.

Backing up the satellite data with a vegetation model allows a more rigorous selection of observation conditions, because gaps in the measurements only reduce the accuracy of the simulations. For future monitoring and archiving programmes, a selection at an early stage of the processing chain is recommended.

Even if this study has only been partly successful at determining the CO₂ exchange between the land vegetation and the atmosphere more accurately, one of the most important results is that satellite data constitute the most important global data set for monitoring the present state of the land biosphere.

7.2 Outlook at further applications

The vegetation model developed here and the method of adjusting it to global observations can easily be applied to a number of other scientific questions. The error analysis of this

study can also be used to evaluate the accuracy of each procedure. Besides this, some of the globally distributed quantities that have been calculated, soil water holding capacity and seasonal changes of the leaf area in particular, can be used directly for other studies and models, for example for models of the atmospheric circulation (weather and climate models).

Conceptually easy is an application to other types of satellite data, such as measurements of the thermal outgoing radiation, active or passive microwaves or other optical data from newer satellites. The surface temperature, measured with mid infrared sensors, depends just on the energy balance that plays an important role in the model; for the case of radar data (i.e. active microwaves), the remote sensing simulator used here could easily be replaced by other models (e.g. MIMICS, Ulaby et al. 1990).

Further applications can also be found for certain diagnostic techniques of the terrestrial biosphere with the help of atmospheric trace gas measurements, because the decisive factors controlling fractionation processes of various CO₂ isotopes – leaf temperature, air humidity and leaf internal CO₂ concentration – are all computed by the vegetation model. For example, the seasonal cycle of C¹⁸O¹⁶O in the atmosphere might constitute a constraint on the calculation of the gross primary productivity (Farquhar et al. 1993). A first simulation by Ciais et al. (1996) could be extended to include this question. A decisive quantity for the fractionation of ¹³CO₂, the ratio of C3 to C4 grasses (Lloyd and Farquhar 1994), is also treated rather thoroughly in this study. However, for an appropriate check of the model, simulations of the oceanic biosphere, such as by Six and Maier-Reimer (1996), and measurements of the O₂/N₂ ratio (Keeling and Shertz 1992) would also have to be taken into account.

An important extension within the research of the global carbon cycle concerns inter-annual variations in atmospheric CO₂ – as opposed to the seasonal variations considered here (cf. Section 1.1). On the one hand, there are indications of an increase of the seasonal cycle's amplitude by ca. 20% since the early 70's (Keeling et al. 1996), on the other hand, Myneni et al. (1997) report similar changes in the vegetation index NDVI between 1981 and 1991, accompanied by a clear rise in spring temperatures. If it were possible to bring these three observations together by having a vegetation model reproduce both changes in the CO₂ signal and in the satellite data on the basis of measured changes in the climate, it would mean a great step further in the understanding of the mechanisms governing inter-annual fluctuations in the global carbon cycle. It is just this link that has been established in this study for a mean annual cycle.

However, the question of accuracy remains important. It is still unknown to what degree and how climate variations lead to changes in vegetation activity on a global scale. This is not surprising, considering the uncertainties involved in determining only the average global CO₂ uptake. Another point is that two different correction methods lead to rather different interannual changes in the NDVI data used by Myneni et al. The fact that for each satellite of the NOAA series (cf. Section 5.2), the overpass time has shifted from the early

to the late afternoon during its respective lifetime has also not been taken into account by the authors. As shown by Koslowsky (1996), only a correction of such angular effects allows a reliable interpretation of interannual trends in such satellite data.

7.3 Concluding remark

Today, a prediction of the changes in the global vegetation and in the global carbon cycle caused by human intervention appears to be one of the most urgent tasks of earth sciences and biology. However, research into the underlying mechanisms still appears to be at the beginning, and this is even true for the current state. Therefore, global measurements of the earth surface from satellites are able to make a valuable contribution to both tasks: they allow an improved diagnosis of the current state, and they offer an important test for prognostic vegetation models. One method that facilitates the use of such satellite data has been developed in this study.

Appendix

Measured and simulated GEMI for 1990

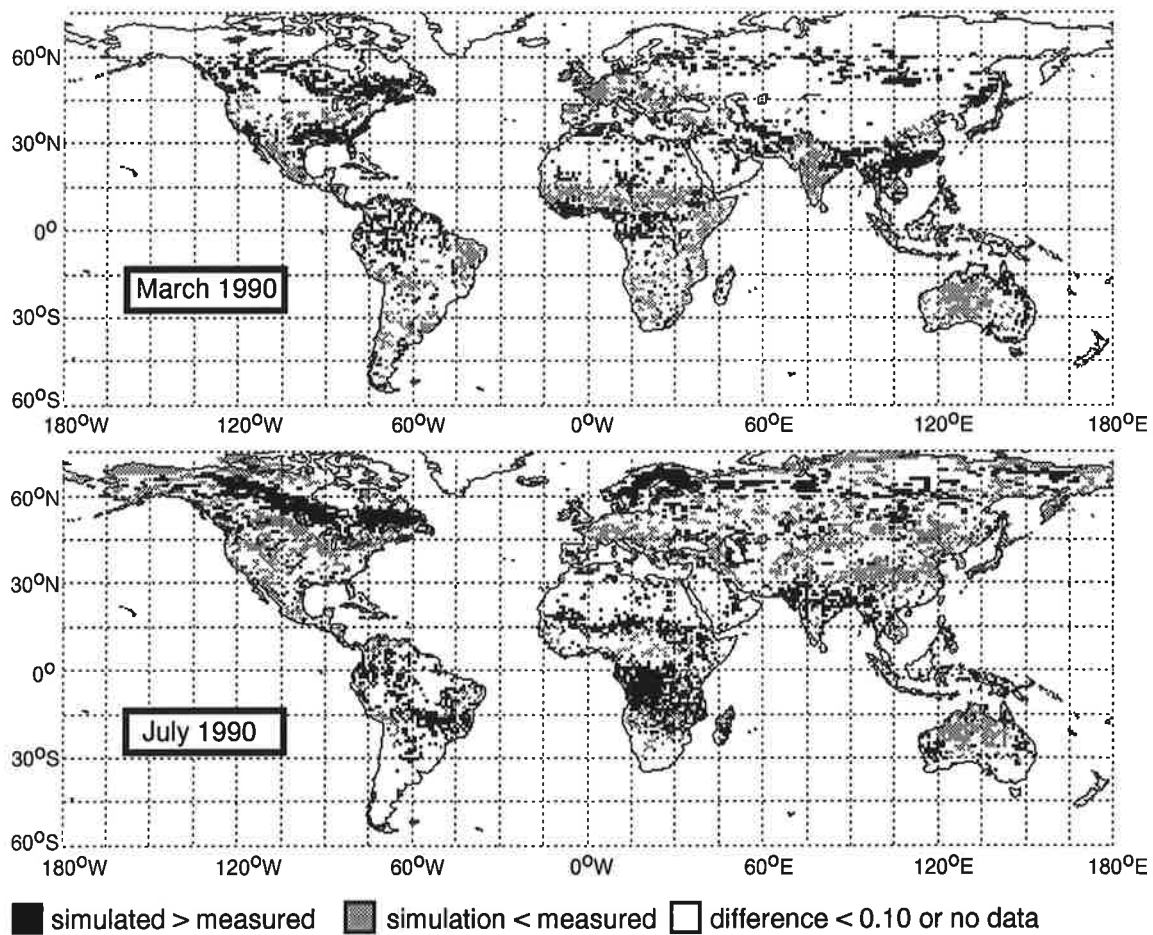


Figure A.1: Check of the simulated GEMI against the satellite derived value, taken from monthly maxima ('max') of 1990, for version 'x0' of the vegetation model. Satellite data have been recalibrated (see Section 4.6).

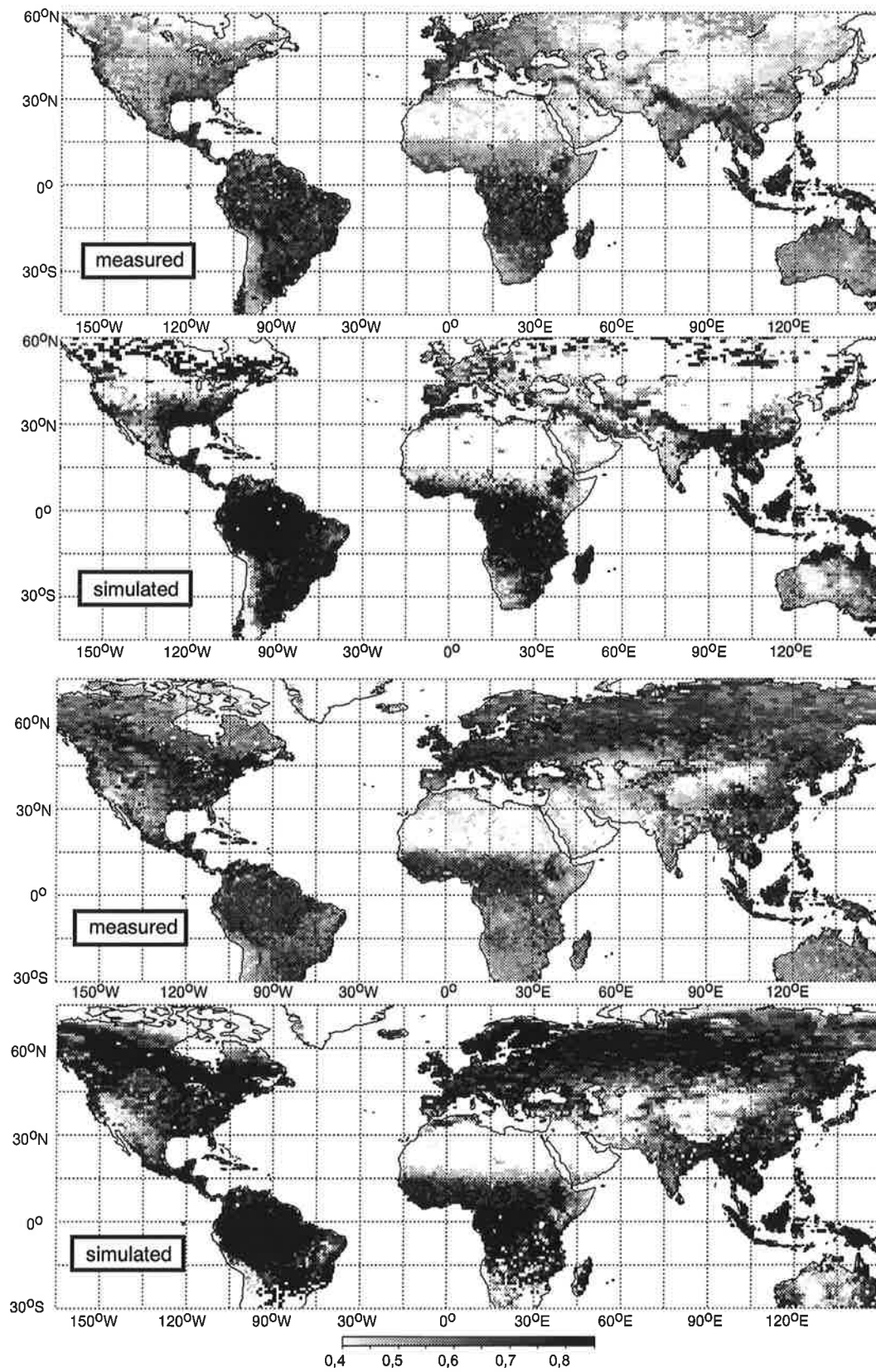


Figure A.2: Measured and simulated values of the vegetation index GEMI for March (top) and July (bottom) 1990 (monthly maxima, version 'x0').

Effective fractional cover with shadows

To account for the formation of shadows during the calculation of light absorption in version 'G' of Table 3.2, the following scheme is used:

Considering only direct solar radiation, the vegetation seen by an observer with the sun in the back appears to cover an area that is equal to the shaded portion of the total area. This apparent fractional cover for direct radiation, f_c^{eff} , is equal to f_c times the ratio of the area shaded by a ground object, here called "clump", including the basal area of the clump itself, and the basal area of the clump. Assuming clumps in the form of cylinders (diameter d and height h) leads to:

$$\begin{aligned} f_c^{eff} &= f_c \frac{4}{\pi} \frac{h}{d} \tan \theta_s \\ &= f_c \frac{4}{\pi} \eta \sqrt{1/\mu^2 - 1} \end{aligned}$$

with the aspect ratio $\eta = h/d$ and the solar zenith angle θ_s , with $\mu = \cos(\theta_s)$. This equation is valid until several shades overlap. In this case f_c^{eff} tends towards a maximum value, $f_{c,max}$, describing the total fractional area covered by the clump formation. (The clumps could for instance be trees in a forest, and the maximum value the forest fraction, with the rest made up of unvegetated areas such as roads or settlements. The aspect ratio of the "super clumps", in this case the forests, is considered zero.) Providing that the positions of the clumps do not correlate, for large numbers of clumps ($N \gg 1$) f_c^{eff} approaches its maximum by an exponential function (which follows from a Poisson distribution of overlapping shadows):

$$f_c^{eff} = f_{c,max} - (f_{c,max} - f_c) \exp \left\{ -\frac{4\eta}{\pi} \sqrt{\frac{1}{\mu^2} - 1} \frac{f_c}{f_{c,max}} \right\}$$

The value for $f_{c,max}$ is given in Table 3.1. As aspect ratio, η , the following expression is used (for natural vegetation and tree crops):

$$\eta = 1 + h_v/7.5$$

with the vegetation height, h_v , in m (see Table 2.1). For agricultural vegetation (except trees), $\eta = 0$ is assumed.

In this model of light absorption, the layering of the vegetation canopy goes from $l = \Lambda_c^{eff} \equiv \Lambda/f_c^{eff}$ to $l = 0$ (Λ is the leaf area index, LAI) along the direction of the solar beam. The lower the sun, the greater is this effect. Therefore, in areas of high levels of insolation where light saturation of photosynthesis is quickly reached, the maximum photosynthetic rate can be shifted efficiently to the morning and evening. Since the portion of direct radiation is particularly large in those areas, f_c^{eff} is probably a reasonable approximation for the effective fractional cover.

However, the problem is far more complicated for diffuse radiation, because there is no preferred direction. The contribution of the diffuse radiation is therefore neglected when

estimating the effect of $\eta > 0$, which should be of little importance for the arid regions referred to above.

Literature

- Adams, J.M., Fauré, H., Fauré-Denard, L., McGlade, J.M. and Woodward, F.I. 1990. Increases in the terrestrial carbon storage from the last glacial maximum to the present. *Nature* 348, 711-714.
- Ajtay, G.L., Ketner, P. and Duvigneaud, P. 1979. Terrestrial primary production and phytomass. In: *The Global Carbon Cycle*. (Bolin, B., Degens, E.T., Kempe, S. and Ketner, P. Eds.), Wiley, New York, pp. 129-182.
- Arpe, K. 1991. The hydrological cycle in the ECMWF short range forecasts. *Dyn. Atmos. Oceans* 16, 33-59.
- Anderson, E.A. 1976. A point energy and mass balance model of a snow cover. *NOAA Tec. Rep. NWS 19*. US Dept. Commerce, Washington D.C., 150 pp.
- Asrar, G. (Ed.), 1989. *Theory and Applications of Optical Remote Sensing*. Wiley, New York, 734 pp.
- Asrar, G., Myneni R.B., and Choudhury, B.J. 1992. Spatial heterogeneity in vegetation canopies and remote sensing of absorbed photosynthetically active radiation: a modeling study. *Remote Sens. Environ.* 41, 85-103.
- Avissar, R. and Pielke, R.A. 1991. The impact of plant stomatal control on mesoscale atmospheric circulation. *Agric. For. Meteorol.* 54, 353-372.
- Barkström, B.R. 1984. The Earth Radiation Budget Experiment (ERBE). *Bull. Amer. Meteor. Soc.* 65, 1170-1185.
- Barnola, J.-M., Raynaud, D., Korotkevitch Y.S. and Lorius, C. 1987. Vostok ice core provides 160,000 year record of atmospheric CO₂. *Nature* 329, 408-414.
- Berling, D.J. and Quick, W.P. 1995. A new technique for estimating rates of carboxylation and electron transport in leaves of C3 plants for use in dynamic global vegetation models. *Global Change Biology* 1, 289-294.
- Bégué, A. 1992. Modeling hemispherical and directional radiative fluxes in regular-clumped canopies. *Remote Sens. Environ.* 30, 219-230.
- Berthelot, B., Dedieu, G., Cabot, F. and Adam, S. 1994. Estimation of surface reflectance and vegetation index using NOAA/AVHRR: Methods and results at global scale. *Communication for the 6th international symposium on physical measurements and signatures in remote sensing*, ISPRS, Val d'Isère, France, 17-21 January.
- Binder, K. (Ed.), 1986. *Monte Carlo Methods in Statistical Physics*, 2nd edition, Springer Verlag, Berlin.
- Bolz, H.M. 1949. Die Abhängigkeit der infraroten Gegenstrahlung von der Bewölkung. *Z. Meteorol.* 7, 201-203.
- Bonan, G.B. 1991. Atmosphere-biosphere exchange of carbon dioxide in boreal forests. *J. Geophys. Res.* 96, 7301-7312.
- Bonan, G.B. 1995. Land-atmosphere CO₂ exchange simulated by a land surface process model coupled to an atmospheric general circulation model. *J. Geophys. Res.* 100, 2817-2831.

- Bowker, D.E., Davis, R.E., Myrick, D.L., Stacy, K. and Jones W. 1985. *Spectral reflectances of natural targets for use in remote sensing studies*. National Aeronautics and Space Administration (NASA): Reference Publication 1139.
- Box, E.O. 1981. *Macroclimate and plant forms: An introduction to predictive modeling in phytogeography*. Junk, Den Haag, 174 pp.
- Box, E.O. and Bai, X.M. 1993. A satellite-based world map of current terrestrial net primary productivity. *Seisan-Kenkyu* 45, 666-672.
- Brakke, T.W., Smith, J.A. and Harnden, J.M. 1989. Bidirectional scattering of light from tree leaves. *Remote Sens. Environ.* 29, 175-183.
- Brutsaert, W. 1982. *Evaporation into the atmosphere*. Reidel Publishing, Dordrecht, Netherlands, 299 pp.
- Budyko, M.I. 1974. *Climate and Life*. Academic Press, New York, 508 pp.
- Bunnik, N.J.J. 1978. *The multispectral reflectance of shortwave radiation of agricultural crops in relation with their morphological and optical properties*. Technical Report, Medelingen Landbouwhogeschool, Wageningen, Netherlands.
- CDIAC 1991. *Trends 1991, a compendium of data on global change* (Boden, T.A., Serpanski, R.J. and Stoss, F.W. Eds.), ORNL/CDIAC-46, Carbon Dioxide Information Center, Oak Ridge National Laboratory, Oak Ridge, Tennessee, U.S.A.
- Chandrasekhar, S. 1960. *Radiative Transfer*. Dover Publications, New York.
- Ciais, Ph., Denning, A.S., Tans, P.P., Berry, J.A. Randall, D.A., Collatz, J.J.G., Sellers, P.J., White, J.W.C. Trolier, M., Meijer, H.J., Francey, R.J., Monfray, P. and Heimann, M. 1996. A three dimensional synthesis study of $\delta^{18}\text{O}$ in atmospheric CO_2 , Part I: Surface fluxes. *J. Geophys. Res.* 102, 5857-5872.
- Collatz, G.J., Berry J.A., Farquhar G.D. and Pierce J. 1990. The relationship between the Rubisco reaction mechanism and models of photosynthesis. *Plant, Cell and Environment* 13, 219-225.
- Collatz, G.J., Ball, J.T., Grivet, C. and Berry, J.A. 1991. Physiological and environmental regulation of stomatal conductance, photosynthesis and transpiration: a model that includes a laminar boundary layer. *Agric. For. Meteorol.* 54, 107-136.
- Collatz G.J, Ribas-Carbo, M. and Berry J.A. 1992. Coupled photosynthesis-stomatal conductance model for leaves of C_4 plants. *Aust. J. Plant Physiol.* 19, 519-538.
- Conway, T.J. and Tans, P. 1990. *Atmospheric CO_2 concentrations — The NOAA/GMCC flask sampling network*. NDP-005/R1, Carbon Dioxide Information Center, Oak Ridge National Laboratory, Oak Ridge, Tennessee, U.S.A.
- Cowan, I.R. 1982. Regulation of water use in relation to carbon gain in higher plants. In: *Physiological plant ecology II: Water Relations and Carbon assimilation*, Vol. 12B. (Lange, O.L., Nobel, P.S., Osmond, C.B. and Ziegler, H. Eds.), Springer Verlag, Berlin, pp. 589-613.
- Cowan, I.R. and Farquhar, G.D. 1977. Stomatal function in relation to leaf metabolism and environment. *Symposium of the Society for Experimental Biology* 31, 471-505.

- Crowley, T.J. 1995. Ice age terrestrial carbon change revisited, *Global Biogeochem. Cycles* 9, 377-389.
- Dai, A. and Fung, I.Y. 1993. Can climate variability contribute to the missing "CO₂" sink? *Global Biogeochem. Cycles* 7, 599-609.
- Deering, D.W., Rouse, J.W., Haas, R.H. and Schell, J.A. 1975. Measuring forage production of grazing units from Landsat MSS data. *Proc. 10th Int. Symp. Remote Sensing Environ.*, University of Michigan, Ann Arbor, U.S.A., pp. 1169-1178.
- DeFries, R.S. and Townshend, J.R.G. 1994. NDVI-derived land cover classifications at a global scale. *Int. J. Remote Sensing* 15, 3567-3586.
- Dickinson, R.E. and Isebrands, J.G. 1991. Leaves as regulators of stress response. In: *Response of Plants to Multiple Stresses*. (Mooney, H.A., Winner, W.E., Pell, E.J. and Chu, E. Eds.), Academic Press, San Diego, U.S.A., pp. 3-33.
- Dickinson, R.E., Henderson-Sellers, A., Rosenzweig, C. and Sellers, P.J. 1991. Evapotranspiration models with canopy resistance for use in climate models, a review. *Agric. For. Meteorol.* 54, 373-388.
- Dickinson, R.E., Henderson-Sellers, A. and Kennedy, P.J. 1993. *Biosphere-atmosphere transfer scheme (BATS) version 1e as coupled to the NCAR community climate model*. NCAR Technical Note NCAR/TN-387+STR. National Center for Atmospheric Research, Boulder, Colorado.
- Dixon, R.K., Brown, S.A., Houghton, R.A., Solomon, A.M., Trexler M.C. and Wisniewski, J. 1994. Carbon pools and fluxes of global forest ecosystems. *Science* 263, 616-617.
- Dolman, A. J., Gash, J.H.C., Roberts, J. and Shuttleworth, W.J. 1991. Stomatal and surface conductance of tropical rainforest. *Agric. For. Meteorol.* 54, 303-318.
- Dozier, J. 1989. Remote sensing of snow in visible and near-infrared wavelengths. In: *Theory and Applications of Optical Remote Sensing*. (Asrar, G. Ed.), Wiley, New York, pp. 527-547.
- DKRZ 1992. *The ECHAM 3 atmospheric general circulation model*. (Deutsches Klimarechenzentrum Modellbetreuungsgruppe Ed.), Deutsches Klimarechenzentrum Technical Report No. 6, Hamburg, 184 pp.
- Duda, R.O. and Hart, P.E. 1973. *Pattern classification and Scene Analysis*. Wiley, New York.
- Dunne, K.A. and Willmott, C.J. 1996. Global distribution of plant-extractable water capacity of soil. *Int. J. Climat.* 16, 841-859.
- Ehrlich, D. and Lambin, E., 1996. Broad scale land-cover classification and interannual climatic variability. *Int. J. Remote Sensing* 17, 845-862
- Eidenshink, J.C. and Faundeen, J.L. 1994. The 1 km AVHRR global data set: first stages in implementation. *Int. J. Remote Sensing* 15, 3443-3462.
- Esser, G. 1991. Osnabrück Biosphere Model: construction, structure, results. In: *Modern Ecology: Basic and Applied Aspects*. (Esser, G. and Overdieck, D. Eds.), Elsevier Publishing, New York.
- Esser, G., Hoffstadt, J., Mack, F. and Wittenberg, U. 1994. *High-Resolution Biosphere Model - Documentation*. Mitteilungen aus dem Institut für Pflanzenökologie der Justus-Liebig-Universität Gießen, Gießen, Germany.

- Etheridge, D.M., Steele, L.P., Langenfelds, R.L. and Francey R.J. 1996. Natural and anthropogenic changes in atmospheric CO₂ over the last 1000 years from air in Antarctic ice and firn. *J. Geophys. Res.* 101, 4115-4128.
- Farquhar, G.D. 1988. Models relating subcellular effects of temperature to whole plant responses. *Symposium of the Society for Experimental Biology* 42, 395-409.
- Farquhar, G.D., von Caemmerer, S. and Berry, J.A. 1980. A biochemical model of photosynthesis in leaves of C₃ species. *Planta* 149, 78-90.
- Farquhar, G.D. and Sharkey, T.D. 1982. Stomatal conductance and photosynthesis. *Ann. Rev. Plant Physiol.* 33, 317-345.
- Farquhar, G.D., Lloyd, J., Taylor, J.A., Flanagan, L.B., Syvertsen, J.P., Hubick, K.T., Wong, S.C. and Ehleringer, R. 1993. Vegetation effects on the isotope composition of oxygen in atmospheric CO₂. *Nature* 363, 439-443.
- Federer, C.A. 1979. A soil-plant-atmosphere model for transpiration and availability of soil water. *Water Resour. Res.* 15, 555-562.
- Federer, C.A. 1982. Transpirational supply and demand: plant, soil, and atmospheric effects evaluated by simulation. *Water Resour. Res.* 18, 355-362.
- Field, Ch. 1991. Ecological Scaling of Carbon Gain to Stress and Resource Availability. In: *Response of Plants to Multiple Stresses*. (Mooney, H.A., Winner, W.E., Pell, E.J. and Chu, E. Eds.), Academic Press, San Diego, U.S.A., pp. 35-65.
- Field, Ch. and Mooney, H.A. 1986. The photosynthesis-nitrogen relationship in wild plants. In: *On the Economy of Plant form and Function*. (Givnish, T.J. Ed.), Cambridge University Press, Cambridge, pp. 25-55.
- Fischer, R.A. and Turner, N.C. 1978. Plant productivity in the arid and semiarid zones. *Ann. Rev. Plant Physiol.* 29, 277-317.
- Flasse, S. and Verstraete, M.M. 1994. Monitoring the environment with vegetation indices: comparison of NDVI and GEMI using AVHRR data over Africa. In: *Vegetation, Modelling and Climate Change Effects*. (Veroustraete, F. and Ceulemans, R. Eds.), Academic Publishing, Den Haag, pp. 107-135.
- Foley J.A., Prentice I.C., Ramankutty N., Levis S., Pollard D., Sitch S. and Haxeltine A. 1996. An integrated biosphere model of land surface processes, terrestrial carbon balance, and vegetation dynamics. *Global Biogeochem. Cycles* 10, 603-628.
- Francey, R.J., Tans P.P., Allison, C.E., Enting, I.G., White, J.W.C. and Trolier, M. 1995. Changes in oceanic and terrestrial carbon uptake since 1982. *Nature* 373, 326-330.
- Friedlingstein, P., Fung, I., Holland, E., John, J., Brasseur, G., Erickson, D. and Schimel, D. 1995. On the contribution of CO₂ fertilization to the missing sink. *Global Biogeochem. Cycles* 9, 541-556.
- Friend, A.D. 1995. PGEN: an integrated model of leaf photosynthesis, transpiration and conductance. *Ecol. Modelling* 77, 233-255.
- Friend, A.D. 1997. Parameterisation of a global daily weather generator for terrestrial ecosystem and biogeochemical modelling. *Ecol. Modelling*, in press.

- Friend, A.D., Stevens, A.K., Knox, R.G. and Cannell, M.G.R. 1996. A process-based, terrestrial biosphere model of ecosystem dynamics (Hybrid 3.0). *Ecol. Modelling* 95, 249-287.
- Fung, I., Prentice, K., Matthews, E., Lerner, J. and Russel, G. 1983. Three-dimensional tracer model study of atmospheric CO₂: Response to seasonal exchanges with the terrestrial biosphere. *J. Geophys. Res.* 88, 1281-1294.
- Fung, I.Y., Tucker, C.J. and Prentice, K.C. 1987. Application of Advanced Very High Resolution Radiometer vegetation index to study atmosphere-biosphere exchange of CO₂. *J. Geophys. Res.* 92, 2999-3015.
- Gates, M.D. 1980. *Biophysical Ecology*. Springer Verlag, New York.
- Geng, S., Penning de Vries, F., and Supit, I. 1986. A simple method for generating daily rainfall data. *Agric. For. Meteorol.* 36, 363-376.
- Gobron, N., Pinty, B., Verstraete, M.M. and Govaerts, Y. 1997. A semi-discrete model for the scattering of light by vegetation. *J. Geophys. Res.* 102, 9431-9446.
- Goel, N.S. and Qin, W. 1994. Influences of canopy architecture on relationships between various vegetation indices and LAI and FPAR: A computer simulation. *Remote Sens. Rev.* 10, 309-347.
- Gollan, T., Turner, N.C. and Schulze, E.-D. 1985. The responses of stomata and leaf gas exchange to vapour pressure deficit and soil water content. III. In the sclerophyllous woody species *Nerium oleander*. *Oecologia* 65, 356-362.
- Goward, S.N., Dye, D.G., Turner, S. and Yang, J. 1993. Objective assessment of the NOAA global vegetation index data product. *Int. J. Remote Sensing* 14, 3365-3394.
- Greenland, D.J. and Kowal, J.M.L. 1960. Nutrient content of the moist tropical forest of Ghana. *Plant and Soil* 12, 154-174.
- Hagemann, S. and Dümenil, L. 1996. *Development of a parameterization of lateral discharge for the global scale*. Max-Planck-Institut für Meteorologie Report Nr. 219, Hamburg.
- Hao, W.M., Liu, M.H. and Crutzen, P.J. 1990. Estimates of annual and regional releases of CO₂ and other trace gases to the atmosphere from fires in the tropics, based on the FAO statistics for the period 1975-1980. In: *Fire in the Tropical Biota*. (Goldammer J.G. Ed.), Springer-Verlag, Berlin, pp. 440-462.
- Hellden, U. 1991. Desertification – time for an assessment? *Ambio* 20, 372-383.
- Heimann, M. 1995. *The TM2 atmospheric transport model*. Deutsches Klimarechenzentrum Technical Report Nr. 10, Hamburg, Germany.
- Heimann, M. 1997. A review of the contemporary global carbon cycle and as seen a century ago by Arrhenius and Högbom. *Ambio* 26, 17-24.
- Heimann, M. and Keeling, C.D. 1989. A three-dimensional model of atmospheric CO₂ transport based on observed winds: 2. Model description and simulated tracer experiments. *AGU Monograph* 55. Washington, American Geophysical Union. 237-275.
- Heimann, M., Keeling, C.D. and Tucker, C.J. 1989. A three-dimensional model of atmospheric CO₂ transport based on observed winds: 3. Seasonal cycle and synoptic time scale variations. *AGU Monograph* 55. Washington, American Geophysical Union. 277-303.

- Heimann, M., Esser, G., Haxeltine, A., Kaduk, J., Kicklighter, D.W., Knorr, W., Kohlmaier, G.H., McGuire, A.D., Melillo, J., Moore, B., Otto, R.D., Prentice, I.C., Sauf, W., Schloss, A., Stitch, S., Wittenberg, U. and Würth, G. 1997. Evaluation of terrestrial carbon cycle models through simulations of the seasonal cycle of atmospheric CO₂: First results of a model intercomparison study. *Global Biogeochem. Cycles*, in press.
- Hillel, D. 1980. *Applications of Soil Physics*. Academic Press, New York, 385 pp.
- Holben, B.N. 1986. Characteristics of maximum-value composite images from temporal AVHRR data. *Int. J. Remote Sens.* 7, 1417-1434.
- Houghton, J.T. 1986. *The Physics of Atmospheres*, 2nd edition, Cambridge University Press, Cambridge, 271 pp.
- Houghton, J.T., Meira Filho, L.G., Callander, B.A., Harris, N., Kattenberg, A. and Makell, K. (Eds.) 1996. *Climate Change 1995*. Intergovernmental Panel on Climate Change, Cambridge University Press, Cambridge.
- Houghton, R.A. 1995. Land-use change and the global carbon cycle. *Global Change Biology* 1, 275-287.
- Huete, A.R. 1988. A soil-adjusted vegetation index (SAVI). *Remote Sens. Environ.* 25, 295-309.
- Huete, A.R. and Jackson, R.D. 1988. Soil and atmosphere influences on the spectra of partial canopies. *Remote Sens. Environ.* 25, 89-105.
- Iacobellis S.F., Frouin R., Razafimpanilo H., Somerville R.C.J. and Piper S.C. 1994. North African savanna fires and atmospheric carbon dioxide. *J. Geophys. Res.* 99D, 8321-8334.
- Jacquemoud, S. and Baret, F. 1990. PROSPECT: A model of leaf optical properties spectra. *Remote Sens. Environ.* 34, 75-91.
- Jacquemoud, S. 1993. Inversion of the PROSPECT and SAIL canopy reflectance model from AVIRIS equivalent spectra. 1. Theoretical study. *Remote Sens. Environ.* 44, 281-292 (special issue on imaging spectrometry).
- Jarvis, P.G. 1976. The interpretation of variations in leaf water potential and stomatal conductance found in canopies in the field. *Philos. Trans. R. Soc. London Ser. B*, 273, 593-610.
- Jarvis, P.G. and McNaughton, K.G. 1986. Stomatal control of transpiration: scaling up from leaf to region. *Adv. Ecol. Res.* 15, 1-49.
- Jones, H.G. 1983. *Plants and Microclimate*. Cambridge University Press, Cambridge, 323 pp.
- Justice, C.O. (Ed.) 1986. Monitoring the grasslands of semi-arid Africa using NOAA-AVHRR data. *Int. J. Remote Sens.* 7, Vol. 11: Special Issue, 1383-1622.
- Kaduk, J. 1996. *Simulation der Kohlenstoffdynamik der globalen Landbiosphäre mit SILVAN - Modellbeschreibung und Ergebnisse*. Max-Planck-Institut für Meteorologie, Examensarbeit Nr. 42, 157 pp.
- Kaduk, J. and Heimann, M. 1994. The climate sensitivity of the Osnabrück Biosphere Model on the ENSO time scale. *Ecol. Modelling* 75/76, 239-256.

- Kaminski, Th., Giering, R. and Heimann, M. 1996. Sensitivity of the seasonal cycle of CO₂ at remote monitoring stations with respect to seasonal surface exchange fluxes determined with the adjoint of an atmospheric transport model. *Physics and Chemistry of the Earth* 21, 457-462.
- Kaminski, Th., Heimann, M. and Giering, R. 1997. A global scale inversion of the transport of CO₂ based on a matrix representation of an atmospheric transport model derived by its adjoint. Beitrag zu XXI NATO/CCMS International Technical Meeting on Air Pollution Modelling and its Application, Clermont-Ferrand, Frankreich, 2.-6. Juni.
- Kattenberg, A., Giorgi, F., Grassl, H., Meehl, G.A., Mitchell, J.F.B., Stouffer, R.J., Tokioka, T., Weaver, A.J. and Wigley T.M.L. 1996. Climate models - projections of future climate. In: *Climate Change 1995*. (Houghton, J.T., Meira Filho, L.G., Callander, B.A., Harris, N., Kattenberg, A. and Makell, K. Eds.), Intergovernmental Panel on Climate Change, Cambridge University Press, Cambridge, pp. 285-357.
- Kaufman, Y.J. 1989. The atmospheric effect on remote sensing and its correction. In: *Theory and Applications of Optical Remote Sensing*. (Asrar, G. Ed.), Wiley, New York, pp. 336-428.
- Kaufman, Y.J. and Holben, B.N. 1993. Calibration of the AVHRR visible and near infrared bands by atmospheric scattering, ocean glint, and desert reflection. *Int. J. Remote Sensing* 14, 21-52.
- Kaufman Y.J., Setzer A., Justice C., Tucker C.J., Pereira M.C. and Fung I. 1988. Remote sensing of biomass burning in the tropics. In: *Fire in the Tropical Biota*. (Goldammer J.G. Ed.), Springer-Verlag, Berlin, 371-399.
- Kauth, R.J. and Thomas, G.S. 1976. The tasseled cap - a graphic description of the spectral-temporal development of agricultural crops as seen by Landsat. In: *Machine Processing of Remotely Sensed Data*. Purdue University, West Lafayette, Indiana, U.S.A., pp. 41-51.
- Keeling, C.D. 1960. The concentration and isotopic abundance of carbon dioxide in the atmosphere. *Tellus* 12, 200-203.
- Keeling, C.D., Bacastow, R.B., Carter, A.F., Piper, S.C., Whorf, T.P., Heimann, M., Mook, W.G. and Roeloffzen, H. 1989. A three-dimensional model of atmospheric CO₂ transport based on observed winds: 1. Analysis of observational data. *AGU Monograph 55*. Washington, American Geophysical Union, 277-303.
- Keeling, C.D, Chin, J.F.S. and Whorf, T.P. 1996. Increased activity of northern vegetation inferred from atmospheric CO₂ data. *Nature* 382, 146-149.
- Keeling, R.F. and Shertz, S.R. 1992. Seasonal and interannual variations in atmospheric oxygen and implications for the global carbon cycle. *Nature* 358, 723-727.
- Kelliher, F.M., Leuning, R. and Schulze, E.-D. 1993. Evaporation and canopy characteristics of coniferous forests and grasslands. *Oecologia* 95, 152-163.
- Kelliher, F.M., Leuning, R. Raupach, M.R. and Schulze E.-D. 1995. Maximum conductances for evaporation from global vegetation types. *Agric. For. Meteorol.* 73, 1-16.
- Kicklighter, D.W., Bondeau, A., Schloss, A.L., Plöchl, M., McGuire, A.D. and workshop participants 1997. Comparing global models of terrestrial net primary productivity (NPP): Global pattern and differentiation by major biomes. Manuscript submitted to *Global Change Biology*.

- Kidwell, K.B. (Ed.) 1990. *Global Vegetation Index User's Guide*. National Oceanic and Atmospheric Administration, Washington D.C.
- Kim, J. and Verma, S.B. 1991a. Modeling canopy stomatal conductance in a temperate grassland ecosystem. *Agric. For. Meteorol.* 55, 149-166.
- Kim, J. and Verma, S.B. 1991b. Modeling canopy photosynthesis: scaling up from a leaf to canopy in a temperate grassland ecosystem. *Agric For. Meteorol.* 57, 187-208.
- Kleidon, A. and Heimann, M. 1997. *A method for determining rooting depth from a terrestrial biosphere model and its impacts on the global water and carbon cycle*. Max-Planck-Institut für Meteorologie Report Nr. 230, Hamburg, 24 pp.
- Knorr, W. and Heimann, M. 1995. Impact of drought stress and other factors on seasonal land biosphere CO₂ exchange studied through an atmospheric tracer transport model. *Tellus* 47B, 471-489.
- Knorr, W., Gobron, N., Martin, Ph., Pinty, B., Verstraete, M.M. and Dedieu, G. 1995. Constraining a climate driven vegetation model with satellite data. In: *Proceedings of the Photosynthesis and Remote Sensing Symposium*, Montpellier, France, 28-30 August.
- Körner, Ch. 1991. Some often overlooked plant characteristics as determinants of plant growth: a reconsideration. *Functional Ecology* 5, 162-173.
- Koslowsky, D. 1996. *Mehrjährige validierte und homogenisierte Reihen des Reflexionsgrades und des Vegetationsindex von Landoberflächen aus täglichen AVHRR-Daten hoher Auflösung*. Meteorologische Abhandlungen des Institutes für Meteorologie der Freien Universität Berlin, Band 9, Heft 1, 248 pp.
- Kurz, W. and Apps, M.J. 1994. The carbon budget of Canadian forests: a sensitivity analysis of changes in disturbance regimes, growth rates, and decomposition rates. *Environmental Pollution* 83, 55-61.
- Lambin, E.F. and Strahler, A.H. 1994. Change-vector analysis in multitemporal space: a tool to detect and categorize land-cover change processes using high temporal-resolution satellite data. *Remote Sens. Environ.* 47, 1-25.
- Lee, T.Y. and Kaufman, Y.J. 1986. Non-lambertian effects on the remote sensing of surface reflectance and vegetation index. *IEEE Trans. Geosc. Remote Sens.* 24, 699-708.
- Leemans, R. and Cramer, W. 1991. *The IIASA climate database for mean monthly values of temperature, precipitation and cloudiness on a terrestrial grid*. RR-91-18. Institute of Applied Systems Analysis, Laxenburg, Austria.
- Leprieur, C., Verstraete, M.M. and Pinty, B. 1994. Evaluation of the performance of various vegetation indices to retrieve vegetation cover from AVHRR data. *Remote Sens. Rev.* 10, 265-284.
- Lieth, H. 1975. Primary production of the major vegetation units of the world. In: *Primary productivity of the biosphere*. (Lieth, H. and Whittaker, R.H. Eds.), Springer Verlag, New York.
- Linacre, E.T. 1968. Estimating the net-radiation flux. *Agr. Meteorol.* 5, 49-63.
- Lindroth, A. and Halldin, S. 1986. Numerical analysis of pine forest evaporation and surface resistance. *Agric. For. Meteorol.* 38, 59-79.

- Lloyd, D. 1990. A phenological classification of terrestrial vegetation cover using shortwave index imagery. *Int. J. Remote Sensing* 11, 2269-2279.
- Lloyd, J. and Farquhar, G.D. 1994. ^{13}C discrimination during CO_2 assimilation by the terrestrial biosphere. *Oecologia* 99, 210-215.
- Long, S.P., Garcia Moya, E., Imbamba, S.K., Kamnalrut, A., Piedade, M.T.F., Scurlock, J.M.O., Shen, Y.K. and Hall, D.O. 1989. Primary productivity of natural grass ecosystems of the tropics: a reappraisal. *Plant and Soil* 115, 155-166.
- Los, S.O., Justice, C.O. and Tucker, C.J. 1994. A global 1° by 1° NDVI data set for climate studies derived from the GIMMS continental NDVI data. *Int. J. Remote Sensing* 15, 3493-3518.
- Loth, B. and Graf, H.F. 1996. *Modelling the snow cover for climate studies*. Max-Planck-Institut für Meteorologie Report Nr. 190, Hamburg, 63 pp.
- Lüdeke, M.K.B., Badeck, F.-W., Otto, R.D., Häger, C., Dönges, S., Kindermann, J., Würth, G., Lang, T., Jäkel, U., Klaudus, A., Ramge, P., Habermehl, S. and Kohlmaier, G.H. 1994. The Frankfurt Biosphere Model: a global process oriented model of seasonal and long-term CO_2 exchange between terrestrial ecosystems and the atmosphere. I. Model description and illustrative results for cold deciduous and boreal forests. *Clim. Res.* 4, 143-166.
- Lugo A.E. and Murphy P.G. 1986. Nutrient dynamics of a Puerto Rican subtropical dry forest. *Journal of Tropical Ecology* 2, 55-72.
- Luxmoore, R.J. 1991. A source sink framework for coupling water, carbon and nutrient dynamics of vegetation. *Tree Physiol.* 9, 267-280.
- Malingreau, J.-P. 1986. Global vegetation dynamics: satellite observations over Asia. *Int. J. Remote Sens.* 7, 1121-1146.
- Malingreau, J.-P., Tucker, C.J. and Laporte, N. 1989. AVHRR for monitoring global tropical deforestation. *Int. J. Remote Sens.* 10, 855-867.
- Martin, Ph. 1993. Vegetation response and feedbacks to climate: a review of models and processes. *Climate Dynamics* 8, 201-210.
- Mascart, P., Taconet, O., Pinty, J.P. and Ben Mehrez, M. 1991. Canopy resistance formulation and its effect in mesoscale models: a HAPEX perspective. *Agric. For. Meteorol.* 54, 319-351.
- Matthews, E. 1983. Global vegetation and land use: New high resolution data bases for climate studies. *J. Clim. Appl. Meteorol.* 22, 474-487.
- Mayaux, P. and Lambin, E. 1997. Tropical forest area measured from global land-cover classifications: Inverse calibration models based on spatial textures. *Remote Sens. Environ.* 59, 29-43.
- McNaughton, K.G. and Jarvis, P.G. 1983. Predicting effects of vegetation changes on transpiration and evaporation. In: *Water Deficit and Plant Growth*. (Kozlowski, T.T. Ed.), Academic Press, New York, pp. 1-47.
- McNaughton, K.G. and Jarvis, P.G. 1991. Effects of spatial scale on stomatal control of transpiration. *Agric. For. Meteorol.* 54, 279-301.

- Meentemeyer, V. 1978. Macroclimate and lignin control of litter decomposition rates. *Ecology* 59, 465-472.
- Melillo, J.M., Prentice, I.C., Farquhar, G.D., Schulze, E.-D. and Sala, O.E. 1996. Terrestrial biotic responses to environmental change and feedbacks to climate. In: *Climate Change 1995*. (Houghton, J.T., Meira Filho, L.G., Callander, B.A., Harris, N., Kattenberg, A. and Makell, K. Eds.), Intergovernmental Panel on Climate Change, Cambridge University Press, Cambridge, pp. 449-481.
- Meyer, D., Verstraete, M.M. and Pinty, B. 1995. The effect of surface anisotropy and viewing geometry on the estimation of NDVI from AVHRR. *Remote Sensing Rev.* 12, 3-27.
- Monsi, M. and Saeki, T. 1953. Über den Lichtfaktor in den Pflanzengesellschaften und seine Bedeutung für die Stoffproduktion. *Japanese Journal of Botany* 14, 22-52.
- Monteith, J.L. 1965a. Light distribution and photosynthesis in field crops. *Annals of Botany* 29, 17-37.
- Monteith, J.L. 1965b. Evaporation and environment. *Symposium of the Society for Experimental Biology* 19, 205-234.
- Monteith, J.L. 1977. Climate and the efficiency of crop production in Britain. *Philosophical Transaction of the Royal Society of London Series B*, 281, 277-294.
- Mooney, H.A. and Winner, W.W. 1991. Partitioning response of plants to stress. In: *Response of Plants to Multiple Stresses*. (Mooney, H.A., Winner, W.E., Pell, E.J. and Chu, E. Eds.), Academic Press, San Diego, U.S.A., pp. 129-141.
- Moore, T.R. 1983. Winter-time decomposition in a subarctic woodland. *Arct. Alp. Res.* 15, 413-418.
- Morison J.I.L. 1987. Intercellular CO₂ concentration and stomatal response to CO₂. In: *Stomatal Function*. (Zeiger, E., Farquhar, G.D. und Cowan, I.R. Eds.), Stanford University Press, Stanford, U.S.A., pp. 229-251.
- Müller, M.J. 1982. *Selected climatic data for a global set of standard stations for vegetation science*. Junk, Den Haag, Netherlands.
- Murphy, P.G. 1975. Net primary productivity in tropical terrestrial ecosystems. In: *Primary productivity of the biosphere*. (Lieth, H. and Whittaker, R.H. Eds.), Springer Verlag, New York.
- Murray, F.W. 1967. On the computation of saturation vapour pressure. *J. Appl. Meteorol.* 6, 203-204.
- Myneni, R.B., Ganapol, B.D. and Asrar, G. 1992. Remote sensing of vegetation canopy photosynthetic and stomatal conductance efficiencies. *Remote Sens. Environ.* 42, 217-238.
- Myneni, R.B., Maggion, S., Iaquinta, J., Privette, J.L., Gobron, N., Pinty, B., Kimes, D.S., Verstraete, M.M. and Williams D.L. 1995. Optical remote sensing of vegetation: modeling, caveats, and algorithms. *Remote Sens. Environ.* 51, 169-188.
- Myneni, R.B., Keeling, C.D., Tucker, C.J., Asrar, G. and Nemani, R.R. 1997. Increased plant growth in the northern high latitudes from 1981 to 1991. *Nature* 386, 698-702.

- Nakazawa, T., Morimoto, Sh., Aoki, Sh. and Masayuki, T. 1993. Time and space variations of the carbon isotopic ratio of tropospheric carbon dioxide over Japan. *Tellus* 45B, 258-274.
- Nepstad, D.C., de Carvalho, C.R., Davidson, E.A., Jipp, P.H., Lefebvre, P.A. Negeiros, G.H., da Silva, E.D., Stone, T.A., Trumbore, S.E. and Vieira, S. 1994. The role of deep roots in the hydrological and carbon cycles of Amazonian forests and pastures. *Nature* 372, 666-669.
- Norwine, J. and Greigor, D.H. 1983. Vegetation classification based on Advanced Very High Resolution Radiometer (AVHRR) satellite imagery. *Remote Sens. Environ.* 13, 67-87.
- Norman, J.M., Garcia, R. and Verma, S.B. 1992. Soil surface CO₂ fluxes and the carbon budget of a grassland. *J. Geophys. Res.* 97, 18845-18853.
- Olson, J.S., Watts, J.A. and Allison, L.J. 1983. *Carbon in live vegetation of major world ecosystems*. Oak Ridge/Tennessee: Environmental Sciences Division Publication Number 1997.
- Oort, A.H. 1983. *Global atmospheric circulation statistics: 1958-1979*. NOAA professional papers 14, Rockville, Maryland, U.S.A.
- Paltridge, G. W. and Platt, C.M. 1976. *Radiative Processes in Meteorology and Climatology*, Elsevier Publishing, New York.
- Paruelo, J.M., Aguiar, M.R. and Golluscio, R.A. 1991. Evaporation estimates in arid environments: an evaluation of some methods for the Patagonian steppe. *Agric. For. Meteorol.* 55, 127-132.
- Paruelo, J.M. and Lauenroth, W.K. 1996. Relative abundance of plant functional types in grasslands and shrublands of North America. *Ecol. Appl.* 6, 1212-1224.
- Paruelo, J.M., Jobbagy, E.G., Sala, O.E., Lauenroth, W.K. and Burke, I.C. 1997. Functional and structural convergence of temperate grassland and shrubland ecosystems. *Ecol. Appl.*, submitted.
- Pearson, R. L. and Miller L.D. 1972. Remote mapping of standing crop biomass for estimation of the productivity of the shortgrass prairie. In: *Proc. 8th Int. Symp. Remote Sens. Environ.*, University of Michigan, Ann Arbor, pp. 1357-1381.
- Philip, J.R. 1957. Evaporation, and moisture and heat fields in the soil. *J. Meteorol.* 14, 139-158.
- Pinker, R.T. and Laszlo, I. 1992. Global distribution of photosynthetically active radiation as observed from satellites. *J. Clim.* 5, 56-65.
- Pinty, B. and Verstraete, M.M. 1991. Extracting information on surface properties from bidirectional reflectance measurements. *J. Geophys. Res.* 96, 2865-2874.
- Pinty, B. and Verstraete, M.M. 1992a. GEMI: A non-linear index to monitor global vegetation from satellites. *Vegetatio* 101, 1335-1372.
- Pinty, B. and Verstraete, M.M. 1992b. On the design and validation of surface bidirectional reflectance and albedo models. *Remote Sens. Environ.* 41, 155-167.
- Pinty, B., Verstraete, M.M. and Dickinson R.E. 1989. A physical model for predicting bidirectional reflectances over bare soil. *Remote Sens. Environ.* 27, 273-288.
- Pinty, B., Leprieur, C. and Verstraete, M.M. 1993. Towards a quantitative interpretation of vegetation indices. Part 1: Biophysical canopy properties and classical indices. *Remote Sens. Rev.* 7, 127-150.

- Potter, S.C., Randerson, J.T., Field, C.B., Matson, P.A., Vitousek, P.M., Mooney, H.A. and Klooster, S.A. 1993. Terrestrial ecosystem production: a process model based on global satellite and surface data. *Global Biogeochem. Cycles* 7, 811-841.
- Prentice, I.C., Cramer, W., Harrison, S.P., Leemans, R., Monserud, R.A. and Solomon, A.M. 1992. A global biome model based on plant physiology and dominance, soil properties and climate. *J. Biogeogr.* 19, 117-134.
- Price, J.C. and Bausch, W.C. 1995. Leaf area index estimation from visible and near-infrared reflectance data. *Remote Sens. Environ.* 52, 55-63.
- Prince, S.D. 1991. A model of regional primary productivity for use with coarse resolution satellite data. *Int. J. Remote Sensing* 12, 1313-1330.
- Prince, S.D. and Goward, S.N. 1996. Global net primary production: The remote sensing approach. *J. Biogeography* 6, 1212-1224.
- Rahman, H. and Dedieu, G. 1994. SMAC: A simplified method for the atmospheric correction of satellite measurements in the solar spectrum. *Int. J. Remote Sensing* 15, 123-143.
- Raich, J.W. and Schlesinger, W.H. 1992. The global carbon dioxide flux in soil respiration and its relationship to vegetation and climate. *Tellus* 44B, 81-99.
- Raich, J.W., Rastetter, E.B., Melillo, J.M., Kicklighter, D.W., Steudler, P.A., Peterson, B.J., Grace, A.L., Moore III, B. and Vörösmarty, C.J. 1991. Potential net primary productivity in South America: application of a global model. *Ecol. Appl.* 1, 399-429.
- Raich, J.W. and Potter C.S. 1995. Global patterns of carbon dioxide emissions from soils. *Global Biogeochem. Cycles* 9, 23-36.
- Ramonet, M. 1994. *Variabilité du CO₂ atmosphérique en régions australes: comparaison modèle/mesures*. PhD thesis, University of Paris 7, 295 pp.
- Richardson, A.J. and Wiegand, C.L. 1977. Distinguishing vegetation from soil background information. *Photogramm. Eng. Remote Sens.* 42, 317-324.
- Ritchie, J.T. 1972. Model for predicting evaporation from a row crop with incomplete cover. *Water Resour. Res.* 8, 1204-1213.
- Robock, A., Vinnikov, K.Ya., Schlosser, C.A., Speranskaya, N.A. and Xue, Y.-K. 1995. Use of midlatitude soil moisture and meteorological observations to validate soil moisture simulations with biosphere and bucket models. *J. Climate* 8, 15-35.
- Rosenberg, N.J. 1974. *Microclimate: The Biological Environment*. Wiley, New York, 315 pp.
- Ross, J. 1975. Radiative transfer in plant communities. In: *Vegetation and the Atmosphere, Vol. 1: Principles*. (Monteith, J. L. Ed.), Academic Press, San Diego, U.S.A., pp. 13-55.
- Ross, J. 1981. *The radiation Regime and Architecture of Plant Stands*. Junk, Den Haag, Netherlands.
- Ruimy, A., Saugier, B. and Dedieu, G. 1994. Methodology for the estimation of terrestrial net primary production from remotely sensed data. *J. Geophys. Res.* 99, 5263-5283.
- Ruimy, A., Dedieu, G. and Saugier, B. 1996. TURC: A diagnostic model of continental gross primary productivity and net primary productivity. *Global Biogeochem. Cycles* 10, 269-285.

- Ruimy, A., Kergoat, L., Bondeau, A. and workshop participants 1997. Comparing global models of terrestrial net primary productivity (NPP): Analysis of differences in light absorption, light-use efficiency and whole plant respiration cost. Manuscript submitted to *Global Change Biology*.
- Running, S.W. 1984. *Documentation and Preliminary Validation of H2OTRANS and DAYTRANS, Two Models for Predicting Transpiration and Water Stress in Western Coniferous Forests*. USDA Forests Service Research Papers RM-252.
- Running, S.W. and Coughlan, J.C. 1988. A general model of forest ecosystem processes for regional applications. I. Hydrological balance, canopy gas exchange and primary productivity. *Ecol. Modelling* 42, 125-154.
- Running, S.W. and Hunt Jr., E.R. 1993. Generalization of a forest ecosystem model for other biomes, BIOME-BGC, and an application for global-scale models. In: *Scaling Physiological Processes: Leaf to Globe* (Ehlinger, J.R. and Field, C. Eds.), Academic Press, San Diego, pp. 141-158.
- Running, S., Nemani, R. and Hungerford R. 1987. Extrapolation of synoptic meteorological data in mountainous terrain and its use for simulating forest evapotranspiration and photosynthesis. *Canadian J. Forestry Res.* 17, 472-483.
- Running, S.W., Justice, C.O., Salomonson, V.V., Hall, D., Barker, J., Kaufman, Y.J., Strahler, A.H., Huete, A.R., Muller, J.-P., Vanderbilt, V., Wan, Z.M., Teillet, P. and Carneggie, D. 1994. Terrestrial remote sensing science and algorithms planned for EOS/MODIS. *Int. J. Remote Sens.* 15, 3587-3620.
- Ryan, M.G. 1991a. Effects of climate change on plant respiration. *Ecol. Appl.* 1, 157-167.
- Ryan, M.G. 1991b. A simple method for estimating gross carbon budgets of vegetation in forest ecosystems. *Tree Physiol.* 9, 255-266.
- Sabins Jr., F. F. 1987. *Remote Sensing: Principles and Interpretation*, 2nd edition, W.H. Freeman and Company, New York.
- Sala O.E., Parton, W.J., Joyce L.A. and Lauenroth W.K. 1988. Primary productivity of the central grassland region of the United States. *Ecology* 69, 40-45.
- Saxton, K.E., Rawls, W.J., Romberger, J.S. and Papendick R.I. 1986. Estimating generalized soil-water characteristics. *Soil Sci. Soc. Am. J.* 50, 1031-1036.
- Schimel, D.S. 1995. Terrestrial ecosystems and the carbon cycle. *Global Change Biology* 1, 77-91.
- Schimel, D.S., Alves, D., Enting, I., Heimann, M., Joos, F., Raynaud, D. and Wigley, T. 1996. The global carbon cycle. In: *Climate Change 1995*. (Houghton, J.T., Meira Filho, L.G., Callander, B.A., Harris, N., Kattenberg, A. and Makell, K. Eds.), Intergovernmental Panel on Climate Change, Cambridge University Press, Cambridge, pp. 76-86.
- Schulze, E.-D. 1986. Carbon dioxide and water exchange in response to drought in the atmosphere and in the soil. *Ann. Rev. Plant Physiol.* 13, 127-141.
- Schulze, E.-D., Turner, N.C., Gollan, T. and Shackel, K.A. 1987. Stomatal Response to air humidity and to soil drought. In: *Stomatal Function*. (Zeiger, E., Farquhar, G.D. and Cowan, I.R. Eds.), Stanford University Press, Stanford, U.S.A., pp. 311-321.

- Schulze, E.-D., Kelliher, F.M., Körner, Ch., Lloyd, J. and Leuning, R. 1994. Relationships among maximum stomatal conductance, ecosystem surface conductance, carbon assimilation rate, and plant nitrogen nutrition: a global ecology scaling exercise. *Ann. Rev. Ecol. Syst.* 25, 629-660.
- Sellers, P.J. 1985. Canopy reflectance, photosynthesis and transpiration. *Int. J. Remote Sensing* 6, 1335-1372.
- Sellers, P.J., Mintz, Y., Sud, Y.C. and Dalcher, A. 1986. The designs of a simple biosphere model (SiB) for use within general circulation models. *J. Atmos. Sci.* 43, 505-531.
- Sellers, P.J., Hall, F.G., Asrar, G., Strebel, D.E. and Murphy, R.E. 1988. The First ISLSCP Field Experiment (FIFE). *Bull. Am. Meteorol. Soc.* 69, 22-27.
- Sellers, P.J., Berry, J.A., Collatz, G.J., Field, C.B. and Hall, F.G. 1992. Canopy reflectance, photosynthesis and transpiration, III. A reanalysis using enzyme kinetics - electron transport models of leaf physiology. *Remote Sens. Environ.* 42, 187-216.
- Sellers, P.J., Tucker, C.J., Collatz, G.J., Los, S.O., Justice, C.O., Dazlich, D.A. and Randall, D.A. 1994. A global 1° by 1° NDVI data set for climate studies. Part 2: The generation of global fields of terrestrial biophysical parameters from the NDVI. *Int. J. Remote Sensing* 15, 3519-3545.
- Sellers, P.J., Randall, D.A., Collatz, G.J., Berry, J.A., Field, C.B., Dazlich, D. A., Zhang, C. and Collelo, G.D. 1996. A revised land surface parameterization (SiB2) for atmospheric GCMs. Part 1: Model formulation. *J. Climate* 9, 676-705.
- Sharkey, D.T. and Ogawa, T. 1987. Stomatal Responses to Light. In: *Stomatal Function*. (Zeiger, E., Farquhar, G.D. and Cowan, I.R. Eds.), Stanford University Press, Stanford, U.S.A., pp. 195-208.
- Shuttleworth W.J. 1988. Evaporation from Amazonian rainforest. *Proc. R. Soc. Lond. B*, 321-346.
- Six, K.D. and Maier-Reimer, E. 1996. Effects of plankton dynamics on seasonal carbon fluxes in an ocean general circulation model. *Global Biogeochem. Cycles* 10, 559-583.
- Solomon, D.K. and Cerling, T.E. 1987. The annual carbon dioxide cycle in a montane soil: observations, modeling, and implications for weathering. *Water Resour. Res.* 23, 2257-2265.
- Stewart, J.B. 1988. Modelling surface conductance of a pine forest. *Agric. For. Meteorol.* 43, 19-35.
- Stohlgren, T.J. 1988. Litter dynamics in two Sierran mixed conifer forests. I. Litterfall and decomposition rates. *Can. J. For. Res.* 18, 1127-1135.
- Taylor, B.R. and Jones, H.G. 1990. Litter decomposition under snow cover in a balsam fir forest. *Can. J. Bot.* 68, 112-120.
- Townshend, J.R.G. 1994. Global data sets for land applications from the Advanced Very High Resolution Radiometer: An introduction. *Int. J. Remote Sens.* 15, 3319-3332.
- Townshend, J.R.G., Justice, C.O., Skole, D., Malingreau, J.-P., Cihlar, J., Teillet, P., Sadowski, F. and Ruttenberg, S. 1994. The 1 km resolution global data set: Needs of the International Geosphere Biosphere Programme. *Int. J. Remote Sens.* 15, 3417-3441.

- Tenhunen, J.D, Pearcy, R.W. and Lange, O.L. 1987. Diurnal variations in leaf conductance and gas exchange in natural environments. In: *Stomatal Function*. (Zeiger, E., Farquhar, G.D. and Cowan, I.R. Eds.), Stanford University Press, Stanford, U.S.A., pp. 323-351.
- Thomas, G. and Henderson-Sellers, A. 1987. Evaluation of satellite-derived land-cover classification by remote sensing: present capabilities and future possibilities. *Climate Change* 11, 313-348.
- Tucker, C.J., Holben, B.N. and Goff, T.E. 1984. Intensive forest clearing in Rondonia, Brazil, as detected by satellite remote sensing. *Remote Sens. Environ.* 15, 255-261.
- Tucker, C.J., Townshend, J.R. and Goff, T.E. 1985. African land-cover classification using satellite data. *Science* 224, 369-375.
- Tucker, C.J., Dregne, H.E. and Newcomb, W.W. 1991. Expansion and contraction of the Sahara desert from 1980 to 1990. *Science* 253, 299-301.
- Turner, N.C. 1986. Adaptation to water deficits: a changing perspective. *Aust. J. Plant Physiol.* 13, 175-190.
- Turner, N.C., Schulze, E.-D. and Gollan, T. 1984. The responses of stomata to vapour pressure deficits and soil water content. I. Species comparison at high soil water contents. *Oecologia* 6, 338-342.
- Ulaby, F.T., Sarabandi, K., McDonald, K., Whitt, M. and Dobson, M.C. 1990. Michigan microwave canopy scattering model. *Int. J. Remote Sensing* 11, 1223-1253.
- Verma, S.B., Baldocchi, D.D., Anderson, D.E., Matt, D.R. and Clement, R.J. 1986. Eddy fluxes of CO₂, water vapor and sensible heat over a deciduous forest. *Boundary Layer Meteorol.* 36, 71-91.
- Verstraete, M.M. 1987. Radiation transfer in plant canopies: Transmission of direct solar radiation and the role of leaf orientation. *J. Geophys. Res.* 92, 10985-10995.
- Verstraete, M.M. 1994. Retrieving canopy properties from remote sensing measurements. In: *Imaging Spectrometry - a tool for Environmental Observations*. (Hill, J. and M egier, J. Eds.), ECSC, EEC, EAEC, Brussels and Luxemburg, pp. 109-123.
- Verstraete, M.M. and Pinty, B. 1996. Designing optimal spectral vegetation indices for remote sensing applications. *IEEE Trans. Geosc. Remote Sensing*, 34, 1254-1265.
- Verstraete, M.M., Pinty, B. and Dickinson, R.E. 1990. A physical model of the bidirectional reflectance of vegetation canopies. 1. Theory. *J. Geophys. Res.* 95, 11775-11765.
- Vogt, K.A., Edmonds, R.L., Antos, G.C. and Vogt, D.J. 1980. Relationships between CO₂ evolution, ATP concentrations and decomposition in four forest ecosystems in western Washington. *Oikos* 35, 72-79.
- Walker, B.H. and Steffen, W. L. (Eds.) 1995. *Global Change and Terrestrial Ecosystems*, Cambridge University Press, Cambridge.
- Walter, H. and Breckle, S.-W. 1990. * kologie der Erde. Vol. 2: Spezielle  kologie der tropischen and subtropischen Zonen*. 2nd edition, Gustav Fischer Verlag, Stuttgart, 461 pp.
- Walter, H. and Breckle, S.-W. 1991. * kologie der Erde. Vol. 4: Spezielle  kologie der gem aigten Zonen au erhalb Euro-Nordasiens*. Gustav Fischer Verlag, Stuttgart, 726 pp.

- Walter, H. and Breckle, S.-W. 1994. *Ökologie der Erde. Vol. 3: Spezielle Ökologie der gemäßigten Zonen Euro-Nordasiens*. 2nd revised edition, Gustav Fischer Verlag, Stuttgart, 586 pp.
- Warnant, P., François, L., Strivay, D. and Gérard, J.C. 1994. CARAIB: A global model of terrestrial biological productivity. *Global Biogeochem. Cycles* 8, 255-270.
- Webb, R.S., Rosenzweig, C.E. and Levine, E.R. 1991. *A Global Data Set of Soil Particle Size Properties*. Digital raster data on 1-degree geographic 180×360 grid. NASA Goddard Institute of Space Studies, New York.
- Weiss, A. and Norman, J.A. 1985. Partitioning solar radiation into direct and diffuse, visible and near-infrared components. *Agric. For. Meteorol.* 34, 205-213.
- Wharton, S.W. 1989. Knowledge-based spectral classification of remotely sensed image data. In: *Theory and Applications of Optical Remote Sensing*. (Asrar, G. Ed.), Wiley, New York, pp. 548-577.
- Wigmosta, M.S., Vail, L. and Lettenmaier, D.P. 1994. A distributed hydrology-vegetation model for complex terrain. *Water Resour. Res.* 30, 1665-1679.
- Wilson, M.F. and Henderson-Sellers, A. 1985. A global archive of land cover and soils data for use in general circulation models. *J. Clim.* 5, 119-143.
- Winston, G.C., Stephens, B.B., Sundquist, E.T, Hardy, J.P. and Davis, R.E. 1995. Seasonal variability in CO₂ transport through snow in a boreal forest. In: *Biogeochemistry of Seasonally Snow Covered Catchments* (Tonnessen, K., Williams, M.W. and Tranter, M. Eds.), Proceedings Boulder Symposium, July 1995, IAHS Publ. no. 228, pp. 61-70.
- Wofsy, S.C., Goulden, M.L., Unger, J.W., Fan, S.-M., Bakwin, P.S., Daube, B.C., Bassow, S.L. and Bazzaz, F.A. 1993. Net exchange of CO₂ in a mid-latitude forest. *Science* 260, 1314-1317.
- Woodward, F.I. 1987. *Climate and Plant Distribution*. Cambridge University Press, Cambridge.
- Woodward, F.I., Smith, T.M. and Emanuel, W. R. 1995. A global land primary productivity and phytogeography model. *Global Biogeochem. Cycles* 9, 471-490.
- Wullschleger, S. D. 1993. Biochemical limitations to carbon assimilation in C3 plants - a retrospective analysis of the A / c_i curves from 109 species. *J. Exp. Bot.* 44, 907-920.
- Zeiger, E., Farquhar, G.D. and Cowan, I.R. (Eds.) 1987. *Stomatal Function*. Stanford University Press, Stanford, U.S.A.

Acknowledgments

I wish to thank Professor Klaus Hasselmann for making it possible that I could spend my time at the Max-Planck-Institut für Meteorologie to write this dissertation. I thank Dr. Martin Heimann for having accepted me into his ever more thriving research group, for his steady and patient support and for having the confidence that after long years some satisfactory result would come out of this piece of work. His enthusiasm and his profound knowledge have also been a great source of motivation. I would also like to thank both for giving me the opportunity to spend part of my work at the EU joint research centre at Ispra, Italy. Here, I shall mention Jean-Paul Malingreau as the head of the department 'Monitoring Tropical Vegetation'. There, I enjoyed to have two advisers, Michel Verstraete and Philippe Martin, whom I owe the decisive inspiration and insight into the fields of remote sensing, and of functional geobotany and agrometeorology. Their support has been decisive for carrying through this project. In this context, I would also like to mention Bernard Pinty, who has always had an open ear for scientific discussions, and Nadine Gobron for letting me use the model of her own dissertation.

Most of all, however, I wish to express my gratitude to Bettina Düker. For most of the time that we have known each other, I have been involved in this work, and therefore she has come to live with me through all the ups and downs of the process. I thank her for always being so motivating, which has given me the strength to continue and eventually to finish up, and for her understanding of my scientific fervour that has, among other things, lead me to spend a full year abroad.

For special help, I also thank Jörg Kaduk, Thomas Kaminski, Axel Kleidon, Bettina Loth, Walter Sauf, Arne Winguth, Yves Govaerts, and the technical division of the 'Deutsches Klimarechenzentrum' and the 'Institute for Remote Sensing Applications'. Katharina Six, Georg Hoffmann, Bernadette Walter, Ola Engelsen, Daniele Ehrlich, Ranga Myneni and the other members and guests of the two institutes have given me valuable ideas and insights during numerous discussions.

- | | |
|---|--|
| EXAMENSARBEIT Nr. 14 März 1992 | Windinduzierte interannuale Variabilität in der Warmwassersphäre von 1981 bis 1987 Teil II: Fluktuationen im Kohlenstoffkreislauf Arne M. E. Winguth |
| EXAMENSARBEIT Nr. 15 Dezember 1992 | Fernerkundung der optischen Eigenschaften von Seen mit Landsat 5 Thematic Mapper Waltraud Manschke |
| EXAMENSARBEIT Nr. 16 Juli 1993 | Baroklin instabile Wellen der Atmosphäre: Empirisch abgeleitete Moden im Vergleich zu quasi-geostrophischer Theorie Reiner Schnur |
| EXAMENSARBEIT Nr. 17 September 1993 | Messung des Wasserdampfstromes in der konvektiven Grenzschicht mit DIAL und RADAR-RASS Christoph Senff |
| EXAMENSARBEIT Nr. 18 November 1993 | Zur saisonalen Variation des ozeanischen Kohlendioxidpartialdrucks Katharina D. Kurz |
| EXAMENSARBEIT Nr. 19 Januar 1994 | Dynamisch-stochastische Vorhersage-Experimente mit Modellen der allgemeinen Zirkulation für einen Zeitraum von 10 Tagen bis 100 Jahren Ulrich Cubasch |
| EXAMENSARBEIT Nr. 20 Februar 1994 | Deposition radioaktiver Tracer in einem Transportmodell der Atmosphäre Stefan Rehfeld |
| EXAMENSARBEIT Nr. 21 Februar 1994 | Der Einfluß vulkanischen Aerosols und simultaner Temperaturanomalien der tropischen Meeresoberfläche (El Niño) auf das Klimasystem Ingo Kirchner |
| EXAMENSARBEIT Nr. 22 Juni 1994 | ENSO induzierte Variabilität im Indischen Ozean Andreas Villwock |
| EXAMENSARBEIT Nr. 23 Juni 1994 | Untersuchungen zu Mechanismus und Vorhersagbarkeit von ENSO mit einem vereinfachten gekoppelten Ozean - Atmosphäre - Modell Moritz Flügel |
| EXAMENSARBEIT Nr. 24 Juli 1994 | Nordatlantische Variabilität in einem Ozeanzirkulationsmodell im Zeitbereich von Dekaden Ralf Weiße |
| EXAMENSARBEIT Nr.25 August 1994 | Inverse Modellierung des atmosphärischen Methan-Kreislaufs unter Verwendung eines drei-dimensionalen Modells des Transports und der Chemie der Troposphäre Ralf Hein |
| EXAMENSARBEIT Nr. 26 August 1994 | Optimierung eines Seegangmodells mit der Adjungierten Methode Georg Barzel |
| EXAMENSARBEIT Nr. 27 März 1995 | Stabile Wasserisotope im allgemeinen Zirkulationsmodell ECHAM Georg Hoffmann |

-
- | | |
|--|--|
| EXAMENSARBEIT Nr. 28 Mai 1995 | The Atmospheric Response to North Atlantic Sea Surface Temperature Anomalies in GCM Experiments Viacheslav V. Kharin |
| EXAMENSARBEIT Nr. 29 Juni 1995 | Einbindung der regionalen troposphärischen Chemie in die Hamburger Klimamodellumgebung: Modellrechnungen und Vergleich mit Beobachtungsdaten Bärbel Langmann |
| EXAMENSARBEIT Nr. 30 Juli 1995 | Messung des Ozonflusses in der unteren Troposphäre mit einem neuen Ozon-DIAL-System und einem Radar-RASS Thorsten Schaberl |
| EXAMENSARBEIT Nr. 31 November 1995 | Untersuchungen troposphärischen Ozons mit DIAL Gunther C. Grabbe |
| EXAMENSARBEIT Nr. 32 November 1995 | Die Schneedecke als Komponente des Klimasystems und ihre Modellierung Bettina Loth |
| EXAMENSARBEIT Nr. 33 Dezember 1995 | Der Einfluß des El Niño/Southern Oscillation Phänomens auf die atmosphärische Zirkulation in den mittleren Breiten der Nordhalbkugel: Beobachtungen und Modellsimulationen Wilhelm May |
| EXAMENSARBEIT Nr. 34 Dezember 1995 | DIAL-Messungen von vertikalen Wasserdampfverteilungen Ein Lasersystem für Wasserdampf- und Temperaturmessungen in der Troposphäre Volker Wulfmeyer |
| EXAMENSARBEIT Nr. 35 Januar 1996 | Der Einfluß von Datenassimilation auf ENSO Simulationen und Vorhersagen Martin Fischer |
| EXAMENSARBEIT Nr. 36 Februar 1996 | Bodengebundene Fernerkundung von Eiswolken im nahen Infrarot Margarita Betancor Gothe |
| EXAMENSARBEIT Nr. 37 März 1996 | Turbulenzcharakteristiken von Golfstromtrajektorien in einem quasigeostrophischen Zirkulationsmodell basierend auf Lagrange'schen Vorticitytracern Miguel Zorita Calvo |
| EXAMENSARBEIT Nr. 38 Mai 1996 | Entwicklung eines Kopplungsverfahrens zur Reduzierung der Rechenzeit von Atmosphäre-Ozean-Modellen Reinhard Voß |
| EXAMENSARBEIT Nr. 39 Mai 1996 | Kombination von Ensemble-Klimavorhersagen am Beispiel ENSO Sven Marcus Metzger (März 1995) |
| EXAMENSARBEIT Nr.40 Juni 1996 | Der Einfluß der quasi-zweijährigen Oszillation auf die allgemeine Zirkulation: Modellsimulationen mit ECHAM4 Marco Andrea Giorgetta |
| EXAMENSARBEIT Nr. 41 Juli 1996 | Sensitivität des Modellklimas eines globalen Zirkulationsmodells der Atmosphäre gegenüber Änderungen der Wolkenmikrophysik Ulrike Lohmann |
| EXAMENSARBEIT Nr. 42 July 1996 | Simulation der Kohlenstoffdynamik der globalen Landbiosphäre mit SILVAN-Modellbeschreibung und Ergebnisse Jörg Kaduk |

-
- | | |
|--|---|
| EXAMENSARBEIT Nr. 43 Oktober 1996 | Zur Dynamik des interhemisphärischen CO₂-Transports im Ozean Christine Weber |
| EXAMENSARBEIT Nr. 44 November 1996 | Erstellung eines adjungierten Modells zur Assimilierung von Daten in ein Modell der globalen ozeanischen Zirkulation Ralf Giering |
| EXAMENSARBEIT Nr. 45 Mai 1997 | Einfluß von Wolken auf den spektralen solaren Strahlungsfluß an der Meeresoberfläche Jens Meywerk |
| EXAMENSARBEIT Nr. 46 Mai 1997 | Simulationen zur Bildung und Entwicklung von stratosphärischem Aerosol unter besonderer Berücksichtigung der Pinatuboepisode Claudia Timmreck |
| EXAMENSARBEIT Nr. 47 Mai 1997 | Assimilation von $\delta^{13}\text{C}$-Daten aus marinen Sedimentbohrkernen in das LSG zur Rekonstruktion der Ozeanzirkulation während des letzten glazialen Maximums Arne M.E. Winguth |
| EXAMENSARBEIT Nr. 48 Juni 1997 | Simulation der $^{18}\text{O}/^{16}\text{O}$-Zusammensetzung von atmosphärischem Sauerstoff Ulrike Seibt |
| EXAMENSARBEIT Nr. 49 November 1997 | Satellitengestützte Fernerkundung und Modellierung des globalen CO₂-Austauschs der Landvegetation: Eine Synthese Wolfgang Knorr |
| EXAMENSARBEIT Nr. 50 Dezember 1997 | Zeitscheibenexperimente mit dem atmosphärischen Zirkulationsmodell T42-ECHAM3 für eine verdoppelte und verdreifachte CO₂-Konzentration unter besonderer Beachtung der Änderungen der nordhemisphärischen troposphärischen Dynamik Jan Perlwitz |

ISSN 0938-5177